Autophagy regulation by the p38 MAP kinase

Dissertation

zur Erlangung des akademischen Grades

doctor rerum naturalium

(Dr. rer. nat.)

genehmigt durch die Fakultät für Naturwissenschaften

der Otto-von-Guericke-Universität Magdeburg

von Svenja Anne Bruns, M. Sc.

geboren am 24.10.1987 in Oldenburg

Gutachter: Prof. Dr. rer. nat. Ingo Schmitz

                Prof. Dr. rer. nat. Michael Thumm

eingereicht am   27.09.2016

verteidigt am   16.02.2017

TABLE OF CONTENTS

1 SUMMARY

The term autophagy describes the intracellular engulfment of cytoplasmic contents in autophagosomes and their lysosomal degradation. Autophagy contributes to basal homeostasis via continuous protein and organelle recycling. It is also important to sustain amino acid and energy levels upon nutrient withdrawal, as well as for fighting invading pathogens. Negative regulation by the Gadd45β-MEKK4-MKK3/6-p38 MAP kinase signaling cascade, which inhibits autophagosome-lysosome fusion, was shown to depend on the functional interaction of p38 with the key autophagy protein ATG5.

During this thesis, the interaction was confirmed *in vitro* and ATG5 mutants were generated to identify residues crucial for kinase-docking. Co-immunoprecipitation experiments with ATG5^{T75A}, L90S and L90Q indicated a reduced interaction with p38. However, a clear functional effect during basal or induced autophagic flux in mutant-reconstituted MEF cells was so far not observed. *In vitro* kinase assays with the conjugate of ATG12 and ATG5 pointed to a p38-specific phosphorylation of ATG12. A preliminary mass spectrometry approach suggested Ser36 or Ser37 of ATG12, instead of one of the canonical S/TP motifs, as target residue for p38-mediated phosphorylation. The generation of a RMCE-based transgenic mouse model, by which the physiological role of the Gadd45β-induced signaling cascade should be further elucidated, resulted in a mosaic expression of the transgene and was terminated.

Analysis of the autophagic response in *S. aureus*-infected fibroblast cells demonstrated the association of the bacteria with ubiquitinylated proteins, the recruitment of autophagy receptors such as p62 and OPTN and subsequent engulfment by LC3-II-positive autophagosomal structures. However, *S. aureus* was able to evade these vacuoles prior to lysosomal degradation by a mechanism that involves activation and recruitment of the host MAP kinase p38.

During the establishment of a high-fat diet induced obesity model with Gadd45β knock out (KO) x GFP-LC3 and GFP-LC3 mice of both genders, in particular the female Gadd45β KO mice displayed an enhanced susceptibility towards the high-fat diet compared to their wild type (WT) counterparts. This observation mainly included increased weight, plasma levels of resting glucose, total and HDL cholesterol as well as enhanced pathology of the liver and scapular fat.

2 INTRODUCTION

2.1 Discovery and principles of (macro-) autophagy

2.1.1 General principles of autophagy

Eucaryotic organisms need to cope with various environmental influences and ensure cellular maintenance and preservation even under unfavorable conditions. Consequently, regulating mechanisms have evolved by which the cells can counteract, e.g. nutrient-withdrawal or invading pathogens. Macroautophagy, hereafter termed autophagy, is a catabolic intracellular self-recycling pathway, which is highly conserved from the single-cell *Saccharomyces cerevisiae* (*S. cerevisiae*) to complex mammal organisms such as humans[1]. Engulfment of cytoplasmic proportions by a double-layered membrane results in the formation of a specific vacuole, named autophagosome. Within this vesicular structure, the captured content is transported to the lysosome, where subsequent fusion leads to the intermediate structure of an autophagolysosome. Thereafter, the degradation of the engulfed cargo is performed by lysosomal enzymes (see Fig. 2.1).
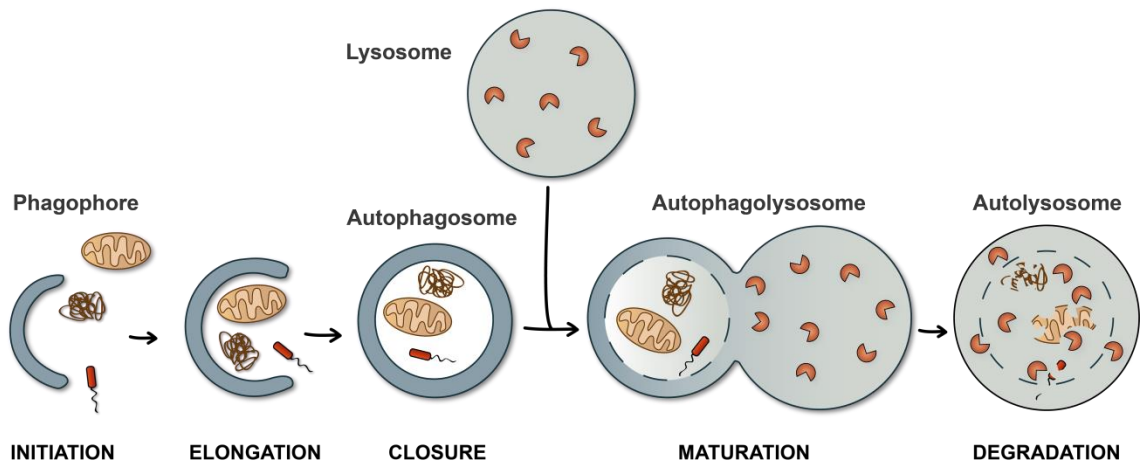
Fig. 2.1: Overview of the different stages of autophagy. Autophagy is a catabolic process by which cytoplasmic portions, containing, e.g. mitochondria, protein aggregates, long-lived-proteins and invasive pathogens, are engulfed in a double-layered vesicle for lysosomal degradation. Depicted here are the different hierarchical steps of autophagy, starting with the *de novo* formation of a double-layered membrane structure named phagophore (initiation). During the elongation, the membrane ends enlarge and engulf bulk or specific cytoplasmic portion. The subsequently formed closed vesicular structure with captured cargo inside is called autophagosome. After optional fusion with endosomal vesicles (not depicted here), the autophagosome is transported to the lysosome for the maturation step. The fusion results in an intermediate autophagolysosome and then reaches the autolysosomal stage, where the cargo is degraded by lysosomal enzymes. Modified from Feng *et al.*[2].

Depending on the environmental conditions, different levels of autophagy and a respectively altered nature of cargo are observed. At a basal level, cells use this degradative pathway for regular protein and organelle turnover. Upregulation of autophagy typically occurs in order to maintain the minimal intracellular supply of amino acids and energy for survival during nutrient-deprivation[3]. Next to this classical role, the autophagic pathway is also able to specifically target unwanted organelles or invading pathogens for degradation (selective autophagy). In addition to direct elimination of pathogens (xenophagy), the latter also provides an important mechanism for immunological signaling, since pathogenic antigens are processed for major histocompatibility complex (MHC) class II-presentation[4].

2.1.2 Discovery of autophagy and the autophagy-related gene family

The term autophagy, which derived from the greek Εαυτός/Eautos and Φάγω/phago, literally means 'self-eating' and was first used by Christian de Duve[5]. The starting point was his study dealing with enzyme pattern distributions, which led to the discovery of lysosomes[6]. Subsequent morphological analysis by electron microscopy (EM) revealed the first characteristics of this vacuole and its 'dense' content[7] and resulted in the term 'cytolysome'. Some years later, in 1962, Ashford and Porter demonstrated that upon glucagon-treatment of hepatocytes whole organelles like mitochondria were frequently enclosed in these putative lysosomes[8]. Novikoff and Essner made similar structural observations and verified the lysosomal character of this vacuole[9]. The first written designation of the term autophagy was performed in a study, which further elucidated the correlation between glucagon and autophagy induction[10,11].

During the following decades, this pathway and especially its mediators were investigated further. For this, a lot of work was performed in yeast, an experimental model facilitating large genetic screens[12,13]. After the identification of the first autophagy-related gene 1 (*ATG1*, former *APG1*) and the respective ATG1 (APG1) protein[14,15], the ATG family of core autophagy mediators subsequently grew[16–18]. With the human ATG12–ATG5 conjugate, the first mammalian counterpart to a respective yeast homologue was found shortly thereafter[19]. Up to now, for many of the more than

30 ATG proteins identified in yeast, mammalian homologues were characterized[20]. Of note, the continuous functional conservation of the autophagic machinery from *S. cerevisiae* to human and throughout a long evolutionary period highlights the importance of this pathway.

2.1.3 Characteristics of microautophagy and chaperone-mediated autophagy

Next to the already described macroautophagy, there are two other types of autophagy known. One mechanistic variant of macroautophagy is microautophagy, where cytoplasmic contents are directly taken up by lysosomes[21,22]. These invaginations or autophagic tubules are mostly induced by nutrient- and nitrogen-starvation and are formed rather unspecifically (mammalian and yeast cells) or specifically (yeast only). The latter includes the sequestration of organelles such as mitochondria (micromitophagy)[23] or of large structures like peroxisome clusters (microperoxyphagy)[24]. The role of microautophagy in the context of macroautophagy is controversially discussed; nevertheless, it is likely to act as a compensatory mechanism, e.g. by maintaining lysosomal size and membrane composition[22].

Chaperone-mediated autophagy (CMA) was only found in mammalian cells, and like microautophagy it does not involve vesicular transport. Instead proteins that undergo CMA are selectively targeted by their amino acid sequence and individually transported to the lysosome for degradation[25]. The recognition and translocation is performed by the heat shock-cognate chaperone protein of 70 kDa (hsc70) chaperone[26]. At the lysosomal membrane, hsc70 interacts with the membrane-spanning receptor LAMP-2A, which facilitates the transport of the meanwhile unfolded target by assembling a pore-forming multi-protein cluster[27]. One function of CMA is the breakdown of proteins during prolonged starvation[28]. Thereby, CMA, like the other forms of autophagy, contributes to the availability of energy and amino acids during nutrient-deprivation. Furthermore, the possibility to target individual proteins results in an important role for CMA during quality control, e.g. under oxidative stress conditions[29].

2.2 Mammalian autophagy - the different stages and their key mediators

2.2.1 Initiation and nucleation

As previously mentioned, autophagy is a multistep process. Thus, it is highly hierarchically organized. The starting point for autophagy initiation is the transmission of a stimulating signal from outside the cell. In order to ensure proper regulation, the nutrient- and energy status as well as the stress level of the cell are constantly reviewed by respective sensors, which themselves start downstream signaling cascades. The central integration of all resulting signals is performed by the mammalian target of rapamycin complex 1 (mTORC1), which includes the serine/threonine kinase mTOR[30–32] (see Fig. 2.2A). According to the cellular needs represented by the incoming information, the complex adjusts the cellular programs. Under nutrient-rich conditions, mTORC1 is constantly activated and stimulates cell growth and proliferation by phosphorylation of downstream substrates. Consequently, catabolic processes as, e.g. autophagy, are inhibited by active mTORC1. This negative regulation is performed by the interaction of the activated mTORC1 with the preinitiation complex of autophagy. This so called UNC-5 like autophagy activating kinase 1 (ULK1) complex consists of the serine/threonine kinase ULK1, ATG13, FAK family kinase-interacting protein of 200 kDa (FIP200) and ATG101 (Fig. 2.2A). Association of mTORC1 results in the inhibitory phosphorylation of ULK1 and ATG13. Upon nutrient-deprivation, mTORC1 is released from the ULK1 complex and the mTOR-sites are dephosphorylated. This in turn enables autophosphorylation of ULK1, which is followed by ULK1-mediated phosphorylation of FIP200 and ATG13[33–35]. At the site of autophagosome initiation, the ULK1 complex activates the nucleation machinery, which is led by the class III phosphatidylinositol 3-kinase (PtdIns3K) complex. Next to the catalytic subunit vacuolar protein sorting 34 VPS34 and the scaffolding protein p150, the complex consists of Beclin1 and the directly bound autophagy-specific factor ATG14L[36] (Fig. 2.2A). The activation of the PtdIns3K complex is also mediated by phosphorylation, where Beclin1 and VPS34 have been shown to be direct targets of ULK1[36,37]. It is noteworthy that also different regulatory complex compositions were identified, e.g. where UV radiation resistance-associated gene (UVRAG) protein alone, or UVRAG together with Rubicon interacts with Beclin1. The exact regulatory effect of these factors is controversially discussed and still a topic

of ongoing research[20,38–40]. The central function of the ATG14L-containing PtdIns3K complex is the synthesis of a local phosphatidyl-3-phosphate (PtdIns(3)P) pool (Fig. 2.2A). This phospho-lipid is essential for the recruitment of further proteins and lipids that drive the *de novo* formation of the first autophagosomal structure, the phagophore[41]. Of note, the origin of the initial membrane stack for this step is still controversially discussed, since there is most likely not only one source to be considered[20,42,43]. For sure, subdomains of the endoplasmatic reticulum (ER) are involved[41,44,45], however mitochondria[46], Golgi complex[47] and parts of the plasma membrane[48] as well as recycling endosomes[49] have also been shown to contribute to the phagophore-formation.

2.2.2 Elongation and closure

Upon PtdIns(3)P synthesis, elongation of the double-layered membrane and completion to a closed autophagosome is performed by subsequent recruitment of ATG proteins, which are mainly organized in two conjugation systems[50]. First, the ATG12–ATG5 conjugate ("–" indicates a covalent binding) is assembled in an ubiquitin-like reaction driven by the E1-like ubiquitin activating enzyme ATG7 and the E2-like ubiquitin conjugating enzyme ATG10[18,19] (Fig. 2.2B). Thereby, the linkage of the C-terminal carboxy group (glycine 140) of ATG12 to the lysine 130-side chain of ATG5 results in an isopeptide bond. Subsequently, the ATG12–5 conjugate interacts with the N-terminus of ATG16L1 in an ATG5-dependent manner. Due to dimerization of ATG16L1 via its coiled-coil domain (CCD), an 800 kDa mega-complex is formed[51]. Recent structural analysis also revealed an independent role for the N-terminal helix in ATG16L1 self-dimerziation[52]. In contrast to the yeast homologue, mammalian ATG16L1 harbors seven C-terminal WD40-repeats, named after the tryptophan-aspartic acid-ending of these repetitive amino acid units. They are structurally organized in a β-propeller and thought to be a platform for interaction of proteins in mammals[51].

Association of ATG12–5 with ATG16L1 is crucial for the autophagosomal-localization of the conjugate. Nevertheless, the dependency is bilateral, since translocation of ATG16L1 was found to be ATG5-dependent[51]. Neither the conjugate,

nor ATG16L1 harbor typical membrane-binding motifs, thus another protein is likely to act as membrane anchor for the ATG12–ATG5-ATG16L1 complex. Indeed, FIP200, part of the ULK1 autophagy initiation complex was shown to be an interaction partner of ATG16L1. Via the FIP200-interacting domain that is located in between the CCD and the WD40-repeats, proper targeting of ATG16L1 and the associated ATG12–5 conjugate to the phagophore is performed[53,54]. However, another study identified the PtdIns(3)P-effector WD-repeat protein interacting with phosphoinosides 2b (WIPI2b) to be essential for the ATG16L1-recruitment under starvation conditions[55]. Of note, the respective mapping revealed a WIPI2b-interaction site on ATG16L1 within the region of amino acid 207 to 242 that is adjacent, but distinct from the previously postulated FIP200-binding motif. Actually, the two sites are localized on opposite surfaces of the folded ATG16L1, thus simultaneous interaction for the formation of an ATG16L1-FIP200-WIPI2b-trimer would be possible. Nevertheless, blocking of the ATG16L1-FIP200-interaction alone did not significantly alter the induction of autophagy. Since the FIP200-binding mutants used in the former studies were also shown to be deficient for WIPI2b-interaction, the observed effects at that time were most likely not due to FIP200- but rather to WIPI2b-dependency[55]. Notably, it has been shown that the ATG12–ATG5-ATG16L1 complex is predominantly found during the phagophore stages and dissociates right before or after closure of the autophagosome[51,56,57].

Functionally, the ATG12–5-ATG16L1 complex has the role of an E3-like ubiquitin conjugating enzyme, which is necessary for the second ubiquitin-like conjugation system (see Fig. 2.2). During a concerted reaction, microtubule-associated protein 1 light chain 3 (MAP1LC3, hereafter short LC3) is processed from the cytosolic LC3-I to the membrane-bound LC3-II by the conjugation to phosphatidylethanolamine (PE)(Fig. 2.2B). First, the immature precursor form of LC3 (pro-LC3) is cleaved by ATG4B to obtain LC3-I, which is characterized by an exposed C-terminal glycine[58]. Afterwards, LC3-I is activated by ATG7 (E1-like) and subsequently transferred to ATG3 (E2-like) for conjugation to PE[59,60]. In contrast to the first ubiquitin-like system, adequate conjugation of the LC3-I-glycine to the amino group of PE is dependent on an additional E3-like activity, which is fulfilled by the ATG12–5 conjugate (Fig. 2.2B). In the first step, ATG3 is bound to ATG12 via a high-affinity interaction motif and afterwards the LC3-I-to-PE conjugation is stimulated by the specific continuous

ATG12–ATG5 conjugation patch[61]. In yeast, the rearrangement of the catalytic center of Atg3 was identified as an underlying mechanism responsible for this activation[62]. The resulting LC3-II is bound to the inner and outer part of the evolving autophagosome and was shown to be crucial for its further biogenesis, including membrane elongation and closure[63–66]. Since LC3-II is associated with the autophagosomal membrane through all following steps, it is the most widely used marker for monitoring autophagy[67,68].
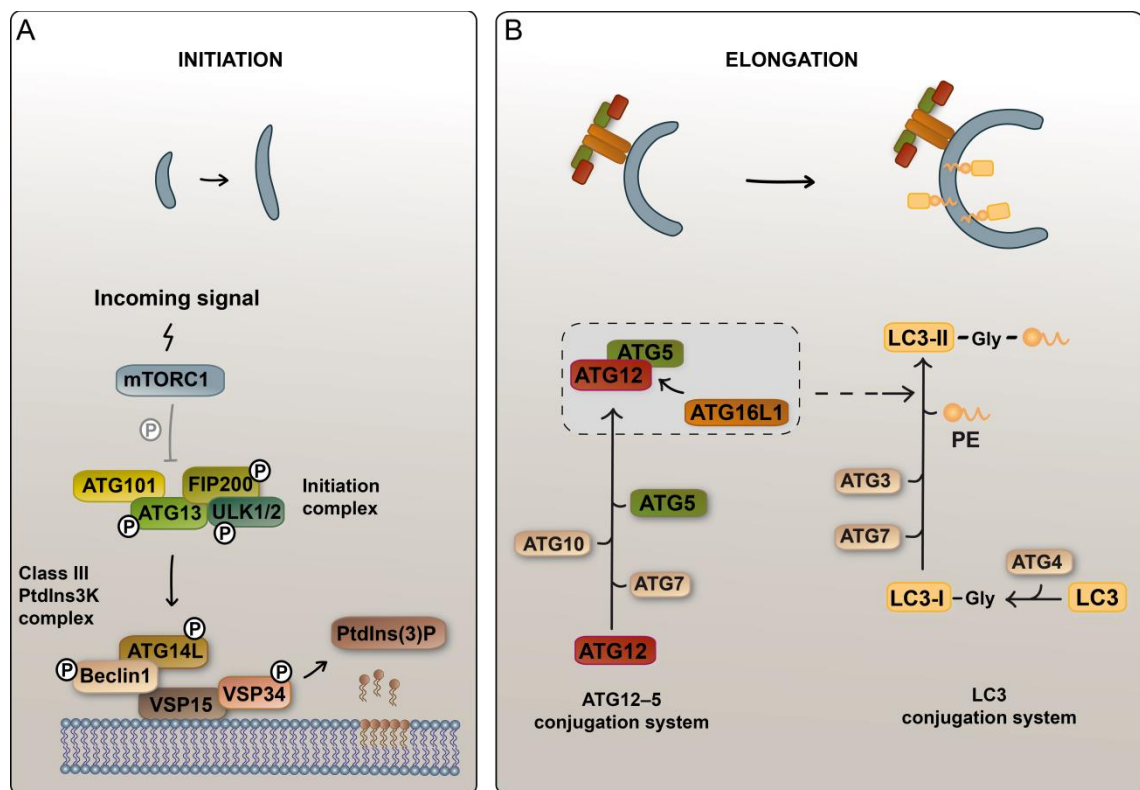
Fig. 2.2: Major molecular mechanisms important for autophagy initiation and elongation of the autophagsomal membrane. (A) Upon an incoming signal, mTORC1 is inactivated and dissociates from the ULK1/2 complex. Subsequently, the inhibitory phosphorylation by mTORC1 is turned to activating (auto-)phosphorylations of the initiation complex by ULK1/2 itself. This leads to the stimulation of the Class III PtdIns3K complex at the site of the forming phagophore. The local production of PtdIns(3)P drives the recruitment of further lipids and autophagy mediators. **(B)** During elongation, the double-layered membrane structure grows further, which is dependent on two ubiquitin-like conjugation systems. First, the ATG12–5 conjugate is formed by a concerted action of the E1-like ubiquitin-activating enzyme ATG7 and the E2-like ubiquitin-conjugating enzyme ATG10. The covalently linked conjugate forms a multimer complex with ATG16L1, which is crucial for binding to the autophagosomal membrane. Furthermore, the formed complex acts as E3-like ubiquitin conjugation enzyme for the LC3 conjugation system. This final conjugation of LC3-I to phosphatidylethanolamine (PE) is already prepared by subsequent activity of ATG4, ATG7 and ATG3. The resulting LC3-II is bound to the inner and outer autophagosomal membrane and has a central role during the recruitment of specific cargo. Modified from Wesselborg and Stork[20] and Green and Levine[69].

Next to the LC3 family with its isoforms LC3A, LC3B, LC3B2 and LC3C[70], another superfamily with analogue functionality exists. The GABARAP/GATE16 proteins originally were identified during membrane trafficking studies[71–73], but are also involved in the formation of autophagosomes[74]. In contrast to the yeast system that solely relies on Atg8, the number of homologs in mammals point to a distinct role for each member. For instance, LC3B and GABARAPL2 (also known as GATE-16) have been shown to act in different time windows[75], however, a detailed investigation of all known members is needed to fully understand their specific role. Importantly, next to membrane-association, LC3-II is also interacting with adaptors, so called autophagy receptors, by their LC3-interacting region (LIR), to specifically recruit cargo to the site of autophagosome formation. The tagging of these cytoplasmic components is usually mediated by ubiquitinylation[76]. In contrast to bulk, rather undirected autophagy, this mechanism is called specific autophagy and will be reviewed in a later chapter, since one form is the specific targeting of bacteria (xenophagy)[77]. Either before or during the fusion of autophagosomes with lysosomes, the outer-bound LC3-II is recycled to LC3-I by ATG4B-mediated cleavage, and thus, not all LC3-II initially involved is degraded[78,79].

2.2.3 Fusion of autophagosomes with lysosomes (maturation)

Upon closure of the autophagosomal membrane, the resulting autophagosomes eventually merge with vesicles originating from the endocytosis route to an amphisome, before fusion with lysosomes occurs in the final step of autophagy[49,80,81]. The underlying molecular mechanisms for autophagosome-lysosome fusion are still not completely understood. Since the Rab proteins, which are members of the subgroup of the Ras-like guanosine triphosphate (GTP)ase superfamily, have been reported to be crucial for the early steps of autophagosome biogenesis[82], their influence on autophagic maturation was analyzed as well[83]. Next to data on Rab24 and Rab8b, numerous studies identified Rab7 as a key mediator for the autophagosome transport to and fusion with lysosomes[84,85]. In line with these findings, downstream effectors of Rab7 were found that are important during autophagy, e.g. the FYVE-coiled coil-containing protein 1 (FYCO1) for autophagosomal transport[86] or the homotypic fusion and protein sorting (HOPS) complex for fusion[87].

In general, the fusion of two vesicular structures results in the combination of both contents and membrane composition into one compartment. Soluble (*N*-ethylmaleimide-sensitive factor) attachment protein receptor (SNARE) proteins are crucial mediators during endocytotic trafficking, since they prepare membrane fusion by locally increasing the permeability and initiating the opening[88]. In principle, they mediate their function by forming a parallel four-helix bundle (Qa, Qb, Qc and R) between SNARE partners localized on both vesicles[89]. Within early autophagosome biogenesis, e.g. the SNAREs vesicle-associated membrane protein 7 (VAMP7) in combination with its partners syntaxin7, syntaxin8 and vesicle transport through interaction with t-SNAREs 1b (Vti1b)[90] was shown to enable homotypic fusion of ATG16L1-positive autophagosome precursors. Indeed, autophagosome-lysosome fusion (maturation) is achieved via help of specific SNARE interactions, since previous studies identified for example the dependency on VAMP7[91] and VAMP8 in combination with Vti1b[92]. A lot of attention has been drawn to the identification of the Qa-SNARE syntaxin17, since it was shown to be specifically recruited to autophagosomes after starvation. Together with the lysosomal R-SNARE VAMP8 and the Qb,c-SNARE synaptosome-associated protein 29 (SNAP29) it promotes autophagosome-lysosome fusion[93] (see Fig. 2.3). Recently, homo-oligomerized ATG14L, a member of the PtdIns3K complex, was identified to stabilize the syntaxin17-SNAP29 complex on autophagosomes via binding to syntaxin17. Is was shown that this priming promotes the functional interaction with the lysosomal VAMP8, thus driving the autophagosome-lysosome fusion[94].

Next to the described classical mediators of trafficking pathways also other factors are implicated in the regulation of autophagosome-lysosome fusion. One example is the tectonin β-propeller repeat containing 1 (TECPR1) protein, which was originally identified in a screening experiment as an interaction partner of ATG5[95]. The following study characterized TECPR1 as a crucial factor specifically for the formation of bacteria-containing autophagosomes and for this purpose it is associated with ATG12–ATG5-ATG16L1 and WIPI2[96]. Another study elucidated a role for TECPR1 in canonical autophagy as well. In detail they showed that the ATG12–5 conjugate needs to switch its complex partner from the former autophagosomal ATG16L1 to the lysosomal TECPR1 during autophagosome maturation[97]. Importantly, inhibition of this exchange by the analysis of TECPR1 knock out (KO) cells resulted in an accumulation

of autophagosomes during stimulation. In contrast to the previous study, direct interaction of the TECPR1 pleckstrin homology (PH) domain with PtdIns(3)P was confirmed by the use of recombinant ATG12–5-TECPR1 complexes. Thus, the accessibility of the PH domain most probably depends on the binding of TECPR1 to ATG5 via the ATG12–ATG5-interacting region (AIR). Due to the specific co-localization of TECPR1 (and subsequently ATG12–5) with lysosomal markers, it was suggested that TECPR1 recruits the ATG12–5 conjugate to lysosomes by simultaneous interaction with ATG5 and PtdIns(3)P[97]. Recent structural analysis were able to narrow down the interaction site of TECPR1 to an ATG5 (Five)-interacting motif (AFIM), that is conserved in the α-helix of both ATG16L1 and TECPR1 resulting in a competitive binding to the ATG12–5 conjugate. Of note, the specific interaction with the conjugate is dependent on the residual part of the helix. Additionally, this study demonstrated an increased binding strength of TECPR1 to ATG5 in a lower pH environment. Taken together, the role of TECPR1 as mediator for autophagosome-lysosome fusion was strengthened by these findings[52] (see Fig. 2.3).
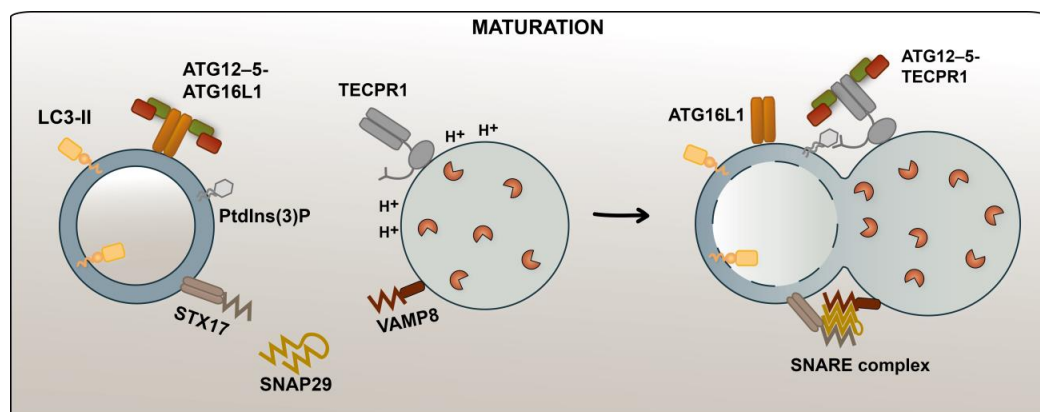
Fig. 2.3: Crucial mechanisms for autophagosome-lysosome fusion (maturation). Fusion of autophagosomes and lysosomes is at first dependent on a close proximity of both vesicular structures. One important factor is the TECPR1 protein, which was shown to have an ATG5-binding motif comparable to ATG16L1 and is associated with lysosomes. Thus, switching the complex partner from the former ATG16L1 to the lysosomal TECPR1 enables tethering. The TECPR1-ATG5 interaction is enhanced in the surrounding of a low pH and further supported by the interplay between the PH domain of TECPR1 and the autophagosomal PtdIns(3)P. The actual fusion of the vesicles is mediated by the specifically located SNARE proteins syntaxin17 (STX17) and VAMP8 together with SNAP29, via the formation of a specific four-helix bundle. Modified from Kim *et al.*[52], Chen *et al.* [97]and Itakura *et al.*[98].

As soon as the fusion of autophagosomes with lysosomes has taken place, the degradation of the captured autophagosomal cargo is started by lysosomal hydrolases[99,100]. Notably, the lysosomal activity is upregulated upon maturation and

depends on mTORC1 suppression[101]. Subsequently, amino acids and other degradation products are released to the cytosol where they can be used for protein synthesis or serve as an energy supply of the cell[102].

2.2.4 Functional and structural aspects of the mammalian ATG12–5 conjugate

As mentioned above, the ATG12–5 conjugate is an essential mediator of autophagy, since it stimulates the ATG3-dependent conjugation of LC3 to PE. Additionally, proper autophagosome-lysosome maturation has been shown to rely on the interaction of ATG5 with TECPR1. In both cases, crystal structure analyses gave a more detailed understanding of the structural background behind these functionalities. In the following overview the most important residues and structural elements of the ATG12–5 conjugate that are known to have functional relevance are summarized[52,97].

Tab. 2.1: Overview about functional relevant structures and residues of ATG12–5

Part	Structure/Residue(s)	Purpose/Functionality
ATG5	K130	Covalent conjugation to ATG12
ATG5	K78, H80, L113, S127, K130, A134, L135, E131, R188, Q200	Interface in ATG12–5 conjugate (E3-like activity)
ATG5	Interface residues and K138, N143, M145, Q146, H150, I168	Continuous patch in ATG12–5 conjugate (E3-like activity)
ATG5	Ubiquitin-fold domain 1 and 2 (UFD-1, UFD-2), N-terminal helix α1	Interaction with ATG16L1
ATG5	V7, I243, P245, T249, P250, W253, L258, H241, N10, R41	Interaction with the ATG5(five)-interaction motif (AFTM) of TECPR1 or ATG16L1
ATG5	P17, Y36, H55	Interaction with the residual helical region of ATG16L1
ATG5	R15, L38, K51	Interaction with the C-terminal unstructured region of TECPR1
ATG12	G140	Covalent conjugation to ATG5
ATG12	N105, F108, A109, P110, N113, Q114, C122, F123, G140	Interface in ATG12–5 conjugate (E3-like activity)
ATG12	Interface residues and V62, G63, L92, Q106, S107 A138, W139	Continuous patch in ATG12–5 conjugate (E3-like activity)
ATG12	K54, K72, W73	Interaction with ATG3

2.3 Kinases as major regulators of autophagy

Basal autophagy contributes to cellular homeostasis and constant self-renewal on the one hand and acts as a survival mechanism that ensures the maintenance of crucial cellular functions during harsh conditions on the other hand. Nevertheless, a prolonged high level of autophagy can also be dangerous and may lead to unwanted cell death[103]. Thus, the ability for tight regulation of autophagy at several steps is important to adjust the level of the autophagic flux according to the cellular needs. This is mainly achieved by protein-protein interactions in combination with posttranslational modifications such as acetylation, ubiquitinylation or phosphorylation[104].

Kinases are crucial players throughout all steps of autophagy. Especially in the initiation phase the hierarchical order of events highly depends on the functionality of kinases. The activation of specific kinase cascades by an incoming signal, such as low nutrient levels (growth factors, amino acids), lack of energy resources (adenosine triphosphate [ATP] level) or cellular stress (hypoxia, DNA damage), mediates the initiation. Usually downstream signal transmission is mediated by subsequent phosphorylation. One example is the Akt kinase, which senses the presence of growth factors. Upon activation, the kinase phosphorylates the tuberous sclerosis 2 (TSC2) protein, which results in the inhibition of the TSC1-TSC2 complex and subsequent mTORC1 activation[105] (Fig. 2.4A). The close interrelation of the network is demonstrated by the contrasting effect of adenosine monophosphate (AMP)-activated protein kinase (AMPK)-mediated TSC2 phosphorylation, which occurs upon high AMP/ATP ratios and results in the inhibition of mTORC1[106] (Fig. 2.4B). Downstream of mTORC1, the inactivation of the ULK1 complex by mTORC1 under nutrient-rich conditions is also mediated by phosphorylation. Therefore, the dissociation of mTORC1 upon autophagy stimulation leads to subsequent (self-)phosphorylation, thus activation, of the ULK1 complex[33,107]. Next to mTORC1, AMPK and Akt have been shown to directly influence the phospho-status of ULK1 depending on the incoming signal[107,108] (Fig. 2.4A and B). Moreover, for some cascades with ULK1-participation feedback mechanisms have been identified, providing another hierarchy of regulation[109,110]. A factor that mediates regulation on multiple levels of the autophagy initiation cascade is activating molecule in Beclin1-regulated autophagy 1 (AMBRA1).

Under basal conditions, AMBRA1 is phosphorylated in an inhibitory manner by active mTOR[111] and anchors the PtdIns3K complex to the cytoskeleton via binding to Beclin1 and the dynein motor complex[112]. Following autophagy induction, the activated ULK1 complex specifically phosphorylates AMBRA1, which leads to ER-translocation of the AMBRA-PtdIns3K complex and thereby promotes the *in situ* formation of a double-layered phagophore. Furthermore, AMBRA stabilizes the functionality of ULK1 when it is released from the mTORC1-mediated inhibition, by induction of tumor necrosis factor (TNF) receptor-associated factor 6 (TRAF6)-mediated ubiquitinylation[111].

2.3.1 Mitogen-activated protein kinases in cellular and autophagic regulation

The group of mitogen-activated protein (MAP) kinases (MAPK), especially the extracellular signal-regulated kinase (ERK) 1/2, has been connected to autophagy in multiple ways. ERK1/2 is, e.g. an effector of the growth factor receptor and it phosphorylates the TSC1-TSC2 heterodimer under nutrient-rich conditions (similar to Akt), which results in mTORC1 activation, and thus, autophagy inhibition[113] (Fig. 2.4A). On the other hand, ERK1/2 can also activate autophagy, if it is induced downstream of AMPK. During this pathway the subsequent activation of TSC leads to a mTORC1 disassembly and moderately enhances the Beclin1 level, which results in autophagy induction[114]. Not only autophagy initiation can be influenced by ERK phosphorylation, but also maturation. A cancer-based study revealed the inhibitory effect of a sustained ERK activation on autophagosome-lysosome fusion[115].

A further member of the MAPK family, the c-jun N-terminal protein kinase 1 (JNK1) has also been shown to regulate autophagy, e.g. during ceramide stimulation or starvation induced-autophagy. As a result of the JNK1-mediated phosphorylation of the anti-apoptotic mediator Bcl-2, Beclin1 is released from the inhibitory heterodimer. Subsequently, Beclin1 completes the PtdIns3K complex, which in turn drives further autophagic flux[116–118] (Fig. 2.4C).

The third prominent subgroup of MAPK is the p38 kinase family. p38 kinases are activated by a variety of different stimuli ranging from growth factors and inflammatory cytokines to environmental stress signals[119–124]. With p38α[119,125],

p38β[126], p38γ[127-129] and p38δ[130,131] four different members have been identified and characterized. The respective studies revealed a sequence identity between all four members of approximately 60%. Nevertheless, the α- and β-form are more similar to each other and the same is observed for p38γ and p38δ[132]. Due to its ubiquitously strong expression pattern, p38α is the best characterized form and will be mainly described below.

A number of studies revealed diverse roles for p38α in the field of autophagy regulation, since the kinase showed pro- as well as anti-autophagic impact depending on the stimuli used and the cell type analyzed. As the kinase was generally found to target substrates in the cytoplasm[133] as well as in the nucleus[134] and to functionally shuttle in between the two subcellular locations[135], the different pools of p38α, which mediate the wide range of responses, are determined by the extracellular stimuli[136]. The first link between p38 and autophagy regulation was identified in rat hepatocytes. After exposure to osmotic stress and subsequent p38-activation autophagy-dependent proteolysis was inhibited[137]. In the same line, p38 activation induced by hypo-osmotic insulin- and amino acid-dependent cell swelling (hydration) exerts an inhibitory effect on autophagosome formation[138].

In terms of metabolism, p38 recently was reported to modulate the glucose-uptake and -utilization in cancer cells under starvation conditions in order to reduce reactive oxygen species production and prevent subsequent cell death[139]. A general suppression of autophagy is performed by p38 to ensure the functionality of T cells. Previously, it was shown that autophagy drives glycolysis, thus is involved in the metabolic program leading to proliferation and expansion[140]. Consistently with these findings, senescent CD8+ T cells display only a low autophagic flux. This adaptation is controlled by p38 in a mTOR-independent regulation pathway that involves the interruption of the ATG9-p38-interacting protein (p38IP) interaction[141]. The importance of ATG9 for autophagy regulation was originally elucidated in HEK293T cells, where this transmembrane protein was shown to be selectively recruited from the *trans*-Golgi network (TGN) and endosomes to autophagic structures upon starvation. This redistribution is crucial for the autophagic flux and was demonstrated to depend on ULK1 and ATG13[47]. So far, the only known direct interaction partner of ATG9 is p38IP and after induction of p38 the formation of the high-affinity p38-p38IP

complex was demonstrated leading to a disturbed functional translocation of ATG9 in cytotoxic T cells. Hence, in this setting p38 activation provides a putative way for a negative feedback loop[142].
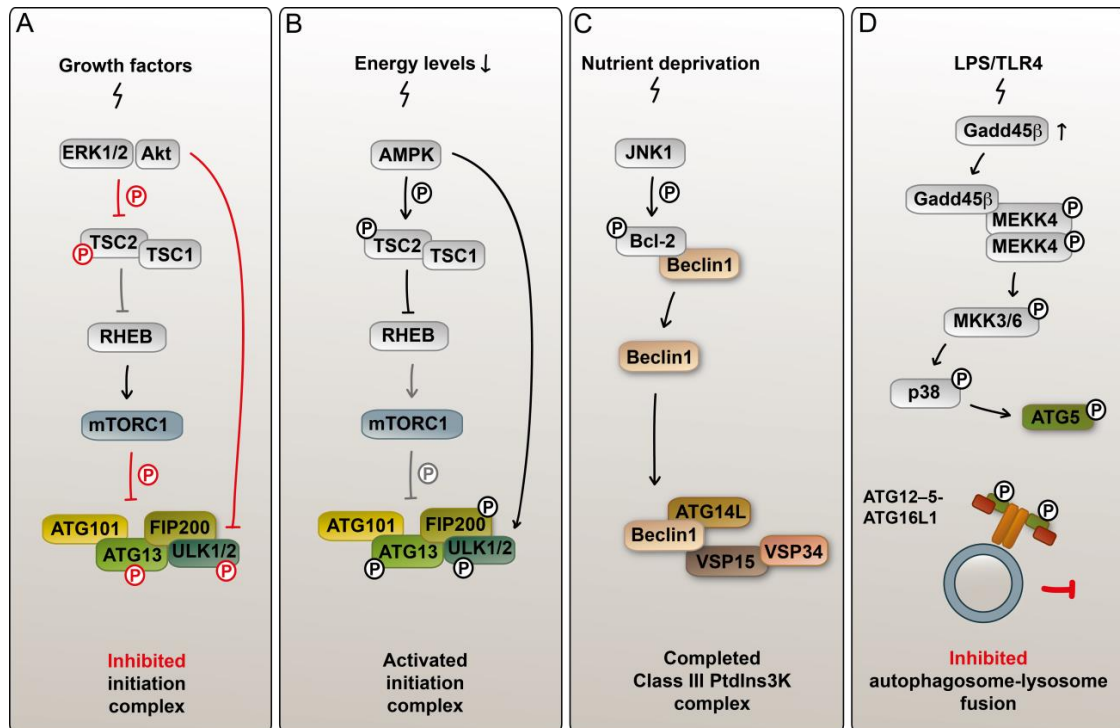
Fig. 2.4: Regulatory roles for selected kinases in the initiation of autophagy. (A) The kinase Akt and the MAPK ERK1/2 are able to negatively regulate the autophagy induction upon growth factor signaling either by phosphorylation of the TSC2-TSC1 complex and subsequent activation of mTORC1, or in the case of Akt additionally by direct interaction with ULK1. **(B)** Low energy levels are transduced by AMPK-mediated phosphorylation of TSC2, which in the end inhibits mTORC1 and results in the activation of the initiation complex. **(C)** Upon starvation, JNK1 phosphorylates the anti-apoptotic protein Bcl-2. This leads to the release of Beclin1 and enables the formation of the functional Class III PtdIns3K complex. **(D)** The Gadd45β-MEKK4-MKK3/6-p38 signaling cascade was reported to lead to phosphorylation of ATG5 by specifically translocated phospho-p38. This results in an impaired autophagosome-lysosome fusion, thus a negative regulation of the autophagic flux. The exposure of cells to LPS, which activates TLR4-signaling, was demonstrated as one possible stimulus for this negative feedback loop. Cartoon according to Wesselborg and Stork[20], Wei *et al.*[117] and Keil *et al.*[133].

Additionally, the p38 MAPK is able to directly regulate maturation, thus a distinct step of the autophagic flux. In a beforehand published study, the specific translocation of phospho-p38 (p-p38) to autophagosomes after activation of the stress sensor protein growth arrest and DNA damage-induced 45 β (Gadd45β)-MAPK/ERK kinase kinase 4 (MEKK4)-mitogen-activated protein kinase kinase 3/6 (MKK3/6) cascade by transient co-expression of Gadd45β and MEKK4 in NIH/3T3 cells was reported. In this regulatory pathway, the activated p38 interacts with ATG5 and induces its subsequent

16

phosphorylation, which results in the inhibition of autophagosome-lysosome fusion. This mechanism is thought to dampen the autophagic flux after a strong initiation signal for example after activation of toll-like receptor 4 (TLR4) by exposure to lipopolysaccharides (LPS)[133] (Fig. 2.4D).

2.3.1.1 Characteristics of p38-substrate interaction during signaling

The upstream kinases directly responsible for p38 activation mainly are MKK3 (favors p38α,γ and δ) and MKK6 (all p38 isoforms), nevertheless also MKK4-dependent phosphorylation of p38 was shown[143–145]. Acceptor of the MKK-mediated dual phosphorylation is a conserved threonine-glycine-tyrosine motif (T180-G-Y182) within the activation loop. The middle residue is specific for the different MAPK families and together with the loop length these characteristics were shown to determine substrate specificity and auto-phosphorylation capacity[146]. As all MAPK, p38 is a serine/threonine (S/T) kinase, thus preferably phosphorylates its substrates at serine-proline or threonine-proline (S/TP) sites. The p38 kinase domain consists of the N- and the C-lobe, which represents the typical architecture of kinases. Of note, the ATP binding site of p38 is localized in the N-lobe, while C-lobe harbors the P+1 region or catalytic cleft, which binds to the phospho-acceptor residues of the substrate during a functional interaction [147](see Fig. 2.5). In general, protein-protein interactions are controlled by the concentration, availability and localization of both partners[136]. Importantly, a common feature of functional interactions between MAPK and their substrates is the prior docking of the kinase via a specific groove at a characteristic site of the substrate. After the upstream activation of p38, the binding of ATP and docking to the substrate usually results in a conformational "closing", which is characterized by the spatial approximation of the γ-phosphate and the substrate target site[148] (see Fig. 2.5). This mechanism was originally identified for JNK and its canonical substrate, the transcription factor c-jun[149]. Functionally this pre-organization of kinase and substrate is thought to largely contribute to specificity and effectiveness of the downstream activation[134,150–152]. In addition, it can also serve as a recruiting platform for further signaling components[153]. Furthermore, in the case of p38, a recent study reported that docking is critical for the allosteric enhancement of p38α-activity, which may prevent uncontrolled phosphorylation mediated by p38[147] (see Fig. 2.5).

The initially reported kinase-groove responsible for docking was termed CD (common docking) domain and is positioned distinct from the activation site. The site was characterized by a surface-exposed stretch of negative-charged residues, in particular Asp313, Asp315, and Asp316 for p38α[154,155]. One of these studies additionally identified Glu160 and Asp161 as a crucial motif (ED motif) for the interaction between p38 and MAPK-activated protein kinases (MAPKAPK)[154].
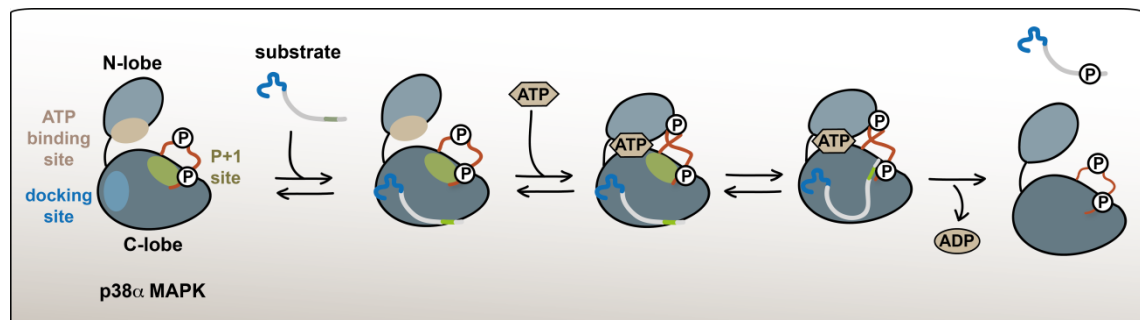
Fig. 2.5: Structural changes in p38α upon substrate docking and ATP binding result in enhanced enzymatic activity. In the first cartoon of the activated p38α, the major interaction regions ATP binding site, substrate docking site and P+1 site (catalytic cleft) of the kinase are depicted. The interaction of the substrate (here MAPKAPK2) docking region (light blue) with the corresponding kinase docking site enables pre-orientation of the substrate and favors subsequent ATP binding. Notably, the order of these two highly rate-determining steps is not completely clear[147]. The resulting conformational change leads to the binding of the substrate's phospho-acceptor site (green) within the P+1 region of the kinase. Subsequently, the substrate becomes phosphorylated and is released together with adenosine diphosphate (ADP) by the rearrangement of the kinase conformation. Cartoon performed according to Tokunaga *et al.*[147].

However, shortly thereafter a further p38 docking groove common for the substrate MEF2A and the upstream kinase MKK3b was described. In this study, Ile116 and Gln120 of p38 were shown to have a crucial impact on the interaction with effector peptides but not the CD or ED residues[156]. Thus, an MAPK-wide valid determination of crucial docking residues or structures may be difficult. Therefore, further investigations comparing different substrates are needed to fully elucidate the underlying mechanisms of substrate-docking.

The corresponding interaction domains on MAPK substrates are the so called docking sites (D sites), which were described throughout a number of different studies for effector molecules such as transcription factors[156], as well as for downstream kinases[157] or phosphatases[158]. Notably, the critical residues are located downstream or upstream of the phospho-acceptor site and spatial variations concerning the distance

to the acceptor site were reported. Typically, a positively-charged basic cluster of arginine and lysine residues is either headed or followed by a hydrophobic motif with leucine, isoleucine and/or valine[155,159] (Tab. 2.2).

Tab. 2.2: Docking sites of p38-interaction partners

Interaction partner	Type	Docking site
ATF2	Transcription factor	VHKHKHEMTLKFGPARN[134]
MEF2A	Transcription factor	RKPDLRVVIPPSS[152,156]
SAP-1	Transcription factor	RSKKPKGLGLAPTLVI[160]
MAPK-interacting kinase 1 (MNK1)	Kinase	LARRRALAQAGRSR[155]
Mitogen- and stress-activated kinase 1 (MSK1)	Kinase	LAKRRKMKKTSTST[161]
MAPK-activated protein kinase 2 (MAPKAPK2)	Kinase	NPLLLKRRKKARALEAAA[157,162]
Ribosomal S6 kinase B (RSKB)	Kinase	APLAKRRKQKLRS[163]
MKP5	Phosphatase	CADKISRRRLQQGKITV[158]

Blue: basic residues; red: hydrophobic residues

Of note, in addition to the described classical D domain also a phenylalanine-xaa-phenylalanine (FxF) motif was shown to have an impact on the selectivity of at least some ERK- and p38-substrate interactions[160,164,165].

2.3.1 Role of the stress sensor Gadd45β in cellular signaling

Recently the stress sensor protein Gadd45β was reported to initiate a signal cascade leading to a distinct p38-mediated negative regulation of the autophagic flux[133]. This finding demonstrated an additional pathway in which Gadd45β can contribute to regulatory signaling. The first Gadd45 gene was originally identified as upregulated transcript in response to growth-arresting stress stimuli, such as ultra-violet light exposure and other genotoxic stressors that led to DNA damage[166,167]. Next to Gadd45α (previously also named DTTIT1), the two other homologue members Gadd45β (MyD118)[168] and Gadd45γ (CR6)[169] were cloned shortly afterwards to complete the highly conserved protein family. With their molecular weight of 18 kDa all Gadd45 proteins are relatively small. Furthermore, all members display unusual high net negative charges, hence are acidic proteins[170]. Since Gadd45 proteins lack

intrinsic enzymatic activity, their regulatory role during stress signaling and differentiation is controlled upstream by transcription levels. Moreover, the mediation of downstream signaling by Gadd45 proteins depends on protein-protein interactions, which induce subsequent posttranslational modifications[171].

The numerous studies investigating the role of Gadd proteins elucidated that these proteins are able to induce diverse and even contrasting cellular responses in apoptosis, terminal differentiation and cell cycle arrest, depending on the tissue and the stimulus investigated. Hence, in particular Gadd45β will be outlined here. Of note, some of the described features overlap with the other two Gadd45 proteins, while others are distinct. Transcriptional upregulation of Gadd45β was originally identified in M1d+ myeloid precursors after stimulation with interleukin 6 (IL-6) in order to stop cell growth and initiate differentiation[168]. In the same study IL-1, LPS and Leukemia inhibitory factor (LIF) were identified as further agents stimulating Gadd45β expression. Thereafter, also transforming growth factor β (TGF-β) and TGF-α were shown to strongly induce Gadd45β transcription via SMAD proteins or the transcription factor nuclear factor-κB (NF-κB) respectively[172–175]. Noteworthy, the intracellular localization of Gadd45β during signaling was shown to be preferably within the nucleus[176].

Downstream signaling of Gadd45β is mediated either by direct interaction with pathway-specific effectors, such as the cell cycle complex cyclin-dependent kinase 1 (cdk1)/cyclinB1[177] and the DNA replication and repair protein proliferating cell nuclear antigen (PCNA)[176] or by initiation of signaling cascades that lead to their activation. Similarly to the two other group members, major downstream signaling pathways initiated by Gadd45β lead to the regulation of the MAPK p38 via direct interaction with the N-terminus of the MAPK kinase kinase (MAPKKK) MEKK4[178,179]. Association of Gadd45β induces conformational changes, which lead to dimerization and subsequent autophosphorylation of this MAPKKK[180]. In turn, activated MEKK4 facilitates the phosphorylation of a downstream MAPK kinase, here MKK3/6[181]. This enables the downstream phosphorylation of p38, a key initiator of diverse cellular programs such as apoptosis[173] and immune cell activation[182,183]. In contrast to this activating role during a MAPK cascade, direct interaction of Gadd45β with the MAPKK MKK7 was shown to inhibit downstream JNK signaling, i.e. upon TNF-α-induced

apoptosis in 3DO T cell hybridoma cells[184]. Of note, this effect was tissue- or cell type-dependent, as murine embryonic fibroblast cells (MEF cells) responded differently during this study.

To summarize some of the cellular responses, Gadd45β was shown to mediate TGF-β-induced apoptosis in HeLa cells and hepatocytes[172,173,175] as well as CD95-ligand dependent programmed cell death in hepatocytes[185]. At the same time, Gadd45β is needed to counteract TNF-α/TNF-R-mediated apoptosis[174,186] and cell survival was also promoted by Gadd45β-overexpression in insulin-producing cells upon IL-1β-stimulation[187]. Exposure to genotoxic stressors led to Gadd45β-dependent negative growth control and DNA repair[176,177]. In the case of terminal differentiation Gadd45β has, e.g. a central role during embryonic bone growth[188] and via demethylation of DNA in the activity-induced adult neurogenesis[189].

2.4 Characteristics of selective autophagy

In early studies autophagy was mainly understood as a bulky, degradative recycling mechanism implemented in basal homeostasis and survival under harsh conditions. However, during recent years the importance of selective targeting of organelles or pathogens by the autophagic machinery was identified. So far, according to the type of engulfed cargo a number of specific terms were defined, such as mitophagy for the degradation of mitochondria, e.g. during the maturation of erythrocytes[190], pexophagy for the reduction of peroxisome number after their accumulation[191], aggrephagy for the removal of dangerous misfolded protein clusters[192] or xenophagy for the elimination of invading pathogens, e.g. during *Salmonella enterica* serovar Typhimurium (*S.* Typhimurium) infection[193].

The recognition of cytoplasmic components and the recruitment of the autophagic machinery are still only partially understood. The accepted general principle is described here. Firstly, ubiquitin is associated with the surface of the cargo. Secondly, autophagic receptors translocate to the site and bind the tagged component via a C-terminal ubiquitin-associated (UBA) domain. Importantly, the receptors additionally harbor an LC3-interacting region (LIR), which enables them to

anchor the ubiquitinylated organelle, protein aggregate or pathogen to the forming autophagosomes[76,194,195]. Classical examples for these adaptor proteins are p62 (also known as SQSTM1)[76] and neighbor of BRCA1 gene 1 (NBR1)[196], which among others were so far identified in mitophagy[197], aggrephagy[76,198,199], pexophagy[200] and xenophagy[201] (see Fig. 2.6).

Nevertheless, this model surely is a simplified version of the actual molecular underlying steps. The detailed mechanisms of recognition including the initial signal for ubiquitinylation, the ubiquitinylated substrates and their ubiquitin ligases or the identity of all involved autophagic receptor proteins have not been comprehensively elucidated for most of the specific autophagy forms, yet[69].
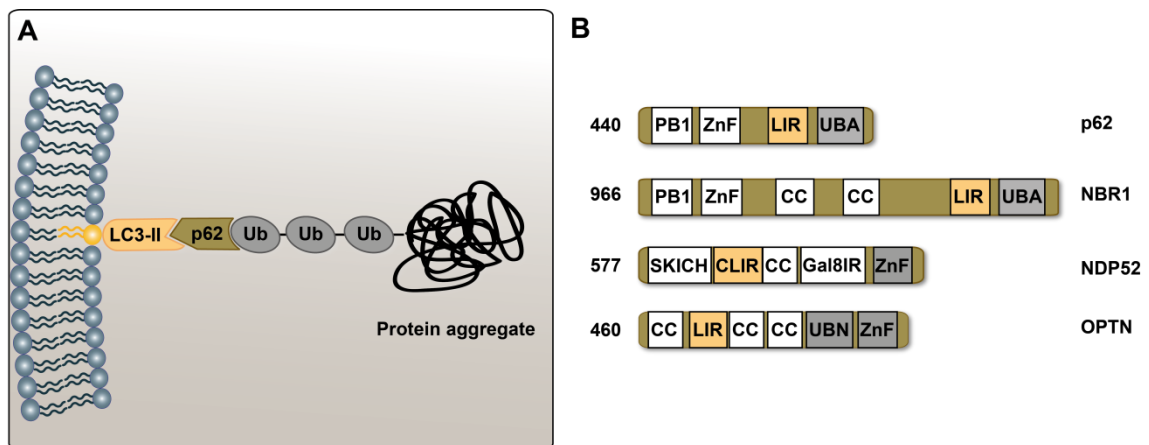
Fig. 2.6: Autophagy receptors are central players during selective autophagy. (A) Model of the interaction between ubiquitinylated protein aggregates and the autophagy receptor p62, which links the cargo to the autophagosomal LC3-II for specific degradation. Modified from Tyedmers *et al.*[202]. **(B)** Structural view on the most prominent autophagy receptors p62, NBR1, nuclear dot protein 52 kDa (NDP52) and optineurin (OPTN). The LC3-interacting region (LIR) is depicted in yellow and the domains responsible for ubiquitin binding in grey. CC: coiled-coil, CLIR: LC3C-specific interaction region, Gal8IR: Galectin8-interaction region, LIR: LC3-interacting region, PB1: Phox and Bem1P, SKICH: skeletal muscle and kidney enriched inositol phosphatase carboxyl homology, UBA: ubiquitin-associated domain. UBN: ubiquitin binding in ABIN and NEMO domain, ZnF: zinc finger. Cartoon performed according to Boyle *et al.*[203].

2.5 Xenophagy, an immunological important form of selective autophagy

Xenophagy was intensively investigated in the past years, since the specific degradation of intracellular pathogens marks a mechanism by which the autophagic machinery largely contributes to cellular immunity. So far, different types of bacteria have been shown to be successfully targeted by autophagy, such as Group A *Streptococcus* (*Streptococcus pyogenes*)[204] and *Salmonella enterica* serovar Typhimurium (*S.* Typhimurium)[193].

The infection with the Gram-negative *S.* Typhimurium serves as a model system for the underlying mechanisms of xenophagy. After evading a cell, a host-derived *Salmonella*-containing vacuole (SCV) is formed around the bacterium[205,206]. The enclosure is driven by the secretion and surface-presentation of multiple virulence factors and ensures bacterial survival and proliferation within the host cell[207–210]. However, a portion of the engulfed bacteria damages the vacuole and escapes into the cytosol, where the bacteria start to highly proliferate[193]. These cytosolic bacteria are recognized by the host ubiquitinylation system and are subsequently coated with ubiquitin[211]. The translocation of the ubiquitin-binding autophagy receptors p62[201], nuclear dot protein 52 kDa (NDP52) also known as calcium binding and coiled coil domain 2 (CALCOCO2)[212] and optineurin (OPTN)[213] results in the association of LC3-containing autophagic structures and autophagic degradation of the bacteria. Importantly, *S.* Typhimurium can also be recognized within SCV, since the secretion of effectors and consequent perforation of the vacuole is sensed by galectin8. This finally results in the translocation of NDP52 and in the recruitment of ubiquitin ligases followed by further xenophagy mediators[214] (see Fig. 2.7).

Notably, in the case of *Salmonella*, more details about the molecular mechanisms during bacteria-host interaction, especially the involvement of ubiquitylation, are elucidated by a study which investigated the global ubiquitinome in infected epithelial cells[215]. Next to the degradative targeting of cytosolic *Salmonella* or SCV, the autophagic machinery can also contribute to proliferation and survival of the bacteria within the SCV. As mentioned above, leaks within the vacuole membrane can lead to recognition by the host antimicrobial mechanisms. The closure of these pores

appeared to be dependent on the translocation of the ATG12–5 conjugate to the SCV, revealing a new role of autophagic components during *S.* Typhimurium infection[216].

Naturally, ancient host-derived antimicrobial pathways like xenophagy resulted in the evolvement of contradictory and hijacking mechanisms on the bacterial side. Indeed, some bacteria have been shown to escape the degradative autophagic machinery by the use of different strategies. *Shigella flexineri* for example secretes the effector lcsB to mask the bacterial surface protein VirG, which otherwise would be recognized by the autophagic machinery, namely by ATG5[217]. The same principle is also true for cytosolic *Listeria monocytogenes* after it disrupts the phagophore with its pore-forming toxin listeriolysine O. To protect itself, the Gram-positive bacterium subsequently recruits host-derived actin structures to cover its "foreign" surface and thereby ensures intracellular motility and spreading[218].
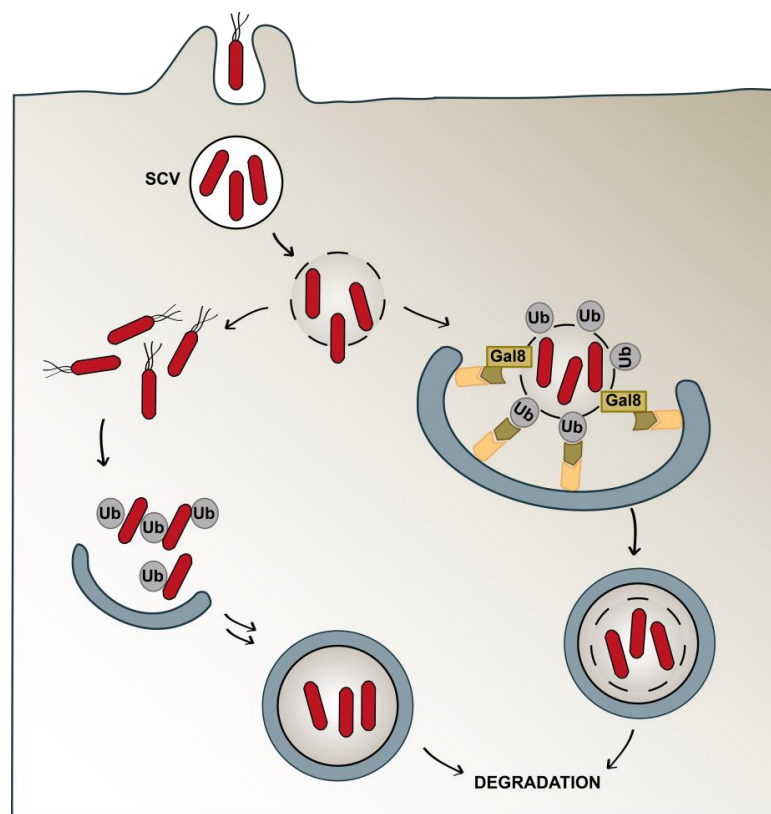
Fig. 2.7: Xenophagy upon *S.* Typhimurium infection. Invasion of the bacteria result in the formation of a protective SCV. Nevertheless, secretion of bacterial virulence factors lead to the disruption of the vacuole, which is specifically sensed by the cytosolic galectin8 (Gal8). Galectin8 binds to NDP52, thus, together with subsequent ubiquitinylation recruits the autophagic machinery, including autophagic receptors (green) and LC3-II, which will drive the degradation of the perforated SCV. Next to this pathway, also escaped cytosolic *S.* Typhimurium can be targeted by autophagic degradation. Here, the recruitment of the downstream xenophagy mediators depends solely on ubiquitinylation. Modified from LaRock *et al.*[219].

24

2.5.1 The Gram-positive pathogen *Staphylococcus aureus*

Staphylococcus aureus (*S. aureus*) is a coccoid-shaped, human pathogen that belongs to the group of Gram-positive bacteria[220,221]. As an opportunistic and non-motile organism, it was shown to reside asymptomatically in the throat[222] and in the nose or on the skin of humans[223,224]. When it comes to pathology, *S. aureus* preferably targets skin and soft tissues and can cause a wide spectrum from minor, severe to even life-threatening infections and associated diseases. These include impetigo, boils, folliculitis, abscess formation, wound infections, endocarditis and septic shock[221,226-228]. The increasing clinical relevance of *S. aureus* mainly results from its high adaptability to treatment with antibiotics. In particular methicillin-resistant *S. aureus* (MRSA)[228] was shown to be a serious problem in hospitals[229–231]. However, not only immune-compromised patients in clinics are at risk of a *S. aureus* infection, but also community-associated MRSA was shown to develop into an emerging epidemic for otherwise healthy populations in the United States[232].

In the case of a cutaneous *S. aureus* infection, the cellular response of the host is mainly characterized by the recruitment of neutrophils that form an abscess, thereby mediating bacterial clearance[233]. Having reached the site of infection, neutrophils phagocytose the bacteria in order to kill them via multiple cellular programs, such as the induction of an oxidative burst or the expression of antimicrobial peptides and proteinases. The translocation of the phagocytes is driven by immune signaling of keranotinocytes and skin-resident immune cells as the first line facing the pathogen. In general this signaling includes the expression of pro-inflammatory cytokines, chemokines and adhesion molecules.

The contributing molecular mechanisms can be divided into four major pathways according to the initially activated surface receptors. In detail, pathogen-associated molecular patterns (PAMPs), here bacterial lipopeptides and lipoteichoic acid are sensed via the pattern recognition receptor (PRR) toll-like receptor 2 (TLR2)[234,235]. A central role is played by the subsequent production of the pro-inflammatory interleukins IL-1α and IL-1β for example by keratinocytes, which activate the IL-1 receptor 1 (IL-1R1)[236,237]. Downstream signaling of both pathways is mediated by the adaptor myeloid differentiation primary response protein 88 (MyD88) and the IL-1 receptor-associated kinase 4 (IRAK4) leading to TRAF6 activation, which in turn

activates transcription factors, i.e. NF-κB and MAP kinases such as ERK, p38 and JNK[238,239]. Thirdly, local enrichment of IL-17A and IL-17F levels stimulate the IL-17 receptor A–IL-17 receptor C complex[240]. The respective intracellular effector NF-κB activator 1 (ACT1) initiates similar downstream signaling pathways compared to MyD88 and IRAK4. Finally, a number of growth factors and cytokines are able to activate signal transducer and activator of transcription 3 (STAT3) signaling, promoting further transcription programs that are important for a proper immune response[241,242].

However, the success of *S. aureus* infection is based on its ability to circumvent many of these host-driven immune responses. In this context, although *S. aureus* was classically identified as an extracellular pathogen, the bacterium was demonstrated to invade and persist within non-professional phagocytes such as fibroblasts as well as in macrophages and neutrophils[243–245]. After phagocytosis, a number of pathogen-specific virulence factors can contribute to the suppression of typical antimicrobial functions[246–250], allowing the bacterium to parasitize within the phagocyte[251–254]. Interestingly, in dendritic cells (DCs) this mechanism was suggested to rely on the inhibited fusion of bacteria-containing autophagosomes with lysosomes[255]. In the respective study, *S. aureus* strains exhibiting different activity levels of the virulence factor locus accessory gene regulator *(agr)* were used to infect bone marrow-derived dendritic cells (BMDC). The authors claim, that a higher level of virulence factors promotes the accumulation of autophagosomes in the infected phagocytes. Subsequently, this inhibition of the autophagic flux favors the escape of the bacteria from autophagic degradation and ensures at least a temporal intracellular survival of *S. aureus*[255].

2.6 Autophagy in the context of metabolic disorders

2.6.1 Lipophagy, a form of selective autophagy

In the past, the catabolic role of autophagy was mainly characterized by the degradation of proteins into free amino acids during nutrient-deprivation or an unbalanced energy status. Nevertheless, the metabolic impact of autophagy is much more evident, since it has been demonstrated, that in the form of lipophagy it

contributes to the breakdown of lipids stored in lipid droplets (LD), especially in liver and adipose tissue[256]. Under nutrient-rich conditions, free fatty acids are internalized by hepatocytes or adipocytes, subsequently transformed to triglycerides and stored in LDs together with cholesterol[257,258]. Whenever cellular energy levels are too low, lipophagy is hormonally induced in parallel to classical lipolysis mediated by cytosolic lipases[259–261]. The exact targeting of the lipid drops is a topic of ongoing research. Clearly, LDs need to be engulfed by an autophagosomal membrane prior to fusion with the lysosome[256]. In line with these findings, a recent report suggests a prominent role for patatin-like phospholipase domain containing 5 (PNPLA5)-mobilized neutral lipids originating from LDs in the *in situ* formation of the autophagosomal membrane[262]. Additionally, one further study reported that the degradation of the LD-associated proteins PLIN2 and PLIN3 by chaperone-mediated-autophagy is crucial for initiation of cytosolic and autophagic lipolysis[263,264].

Depending on the LD-size, either the complete drop or a portion is captured within an autophagosome during lipophagy. After the maturation step, lysosomal lipases perform the hydrolysis of the triglycerides[256]. The resulting free fatty acids are released into the cytosol and directly serve as a source of energy during autonomous mitochondrial or peroxisome oxidation[265] or are transported to other tissues. Recent work demonstrated that the transcription factor EB (TFEB) is a central mediator of lipophagy regulation upon starvation. Notably, this does not only include the upregulation of autophagic players and the stimulation of the lysosome biogenesis, but TFEB also enhances the capacity for free fatty acid utilization in mitochondria and peroxisomes[266]. Furthermore, TFEB modulates the enzymatic content of the lysosome towards lipases, which was reported from a study with *Caenorhabditis elegans*[267].

2.6.2 Obesity and autophagy

Obesity is defined by excessive total body fat and comes along with a massive pathological increase of - preferable abdominal - white adipose tissue (WAT). Obesity is associated with the prevalence and development of several diseases, such as type 2 diabetes (insulin resistance) and hypertension. Taken together, these risk factors are combined in the term metabolic syndrome[268].

From the already described linkage between autophagy and the proper management of energy and nutrient status, it seems obvious that challenging the system permanently, for example in diet-induced obesity, will lead to alterations in the autophagic flux. Prolonged high energy and nutrient levels influence in particular the central metabolic organs and tissues, which are liver, pancreas and adipose tissue. Next to the described role in lipid metabolism, hepatic autophagy was identified to regulate blood glucose[269] and amino acid levels[270]. To maintain the glucose concentration in the bloodstream, glucogenic amino acids released from autophagic degradation are converted to glucose via gluconeogenesis. When it comes to lipid-dependent autophagy regulation in hepatocytes, sustained high lipid levels were shown to inhibit the autophagic flux in these cells[256]. Further studies revealed, that this impairment led to intracellular ER stress and unresponsiveness towards insulin stimulation[271].

The total adipose tissue is mainly composed of the WAT and brown adipose tissue (BAT), which are characterized by distinct functions, anatomical location and morphological structure. White adipocytes are defined by a single large fat lobule and serve as main lipid storage and supply according to the energetic needs of the organism. Brown adipocytes contain, in addition to multiple lipid droplets a high number of mitochondria. Contrary to WAT, hydrolysis of triglycerides in BAT is preferably used for autonomous heat production[272–275]. Conditional KO studies performed *in vivo* and *in vitro* revealed that autophagy plays a central role in adipogenesis, since the deletion of ATG5 and ATG7 resulted in an impaired differentiation of functional white adipocytes from their progenitor cells. This comes along with an increased number of mitochondria and multiple small lipid droplets in the resulting cell population. Additionally, adipose-specific deletion of ATG7 led to an increased insulin sensitivity[276,277]. Another report observed similar findings in ATG5 knock down cell culture experiments and an ATG7 knock out-mouse model. They interpreted their results in a slightly different way pointing out the morphological and functional shift towards a BAT-like phenotype upon defective autophagy. Thus, in their argumentation, autophagy in particular maintains the balance between the two adipose tissues[278]. Taken together, these findings suggest a central role of the specific or bulk autophagic degradation of mitochondria during WAT adipogenesis[279].

In contrast to the liver, obesity was shown to induce autophagy in adipose tissue[280]. This correlation was underlined by the striking finding, that mice deficient for adipose-specific autophagy were resistant to high-fat diet-induced obesity[276].

2.7 Aims of the thesis

Autophagy is characterized as a catabolic, intracellular degradation and recycling mechanism starting with the engulfment of cytoplasmic components by a *de novo* formed double-layered membrane. The resulting vacuole is named autophagosome and subsequently fuses with a lysosome leading to lysosomal degradation of the captured cargo. Basal levels of autophagy contribute to regular protein and organelle turnover, thereby ensuring cellular homeostasis. Unfavorable conditions such as nutrient withdrawal or the invasion of pathogens induce the autophagic flux to either provide energy and building blocks for maintenance or to use the autophagic machinery for efficient clearance of the pathogen[1]. In a previous study, the Gadd45β-MEKK4-MKK3/6-p38 MAP kinase signaling cascade was shown to specifically inhibit the fusion of autophagosomes with lysosomes by an interaction of p38 with ATG5. This mechanism is suggested to serve as a negative feedback loop, probably downregulating the autophagic flux after a strong induction for instance upon LPS/TLR4 stimulation[133].

The first aim of this thesis was the generation of a transgenic mouse model, which would allow the investigation of further physiological roles for this pathway. For this, next to ATG5 wild type (WT) the two mutant forms ATG5^{T75A} (mimics inhibited regulation) and ATG5^{T75E} (mimics enhanced regulation) were introduced in the ROSA26 locus under the control of the EF1α promoter using recombinase-mediated cassette exchange (RMCE). Moreover, the interaction of the MAPK p38 with ATG5 was investigated to identify crucial residues for docking of p38 during this thesis. This included the generation of potential docking site mutants of ATG5 according to other known p38-substrates[159] and their analysis via co-immunoprecipitation experiments. Furthermore, functional effects on the autophagic flux that may result from an impaired interaction with p38, were examined.

Xenophagy describes a specific form of autophagy, by which invading pathogens are targeted for autophagosomal degradation[281]. However, this host-defense mechanism was demonstrated to be bypassed by some types of bacteria, like *S.* Typhimurium[193]. *S. aureus* was previously shown to escape autophagic degradation. However, the detailed interplay between *S. aureus* and the autophagy machinery was still unclear[282,283]. During this thesis, the *S. aureus*-mediated autophagic response was investigated in fibroblast cells especially with regard to the factors involved in the targeting of the bacteria and the bacterial escape from autophagic degradation.

Autophagy was reported to be a central mechanism contributing to typical concomitants of obesity like insulin-resistance and white adipose tissue (WAT) mass elevation[276,284]. During this thesis, an experimental setup for a high-fat diet-induced obesity model was established. For this, Gadd45β KO x GFP-LC3 and GFP-LC3 transgenic mice were fed with high-fat and control diet, monitored by measuring weight and blood parameters and further analyzed by employing histology and flow cytometry after the end-point.

3 MATERIALS

3.1 Chemicals

Chemicals were purchased by Sigma Aldrich (St. Louis, MO/USA) or Carl Roth (Karlsruhe, Germany) if not mentioned otherwise.

3.2 Material and devices for cloning procedure

Tab. 3.1: Plasmids either used for or generated by cloning or used for transfection

Name	Usage	Origin
pEF/myc/cyto (empty)	Cloning and expression of ATG5 mutants in HEK293T cells, transfection control	Invitrogen-Thermo Fisher Scientific (Waltham, MA/USA)
pEF/myc/cyto-ATG5 WT **pEF/myc/cyto-ATG5 T75A** **pEF/myc/cyto-ATG5 T75E** **pEF/myc/cyto-ATG5 K51E/K53E** **pEF/myc/cyto-ATG5 K58E/R61S** **pEF/myc/cyto-ATG5 K78E/H80D** **pEF/myc/cyto-ATG5 L90S** **pEF/myc/cyto-ATG5 L90Q** **pEF/myc/cyto-ATG5 E73K**	Expression of ATG5-c-myc (wild type and mutant forms)	Keil *et al.*[133] Keil *et al.*[133] Keil *et al.*[133] Cloned in this thesis Cloned in this thesis Cloned in this thesis Cloned in this thesis Cloned in this thesis Cloned in this thesis
pcDNA3.1/Hygro (+) (empty)	Transfection control for co-immunoprecipitation experiments	Invitrogen-Thermo Fisher Scientific
pcDNA3.1/Hygro FLAG-p38	Expression of FLAG-p38	Cloned in master thesis: Bruns[285]
pBABE-puro (empty)	Retro-viral transduction	Addgene (Cambridge, MA/USA)
pBABE-puro-ATG5 WT **pBABE-puro-ATG5 T75A** **pBABE-puro-ATG5 T75E** **pBABE-puro-ATG5 L90S** **pBABE-puro-ATG5 L90Q** **pBABE-puro-ATG5 E73K**	Stable reconstitution of ATG5 knock out murine embryonic fibroblast (MEF) cells via retro-viral transduction	Cloned in this thesis Cloned in this thesis Cloned in this thesis Cloned in this thesis Cloned in this thesis Cloned in this thesis
pCMV-Gag-Pol **pVSV-G**	Production of retro-viral particles for transduction	Prof. Dr. Stefan Ludwig, University of Muenster
pMSCV-Bsd-mCitrine-hLC3B	Retro-viral transduction of parental and reconstituted ATG5 MEF cells	PD Dr. Bjoern Stork, University Clinic Duesseldorf
pEGFP-C1-OPTN	Expression of GFP-optineurin	Prof Dr. Ivan Dikic, Goethe University Frankfurt[213]

Name	Usage	Origin
pMRX-Cre	Expression of *Cre* recombinase	PD Dr. Andreas Krueger, Hannover Medical School
pTAR-EF1α-antiflox (empty)	Cloning of constructs for transgenic mice	Prof. Dr. Dagmar Wirth, Helmholtz-Centre for Infection Research, Braunschweig
pTAR-EF1α-antiflox-ATG5 WT **pTAR-EF1α-antiflox-ATG5 T75A** **pTAR-EF1α-antiflox-ATG5 T75E**	Expression in embryonic stem cells (transgenic mice)	Cloned in this thesis Cloned in this thesis Cloned in this thesis

3.2.1 Restriction

In order to cut vector DNA, the appropriate restriction enzymes from New England Biolabs (NEB; Ipswich, MA/USA) were used.

Tab. 3.2: Restriction enzymes

Restriction enzyme	Recognition site	Reaction buffer	BSA*	Cat. no.
BamHI-HF	5'...G|GATCC...3' 3'...CCTAG|G...5'	NEB 4	No	R3136
KpnI-HF	5'...GGTAC|C...3' 3'...C|CATGG...5'	NEB 4	Yes	R3142
NcoI-HF	5'...C|CATGG...3' 3'...GGTAC|C...5'	NEB 4	No	R3139
NruI	5'...TCG|CGA...3' 3'...AGC|GCT...5'	NEB 3	No	R0192
SalI-HF	5'...G|TCGAC...3' 3'...CAGCT|G...5'	NEB 4	No	R3138
XhoI	5'...CTCGAG...3' 3'...GAGCTC...5'	NEB 4	Yes	R0146

*BSA: Bovine serum albumin

3.2.2 Polymerase chain reaction

For polymerase chain reactions (PCR) during cloning and for complementary DNA (cDNA) amplification a ready-to-use 2x Phusion Flash High-Fidelity PCR Master Mix (Thermo Fisher Scientific; Waltham, MA/USA), with the proof-reading Flash II DNA Polymerase, was used in a final concentration of 1x.

Colony-PCR was performed with the KAPA2G™ Fast 2x Ready-Mix with Dye (KAPA Biosystems; Wilmington, MA/USA) in a final concentration of 1x. During site-directed mutagenesis, the Phusion Hot Start II DNA Polymerase (Finnzymes-Thermo Fisher Scientific) in combination with the Phusion HF Reaction Buffer (Finnzymes-Thermo Fisher Scientific) and desoxynucleotides (dNTPs) were used. Genotyping PCR was performed by using the KAPA Fast HotStart Mouse Genotyping Kit (Kapa Biosystems).

All primers were ordered via Eurofins MWG Operon (Ebersberg, Germany) in a salt free preparation and without additional modifications if not mentioned otherwise.

Tab. 3.3: Oligonucleotides used for cloning

Oligonucleotide	Sequence (5'-> 3')	Usage
ATG5restr.NEW fwd	GCT GGT ACC CCA TGG CGA TGA CAG ATG ACA AAG ATG TG	Cloning for ATG5 mutagenesis
ATG5restr.NEW rev	TGC GGA TCC CTC GAG GCT TCT ATC TGT TGG CTG TGG G	
ATG5 E73K fwd	GAT ATG GTT TGA ATA TAA AGG CAC ACC ACT GAA ATG G	Cloning for ATG5 mutagenesis
ATG5 E73K rev	CCA TTT CAG TGG TGT GCC TTT ATA TTC AAA CCA TAT C	
ATG5 L90Q fwd	GCT ATT TGA TCT TCA AGC ATC AAG TTC AGC TC	Cloning for ATG5 mutagenesis
ATG5 L90Q rev	GAG CTG AAC TTG ATG CTT GAA GAT CAA ATA GC	
ATG5 L90S fwd	GCT ATT TGA TCT TTC TGC ATC AAG TTC AGC TC	Cloning for ATG5 mutagenesis
ATG5 L90S rev	GAG CTG AAC TTG ATG CAG AAA GAT CAA ATA GC	
TU Mut 3 fwd	GGC ACA CCA CTG AAT GGG ATT ATT CCA ATT GGT TTG C	Cloning for ATG5 mutagenesis
TU Mut 3 rev	GCA AAC CAA TTG GAT AAT CCC ATT CCA GTG GTG TGC C	
ATG5 rec. Fwd	GCT GGA TCC ATG ACA GAT GAC AAA GAT G	Cloning for ATG5 reconstitution
ATG5 rec rev	TGC GTC GAC CTA TGC GGC C	
ATG5 fwd	TGC TTC GAG ATG TGT GGT TTG GAC G	ATG5 sequencing
ATG5 rev2	TCC ATC TGC AGC CAC AGG ACG A	
ATG5Maus-P fwd*	CCA TGG CGA TGA CAG ATG AC	pTAR cloning
ATG5Maus-P rev*	CTA TGC GGC CCC ATT CAG	
pTAREF1 antiflox	GTC GAG TAA GTC ACG ATG CTA TCG	pTAR sequencing

*HPLC purification and 5'-phosphate modification

Tab. 3.4: Oligonucleotides used for genotyping and reverse transcriptase PCR

Oligonucleotide	Sequence (5'-> 3')	Usage
Actin fwd (MSYS)	TGG AAT CCT GTG GCA TCC ATG AAA C	Semi-quant. RT PCR
Actin rev (MSYS)	TAA AAC GCA GCT CAG TAA CAG TCC G	
EMCV-IRES fwd	AAG AGT CAA ATG GCT CTC CTC AAG CGT ATT	Semi-quant. RT PCR, Genotyping
mATG5-Neo rev	GTC TGT TGT GCC CAG TCA TAG CCG AAT AG	
GFP-LC3 up	ATA ACT TGC TGG CCT TTC CAC T	
GFP-LC3 down	CGGGCC ATT TAC CGT AAG TTA T	Genotyping
GFP-LC3 neo	GCA GCT CAT TGC TGT TCC TCA A	
Gadd45β KO up	GCT GTG GAG CCA GGA GCA GCA	
Gadd45β KO down	ATA TGC AAG CGA TCT GTC TTG CTC	Genotyping
Gadd45β KO neo	AAG CGC ATG CTC CAG ACT GCC TT	
Cre total fwd	ACG ACC AAG TGA CAG CAA TG	Genotyping
Cre total rev	CTC GAC CAG TTT AGT TAC CC	
wt ROSA26 fwd	GGA GCG GGA GAA ATG GAT ATG	Genotyping
wt ROSA26 rev	TGA GTT GTT ATC AGT AAG GGA GCT GCA GTG	

3.2.3 Ligation and transformation in *Escherichia coli*

To ligate the insert and vector backbone, the T4 DNA Ligase in combination with the respective 10x T4 Ligase Reaction Buffer from Thermo Fisher Scientific was used. To avoid self-ligation of blunt end fragments, the vector backbone was treated with Antarctic Phosphatase and the respective phosphatase reaction buffer (NEB) before ligating the insert. The transformation of the ligated construct was performed in *Escherichia coli* (*E. coli*) strain Top10 (Thermo Fisher Scientific). During transformation and plasmid amplification, *E. coli* bacteria were cultured in lysogeny broth medium either with or without agar and with or without antibiotics, depending on the type of cultivation.

Tab. 3.5: Media and antibiotics for *E. coli* cultivation

Medium/Antibiotic	Cat. no.	Composition/Company
Lysogeny broth (LB)	-	10 g trypton, 5 g yeast extract, 5 g NaCl, 4 g NaOH; add dH$_2$O to 1 L // for agar plates include 18 g agar
Ampicillin	A0839	AppliChem (Darmstadt, Germany)
Kanamycin	A1493	AppliChem

3.2.4   DNA gel electrophoresis

Separation of DNA fragments by gel electrophoresis was performed in Perfect Blue™ Gel System Mini M or Mini ExW (Peqlab Biotechnologie) devices with TAE buffer. Ethidium bromide intercalation was documented via ultra-violet (UV) light of 312 nm in a gel documentation system (INTAS Science Imaging Instruments; Göttingen, Germany).

Tab. 3.6: Reagents and buffers for DNA gel electrophoresis

Reagent/Buffer	Cat. no.	Composition/Company
Agarose	732-2789	Peqlab Biotechnologie
Ethidium bromide solution (1%)	2218.1	Carl Roth
6x MassRuler DNA Loading Dye	R0621	Thermo Fisher Scientific
GeneRuler 1kb Plus DNA ladder	SM1333	Thermo Fisher Scientific
MassRuler Low Range DNA ladder	SM0383	Thermo Fisher Scientific
TAE buffer	-	40 mM Tris base, 1 mM EDTA, 20 mM acetic acid, pH 8.5

3.3 Devices, cells and materials for cellular biology and biochemistry methods

3.3.1   Utilized mammalian cell lines

The parental adherent cell lines ATG5 wild type (WT) and ATG5 knock out (KO) murine embryonic fibroblast (MEF) cells[57,270], NIH/3T3 WT cells, p38 WT MEF and p38 KO MEF cells[286] and HEK293T cells were cultured in high glucose Dulbecco's Modified Eagle's Medium (DMEM), supplemented with 10% fetal calf serum (FCS) and depending on the experiment with or without 50 µg/mL penicillin/streptomycin. The NIH/3T3 cells[133]stably transduced with GFP-LC3, the retro-virally ATG5 KO MEF cells reconstituted with ATG5 (WT and T75A, T75E, L90S, L90Q or E73K mutant) were cultured as the parental lines above. The same handling was needed for the mCitrine-hLC3B-transduced ATG5 WT, ATG5 KO and ATG5-reconstituted MEF cell lines.

3.3.2   Materials, reagents and devices for culturing of cells

Cell cultivation was performed in Standard.F 25 cm^2, 75 cm^2 and 175 cm^2 flasks, in 48-, 12-, 6-well plates or 3.5 cm^2 or 10 cm^2 dishes (Sarstedt; Nürnbrecht, Germany). A Vacusafe Vacuum Aspiration System (Integra Biosciences; Bibertal, Germany) was used to aspirate the liquid during handling. Additionally, 0.5 mL, 1.5 mL and 2 mL tubes (Sarstedt) as well as 15 mL and 50 mL Falcon tubes (Greiner bio-one; Frickenhausen, Germany) were used for the different experimental preparations. Furthermore, 5 mL, 10 mL and 25 mL sterile serological pipettes (Sarstedt) and a Pipetboy (Integra Biosciences), sterile 10 µL, 200 µL and 1000 µL TipOne graduated tips with and without filters (Starlab; Hamburg, Germany) and single channel PEQpettes (Peqlab Biotechnologie) were utilized. For viral particle production, sterile syringe filters (0.45 µm, Merck Millipore; Billerica, MA/USA) and syringes with a proper Luer-Lok™ Tip (10 mL, 20 mL, 60 mL, Becton, Dickinson and Company (BD); Franklin Lakes, NJ/USA) were used.

Cell handling was performed in SterilGARD® III Advance sterile hoods (The Baker Company; Sanford, ME/USA) and the cells were kept in a Heracell™ 240i CO_2 incubator (Thermo Fisher Scientific) at 37 °C, with 95% humidity and 5% CO_2. Centrifugation of cells was performed in a Megafuge 1.0 (Heraeus; Hanau, Germany),

or in the Eppendorf centrifuge 5810R (Eppendorf; Hamburg, Germany). For cell counting either a BLAUBRAND® Neubauer Improved Counting Chamber (Brand; Wertheim, Germany) and the Eclipse TE200 inverted microscope TE (Nikon; Tokio, Japan) or the automated counting system Cellometer® Auto T4 (Nexcelom Bioscience; Lawrence, MA/USA) with respective counting slides was used. Cells were frozen in freezing medium (see Tab. 3.7) in CryoTube™ Vials (Nunc-Sigma Aldrich) and placed in Mr. Frosty 1 °C Freezing Container (Nalgene-Thermo Fisher Scientific) for long-term storage in liquid nitrogen.

Tab. 3.7: Media, supplements and buffers for cell culture maintenance

Medium/Supplement/Buffer	Cat. no.	Composition/Company
Dulbecco's modified eagle medium (DMEM), high glucose	11965092	GIBCO™ Thermo Fisher Scientific
Fetal calf serum (FCS)	A15-101	PAA laboratories-GE Healthcare (Chalfont St Giles, GB)
Phosphate-buffered saline (PBS), pH 7.4	10010023	GIBCO™ Thermo Fisher Scientific
Penicillin/Streptomycin (5000 U/mL)	15070063	GIBCO™ Thermo Fisher Scientific
Trypsin/EDTA (0.05%)	25300054	GIBCO™ Thermo Fisher Scientific
Blasticidin	ant-bl-1	InvivoGen (San Diego, CA/USA)
G418-BC	A2912	Biochrom-Merck Millipore (Berlin, Germany)
Puromycin	P8833	Sigma Aldrich
Dimethyl sulfoxide (DMSO)	A994.1	Carl Roth
Freezing medium	-	10% DMSO in FCS

Tab. 3.8: Stimulating media and reagents

Stimuli	Cat. no.	Company
Hank's balanced salt solution (HBSS) calcium, magnesium	24020083	GIBCO™ Thermo Fisher Scientific
Bafilomycin A1	BML-CM110-0100	Enzo Life Sciences (Lörrach, Germany)
E64-d	BML-PI107-0001	Enzo Life Sciences
Pepstatin A	P5318	Sigma-Adrich

Tab. 3.9: Transfection reagents for cell culture

Buffer/Kit	Cat. no.	Composition/ Company	Usage
1x HBS	-	21 mM HEPES, 137 mM NaCl, 50 mM KCl, 6 mM Dextrose, 0.7 mM $Na_2HPO_4(7\ H_2O)$, adjust pH to 7.1	Transient transfection of HEK293T cells (Calcium Phosphate Method)
2.5 M CaCl₂	-	in PBS	
Polybrene®	AL-118	Sigma Aldrich	Viral transduction (enhances effectivity)
jetPEI®	101-40N	Polyplus transfection (Illkirch-Graffenstaden, France)	Transient transfection of mouse embryonic fibroblasts
jetPRIME®	114-07	Polyplus transfection	Transient transfection of mouse embryonic fibroblasts

3.3.3 Buffers for cell lysis (Western blot)

Tab. 3.10: Buffers for cell lysate preparation

Usage	Buffer	Composition
Washing	1x PBS	117 mM NaCl, 1.1 mM KCl, 1.6 mM KH_2PO_4, 11.3 mM NaH_2PO_4
Additive for lysis buffer	100x small protease inhibitors (SPI)	100 µg/mL apotinin, 100 µg/mL leupeptin, 100 µg/mL pepstatin A, 100 µg/mL chymostatin
Cell lysis (including nuclear proteins) for Western blot	TPNE	1x PBS ad 300 mM NaCl, 1 mM EDTA, 1% v/v Triton™ X-100 // add 1x SPI, 1 mM phenylmethylsulfonyl fluoride (PMSF) and 0.4 mM Na_3VO_4 freshly
Cell Lysis (cytoplasmic proteins, immuno-precipitation) for Western blot	DISC	30 mM Tris base/HCl, 150 mM NaCl, 10% v/v Glycerol, 1% v/v Triton™ X-100, 2 mM EDTA, 10 mM NaF, adjust pH to 7.4 // 1x SPI, 1 mM PMSF and 0.4 mM Na_3VO_4 freshly added

3.3.4 Buffers and reagents for *in vitro* kinase assays

All recombinant proteins ATG5 WT, ATG5[T75A], ATG12–5 full length, p38 WT and p38[K53A] (KM) and ATG12–5 truncated (ATG12 53-140) were generated and kindly provided by Dr. Caroline Behrens and Dr. Milica Bajagic (group of Dr. Andrea Scrima,

Helmholtz-Centre for Infection Research, Braunschweig) in the course of a collaboration.

Tab. 3.11: Buffers and reagents for *in vitro* kinase assays

Buffer/Reagent	Composition/Cat. No.	Company
Kinase buffer	0.5 mM DTT, 25 mM glycerophosphate, 250 µM ATP, 25 mM HEPES pH 7.5, 1 mM NaVO$_3$, 10 mM MgCl$_2$, 5 mM MnCl$_2$	-
Antarctic Phosphatase with reaction buffer	M0289S	NEB
TPEN	P4413	Sigma Aldrich

3.3.5 Reagents, buffers and devices for sodium dodecyl sulfate polyacrylamide gel electrophoresis

Tab. 3.12: Buffers and additives for the preparation of polyacrylamide gels and the performance of sodium dodecyl sulfate (SDS)-polyacrylamide gel electrophoresis (PAGE)

Buffer/Additive	Cat. no.	Composition/Company
Pierce BCA Protein Assay Kit	23225	Pierce-Thermo Fisher Scientific
Lower buffer (SDS gel)	-	1.5 M Tris base, 14 mM SDS, adjust pH to 8.8 (with HCl)
Upper buffer (SDS gel)	-	137 mM Tris base, 7 mM SDS, adjust pH to 6.8 (with HCl)
Ammonium persulfate (APS)	A3678	100 mg/mL in H$_2$O // Sigma Aldrich
Rotiphorese® Gel 30 (37.5:1)	3029.1	Carl Roth
N,N,N',N'-tetramethylethylendiamin (TEMED)	2367.1	Carl Roth
5x Reducing sample buffer (RSB)	-	50 mM Tris base, 50% v/v glyercol, 10% w/v SDS, 25% v/v β-mercaptoethanol, 0.0025% w/v bromphenol blue adjust pH to 6.8
PageRuler Prestained Protein ladder	26616	Thermo Fisher Scientific
1x Running buffer	-	25 mM Tris base, 1% v/v SDS

.

3.3.6 Reagents, buffers and devices for protein transfer (Western blot) and protein detection via chemiluminescence

Tab. 3.13: Materials and buffers for performing protein transfer and membrane preparation

Buffer	Cat. no.	Composition/Company
Amersham Hybond P 0.45 PVDF membrane	10600023	GE Healthcare Life Sciences (Little Chalfont, Great Britain)
1x Transfer buffer	-	25 mM Tris base, 192 mM glycerol, 1% v/v SDS, 20% v/v methanol
Blocking buffers	T145.3	5% w/v powdered milk in TBS-T // milk powder: Carl Roth
	BSA-PF-1U	5% w/v BSA (protease free) in TBS-T // BSA: Capricorn Scientific (Ebsdorfergrund, Germany)
TBS	-	137 mM NaCl, 2.68 mM KCl, 24.76 mM Tris base, adjust pH to 7.4
TBS-T washing buffer	-	TBS with 0.05-0.1% v/v Tween®20

Tab. 3.14: Further materials and reagents for performing protein detection via chemiluminescence

Reagent/Material	Cat. no.	Composition/Company
Amersham ECL Select Western Blotting Detection Reagent	RPN2235	GE Healthcare Life Sciences
Amersham Hyperfilm™ ECL 18x24 cm/12.7x17.8 cm	28906837/ 28906835	GE Healthcare Life Sciences
SuperSignal® West Dura Extended Duration Substrate	34075	Thermo Fisher Scientific
WesternSure ECL substrate	926-80200	LI-COR (Lincoln, NE/USA)
Self-made ECL	-	Solution A: 200 mL 0.1 M Tris base, 50 mg luminol sodium salt
		Solution B: 11 mg para-hydroxycoumarin acid in 10 mL DMSO// use 1:100
		30% H_2O_2 // use 1:2000
10x ReBlot Plus Mild/Strong Antibody Stripping Solution	2502/2504	EMD Millipore (Billerica, MA/USA)
Self-made solution to inactivate Horseradish Peroxidase (for anti-phospho antibodies)	-	1% NaN_3 in TBS-T

Tab. 3.15: Primary antibodies for Western blotting and immunofluorescence (IF) experiments and primary antibody-bead conjugates

Antibody/ Conjugate	Cat. no.	Reactivity	Isotype	Species	Company
α-tubulin (DM1A) (mAb)	T9026	h,m,b,ch	IgG1	mouse	Sigma Aldrich
ATG5 D5F5U mAb	12994	h,m,r	IgG	rabbit	Cell Signaling Technology (CST; Danvers, MA/USA)
ATG16L1 D6D5 mAb	8089	h,m,r	IgG	rabbit	CST
c-myc	C3956	-	IgG	rabbit	Sigma Aldrich
FLAG®	F7425	-	IgG	rabbit	Sigma Aldrich
β-actin AC-74 (mAb)	A2228	all	IgG2a	mouse	Sigma Aldrich
LC3A/B	4108	h,m,r	IgG	rabbit	CST
p38	9212	h,m,r,mk,gp	IgG	rabbit	CST
Phospho-p38	9211	h,m,r,mk, dm,pg,sc	IgG	rabbit	CST
Phospho-p38 D3F9 XP mAb	4511	h,m,r,mk, mi,pg,sc	IgG	rabbit	CST
p62 (SQSTM) 2C11	H00008878-M01	h,m	IgG2a	mouse	Abnova, (Taipei City, Taiwan)
Phospho-Thr 42H4 (mAb)*	9386	all	IgM	mouse	CST
Phospho-Thr-Pro 101(mAb)*	9391	h,m,r,all	IgM	mouse	CST
TECRP1 D6C10 (mAb)	8097	h,m,r	IgG	rabbit	CST
Ubiquitin FK2	BML-PW8810-0100	all	IgG1	mouse	Enzo Life Sciences
ANTI-FLAG® M2 Affinity Gel (agarose)	A2220	-	IgG1	mouse	Sigma Aldrich
Myc-Tag (9B11) (mAb) (Magnetic Bead Conjugate)	5698	-	IgG2a	mouse	CST

*: used in combination with BSA; mAb: monoclonal antibody; h: human, m: mouse, r: rat; mk: monkey; gp: guinea pig, Dm: *Drosophila melanogaster*, pg: pig; sc: *Saccharomyces cerevisiae*

Tab. 3.16: Secondary horseradish peroxidase (HRP)-conjugated antibodies for Western blotting

Antibody conjugate	Cat. no.	Company
Goat anti-mouse IgG1-HRP	1071-05	Southern Biotech (Birmingham, AL/USA)
Goat anti-mouse IgG2a-HRP	1081-05	Southern Biotech
Goat anti-mouse IgG2b-HRP	1091-05	Southern Biotech
Goat anti-mouse IgM-HRP	1021-05	Southern Biotech
Goat anti-rabbit IgG-HRP	4030-05	Southern Biotech

3.4 Devices and materials for microbiology methods (bacterial infection)

3.4.1 Bacterial strains and cultivation

For infection of MEF cells, the *Staphylococcus aureus* strain SH1000 was used[287]. In case of immunofluorescence analysis, a RFP-expressing modified version of the SH1000 strain was utilized[288]. *Salmonella enterica* serovar Typhimurium (*S.* Typhimurium), which was used as reference pathogen, was kindly provided by the group of Prof. Dr. Dunja Bruder (Helmholtz-Centre for Infection Research, Braunschweig / Otto-von-Guericke-University, Magdeburg).

Tab. 3.17: Media, antibiotics and lysing reagents for bacterial infections

Medium/Antibiotic	Cat. no.	Composition/Company
Lysogeny broth (LB)	-	10 g trypton, 5 g yeast extract, 5 g NaCl, 4 g NaOH; add dH_2O to 1 L // for plates include 18 g agar
Tryptic soy broth (TSB)	22092	Sigma Aldrich (St. Louis, MO/USA) // for plates include agar
Ampicillin	A0839	AppliChem
Chloramphenicol	3886	Carl Roth
Lysostaphin	L9043	Sigma Aldrich
Gentamycin	G1397	Sigma Aldrich

3.4.2 Devices, materials and reagents for *S. aureus* infection experiments

For immunofluorescence (IF) experiments cells were plated on 18 mm cover slips (Menzel-Gläser, Thermo Fisher Scientific) that cover the bottom of a 12-well plate. After all staining and washing steps were performed, the slips were placed on Superfrost plus microscope slides (Thermo Fisher Scientific) with Fluorescence Mounting Medium (DAKO-Agilent Technologies, Hamburg, Germany) and were analyzed with a confocal UltraViewVox Spining Disc Module (Perkin Elmer; Waltham, MA/USA) combined with a Nikon Ti Eclipse inverted microscope (Nikon; Tokio, Japan).

Tab. 3.18: Buffers, secondary antibodies and (staining) reagents for IF experiments

Antibody/(Staining) Reagent/Buffer	Cat. no.	Composition/ Company
Goat anti-mouse IgG1 Secondary Antibody Alexa Fluor® 488 conjugate	A21121	Invitrogen-Thermo Fisher Scientific
Goat anti-mouse IgG1 Secondary Antibody Alexa Fluor® 633 conjugate	A21126	Invitrogen-Thermo Fisher Scientific
Goat anti-mouse IgG2a Secondary Antibody Alexa Fluor® 633 conjugate	A21136	Invitrogen-Thermo Fisher Scientific
Chicken anti-rabbit IgG Secondary Antibody Alexa Fluor® 488 conjugate	A21441	Invitrogen-Thermo Fisher Scientific
Goat anti-rabbit IgG Secondary Antibody Alexa Fluor® 633 conjugate	A21070	Invitrogen-Thermo Fisher Scientific
LysoTracker Deep Red	L12492	Thermo Fisher Scientific
CytoID Autophagy Detection Kit	ENZ-51031	Enzo Life Sciences
Paraformaldehyde (PFA), 36.5%	F8775	Sigma Aldrich
Saponin	47036	Sigma Aldrich
BSA Fraction V	K41-001	PAA laboratories–GE Healthcare Life Sciences
Permeabilization buffer	-	0.001% v/v saponin, 4% w/v BSA Fraction V in PBS

3.5 Mouse strains, devices and materials for mouse and primary murine cell methods

3.5.1 Mouse strains

For the high-fat diet experiments GFP-LC3 mice[289] and Gadd45β KO[290] x GFP-LC3 mice were used. The blastocyst injection for the generation of ATG5 transgenic mice was performed in a F1 129 x BL6 genetic background[291] and the backcrossing was done with C57BL/6J WT mice.

3.5.2 Materials and devices used for high-fat diet experiments

Tab. 3.19: Diet, reagents and materials for high-fat diet experiment

Reagent/Material	Composition	Cat. no.	Company
ssniff® EF R/M acc. D12451 (I) mod. (high-fat diet)	Metabolizable Energy (ME) 27% protein 31% carbohydrates 42% fat	E15744-34	SSNIFF Spezialdiäten (Soest, Germany)
ssniff®EF acc D12450B (I) mod. (control diet)	Metabolizable Energy (ME) 26% protein 65% carbohydrates 11% fat	E15745-04	SSNIFF Spezialdiäten
Brand® micro hematocrit capillary	-	749311	Brand
Heparin 25 000 IE/5 mL	-	-	Ratiopharm (Ulm, Germany)
Cholesterol Stripes HDL Cholesterol Stripes Glucose Stripes Triglyceride Stripes	-	1074065 1208756 0744948 0745049	Roche diagnostics (Risch, Switzerland)

The measurement of metabolic parameters in the serum of mice was performed by a Reflotron® Plus device (Roche diagnostics, Risch, Switzerland).

3.5.3 Devices and antibodies used for flow cytometry

Cell populations were analyzed in a BD® FACS Canto or a BD® LSR II Flow Cytometer (BD Biosciences; Franklin Lakes, NJ/USA) after fluorescent labelling. The sorting and isolation of specific cell populations was performed with a BD® FACS Aria II device (BD Biosciences).

Tab. 3.20: Buffers used for flow cytometry sample preparation

Usage	Buffer	Composition
Lysis of red blood cells	ACK	0.15 M NH_4Cl, 1 mM $KHCO_3$, 0.1 mM EDTA, adjust pH to 7.3 (with NaOH)
Antibody stainings	FACS	2% BSA w/v, 0.01% v/v NaN_3 in PBS
	10x Annexin V Binding	0.1 mM HEPES, 1.4 M NaCl, 25 mM $CaCl_2$, adjust pH to 7.4

Tab. 3.21: Murine antibodies and reagents used for analysis via flow cytometry

Reactivity	Fluorochrome	Isotype	Clone/Cat. no.	Company
AnnexinV	APC	-	550475	BD Pharmingen
CD3	Horizon V450	Rat IgG2b, κ	17A2/561389	BD Horizon
CD4	Horizon V500	Rat IgG2a, κ	RM4-5/560782	BD Horizon
CD4	PE	Rat IgG2a, κ	RM4-5/553049	BD Pharmingen
CD8	PE-Cy7	Rat IgG2a, κ	53-6.7/100722	Biolegend (San Diego, CA/USA)
CD19	APC-Cy7	Rat IgG2a, κ	6D5/115530	Biolegend
CD25	APC	Rat IgG1, λ	PC61/102012	Biolegend
CD44	PE	Rat IgG2b, κ	IM7/12-0441-93	Affimetrix/eBioscience (San Diego, CA/USA)
CD62L	PerCP Cy5.5	Rat IgG2a, κ	MEL-14/45-0621-82	Affimetrix/eBioscience

4 EXPERIMENTAL PROCEDURES

4.1 Molecular Biology

4.1.1 Cloning

4.1.1.1 Restriction of DNA

For cloning inserts into a new vector backbone digestion with the respective restriction enzymes was performed. If the insert sequence did not contain the proper recognition sequence, the recognition sequence was introduced via a polymerase chain reaction (PCR) beforehand (see 4.1.1.6). Typically, a 50 µL-reaction containing 1 µg amplified insert or 1-3 µg vector DNA, 0.5 µL 100x BSA (optional), 5 µL restriction enzyme buffer and 1 µL of each enzyme (see Tab. 3.2) was prepared and incubated in a peqSTAR 96x Universal Thermocycler (Peqlab Biotechnologie) or a waterbath according to manufacturer's instructions. After restriction, the DNA fragments were separated by DNA gel electrophoresis.

4.1.1.2 DNA gel electrophoresis

The necessary amount of agarose was boiled with 1x TAE buffer (see Tab. 3.6) to reach a percentage of 0.5 to 2% depending on the size of the expected fragments. 1:10000 v/v of 1% ethidium bromide solution was added before pouring. The set gel was loaded with loading dye-charged sample and the power supply was adjusted to 10 V/cm. The separation was typically performed for 45 min and the intercalation of ethidium bromide in the DNA-fragment was visualized with UV light (312 nm) at an INTAS gel documentation system (see 3.2.4).

4.1.1.3 Isolation of DNA after gel electrophoresis

To recover the separated DNA fragments from the agarose gel, the respective band was cut and the gel slice was processed with the help of the Zymoclean™ Gel Recovery Kit (Zymo Research; Irvine, CA/USA) according to the manufacturer's instructions. DNA concentration and purity was determined at a NanoDrop 1000 spectrophotometer (Peqlab Biotechnologie) by analyzing the absorbance at 260 nm and 280 nm. The calculation of the concentration from the measured absorbance relies on the Lambert-Beer's law.

$$A = \varepsilon \cdot b \cdot c$$

A = absorbance

ε = coefficient of extinction (L $\cdot$ mol^{-1} $\cdot$ cm^{-1})

b = path length (cm)

c = concentration (mol/L)

This equation is modified for the measurement of nucleic acids as follows (adjustment of the extinction coefficient unit):

$$c = (A \cdot \varepsilon) \cdot b^{-1}$$

c = concentration (ng/µL)

A = absorbance

ε = coefficient of extinction (ng $\cdot$ cm $\cdot$ µL^{-1})

b = path length (cm)

4.1.1.4   Ligation of DNA fragments

Typically 1:1 and 1:3 ratios of cleaved vector backbone to insert were prepared in a 20 µL-ligase reaction with 1 µL T4 ligase and 2 µL 10x Ligase Buffer (Thermo Fisher Scientific). The ligation reaction was incubated over night at 16 °C.

4.1.1.5   Transformation and plasmid amplification

In order to amplify and isolate plasmid DNA, *E. coli* bacteria were transformed with the vector. Half of the ligation reaction was added to one aliquot of chemically competent Top10 *E. coli* bacteria. The suspension was mixed by tapping and incubated on ice for 30 min. Afterwards DNA uptake was initiated via a 42 °C heat shock for 30 sec. After a short cooling on ice, 500 µL pre-warmed LB medium were added and the sample was incubated for 30 min at 37 °C with shaking in a Eppendorf Thermomixer comfort 5355 (Eppendorf, Hamburg). Finally, the sample was plated on LB agar plates supplemented with the appropriate antibiotic. The plates were incubated at 37 °C over night.

The identification of positive clones was performed in two different ways. Several clones from the plate were either taken for liquid cultivation followed by plasmid isolation via the QIAprep Spin Miniprep Kit (Qiagen, Hilden, Germany) according to manufacturer's manual and (analytic) restriction (see 4.1.1.1) or for analysis by colony PCR (see 4.1.1.7). All constructs were verified by sequencing, therefore the DNA was usually prepared premixed with primer according to manufacturer's protocol and sent to Eurofins MWG Operon.

4.1.1.6   Amplification of DNA by polymerase chain reaction

Typically, a total sample volume of 50 µL was prepared, which consisted of 25 µL 2x Phusion Flash Master Mix, 25 ng DNA template and 0.5 µM each forward and reverse primer (see Tab. 3.3 and Tab. 3.4). In general, the following 3-step protocol was used as a template and adjusted according to the utilized primers and templates.

Step	Temperature/Time	Cycle number
Initial denaturation	98 °C/10 s	1x
Denaturation	98 °C/1 s	
Annealing	X °C/5 s	30x
Elongation	72 °C/15 s per kb	
Final extension	72 °C/1 min	1x
Storage	8 °C	

The annealing temperature of the used primer pair was calculated according to the manufacturer's instructions and all PCRs were performed in a peqSTAR 96x Universal Thermocycler (Peqlab Biotechnologie).

4.1.1.7   Amplification of DNA by Colony-PCR

To allow for parallel and fast analysis of numerous clones after transformation the clones were directly used as PCR template. For this purpose 10 µL-reactions with 5 µL KAPA2G™ Fast 2x Ready-Mix with Dye, 0.5 µM of insert-specific forward and reverse primer (see Tab. 3.3 and Tab. 3.4) and a small portion of an *E. coli* colony were prepared.

Step	Temperature/Time	Cycle number
Initial denaturation	95 °C/3 min	1x
Denaturation	95 °C/15 s	
Annealing	X °C/15 s	35x
Elongation	72 °C/15 s per kb	
Final extension	72 °C/5 min	1x
Storage	8 °C	

Afterwards the PCR samples were analyzed by DNA gel electrophoresis (see 4.1.1.2) to check for the amplification of the desired fragment.

4.1.1.8   Purification of amplified DNA by ethanol precipitation

To purify the DNA product after a PCR, 0.1 volumes of 3 M sodium acetate (pH 5.2) followed by 2 volumes of pure cold ethanol were added to the PCR sample. After a 10 min-incubation step on ice, the sample was centrifuged (4 °C, 14000 rpm, 25 min). The resulting DNA pellet was washed once with 500 µL 70% ethanol at room temperature (RT), followed by another centrifugation step (4 °C, 14000 rpm, 15 min), after which the supernatant was carefully aspirated completely. The DNA pellet was resuspended in dH_2O and the concentration was determined at the NanoDrop 1000 spectrophotometer (Peqlab Biotechnologie) by analyzing the absorbance at 280 nm and 260 nm.

4.1.1.9   Overlap-Fusion-Mutagenesis

The introduction of specific point mutations in a target coding sequence (CDS) was performed with a four primer system. The outer primer pair covered the beginning and the end of the coding sequence and contained restriction sites that needed to be introduced for the later cloning procedure. Additionally, two inner primers were designed, which were complementary to each other and included the mutated residues preferably in the middle of the primer sequence.

First, two separate PCRs were performed, where one primer of the outer and one of the inner pair were combined in the way that the reaction results in a 5'-half and a 3'-half of the coding sequence, respectively. Both parts now had a sequence overlap in the mutated region. This first step of the mutagenesis was performed similar to the regular PCR protocol (see 4.1.1.6) with a purification step via ethanol precipitation (see 4.1.1.8) in the end. Before performing the purification, 5 µL of the PCR were analyzed by DNA gel electrophoresis (see 4.1.1.2) to test for the successful amplification.

During the second reaction, the two sequence halves from the previous step were combined. Single stands of the 5' and the 3' part were formed as a result of the initial denaturation. These were subsequently annealed with each other according to their complementary (mutated) region, hence, resulting in a partially single-stranded fusion product of the 5'- and the 3' part. To achieve this intermediate, 50 ng of both parts from the previous PCR were added, along with 4 µL 5x Phusion HF Reaction Buffer, 0.2 mM desoxynucleotides (dNTPs), 0.3 µL Phusion Hot Start II DNA Polymerase

(see 3.2.2) and dH$_2$0, to a 20 μL-reaction. The cycler was adjusted to perform a protocol with an increased denaturation time but only 10 cycles.

Step	Temperature/Time	Cycle number
Initial denaturation	98 °C/2 min	1x
Denaturation	98 °C/35 s	
Annealing	68 °C/25 s	10x
Elongation	72 °C/30 s	
Final extension	72 °C/10 min	1x
Storage	8 °C	

After the program was finished, a 10 μL-primer mix was added containing 0.5 μM of each of the outer primers, 2 μL 5x Phusion HF Reaction Buffer and 0.3 μM dNTPs per sample. Next, the protocol below was started.

Step	Temperature/Time	Cycle number
Initial denaturation	98 °C / 2 min	1x
Denaturation	98 °C / 35 s	
Annealing	68 °C / 25 s	35x
Elongation	72 °C / 30 s	
Final extension	72 °C / 10 min	1x
Storage	8 °C	

With this last PCR, the single-stranded parts were completed into a double strand by the polymerase. In the end, the finished PCR product was isolated by ethanol precipitation and further processed for cloning into the desired expression vector.

4.1.2 Genotyping of mouse tissue

Mouse tissue was digested and further processed for PCR by using the KAPA Fast Mouse Genotyping Kit (see 3.2.2) according to the manufacturer's instructions. The PCR conditions were adjusted according to the mouse line-specific primers (see Tab. 3.4).

4.1.3 Sequencing of reconstituted cells via RNA isolation and synthesis of cDNA

After the viral or transfection-based reconstitution of KO cells with either the WT protein or mutant forms (see 4.2.2 and 4.2.3), the expression of the introduced coding sequence was verified by isolation of the total RNA from these cells.

For this, the RNeasy™ Mini Plus Kit (Qiagen) was used in combination with the QIAshredder™ columns (Qiagen) according to the manufacturer's instructions. The concentration and purity of the isolated RNA was measured at the NanoDrop 1000 spectrophotometer. Subsequently, 1 µg RNA was used for cDNA single-strand synthesis via the RevertAid First Strand cDNA Synthesis Kit (Thermo Fisher Scientific). In this reaction a 1 to 1 combination of oligo(dT)$_{18}$ and random hexamer primers was used. All steps were performed according to the respective manual.

Next, the synthetized cDNA was used as a template for the final PCR, which was specific for the CDS of the reconstituted protein (see 4.1.1.6). A small volume of the PCR sample was analyzed by DNA gel electrophoresis (see 4.1.1.2) to check for successful amplification of the desired fragment and to verify the accuracy of the RNA isolation and the cDNA synthesis via the included control samples. The residual PCR product was purified by ethanol precipitation (see 4.1.1.8), premixed with sequence-specific primers and sent for sequencing.

4.2 Cell Biology and biochemistry methods

4.2.1 Transient transfection of adherent cells with plasmid DNA

For transient transfection of adherent cells with plasmid DNA, depending on the cell type different approaches were used. HEK293T cells were transfected by the calcium phosphate transfection method. In this method, DNA-calcium phosphate precipitates are formed and internalized by the cells. HEK293T cells were seeded the day before transfection typically in 10 cm^2 dishes ($2 \cdot 10^6$ cells) or 6-well plates ($3.5 \cdot 10^5$ cells). The following morning the medium was changed to 8 mL (dish) or 1.4 mL (well) fresh DMEM and the transfection mix was prepared. For each 10 cm^2 dish 15 µg plasmid DNA (6-well: 5.1 µg) were mixed with 500 µL 1x HBS buffer (6-

well: 86 µL). Next, 30 µL 2 M CaCl$_2$ (6-well: 5.1 µg) were added and the sample was immediately mixed by short vortexing (buffers see Tab. 3.9). Afterwards, the mix was incubated for 20 min at RT. Finally, the mix was dropwise distributed on the seeded cells.

Transient transfection of MEFs was performed, either by using the jetPEI® or the jetPRIME® transfection reagent from Polyplus transfection (see Tab. 3.9). The transfection was performed according to the manufacturer's manual.

4.2.2 Production of retro-viral particles

In order to stably introduce foreign DNA in adherent cells, a retro-viral approach was utilized. In order to produce retro-viral particles, HEK293T cells were transiently transfected via the calcium phosphate method (see 4.2.1).

Together with retro-viral vector, e.g. pBABEpuro (see Tab. 3.1), which carries the desired coding sequence, two plasmids for retro-viral particle production and packaging were included. The gag/pol-plasmid codes for inner structure proteins of the virus (gag) and the reverse transcriptase (pol) whereas the pVSV-G-vector encodes the envelope protein of the vesicular stomatitis virus (VSV), which allows entry of almost every cell type (see Tab. 3.1). Typically, for a 10 cm^2 dish the transfection mix consisted of 8 µg p-gag/pol, 2.5 µg pVSV-G and 3.5 µg retro-viral plasmid. One day after transfection, the medium was exchanged. On day 2 after transfection, the medium was exchanged again and the virus particle containing supernatant of the HEK293T was collected, sterilized by filtration (0.45 µm) and stored in the fridge. On day 3 after transfection all steps were repeated as on day 2 after transfection, afterwards both supernatants were combined and stored at 4 °C.

4.2.3 Retro-viral transduction of MEF cells

To perform the transduction with the produced retro-viral particles, the parental cells, here MEF, were seeded on day 0. Usually 1.25·10^6 cells were plated per well of a 6-well plate. On the day of transduction, the old medium was aspirated and RT-prewarmed virus supernatant was added to the cells. To ensure transduction success, different volumes (100 µL, 300 µl, 1000 µL) were used. Thereafter, fresh medium was

added to a final volume of 1.5 mL. In order to enhance the efficiency of the retro-viral transduction the medium-supernatant mix was additionally supplemented with 8 μg/mL polybrene (Sigma Aldrich; St. Louis, MO/USA), which increases the adsorption of the virus on the membrane of target cells. In the next step, the 6-well plate was centrifuged (2300 rpm, 30 °C, 90 min) to accelerate the sedimentation of the viral particles. Finally, 1 mL prewarmed medium was added per well and the cells were incubated (37 °C, 5% CO_2, 95% humidity).

On the day after the first retro-viral transduction, the procedure was repeated in the very same manner. On day 1 after the two subsequent transductions, depending on the cell density, the cells were either left to rest after the media exchange or were splitted. On the following day, the selection of transduced cells was started. For splitting of the transduced cells, medium was supplemented with the respective selection marker. Here puromycin (for ATG5) or blasticidin (for mCitrine-hLC3B) were used (see Tab. 3.7). The working concentration was determined beforehand by a titration experiment. Depending on the retro-viral plasmid used, the transduced MEFs were selected either by 3 μg/mL puromycin or 5 μg/mL blasticidin for at least two weeks. In this study bulk populations were selected and used for the later experiments.

4.2.4 Hank's buffered saline solution and bafilomycin A1 treatment for autophagy measurements

On day 0 of the experiment, typically $4 \cdot 10^5$ MEF cells were seeded per well of a 6-well plate. Four wells were prepared per cell line. On day 1, the stimulation was performed. For this, the medium was changed, in which two of the prepared wells got fresh DMEM and the other two wells got the starvation medium Hank's buffered saline solution (HBSS) (see Tab. 3.8). After 2 h of incubation, bafilomycin A1 (BafA1) (see Tab. 3.8) was added in a final concentration of 100 nM to one of the DMEM- and to one of the HBSS-wells. The other two wells were supplemented with the same volume of DMSO as a solvent control. After another 2 h of incubation, the samples were harvested.

4.2.5 Harvesting and cell lysis for Western blot analysis

After a transfection, stimulation or infection experiment, total protein lysis was performed for Western blot analysis. For this, the adherent cells were harvested with 0.05% trypsin/EDTA, suspended in PBS and the suspension was centrifuged (4000 rpm, 5 min, 4 °C). The pellet of one well from a 6-well plate or a 3.5 cm^2 dish typically consisted of 5 to $12 \cdot 10^5$ cells. The pelleted cells were resuspended in 50 to 80 μL cold TPNE lysis buffer freshly supplemented with PMSF, NaVO$_3$ and SPI (see Tab. 3.10). For immunoprecipitation experiments, DISC lysis buffer with the same fresh supplements (see Tab. 3.10) was used. Moreover, since larger cell numbers from $1 \cdot 10^7$ to $2 \cdot 10^7$ cells were utilized for these immunoprecipitation experiments, the lysis was performed in 1 to 1.5 mL lysis buffer. After a 20 min-incubation on ice, the samples were centrifuged (14000 rpm, 15 min, 4 °C) in an Eppendorf table centrifuge 5417R to remove the debris. The supernatants were transferred to a new tube and used for the determination of protein concentration by bicinchoninic acid (BCA) assay according to manufacturer's instructions (see Tab. 3.12).

4.2.6 Co-immunoprecipitations of ATG5-c-myc or FLAG-p38

Typically, $1 \cdot 10^7$ HEK293T cells transiently transfected with ATG5-c-myc and FLAG-p38 (see 4.2.1) were lysed in cold DISC lysis buffer (see Tab. 3.10). For endogenous immunoprecipitation experiments, $2 \cdot 10^7$ ATG5 KO MEF cells reconstituted with ATG5-c-myc were used.

Part of the resulting lysate was saved as input, supplemented with 5x RSB (see Tab. 3.12) and heated for 5 min at 95°C. The residual lysate was incubated with the desired bead suspension (see Tab. 3.15). For co-precipitations via ATG5-c-myc 20 uL of the myc-tag magnetic bead conjugate were used per sample. The beads were washed once with 1x TBS buffer (see Tab. 3.13) before usage. The incubation was performed on a rotating wheel at 4 °C over night. With help of a magnetic stand the beads were washed 5x with 600 μL DISC lysis buffer (see Tab. 3.10). After the last washing step 25 μL 1x RSB were added to the beads and the sample was heated for 5 min at 95 °C. The supernatant was analyzed by SDS-PAGE and Western blotting (see 4.2.7 and 4.2.8)

If the precipitation was performed via FLAG-p38, 40 uL of the anti-FLAG® M2 affinity gel were used per sample. The bead suspension was washed with 1x TBS prior to usage. The incubation was performed on a rotating wheel at 4°C for 4 h. Afterwards the beads were washed 5x by adding 600 μL DISC lysis buffer and a centrifugation step (6000 rpm, 4 °C, 2 min). After the final washing step, all the liquid was aspirated with a Hamilton syringe (Hamilton; Reno, NV/USA). The further preparation of the beads for SDS-PAGE was similar to the myc-bead samples (see above).

4.2.7   Separation of denatured proteins by SDS-PAGE

After the total protein concentration of lysates was determined via BCA assay (Tab. 3.12) according to manufacturer's instructions, the volume for 20 to 30 μg protein was supplemented with 5x RSB and heated for 5 min at 95 °C. Depending on the molecular weight of the proteins of interest a 10%, 12% or 15% SDS polyacrylamid gel (see Tab. 3.12) was prepared. The separation was usually performed in BioRAD Mini-PROTEAN Tetra Cell Systems or for larger sample sets in the PerfectBlue™ Vertical Double Gel System Twin ExW S (Peqlab Biotechnologie). The chambers were prepared with 1x running buffer (see Tab. 3.12) and the power supplies (Bio-Rad; Hercules, CA/USA) were adjusted to 80 to 100 V. Afterwards the gel was either used for Western blotting or coommassie staining. For the later the gel was directly placed in InstantBlue™ (Expedion; San Diego, CA/USA) and incubated for 1 h with gentle shaking.

4.2.8   Transfer of the separated proteins by Western blot

For wet blotting, the protein transfer to the methanol-activated PVDF membrane was performed in a Mini Trans-Blot® System or a Criterion® System (both Bio-Rad) filled with cold 1x transfer buffer (see Tab. 3.13) for 1 h 45min at 100 V. If semi-dry blotting was necessary, a Novex® Semi-Dry-Chamber (Peqlab Biotechnologie) was used. Here the power supply was adjusted to 30 V and 0.35 A for 1 h 45min.

Afterwards, the membrane was blocked either in 5% nonfat milk/TBS-Tween or in 5% BSA (protease free)/TBS-T (see Tab. 3.13) for at least 30 min with gentle shaking. In the next step, the membrane was incubated with the primary antibody

diluted (1:300 to 1:4000) in blocking buffer supplemented with 0.01% NaN_3 at 4 °C over night (see Tab. 3.15). On the next day, unbound primary antibody was removed during 4 times 10 min of washing in TBS-T. Afterwards the membrane was incubated with secondary antibody diluted (1:5000 to 1:20000) in blocking buffer for 1 h at RT (see Tab. 3.16). Subsequently, the membrane was washed 4x for 10 min in TBS-T.

Depending on the expected signal strength the membrane was developed either with self-made ECL, SuperSignal® West Dura, WesternSure® ECL substrate or Amersham® ECL Select® (see Tab. 3.14). The chemiluminescence was detected by the Fusion FX-7 camera (Vilber Lourmat, Eberhardzell, Germany) or the Amersham® Hyperfilms (see Tab. 3.14) and the Curix-60 developing system (AGFA; Mortsel, Belgium). For re-probing the membrane with the next antibody, the membrane was incubated with ReBlot plus stripping solution from Millipore or a self-made solution, that inactivates the horseradish peroxidase (see Tab. 3.14) for 25 min at RT.

4.2.9 Production of recombinant proteins

Recombinant proteins for *in vitro* kinase assays were produced by Dr. Caroline Behrens and Dr. Milica Bajagic (group of Dr. Andrea Scrima, Helmholtz-Centre for Infection Research, Braunschweig). Depending on the desired protein, different expression approaches were necessary. The covalently conjugated human strep-tagged ATG12–5 protein was expressed in insect cells. His-tagged hATG5 WT, all mutant forms for ATG5 and the ATG12–5 truncated (ATG12–5 tr) protein were produced in the *E. coli* strain Rosetta after induction via isopropyl β-D-thiogalactoside (IPTG). To gain the active phosphorylated form of the human p38 kinase, the protein was co-expressed with the upstream mitogen-activated protein kinase kinase (MKK) 3/6 in Rosetta. The bacterial pellet was lysed and the lysate was loaded on a column specifically for the tag of the target protein. After several washing steps, the target protein was eluted from the column by using a high concentration of competing agent, e.g. imidazole for his-tag or desthiobiotin for strep-tag. Afterwards the agent was removed via dialysis. The protein concentration was determined by the NanoDrop1000 spectrophotometer using the Protein A280 module, where the specific molar extinction coefficient and molecular weight were entered manually for each sample.

4.2.10 *In vitro* kinase assays with p38 MAP kinase and different forms of ATG5

In the performed *in vitro* kinase experiments active, phosphorylated p38 MAPK or an kinase-inactive p38^{K53A} mutant (KM) was incubated with different substrate candidates namely ATG5 WT, the mutant ATG5^{T75A} and ATG12–5 full length conjugate or the truncated form of ATG12–5 (ATG12 52-140) in the presence of ATP.

Typically, 200 ng kinase and 1 μg substrate were added with 1x kinase buffer (see Tab. 3.11) to a total volume of 25 μL and incubated for 1 h at 37 °C with 300 rpm of shaking. Afterwards the sample was supplemented with 5x RSB and heated for 5 min at 95 °C. Usually, the *in vitro* kinase samples were processed via SDS-PAGE followed by Western blot (see 4.2.7 and 4.2.8). Incubation of the membrane with antibodies directed against phospho-threonine (see Tab. 3.15) resulted in a signal at the respective molecular weight, if the substrate was phosphorylated at a threonine residue.

4.2.10.1 Dephosphorylation of ATG12–5 prior to in vitro kinase assay

The production of recombinant ATG12–5 full length in insect cells resulted in a pre-phosphorylated form of the isolated protein-conjugate. Therefore, ATG12–5 full length was treated with a phosphatase prior to the incubation with the kinase.

In a batch sample 5 ug ATG12–5 and 25 units Antarctic Phosphatase (see Tab. 3.11) were incubated in 1x Phosphatase Reaction Buffer for 30 min at RT with 300 rpm shaking. Afterwards, the zinc-chelator N,N,N',N'-tetrakis (2-pyridylmethyl)ethane-1,2-diamine (TPEN, see Tab. 3.11) was added to a final concentration of 1 mM and the sample was incubated for 10 min at RT with 300 rpm shaking. This treatment inactivated the zinc-dependent phosphatase with respect to the following kinase reaction. The kinase reaction condition was adjusted by 3x kinase buffer, before (per μg of ATG12–5 full length) 200 ng of the p38 MAPK were added. Depending on the desired analysis, the sample was either processed for SDS PAGE and Western blot (see 4.2.7 and 4.2.8) or for mass spectrometry.

4.2.11 Mass spectrometry analysis of *in vitro* kinase samples

For analysis of the phosphorylation site by liquid chromatography-mass spectrometry/mass spectrometry (LC-MS/MS), *in vitro* kinase assay samples were supplemented with 2 volumes of 8 M urea. All further steps were performed by Dr. Josef Wissing and co-workers from the mass spectrometry facility (Helmholtz-Centre for Infection Research). In order to isolate the denatured proteins, they were precipitated by GlycoBlue (Ambion, Thermo Fisher Scientific) over night. After re-solubilization of the dried protein pellet, digestion of the proteins was performed with LysC or AspN in a final ratio of 50 to 1 (protein to protease) over night. The isolated peptide pellet was desalted by the use of RP18 material (Merk Millipore). Therefore, re-solubilization in 3% acetonitrile (ACN) containing 0.2% trifluoroacetic acid (TFA) was performed before adsorption to the material. A dilution of 60% ACN containing 0.2% TFA was used for the elution of the peptides that were re-buffered in 3% ACN containing 0.2% TFA for the fragmentation. The analysis was performed on a Dionex UltiMate 3000 n-RSLC system connected to an LTQ Orbitrap Velos mass spectrometer or to a Fusion mass spectrometer (Thermo Scientific). For the LC, peptides were loaded onto a C_{18} pre-column and subsequently fractionated on a C_{18} analytical column with a linear 30-min gradient of 3-80% ACN in 0.1% TFA. The effluent from the column was electro-sprayed (Pico Tip Emitter Needles, New Objectives; Woburn, MA/USA) into the mass spectrometer. The following collision-induced dissociation within the ion trap was restricted to a maximum of 10 doubly- and triply-charged peptides, which are automatically identified. For the raw data processing utilized search parameters included the chosen enzyme, a maximum of two missed cleavages; methylthio-carbon as fixed modification and oxidation (methionin) and phosphorylation (serine, threonine, and tyrosine) as variable modification. The peptide tolerance was set at 10 part per million (ppm) and the MS/MS tolerance restricted to 0.4 Da.

4.3 Microbiology methods (bacterial infection experiments)

4.3.1 *S. aureus* infection experiments for Western blot sample preparation

For analysis of *S. aureus*-infected fibroblasts by Western blot, on day 0 of the experiment MEF cells were seeded in $3.5\,cm^2$ dishes. The number of seeded cells ranged for ranged between $2 \cdot 10^5$ and $4 \cdot 10^5$ per dish, depending on the cell line. A 5 mL-over night culture of the bacterium was prepared by suspending one *S. aureus* SH1000 colony (see 3.4.1) in TSB medium (see Tab. 3.17) without antibiotics. The cultivation was performed at $37\,°C$ and with 180 rpm of shaking. During some experiments, *S.* Typhimurium (see 3.4.1) infection was performed in parallel as a control. In comparison to *S. aureus*, the cultivation of *S.* Typhimurium was performed in LB medium supplemented with 50 µg/mL ampicillin.

On day 1, a fresh 1%-pre-culture of the bacteria was started from the over night suspension and the growth of the bacteria was monitored by measuring the OD_{600} at an Ultrospec 2000 UV/visible Spectrophotometer (Pharmacia Biotech-GE Healthcare Life Sciences; Little Chalfont, Great Britain). The early exponential phase of *S. aureus* was determined by an OD_{600} between 1 to 1.3. To harvest the bacteria at this stage 1 mL of the suspension was centrifuged (4000 rpm, 5 min) and the pellet was washed once with cold PBS. After another centrifugation step, the pellet was resuspended in 1 mL PBS. The number of bacteria per volume is calculated by using the experimental verified approximation that an $OD_{600}=1$ is equal to a concentration of $1 \cdot 10^8$ bacteria/mL. Depending on the desired multiplicity of infection (MOI), the needed volume of the bacteria suspension is added to the adherent cells. *S. aureus* infections were usually performed with MOI=8, whereas for *S.* Typhimurium infections a MOI=100 was used[288].

After the bacteria were added to the fibroblasts, the cells were placed in the incubator for 90 min to let the (non-motile) *S. aureus* settle down and invade eukaryotic cells. During the subsequent treatment of 12 min with 10 µg/mL lysostaphin (see Tab. 3.17), all the extracellular *S. aureus* cells were lysed. The kinetic was initiated by replacing the medium after this step. In terms of *S.* Typhimurium further invasion was stopped after 60 min by performing four washing steps with PBS

and supplementing the medium with gentamycin (100 µg/mL) to kill the residual
S. Typhimurium cells.

Samples were harvested according to the time points of the kinetic. The pellet was
processed for Western blot analysis via lysis with TPNE lysis buffer (see Tab. 3.10,
4.2.5, 4.2.7 and 4.2.8).

4.3.2 *S. aureus* infection experiments for immunofluorescence sample preparation

In order to analyze the *S. aureus* infection via immunofluorescence (IF),
fibroblasts were seeded in a 12-well plate primed with cover slips. Depending on the
cell type $5 \cdot 10^4$ to $8 \cdot 10^4$ cells were plated per well.

The immunofluorescence experiments were performed with the RFP-expressing
SH1000 strain (see 3.4.1). In comparison to the WT strain, it was cultured in
chloramphenicol-supplemented (30 µg/mL) medium. Despite this, all the cultivation
and preparation steps were similar to the WT SH1000 protocol. In general, the
infection procedure was performed identically to the preparation of Western blot
samples. Instead of exchanging the medium via aspiration and refilling after the
lysostaphin treatment, the cover slips were carefully transferred into a new well with
fresh medium at this step. If staining of acidic or lysosomal compartments via the
CytoID® Autophagy Detection Kit or LysoTracker Deep Red (see Tab. 3.18) was
performed, the respective reagents were added to the medium 15 min prior to
harvesting. For CytoID 3 µL per well and for LysoTracker a concentration of 16 nM
was used.

After the kinetic was finished, the cover slip was dip-washed in PBS followed by
fixation of the cells in pre-warmed 4% paraformaldehyde (PFA) for 10 min at 37 °C.
Subsequently, dip-washing in PBS was performed to remove residual PFA. If no
(additional) stainings were needed, the cover slip was placed up-side-down on a glass
slide with mounting medium (DAKO-Agilent Technologies). In order to allow for
complete mounting, the slides were incubated at RT for at least 2 h before they were
transferred to 4°C for storage.

Permeabilization of the cells was needed to stain for intracellular proteins. For this, the washing step of the cover-slip after the PFA fixation was followed by incubation in permeabilization buffer (see Tab. 3.18) for 45 min at RT. On a parafilm stripe a 50 uL-drop with the desired first antibody dilution (1:250 to 1:500) in 2% FCS was prepared (see Tab. 3.15) and the respective cover slip was placed on the drop up-side-down. The incubation was performed at 4 °C overnight.

On next day, the cover slip was dip-washed in permeabilization buffer and incubated with the respective secondary fluorochrome-tagged antibody (see Tab. 3.18) in permeabilization buffer for 1 h at RT. After dip-washing the slip with permabilization buffer and PBS, the slip was placed on glass slides with mounting medium.

4.3.3 *S. aureus* infection analyzed by transmission electron microscopy

Infection of NIH/3T3 cells with *S. aureus* was performed in a 10 cm^2 plate with a MOI=18. The analyzed time points were 2 and 3 h post infection (hpi). All further steps were performed by Prof. Dr. Manfred Rohde and Ina Schleicher (Helmholtz-Centre for Infection Research, Braunschweig).

For visualization of intracellular membranes within the infected NIH/3T3 fibroblasts, two different fixation schemes were applied. The so called O-T-O method describes an alternate treatment with osmium tetroxide, the osmiophilic thiocarbohydrazide and again osmium tetroxide. Osmium tetroxide itself especially accumulates in lipid-containing components of the cell, but the resulting contrast and resolution in the microscopy images are relatively weak. To solve this problem thiocarbohydrazide is used for bridge formation. With one end it binds to the already present osmium tetroxide and attracts with the other part an additional amount of osmium tetroxide during the second exposure. This accumulation method results in an increased contrast and resolution predominantly in compartments with high lipid content, e.g. membranes[292].

In detail, the samples were fixed with 2.5% glutaraldehyde and 5% formaldehyde prior to treatment with osmiumferrocyanide (1% osmium tetroxide and 1.5%

ferrocyanide). Subsequently, the samples were incubated with 1% thiocarbohydrazide followed by a second osmiumferrocyanide-treatment. Embedding was performed in 1.75% agar, afterwards the samples were sliced into small cubes. Graded acetone series were used for the following dehydration. The final preparation step included the embedding into the epoxy low viscosity resin.

In the second fixation scheme, the samples were fixed with 1% glutaraldehyde and 5% formaldehyde in PBS. After washing with PBS the samples were further treated with 1% aqueous osmiumtetroxide for 1 h, washed and incubated with 4% aqueous uranyl acetate for 1 h. After washing with PBS the samples were further processed as for the O-T-O method.

The prepared samples were processed with a diamond knife to obtain ultrathin sections, which were collected onto butvar-coated grids. For counterstaining, uranyl acetate and lead citrate were used. Examination was performed in a Zeiss TEM 910 (Zeiss, Oberkochen, Germany) at an acceleration voltage of 80 kV and at calibrated magnifications. Images were recorded digitally at calibrated magnifications with a Slow-Scan CCD-Camera (1024x1024, ProScan, Scheuring, Germany) with ITEM-Software (Olympus 484 Soft Imaging Solutions, Muenster, Germany). Contrast and brightness were adjusted with Adobe Photoshop CS5.

4.4 Mouse and primary murine cell methods

4.4.1 High-fat diet experiment

During the high-fat diet (hfd) experiment, high-fat versus control diet (see Tab. 3.19) were fed to male and female animals of two different genotypes, GFP-LC3 (WT) and Gadd45β KO x GFP-LC3 (Gadd45β KO) mice (see 3.5.1). Four groups per genotype – male: high-fat versus control and female: high-fat versus control - were assembled with a starting number of six mice each. To keep initial differences as little as possible, a minimal number of litters were used to set the groups. The starting age of the mice was 12 to 14 weeks and the feeding was performed for 17 weeks. Because of the strict requirements in terms of sex, gender, litters and age the desired number of Gadd45β KO mice was only available a few weeks later, therefore the feeding-start

of this group was shifted respectively. Every week, at the same day and time, the weight of the animals was measured.

4.4.1.1 Retro-orbital blood collection during high-fat diet experiment

After 8 or 10 weeks and 15 or 17 weeks of feeding, blood was taken and the plasma was analyzed for the concentration of different metabolic parameters. Two different methods of blood drawing were used: punctuation of the retro-orbital plexus (for all half-time measurements and the final measurement of WT mice) and heart blood after sacrificing of the mice (final measurement of Gadd45β KO mice).

For retro-orbital blood collection, the mice were subdivided in two groups, which were handled on two following days. 100 μL of the collected blood were transferred to a new tube prepared with 20 μL 0.02 M EDTA or 20 μL 1:2000 Heparin (see Tab. 3.19) as anti-coagulant. The collected samples were stored on ice before they were centrifuged (12000 rpm, 3 min, 4 °C) to separate the plasma from the pelleted cellular components.

4.4.1.2 Measurement of metabolic parameters in the plasma of high-fat diet-fed and control diet-fed mice

The isolated plasma was used for measuring the glucose, triglyceride, cholesterol and high density lipoprotein (HDL) cholesterol concentrations via the respective test stripes (see Tab. 3.19) and a Reflotron® device (Roche diagnostics). Since 30 μL of plasma were needed per stripe, two rounds of retro-orbital blood collection were performed with a gap of 2 weeks in between to measure all four parameters for one mouse.

4.4.2 Preparation of organs and tissues for histology

During the first preparation of mice from the high-fat diet experiment, advice and help was provided by Dr. Marina Pils and the mouse pathology team (Helmholtz-Centre for Infection Research, Braunschweig). The mice were sacrificed by CO_2, afterwards the thorax was opened and the heart blood was collected using a syringe. Next, the whole liver was isolated for histology. A small part (approximately 2 mm x 4 mm) of the big right lob was separated for cryo-conservation in liquid

nitrogen. The residual organ was placed on a transfer paper and transferred into a formalin filled jar. Subsequently, the gonadal fat was isolated, for the male animals the testis were fixed by a forceps and the surrounding fat pads were pulled out carefully. In the case of the female animals the identification of the fat pads was more difficult in general, here the oviduct and the ovaries were used for orientation. The fat pads were analyzed with reference to their weight and stored in formalin for histological analysis later on. Afterwards the spleen and peripheral lymph nodes were isolated for flow cytometry analysis (see 4.4.3).

Finally, the scapular fat pad, which covers the shoulders, was isolated. The skin was detached and the subjacent fat tissue was carefully sliced. It was transferred to a histology cassette and placed in a formalin jar.

4.4.2.1 Histological procedure and scoring

All steps were performed by the mouse pathology platform (Helmholtz-Centre for Infection Research). The isolated organs and tissues were fixed in 4% formaldehyde (neutrally buffered) for 24 h to 48 h and afterwards embedded in paraffin. Afterwards, sections of 3 µm thickness were stained by hematoxylin-eosin (H&E), before they were evaluated blinded to the experimental groups using a light microscope. Scoring of the pathological tissue alterations was performed according to the following classification:

Tab. 4.1: Histological scoring system

Grade of change	Score
No change	0
Low-grade	1
Moderate	2
Severe	3

Depending on the tissue, different attributes were evaluated as single scores first. For liver the inclusion of fat drops, the grade of inflammation and the area involved were analyzed. In scapular fat tissue the size of the lipocytes and of the brown fat cells as well as the grade of inflammation were reviewed. The gonadal fat pad was evaluated with respect to the size of the lipocytes and the grade of inflammation. For each organ or tissue all single scores were added to obtain the final score.

4.4.3   Isolation of organs and preparation of cells for flow cytometry

For flow cytometry analysis, spleen and peripheral lymph nodes were isolated. The latter consisted of cervical, axillary, brachial and inguinal lymph nodes. After the isolation, the organs were mashed through a 70 μm Falcon® cell strainer (Thermo Fisher Scientific). The cells were suspended in PBS and centrifuged and the resulting pellet was resuspended in 1 mL ACK lysis buffer (see Tab. 3.20). The lysis was stopped after 1 min by adding PBS and the suspension was centrifuged. After resuspension in 1 mL PBS, the suspension was filtered through 30 μm Cell Trics ® (Sysmex-Partec, Goerlitz, Germany), before determining the cell number at the automated counting system Cellometer® Auto T4 (Nexcelom Bioscience).

4.4.4   Isolation of cell populations by flow cytometry (sorting)

The parental lines ATG5 WT and ATG5 KO, as well as the retro-virally reconstituted ATG5 WT and ATG5 mutant MEFs were transduced with mCitrine-hLC3B (see 4.2.2 and 4.2.3). The fluorescent-protein-tagged LC3B now allowed a flow cytometry-based fast readout of the autophagic capacity in these cells upon stimulation.

After the transduction and selection for the different lines, the resulting mCitrine-hLC3B-positive bulk cultures were inhomogeneous in their basal mCitrine expression profile. Therefore, all the lines were prepared for a cell sorting experiment to obtain populations that were more uniformal in their mCitrine-LC3B-expression. This approach was realized with the support of the cell sorting facility (Dr. Lothar Gröbe, Helmholtz-Centre for Infection Research, Braunschweig).

At least $1.5 \cdot 10^{7}$ adherent MEFs per cell line were detached by trypsin/EDTA treatment, washed once and resuspended in 2 mL PBS. Afterwards, the cell suspension was processed in a FACS Aria II flow cytometer (BD) with a FITC filter setting to isolate a mCitrine-positive population with medium-high expression. The sorting was finished as soon as $1 \cdot 10^{6}$ cells with the desired expression were collected. The isolated cell population was centrifuged, the pellet was resuspended in medium and the cells were plated in a 3.5 cm^{2} dish for cultivation.

4.4.5 Analysis of cell populations by flow cytometry

4.4.5.1 Flow cytometry analysis of HBSS- and bafilomycin A1-treated mCitrine-hLC3B-positive MEF cells

For analyzing autophagy via flow cytometry, typically $2 \cdot 10^5$ cells well of a 12-well plate with four wells per cell line were seeded the day before. On the next day the cells were stimulated with HBSS and BafA (see 4.2.4).

After the stimulation was finished, the adherent cells were washed with PBS and detached with trypsin/EDTA. The cell suspension was collected in 5 mL FACS tubes and centrifuged (1500 rpm, 5 min, 4 °C). Another washing step with PBS was performed to remove residual medium or trypsin/EDTA. In order to exclude dead cells, an AnnexinV staining was performed. The cell pellet was resuspended in 125 µL AnnexinV Master Mix, which consisted of 3 µL AnnexinV-APC (see Tab. 3.21) diluted in 1x AnnexinV binding buffer (see Tab. 3.20). The cells were incubated in the master mix at RT in the dark for 15 min and afterwards 125 µL binding buffer were added and the sample was measured in the FACS Canto flow cytometer.

4.4.5.2 Flow cytometry analysis of primary murine cells with staining of surface markers

When primary mouse cells from high-fat diet experiments were analyzed by flow cytometry, the cells were isolated from the respective organ and ACK lysis of red blood cells was performed (see 4.4.3). After the cell number was determined per sample $1 \cdot 10^6$ cells were transferred to a small FACS tube. The cells were centrifuged (1500 rpm for 5 min, 4 °C) and in parallel the live/dead staining master mix with Live/Dead® Fixable Blue Dead Cell Stain Kit (1:1000) from Thermo Fisher Scientific was prepared in PBS. The pellets were resuspended in 100 µL mix by brief vortexing and incubated at 4 °C in the dark for 30 min. Afterwards the cells were washed twice with 500 µL cold PBS.

For the surface marker staining of the different immune cell populations, a multicolor mix with the desired antibody-fluorochrome conjugates was prepared. In terms of the high-fat diet experiments the panel consisted of the surface markers CD3, CD4, CD8, CD19, CD25, CD44 and CD62L (see Tab. 3.21). The necessary dilutions ranged from 1:200 to 1:3000 and were prepared in FACS buffer (see Tab. 3.20). 100 µL

of the mix were added to the cell pellet after live/dead staining was completed and resuspension was performed by brief vortexing. The samples were incubated at 4 °C in the dark for 20 min. Afterwards 250 µL FACS buffer were added and the cells were centrifuged. The pellet was resuspended in 250 µL FACS buffer and the samples were measured at the LSR II FACS device.

4.4.6 Generation of transgenic mice via recombinase-mediated cassette exchange-targeted embryonic stem cells

Cloning of the recombinase-mediated cassette exchange (RMCE)-compatible vector construct was performed (see Tab. 3.1), where the exchange vector pTAR-EF1α-antiflox and the amplified ATG5 WT-c-myc, ATG5^{T75A}-c-myc and ATG5^{T75E}-c-myc coding sequences were blunt-end cut via NruI (NEB). To avoid self-ligation, the linearized plasmid was treated with Antarctic Phosphatase (see Tab. 3.11) prior to the ligation which was then followed by transformation in *E. coli*. The identification of positive clones was performed using colony PCR (see 4.1.1.7). After the plasmid amplification and isolation via QIAprep® Spin Miniprep Kit (Qiagen), the orientation of the ATG5 CDS was determined via sequencing.

The further steps, e.g. targeting of the murine ES cells with the exchange vector (including the inverse oriented ATG5 CDS), introducing of the selected ES cells via blastocyst injection in the F1 129 x BL6 mice and generation of chimeric animals that gave rise to transgenic offspring, were performed by the group of Prof. Dr. Dagmar Wirth (Helmholtz-Centre for Infection Research, Braunschweig)[291,293].

Subsequently, the backcrossing to a C57BL/6J background was started with the transgenic colony. Characterization of the C57BL/6J-backcrossed transgenic mice in terms of transgene expression was performed with the help of Sara Behme from the group of Prof. Dr. Dagmar Wirth. Thereupon, total RNA was isolated from spleen and liver of transgene-positive animals, which had been identified by genotyping. Afterwards, the RNA was transcribed to cDNA and a β-actin- or EMCV-IRES/neo-specific PCR was performed.

4.5 Analysis of data and generation of figures

4.5.1   Analysis of flow cytometry data

The analysis of flow cytometry data was performed with FlowJo version 10.0.8 (FlowJo LLC. Tree Star Inc; Ashland, OR/USA).

4.5.2   Analysis of sequencing data

The analysis of sequencing data was performed with Geneious version 5.6.7 (http://www.geneious.com, Kearse *et al.*[294]).

4.5.3   Image analysis and Western blot quantification

Microscope images were analyzed by Volocity version 6.0 (Perkin Elmer Inc.; Waltham, MA/USA) and processing of images was done with the help of Adobe Photoshop CS5 and Adobe Illustrator CS5 (Adobe Systems Inc.; San Jose, CA/USA). For quantification of Western blot signals, the ImageJ software was used[295].

4.5.4   Generation of figures

For visualizing the data in graphs, the Graph Pad Prism software version 5.0c (Graph-Pad-Software-Inc; La Jolla, CA/USA) together with Adobe Illustrator CS5 (Adobe Systems Inc.; San Jose, CA/USA) was used. Error bars were either shown as standard deviation (SD) or standard error of the mean (SEM). Surface structures of ATG5 and ATG12–5 were generated by the use of the PyMOL software (The PyMOL Molecular Graphics System, Version 1.8 Schrödinger, LLC). Cartoons displayed in the introduction part were prepared in Adobe Illustrator CS5.

5 RESULTS

5.1 Generation of ATG5 WT, ATG5^{T75A} and ATG5^{T75E} transgenic mice via recombinase-mediated cassette exchange

In a previously published study, the autophagy protein ATG5 was identified as a new phosphorylation target of the MAPK p38[133]. The ATG5-p38 interaction was identified to be a negative regulation mechanism, by which the autophagic flux can be blocked prior to the autophagosome-lysosome fusion. The threonine 75 (T75) residue of ATG5 was shown to play an essential role during the interaction with the kinase p38. Of note, this residue is part of a threonine-proline (TP) motif and highly conserved from mice to human. Since p38 phosphorylates its substrate typically at serine-proline and/or threonine-proline (S/TP) motifs, the hypothesis was, that T75 acts as phospho-acceptor site. ATG5 KO MEFs that were reconstituted with ATG5^{T75A} (putative phospho-defective) or ATG5^{T75E} (putative phospho-mimetic) showed a significantly increased (T75A) or decreased (T75E) autophagic flux in several *in vitro* approaches[133].

5.1.1 Strategy for the recombinase-mediated cassette exchange in compatible murine ES cells

A suitable transgenic mouse model is a powerful tool to elucidate the physiological role of a regulation mechanism. In line with the described previous *in vitro* experiments, transgenic mice, which ubiquitously expressed a c-myc-tagged version of either ATG5 WT, ATG5^{T75A} or ATG5^{T75E} were designed. The coding sequence (CDS) of each protein was integrated in the murine ROSA26 locus and the expression was controlled by the human elongation factor 1α (EF1α) promoter in the above models. The genomic integration in a previously established G412 murine embryonic stem (mES) cell line was facilitated by recombinase-mediated cassette exchange (RMCE) of an exchange vector harboring the desired transgene sequence, here the ATG5-c-myc CDS (Fig. 5.1)[291,293].
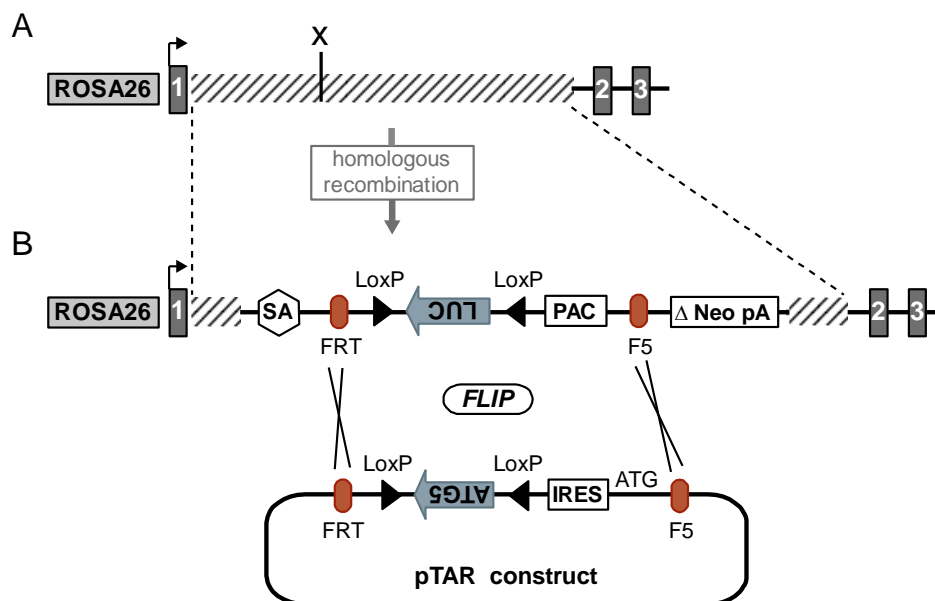
Fig. 5.1: The ROSA26 locus in RMCE-compatible G4B12 ES cells is targeted by the exchange vector pTAR. (A) The wild type ROSA26 locus in the utilized mES cell line has been modified via homologous recombination. This resulted in a RMCE-compatible expression cassette structure, where the implemented LUC-cassette was flanked with two different FRT sites (FRT and F5). Thereby, the targeted exchange to the desired ATG5-cassette by site-directed, *flip* recombinase (FLIP)-mediated recombination was enabled. **(B)** Subsequently, co-expression of the recombinase and the cloned exchange vector (pTAR construct) was performed in the RMCE-compatible G4B12 mES cells. Hence, the targeted mES cells afterwards contained the ATG5-c-myc CDS in an inverse orientation flanked by oppositely oriented loxP-sites and followed by an IRES element. The exchange reconstituted the start codon-defective, neomycin phosphotransferase gene (Δ Neo pA), which enabled the selection of successfully targeted ES cells by G418 treatment. Boxes (1,2,3): exons; x: XbaI recognition site; SA: splice acceptor site; FRT: FRT wild type site; F5: FRT F5 mutant site; LoxP: LoxP wild type site; LUC: luciferase; ATG5: coding sequence of ATG5 WT-, ATG5[T75A]- or ATG5[T75E]-c-myc; PAC: puromycin N-acetyltransferase gene; IRES: internal ribosome entry site; ATG: starting codon; Δ Neo pA: start codon-defective neomycin phosphotransferase gene and polyadenylation (pA) signal. Modified from Sandhu *et al.*, 2011[293].

5.1.2 Strategy to generate transgenic mice and to induce functional transgene expression

Successfully transfected G4B12 mES cells were selected by G418 treatment and subsequently transferred to 129 x BL6 recipient females by blastocyst injection. The resulting transgenic mice carried the ATG5-c-myc CDS in the ROSA26 locus still in an inverse orientation. Hence, a non-functional variant of the protein was expressed. Once these transgenic mice were crossed with a (tissue-specific) *Cre* recombinase-expressing mouse line, the ATG5-c-myc sequence was cleaved and inverted in a *Cre*-dependent manner via the two flanking loxP-sites (see Fig. 5.2A).

In theory this inversion is fully reversible, which would result in an average expression of 50% for the functional protein. By the usage of two different flanking lox pairs, the balance could be shifted to gain maximal protein expression (see Fig. 5.2B).
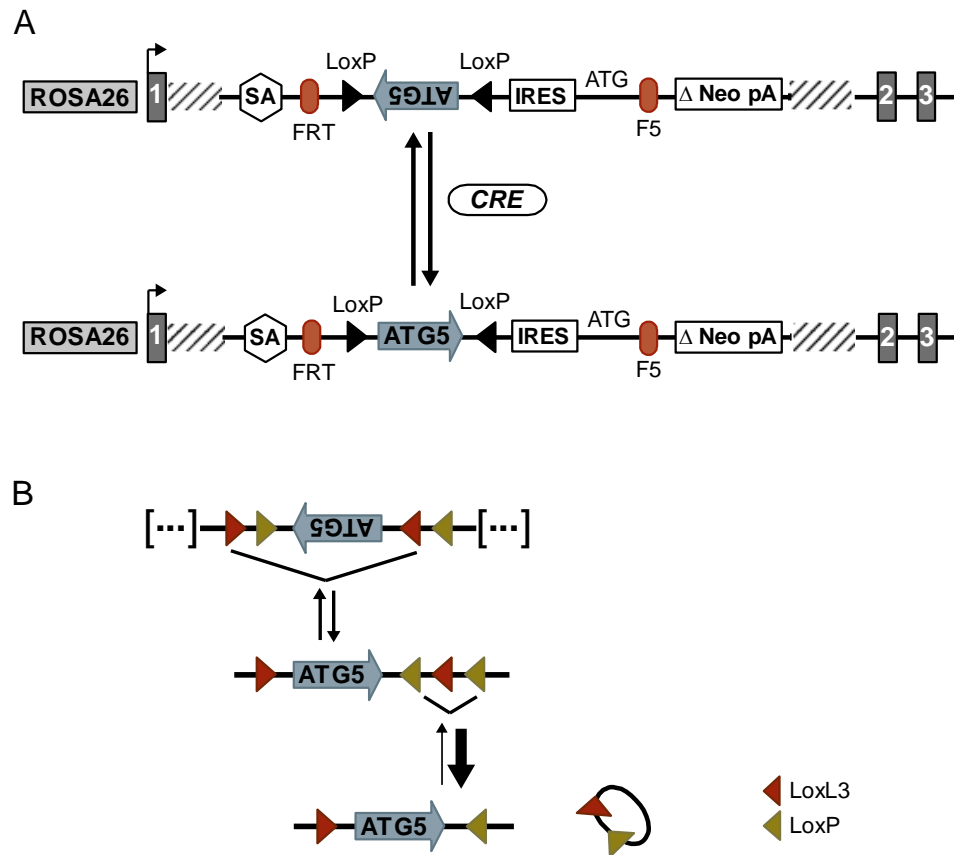
Fig. 5.2: Strategy of *Cre* recombinase-mediated inversion in the RMCE transgenic mouse model. (A) Schematic structure of the ROSA26 locus with successfully inserted ATG5-c-myc. These mice were subsequently crossed to a *Cre* recombinase (*CRE*)-expressing mouse line. The *Cre*-mediated inversion is reversible, resulting in a 50% expression of the functional protein of interest. Boxes (1,2,3): exons; SA: splice acceptor site; FRT: FRT wild type site; F5: FRT F5 mutant site; ATG5: coding sequence of ATG5 WT-c-myc, ATG5[T75A]-c-myc or ATG5[T75E]-c-myc; IRES: internal ribosome entry site; ATG: starting codon; Δ Neo pA: start codon defective neomycin phosphotransferase gene and polyadenylation signal (pA). Modified from Sandhu *et al.*[293]. **(B)** The implementation of an additional lox pair (LoxL3) in a specific orientation induces a *Cre*-mediated excision reaction after the inversion. Thereby, the equilibrium is almost completely shifted towards the desired orientation of the ATG5 CDS.

5.1.3 Cloning of the ATG5-c-myc CDS in the exchange vector pTAR-EF1α-antiflox

ATG5 WT-c-myc, ATG5[T75A]-c-myc and ATG5[T75E]-c-myc CDS were cloned into the exchange vector pTAR-EF1α-antiflox by NruI-mediated blunt-end cloning (Fig. 5.3). The inverted orientation and integrity of the insert were verified by sequencing.
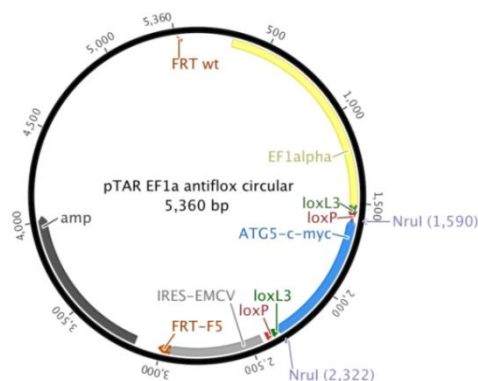
Fig. 5.3: Schematic representation of the cloned pTAR-EF1α-antiflox-ATG5-c-myc exchange vector. Analogue to the cassette shown in Figure 5.2, the vector contains the EF1α promoter, followed by the loxP- and loxL3-flanked, inverse-oriented ATG5-c-myc sequence. The IRES sequence is the last element within the expression cassette, which is bordered by FRT and FRT-F5. Cloning was performed via the NruI restriction sites. Due to cloning purposes, the plasmid also harbors the ampicillin resistance gene (amp). The graph was created in Geneious[294].

5.1.4 Characterization of the cloned pTAR-EF1α constructs

The cloned constructs were analyzed via a co-expression experiment in HEK293T cells, prior to the ES cell transfection. In the control samples, no ATG5-c-myc expression was detectable. Upon co-transfection with a *Cre* expression vector, the inversion occurred as expected, which was shown by ATG5-c-myc expression. ATG5-c-myc was expressed predominantly in its free, unconjugated form (Fig. 5.4).
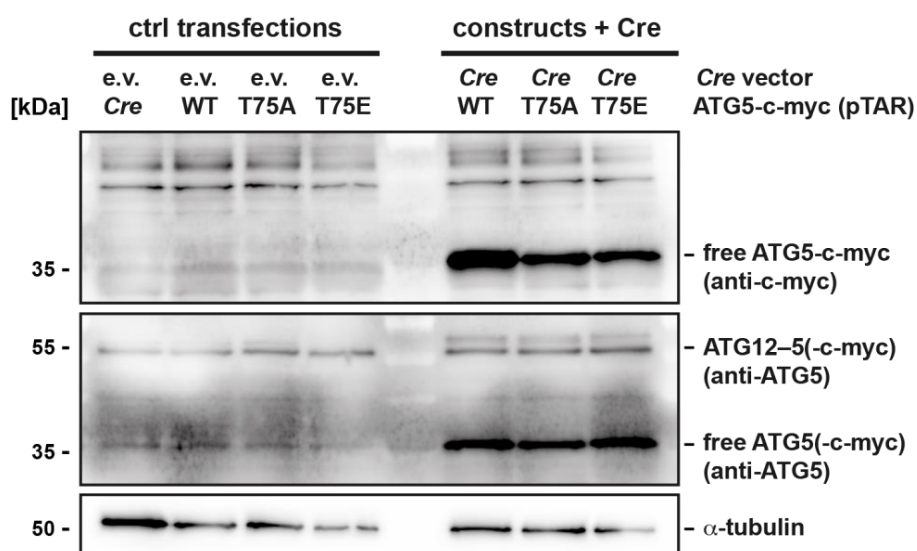
Fig. 5.4: Functional test of inverse cloned pTAR-EF1α-antiflox-ATG5-c-myc constructs in HEK293T cells. Western blot of HEK293T cells, co-transfected with either the empty vector (e.v.) or the *Cre* expression vector in combination with the different pTAR-EF1α-antiflox-ATG5-c-myc constructs. To check for equal protein loading the membrane was probed with α-tubulin.

After the RMCE-compatible ES cell line was successfully transfected with the different pTAR constructs, the cells were analyzed by Western blot (Fig. 5.5). Of note, the test-targeting was performed with exchange plasmids harboring a non-inverted ATG5-c-myc CDS, therefore no inversion (*Cre* expression) was necessary. Again, the expression of ATG5-c-myc was clearly detectable in comparison to non-transfected ES cells. Noteworthy, in the ES cells the expressed ATG5-c-myc was conjugated to ATG12, which is the functional form of ATG5 in terms of autophagy (Fig. 5.5).
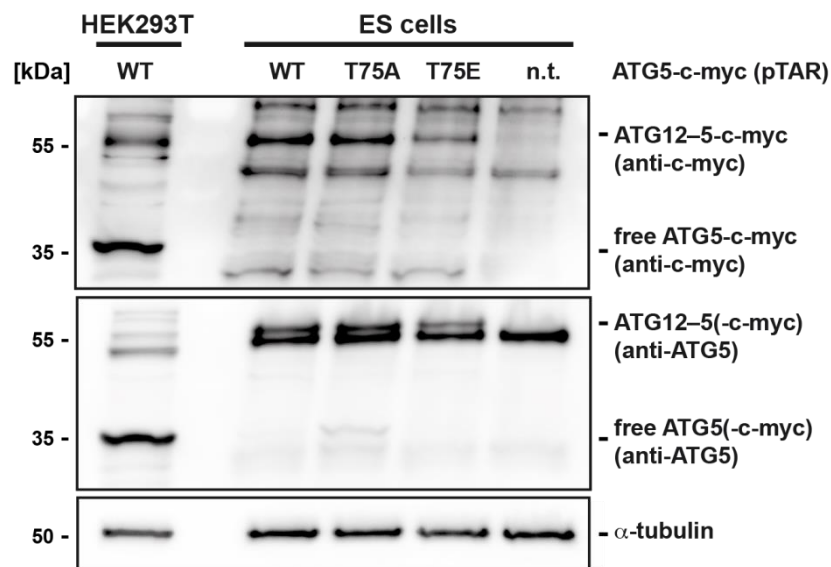
Fig. 5.5: Test expression of pTAR-EF1a-antiflox constructs with regular oriented inserts in RMCE-targeted ES cells. Western blot of ES cells that previously were targeted with pTAR constructs harboring the ATG5-c-myc CDS in the forward orientation. ATG5-c-myc-transfected HEK293T cells and non-targeted (n.t.) ES cells were used as control samples. The loading of equal protein amounts was tested by probing the membrane with α-tubulin.

5.1.5   Analysis of the transgenic mice indicated a mosaic expression of the transgene

The characterized constructs were used for the RMCE in murine G4B12 ES cells and the selected cells were transferred in the blastocysts of F1 129 x BL6 recipient mice. These chimeras gave rise to transgenic animals, which were identified by genotyping PCR. For this amplification, a primer pair specific for the internal ribosome entry site (IRES) and the neomycin phosphotransferase gene (neo) was utilized. The positively tested animals were backcrossed to C57BL/6J for six generations. The expression of the introduced cassette was analyzed based on the respective mRNA synthesis by a semi-quantitative reverse transcriptase PCR (RT PCR) experiment in F6

mice (Sara Behme and Prof. Dr. Dagmar Wirth, Helmholtz-Centre for Infection Research, Braunschweig). Total RNA was isolated from liver and spleen tissue of four male and two female transgenic animals, which were previously analyzed via genotyping (Fig. 5.6A). Notably, all mice were offspring from the same breeding pair, the mice #2 to #6 were from the same litter.
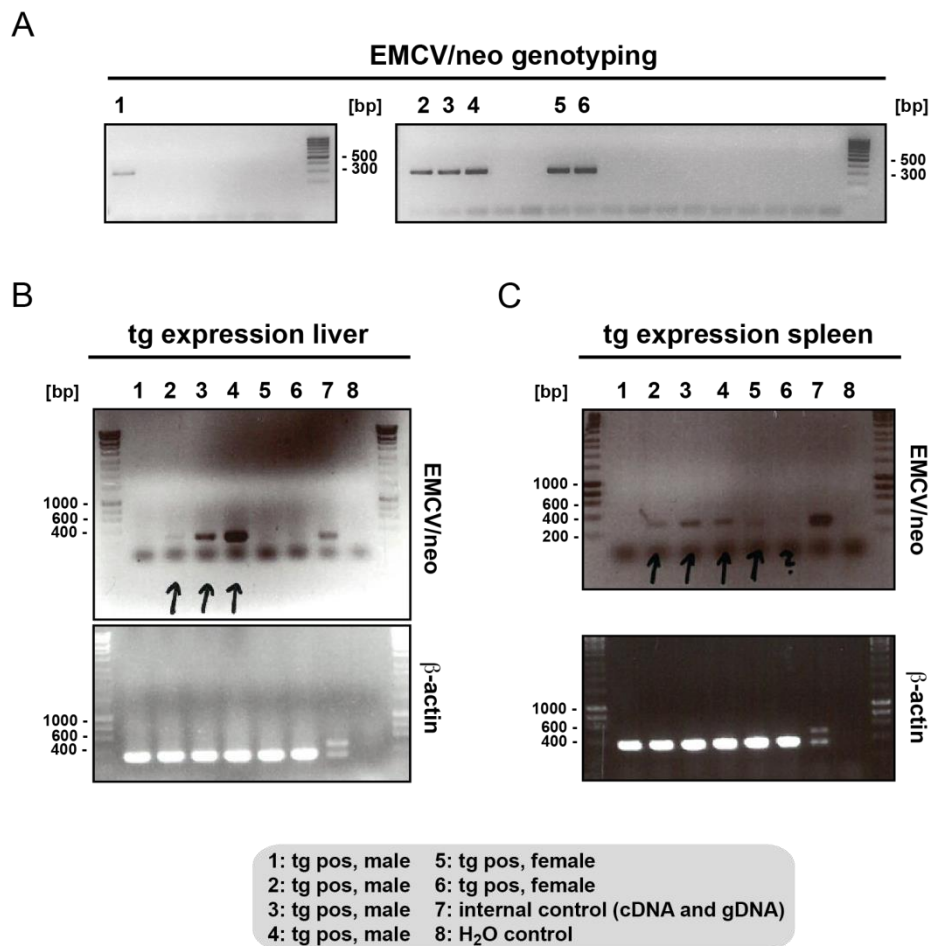
Fig. 5.6: Analysis of the transgene expression in liver and spleen of F6-C57BL/6J backcrossed transgenic mice revealed a mosaic pattern. (A) Genotyping PCR of F6 mice from the C57BL/6J-backcrossing. Notably, the mice #2 to #6 are littermates, whereas the mouse #1 is from a previous litter of the same breeding pair. By the usage of an IRES/neo primer pair, transgenic animals were identified. **(B)** RT PCR experiment with total RNA of liver tissue from six transgenic F6 mice as in (A). In total two PCRs were performed, the EMCV/neo primer combination was used to amplify part of the expression cassette and a β-actin-specific PCR was performed to control the levels of template cDNA. The purity of the initial RNA isolation was verified by an internal genotyping sample. Only this control sample showed an additional band originating from amplification of genomic DNA (gDNA). **(C)** Similar experiment to (B), here performed with RNA isolated from the spleen.

When it came to the liver, significant expression of the cassette was only detectable in two male mice and the amount of the transcript differed remarkably (Fig. 5.6B). Analysis of the spleen samples revealed specific amplification for the same two mice from above and one additional male mouse. Additionally, one female mouse showed significant expression of the cassette. In total, here the amount of transcript was more uniformly between the mice, than in the liver (Fig. 5.6C). This result was in line with previous RT PCR data from earlier generations (data not shown – personal communication with Prof. Dr. Dagmar Wirth). Taken together, it became obvious, that although the implementation of the cassette in the ROSA26 locus was successful in the backcrossed littermates (see Fig. 5.6A), the expression under the Ef1α promoter was not ubiquitous but mosaic. Since the transgene expression cannot be predicted, consequently, the required dominant expression in comparison to the endogenous ATG5 protein is not ensured. As a result, the analysis of an ATG5 mutant-specific physiological effect was not possible within this mouse model. This led to the termination of the project.

5.2 The role of ATG5 during p38-mediated autophagy regulation

5.2.1 The effect of the ATG5 mutants T75A and T75E on the autophagic flux is not mediated by an altered interaction with ATG16L1 or TECPR1

It has been shown previously, that the T75 of ATG5 plays an important role in the p38-mediated regulation of autophagy. Mutation of this residue to alanine or glutamate resulted in an increased or reduced autophagic flux, respectively[133]. However, how the interaction of p38 and ATG5 is maintaining the inhibition of autophagosome-lysosome fusion on a molecular level still needs to be clarified. Noteworthy, the formation of autophagosomes requires the ATG12–ATG5 conjugate[18]. For the initial attachment of ATG12–5 to the autophagic membrane, the conjugate needs to assemble with ATG16L1[51]. During the maturation step, the fusion of autophagosomes with lysosomes is dependent on an exchange of the ATG12–5-

binding partner from the former autophagosomal ATG16L1 to the lysosome-attached TECPR1 protein[97].

In line with these previous findings one hypothesis was that the phenotype observed in ATG5^{T75A}- and ATG5^{T75E}-reconstitued fibroblasts is mediated by an altered interaction with ATG16L1 and/or TECPR1. To investigate this hypothesis, a co-immunoprecipitation experiment with the reconstituted MEFs was performed. Comparing ATG5 WT-c-myc, ATG5^{T75A}-c-myc and ATG5^{T75E}-c-myc cells a similar interaction with ATG16L1 and TECPR1 was observed. Of note, equal protein loading in the input and the specificity of the detected precipitation signals were confirmed by probing with α-tubulin (Fig. 5.7).
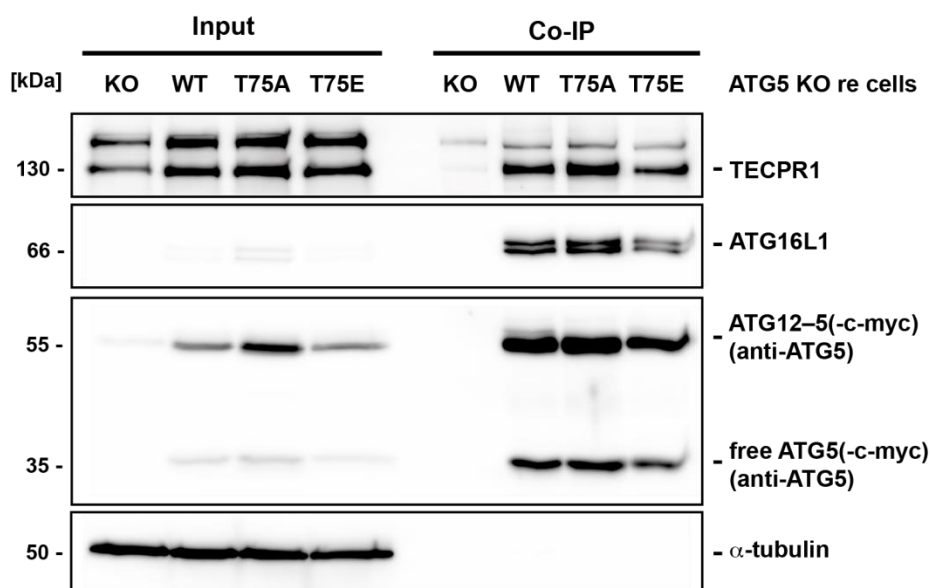
Fig. 5.7: Interaction of ATG12–5 with ATG16L1 and TECPR1 is not altered, comparing ATG5 WT-c-myc with ATG5^{T75A}-c-myc and ATG5^{T75E}-c-myc MEF cells. Co-immunoprecipitation experiments were performed via the c-myc-tag in ATG5-c-myc-reconstituted cell lines. Equal loading (input) and specificity of the precipitation (Co-IP) was analyzed by probing the membrane with α-tubulin.

5.3 Analysis of the ATG5-p38 interaction

5.3.1   The ATG5-p38 interaction is detectable in transfected cells

So far, the interaction of ATG5 and p38 has not been shown directly in cell culture. The first successful co-immunoprecipitation (Co-IP) experiments were performed during the master thesis[285]. This work was continued more thoroughly during this

thesis. After transient co-transfection of ATG5-c-myc and FLAG-p38 in HEK293T cells, two way co-precipitation experiments were performed. First, anti-FLAG beads were used to precipitate FLAG-p38 (bait) and check for co-precipitated ATG5-c-myc (prey). ATG5-c-myc was clearly visible in the double transfected sample but not in the controls (Fig. 5.8A). The interaction was also confirmed the other way around by the usage of anti-c-myc-specific beads (Fig. 5.8B).
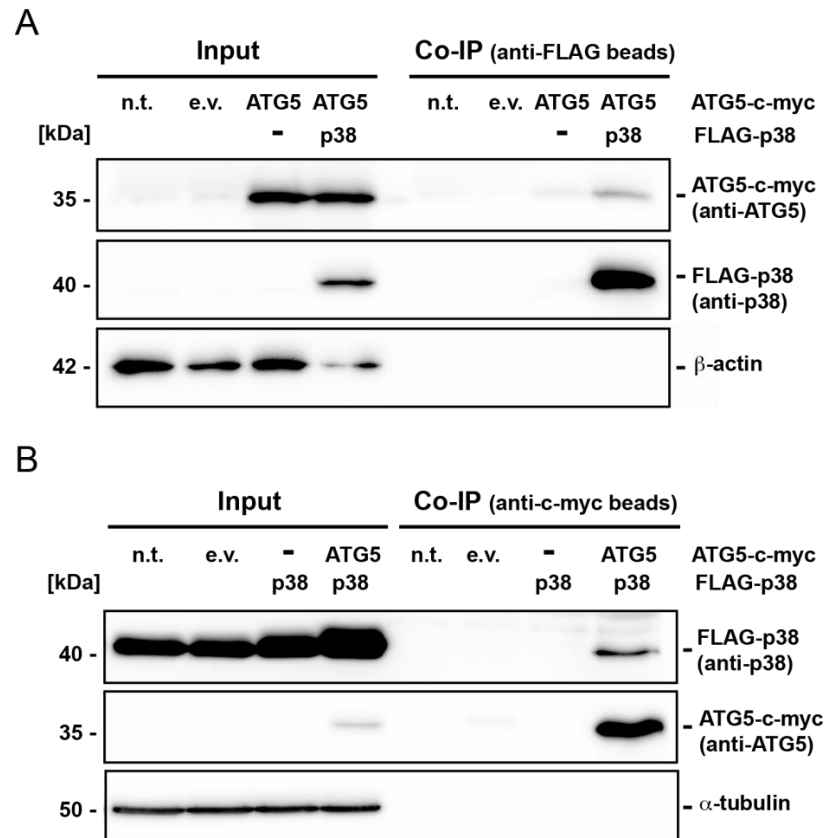
Fig. 5.8: Interaction of ATG5 with p38 is detectable in HEK293T cells after co-expression. HEK293T cells were either left untreated (not transfected, n.t.), co-transfected with both empty vectors (e.v.), with the prey vector only or with ATG5-c-myc and FLAG-p38. **(A)** Co-immunoprecipitation was performed by using anti-FLAG beads. Equal input loading and the absence of background binding in the IP samples, was shown via probing the membrane with β-actin. **(B)** Co-immunoprecipitation was performed via the c-myc-tag of ATG5. Probing the membrane with α-tubulin served as a control of equal input loading and specificity of the precipitation.

5.3.2 Identification of possible p38-docking residues in the linear ATG5 sequence

Importantly, the specific interaction of MAP kinases such as p38, with their substrates is coordinated and mediated by so called docking sites (D sites). These

sequences typically consist of characteristic residue stretches on the substrate surface, which act as a platform for correct positioning of the kinase and thereby facilitate a fast and accurate transfer of the phosphate[155,296]. The comparison of known p38 substrates identified characteristic similarities in their respective docking sequences. Typically, a docking site is started by one or more hydrophobic leucine residues and followed by a stretch of basic amino acids, which is composed of arginine and lysine residues[159]. The analysis of the linear human ATG5 (hATG5) coding sequence showed similar amino acid patterns, which were located nearby the putative phosphorylation motif T^{75}P (Fig. 5.9).

```
  1 MTDDKDVLRD VWFGRIPTCF TLYQDEITER EAEPYYLLLP RVSYLTLVTD 50
 51 KVKKHFQKVM RQEDISEIWF EYEGTPLKWH YPIGLLFDLL ASSSALPWNI 100
101 TVHFKSFPEK DLLHCPSKDA IEAHFMSCMK EADALKHKSQ VINEMQKKDH 150
151 KQLWMGLQND RFDQFWAINR KLMEYPAEEN GFRYIPFRIY QTTTERPFIQ 200
201 KLFRPVAADG QLHTLGDLLK EVCPSAIDPE DGEKKNQVMI HGIEPMLETP 250
251 LQWLSEHLSY PDNFLHISII PQPTD 275
```

possible phosphorylation motive
hydrophobic residues
basic residues

Fig. 5.9: The linear coding sequence of human ATG5 consists of putative p38-docking clusters. The threonine 75 is highlighted in green. With respect to nearby located potential docking residues, hydrophobic clusters are shown in red and basic residues are marked in blue.

5.3.3 Mutagenesis of the hATG5 sequence to obtain the mutants ATG5$^{K51E/K53E}$, ATG5$^{K58E/R61S}$ and ATG5$^{K78E/H80D}$

To elucidate whether the identified potential docking pattern is indeed involved in the functional interaction of ATG5 and p38, mutagenesis of putative critical amino acids was performed. The first series of experiments was performed during the master thesis, where due to a problem in the cloning procedure the expression of the mutants was not successful[285]. The revised mutant constructs containing the CDS of ATG5$^{K51E/K53E}$, ATG5$^{K58E/R61S}$ and ATG5$^{K78E/H80D}$ were verified by sequencing and transient transfection. This characterization showed a lightly lower expression level of the K78E/H80D mutant protein (Fig. 5.10A and B).
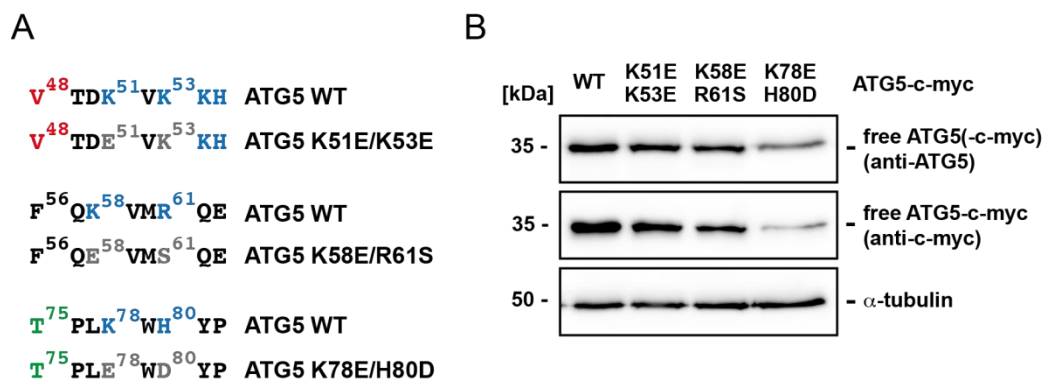
Fig. 5.10: Mutagenesis of hATG5 to obtain possible p38-docking site mutants. (A) Overview of the three generated ATG5 mutants in the context of the predicted docking site. The color code is similar to Figure 5.9, mutated residues are depicted in grey. **(B)** Expression test of the cloned ATG5-c-myc mutant plasmids after transient transfection in HEK293T cells. Probing of the membrane with α-tubulin was performed to control equal loading.

5.3.4 The ATG5 mutants K51E/K53E and K58E/R61S did not show alterations in the interaction with p38

Potential differences in the interaction of p38 and the ATG5 mutants compared to the WT were analyzed via a co-immunoprecipitation approach after transient transfection of HEK293T cells. Overall, no significant alterations in the interaction to p38 were observed between the WT protein and the tested ATG5 mutants (Fig. 5.11).
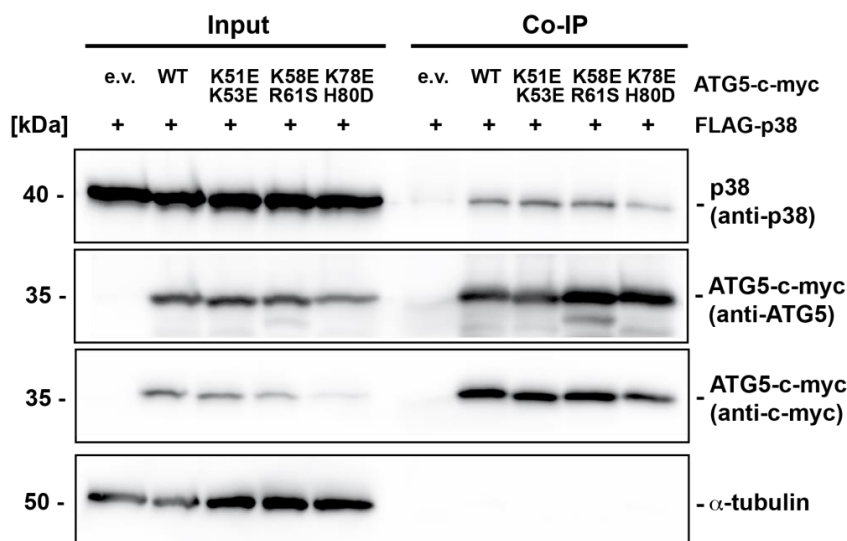
Fig. 5.11: The potential ATG5 docking mutants ATG5[K51E/K53E] and ATG5-[K58E/R61S] did not show an altered interaction with p38. The co-immunoprecipitation was performed using anti-c-myc beads. ATG5 WT and ATG5 mutants represented the bait and FLAG-p38 the prey. The loading and specificity control was performed by probing the membrane with α-tubulin.

Altogether, a slightly reduced interaction of the ATG5$^{K78E/H80D}$ mutant with p38 was detectable in comparison with ATG5 WT.

5.3.5 Threonine 75 of ATG5 is not the target of p38-mediated phosphorylation but is important for proper interaction

To verify the role of T75 as a phospho-acceptor site of p38-mediated phosphorylation, an *in vitro* kinase experiment was performed in cooperation with Dr. Caroline Behrens and the mass spectrometry facility (Dr. Josef Wissing/Prof. Dr. Lothar Jänsch and co-workers, Helmholtz-Centre for Infection Research, Braunschweig). After incubation of the recombinant ATG5 with activated phosphorylated p38 in the presence of 5 mM ATP, the reaction was prepared for LC-MS/MS (Tab. 5.1).

Tab. 5.1: LC-MS/MS analysis after *in vitro* kinase assay of ATG5 and p38 did not confirm a phosphorylation at threonine 75

Selected peptide sequences*	Peptid ratio Phosphorylated to non-phosphorylated
M**T²**DDKDVLR	18%
IYQ**T¹⁹²T¹⁹³T¹⁹⁴**ERPFIQK	2%
EVCP**S²²⁵**AIDPEDGEK(K)	55%
QEDISEIWFEYEG**T⁷⁵**PLK	0%

*Total coverage of ATG5 coding sequence: 60.73%

Surprisingly, the peptide including T75 was not phosphorylated, instead three other phospho-peptides with the phosphorylated residues T2, T192 or T193 or T194 and S225 were identified (Tab. 5.1). In order to elucidate the role of T75 during the interaction of ATG5 and p38 co-immunoprecipitation experiments in double-transfected HEK293T cells were performed with the T75A and the T75E mutant (Fig. 5.12).
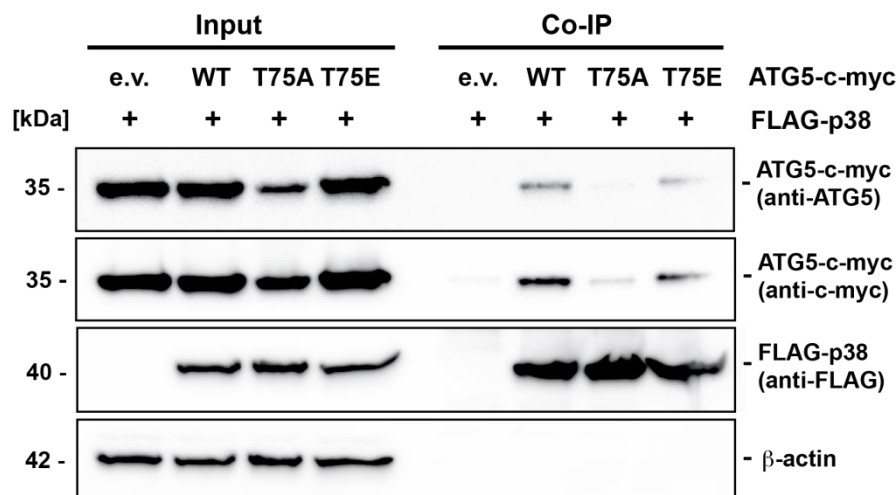
Fig. 5.12: The mutation of the polar threonine 75 to a hydrophobic alanine (T75A) in ATG5 resulted in a reduced interaction of ATG5 with p38. Co-immunoprecipitation experiments with anti-FLAG beads in HEK293T cells transiently transfected with FLAG-p38 and either an empty vector (e.v.), ATG5 WT, ATG5[T75A] or ATG5[T75E]. Equal loading of the input and the specificity of the precipitation was controlled by probing the membrane with β-actin.

While the interaction of p38 with ATG5[T75E] comparable to the WT sample, a clear reduction of the signal was demonstrated for the precipitation of ATG5[T75A], indicating that the polar side chain of the threonine at this position is important for the binding to the kinase.

5.3.6 Analysis of the 3D structure of ATG12–5 led to generation of new potential docking mutants

Referring to the above shown co-immunoprecipitation data, the hypothesis for the role of T75 now was that the previously published mutational effect is based on a crucial role during proper kinase docking. Kinase-substrate interactions are generally influenced by sterically properties of both partners. Thus, surface specificities of the functionally folded ATG5 compared to the linear ATG5 sequence need to be considered. Since the crystal structure of the ATG12–5 complex has been published[61], analysis of the 3D structure was performed. Amino acids that are directed outwards and in close spatial proximity to T75 were of particular interest. These residues represent candidates for another mutagenesis approach, aiming to determine the docking site for p38. According to already known docking sites for p38, which often include a leucine, L90 was chosen. With respect to its orientation to T75 and its

surface exposure, also the glutamate 73 was mutated. Taken together, with ATG5^{L90S}, ATG5^{L90Q} and ATG5^{E73K} three new mutants were generated, where the exchanged amino acid is supposed to disturb the former interactions (Fig. 5.13).
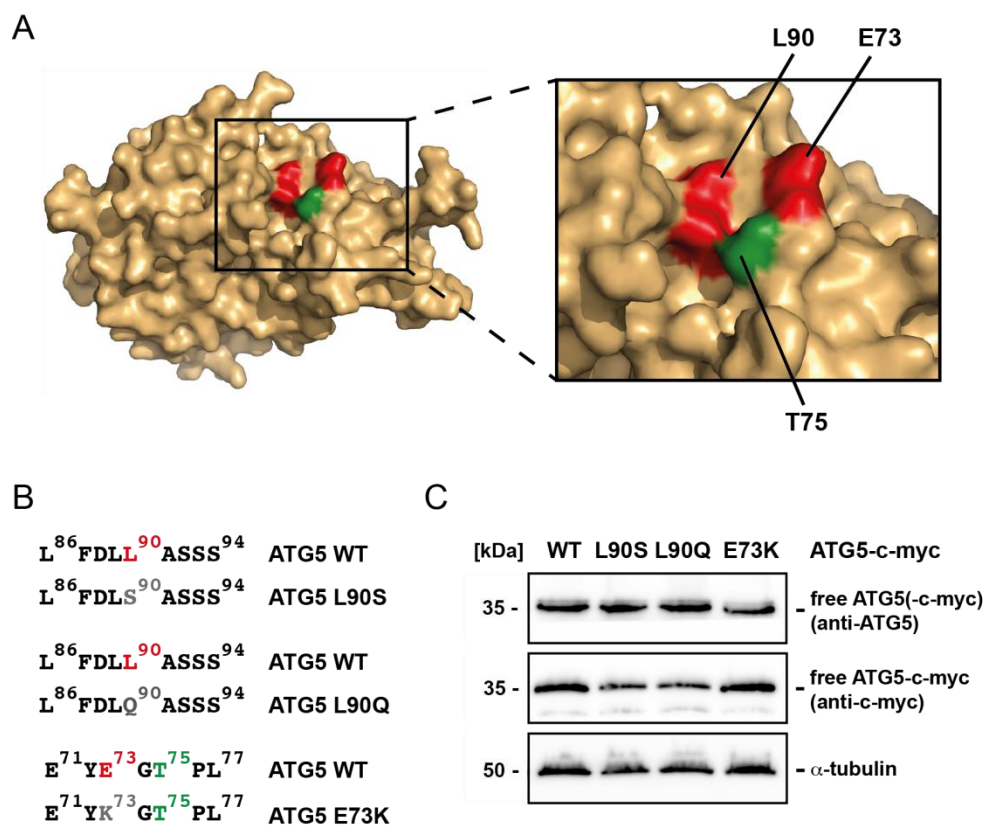
Fig. 5.13: The 3D structure of the ATG12–5 conjugate led to the design of the new potential ATG5 docking mutants ATG5^{L90S}, ATG5^{L90Q} and ATG5^{E73K}. (A) 3D structure of the human ATG5 (light orange, Protein Data Bank [PDB] ID: 4GDK) with the mutated residues highlighted in different colors. Leucine 90 (L90) and glutamate 73 (E73) are depicted in red, T75 is displayed in green. **(B)** Sequence extract of the new ATG5 docking mutants, where the former, mutated residues are colored in red, T75 is highlighted in green and the new amino acids are marked in grey. **(C)** Expression control after transient transfection of HEK293T with the cloned constructs. Equal loading was controlled by probing the membrane with α-tubulin.

5.3.7 ATG5 mutants ATG5^{L90S} and ATG5^{L90Q} displayed reduced interaction with p38

The newly generated ATG5 mutants were co-immunoprecipitated with FLAG-p38 in HEK293T cells. Additionally the mutant ATG5$^{K78E/H80D}$ (Fig. 5.10) was included, since the tendency observed in the first interaction study (Fig. 5.11) needed further verification. This time the precipitation was performed via the FLAG-tag, in order to reduce the impact of differences between the ATG5 mutant expression levels. The

interaction of the mutant ATG5$^{K78E/H80D}$ with p38 was again confirmed to be lower in comparison to WT. When it came to the two new mutants ATG5^{L90S} and ATG5^{L90Q}, a clear reduction in the interaction with p38 was detectable, whereas the ATG5^{E73K} mutant in total was a rather similarly co-precipitated compared to the ATG5 WT sample (Fig. 5.14).
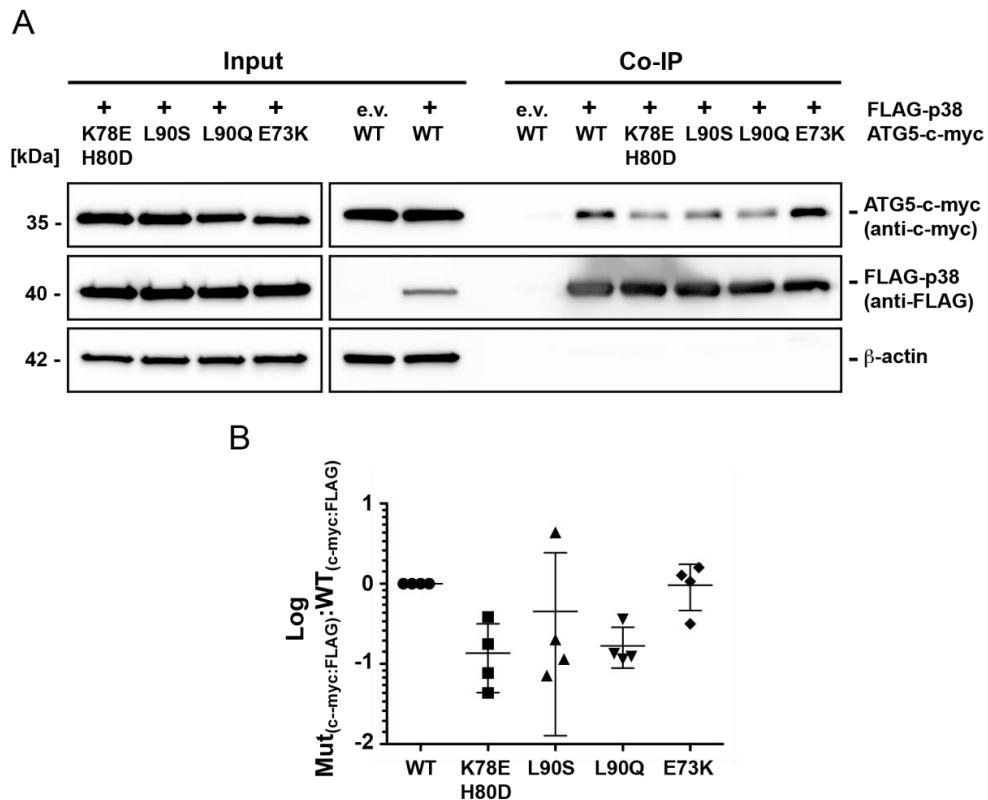
Fig. 5.14: The potential ATG5 docking mutants ATG5$^{K78E/H80D}$, ATG5^{L90S} and ATG5^{L90Q} displayed a reduction in the interaction with p38. The precipitation was performed using anti-FLAG beads, thus, p38 represented the bait and ATG5 the prey. The protein loading control was performed by probing with β-actin. **(A)** A representative blot of four repetitions is shown. **(B)** Quantification of the Western blots was performed as follows: the ratio of the ATG5 (c-myc) to p38 (FLAG) signal strength was calculated for each sample before all ratios were normalized to the ratio calculated for ATG5 WT sample. The quantitative analysis was done with ImageJ, error bars display the SD of the mean.

5.3.8 Generation of docking mutant-reconstituted ATG5 KO MEF cells

Stable mutant-reconstituted ATG5 KO MEF cell lines were generated to identify any functional consequence of the reduced ATG5-p38 interaction. Thereupon, a retro-viral approach with the ATG5 WT and all the mutants except ATG5$^{K78E/H80D}$ was performed. The excluded mutant was not folded correctly, which had been observed

meanwhile in expression tests for recombinant protein production (data not shown – personal communication with Dr. Caroline Behrens).

The steady-state expression of reconstituted ATG5, as well as of the two autophagy proteins LC3-I/II (isoforms A and B) and p62 was verified by Western blot. In total, the ATG5 level of the reconstituted cells was slightly higher compared to the reference WT MEF cells, consequently, a small amount of free ATG5 was detectable in the WT, T75A, T75E and L90S cells. The total levels of the LC3 isoforms A and B (LC3A/B) were slightly reduced in the T75A and T75E cell line, compared to the not reconstituted WT cells, while a more pronounced reduction was detected for the ATG5^{L90Q} and the ATG5^{E73K} line. In terms of the LC3A/B-I to LC3-II ratio in the WT control cells a shift towards the membrane-bound LC3-II is visible. Overall, the reconstituted lines showed a more equal ratio of the two LC3 forms. The p62 level was similar between the reference and the reconstituted lines. In general, the reconstitution was successful, since the reconstituted WT cells were overall comparable to the WT control cells (Fig. 5.15). The differences shown in the total LC3 protein level may already point to mutation-dependent alterations in the autophagic functionality.
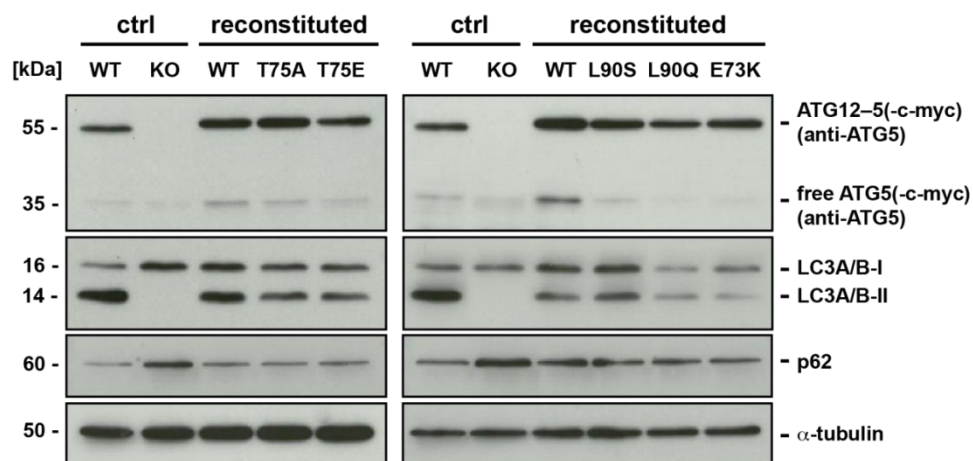
Fig. 5.15: Autophagy protein levels of the ATG5 KO MEFs, which were retro-virally reconstituted with ATG5-c-myc WT and the putative docking mutants. ATG5 WT and the parental ATG5 KO MEFs were included as reference cells. Equal protein loading the membrane was probed with α-tubulin.

5.3.9 Functional analysis of the generated mutant cell lines ATG5^{T75A}, ATG5^{L90S}, ATG5^{L90Q} and ATG5^{E73K}

After the steady-state levels for LC3 were evaluated, next the autophagic machinery of the reconstituted cell lines was challenged by starvation-induced autophagy. For this purpose, cells were incubated with Hank's balanced salt solution (HBSS) in the presence or absence of bafilomycin A1 (BafA). HBSS consists of osmotic salt concentrations and provides essential ions, but lacks nutrients. Thus, prolonged incubation in HBSS leads to starvation-induced autophagy. BafA is an inhibitor of lysosome-dependent proteolysis and was used to artificially block the flux at the autophagosomal stage[297]. This block results in the accumulation of otherwise degraded "autophagy drivers" like LC3A/B-II or p62. The amount of LC3A/B-II in the condition where both, HBSS and BafA (HBSS together with Baf) were added, in comparison to the HBSS-only sample, for example serves as readout for the strength of the induced autophagic flux. The basal level of autophagy was ascertainable by determining the LC3A/B-II level during DMEM cultivation in the presence and absence of BafA.

All four possible conditions (DMEM/non-treated, BafA, HBSS, HBSS together with BafA) were probed to analyze the LC3A/B-II level in the reconstituted ATG5 WT and mutant cell lines by Western blot. The non-reconstituted MEF cells were included as reference (Fig. 5.16A). For each sample, the quantified LC3A/B-II level was normalized to the respective loading control. Afterwards all ratios of one cell line were normalized to the respective DMEM-only (non-treated) sample (Fig. 5.16B). These calculations allowed to measure ATG5 mutant-dependent differences during the induction of autophagic flux.

A

B
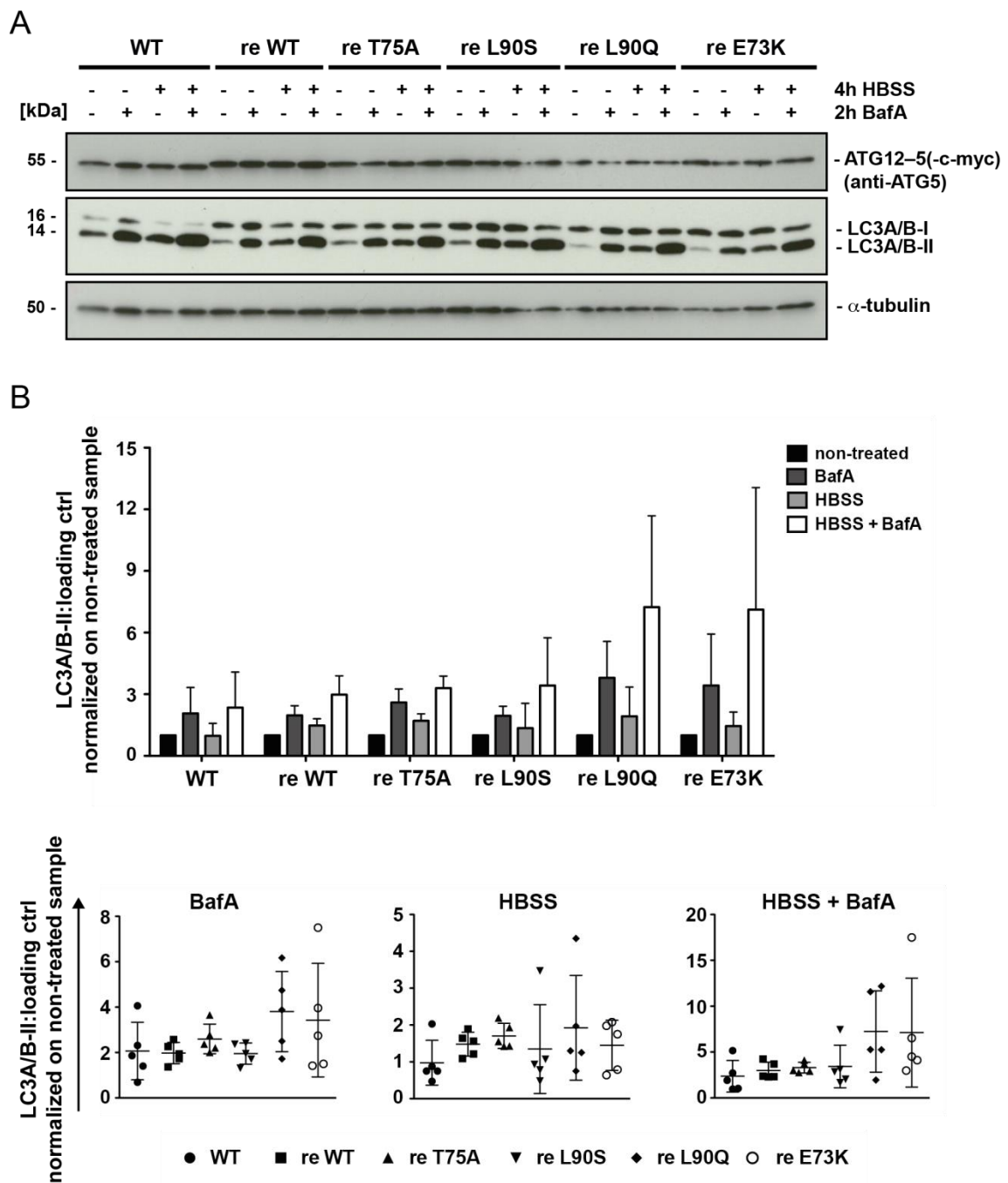
Fig. 5.16: HBSS and BafA-treated mutant cell lines ATG5^T75A, ATG5^L90S, ATG5^L90Q and ATG5^E73K showed no significant functional alterations in basal and starvation induced autophagy compared to WT cells. (A) Representative Western blot of the HBSS/BafA treatment. The LC3A/B-II signal was normalized on the respective loading control signal by using ImageJ-based quantification. Non-reconstituted WT cells were included as a control. Incubation with BafA (100 nM) was performed during the last 2 h of HBSS treatment. **(B)** Combination of five independent experiments. Within each line all calculated LC3A/B-II-to-loading control ratios were normalized to the respective non-treated sample. Data is represented as the mean ±SD. Upper part: Visualization of the results in a bar graph grouped by cell lines. Lower part: Visualization of the results in different scatter plots separated by the treatments.

Overall, after incubation with BafA the amount of LC3A/B-II was raised and it decreased almost to the non-treated sample level after 4 h of starvation (HBSS). The addition of BafA during HBSS treatment resulted in the strongest LC3A/B-II accumulation. Within all samples the WT- and T75A-reconstituted cells displayed a comparable pattern to the reference WT line. Considering the single outliers in the ATG5[L90S] line, in total no significant alterations in comparison to the reconstituted WT line were observed. For the ATG5[L90Q] cell line, a tendency towards higher basal autophagy (BafA sample) as well as a slightly higher induced autophagic flux (HBSS together with BafA sample) was detected. Neither the ATG5[E73K]-reconstitued cell line showed a clear or consistent pattern through all experiments, but only displayed a tendency towards slightly enhanced basal and induced autophagic flux. With all repetition experiments taken into account, the calculated LC3A/B-II amount had a significantly higher spread in the mutant cell lines (Fig. 5.16B).

Another method to measure the autophagy-dependent change of LC3 is by using a flow cytometry-based approach after stable transfection of the cells with a fluorophore-LC3 fusion protein. According to the induced autophagic flux in the tested cell populations, the fluorophore-intensity histogram, which represents the total LC3 amount, will shift left (lower amount of LC3 resulting from more degradation/higher flux) or right (higher amount of LC3 resulting from less degradation/lower flux)[298]. To use this high-throughput technique, the ATG5 mutant MEF cell lines, as well as the reference WT and KO MEF cell lines, were retro-virally transduced with a mCitrine-hLC3B (human LC3, isoform B) construct. Unfortunately, the resulting bulk selected cell lines displayed different citrine expression profiles in the non-treated condition. A reduction of the expression level inhomogeneity was needed to be able to interpret mCitrine-LC3-alterations between different cell lines. For this, all cell lines underwent a sorting procedure, which led to a more comparable mCitrine-expression profile (Fig. 5.17A).

Next, the sorted cell lines were treated with HBSS and BafA as previously described and analyzed via flow cytometry to investigate the autophagic flux. Representative histograms for the reference cells and the reconstituted WT cells are visualized as an example (Fig. 5.17B). The representative histograms for the reference cells (ATG5 WT) displayed the expected mCitrine-hLC3B pattern according to the

different conditions. Inhibition of autophagic degradation by treatment with BafA resulted in an increased amount of LC3 compared to the non-treated sample (slight shift to the right). To remember, the observed shift corresponds to the intensity of basal autophagy. Incubation of the cells in HBSS medium led to an increased autophagic flux (starvation-induced autophagy), which is represented by a lower amount of mCitrine-hLC3B. Addition of BafA (HBSS together with BafA) again restored the amount of measurable mCitrine-hLC3B (Fig. 5.17B, upper part). In contrast to the clear response of the reference cells, for the ATG5 WT-reconstituted ATG5 KO MEF cells only weak stimulation-dependent changes in the mCitrine-hLC3B histograms were demonstrated (Fig. 5.17B, lower part).
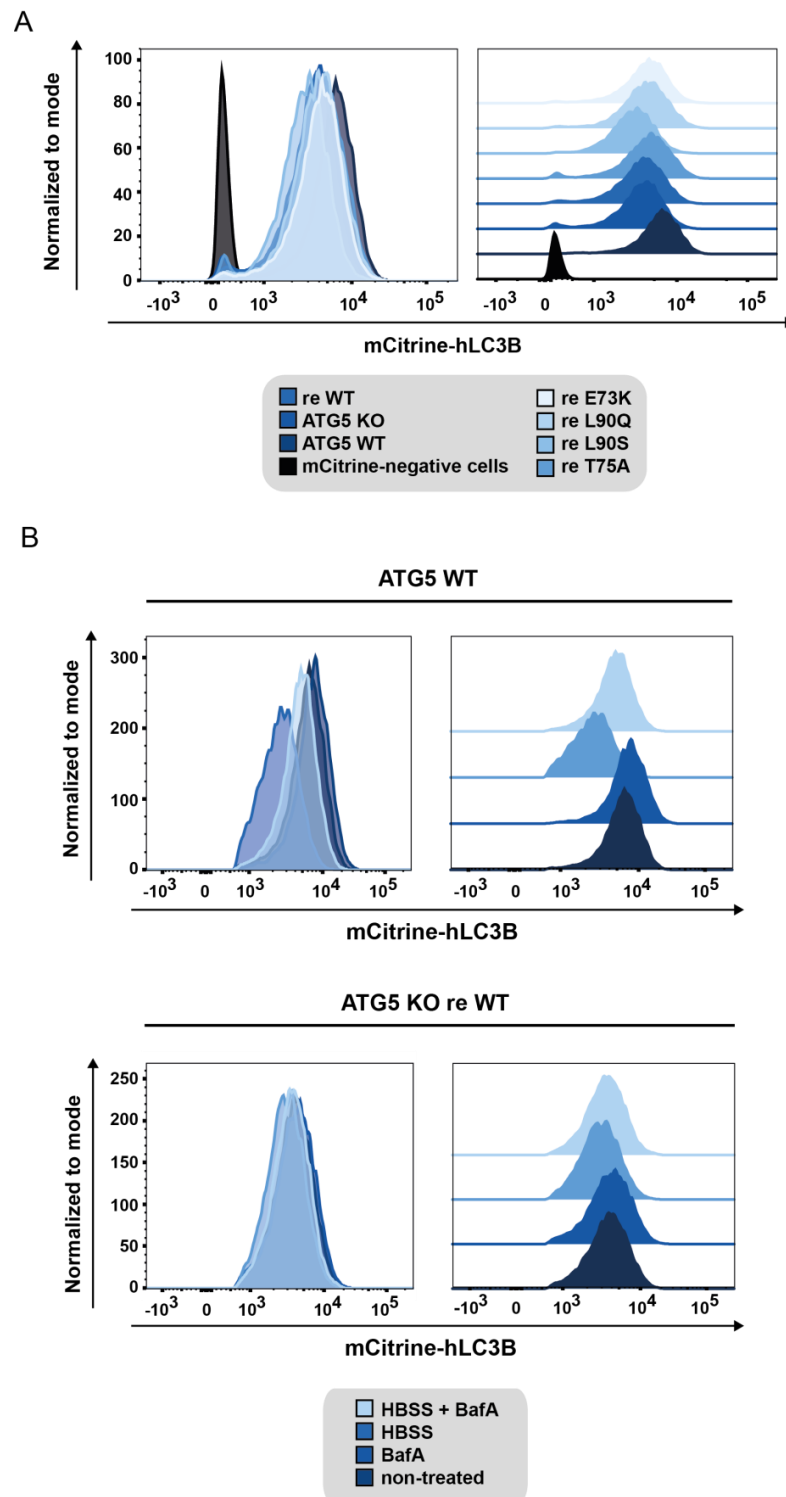
Fig. 5.17: ATG5 WT-reconstituted mCitrine-hLC3B-transduced cell lines displayed only a marginal response towards autophagy stimulation. (A) The sorting of all mCitrine-hLC3B-transduced cell lines resulted in a more comparable LC3-level under non-stimulating conditions. However, differences in the basal LC3-levels were still detectable. **(B)** After HBSS treatment with or without BafA, the comparison of the histograms from reference (ATG5 WT) and reconstituted WT (ATG5 KO re WT) cells showed the expected condition-dependent shifts in the reference samples. Notably, the ATG5-WT-reconstituted cells only displayed a minimal change in the mCitrine-hLC3B-derived fluorescence intensity upon autophagy stimulation.

89

For all samples the geometric mean fluorescence intensity (gMFI) was calculated to facilitate comparison between the different treatments. Similarly to the Western blot experiments, in each cell line the calculated gMFIs were normalized to the untreated sample, which enabled a comparison between the analyzed cell lines. As expected, the ATG5 KO cells showed no difference in the gMFI that would result from the stimulation with BafA, HBSS or both, as these cells lack the ability to convert LC3-I to LC3-II and consequently are defective for canonical autophagy (Fig. 5.18).

Next, the total mCitrine-hLC3B levels of the not-reconstituted reference cells and the ATG5 WT-reconstituted cells were compared. As already seen from the histograms (Fig. 5.17), the reconstituted ATG5 WT cells displayed a less accentuated response to the HBSS and BafA treatment in general, which is even more obvious in the here shown bar-graph representation. Comparing the respective untreated condition to the starvation-induced (HBSS) condition, the expected reduction of the mCitrine-LC3B gMFI was significantly more pronounced in the reference cells. Consequently, the recovery of the mCitrine level in the co-treated sample (HBSS together with BafA) was more evident in these cells (Fig. 5.18). Thus, differences in the autophagic flux between non-reconstituted and reconstituted cells increase, if the total LC3 level and not only LC3-II is used as readout.

Comparing the reconstituted lines with each other, the LC3-levels in the ATG5^{T75A} cells were comparable to the ATG5 WT line throughout all conditions. The effect of the co-treatment (HBSS together with BafA) was further reduced in the ATG5^{L90Q} cell line, suggesting that in these cells the autophagy level was even less. Finally, in the ATG5^{L90S} and ATG5^{E73K} mutant cell lines, basically no response in the gMFI upon addition of BafA was detected. Taken together, in this experimental setting the mutation of ATG5 at leucine 90 or glutamate 73 resulted in a somewhat reduced autophagic capacity, but overall only small differences were detected in comparison to the reconstituted WT counterpart cells (Fig. 5.18).
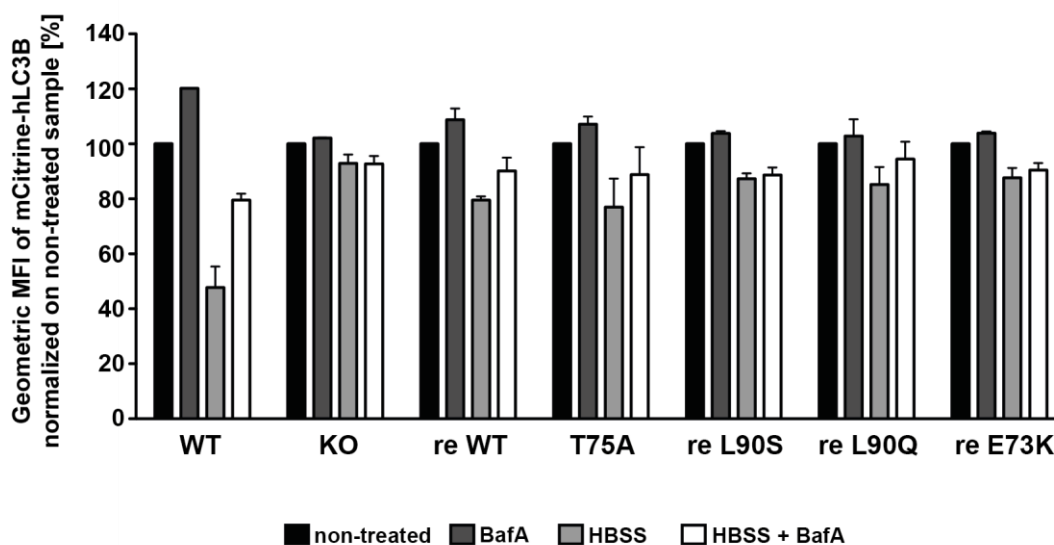
Fig. 5.18: HBSS and BafA treatment of ATG5 WT or ATG5 mutant mCitrine-hLC3B-positive cell lines in comparison to reference lines displayed only minor differences in the autophagic flux. The mCitrine-hLC3B-positive population was identified according to the unstained control. The respective geometric mean of fluorescence intensity (gMFI) was calculated by FlowJo for each sample. Normalization was performed based on the gMFI calculated for the non-treated sample separately for each cell line. Data are represented as the mean ±SD of two independent experiments.

5.3.10 Possible phosphorylation sites within the ATG12-part of the ATG12–5 conjugate

Mass spectrometry analysis demonstrated that T75 is not the target residue of the p38-mediated phosphorylation. It needs to be considered that ATG5 does not function as a single protein during autophagy but is conjugated to ATG12. Taking into account the other possible candidate residues for p38-mediated phosphorylation, the sequence and 3D structure of the ATG12–5 conjugate was consulted again with focus on ATG12. Despite its small size of about 16 kDa, the linear sequence of ATG12 revealed five S/TP motifs representing potential canonical phosphorylation targets of the p38 MAPK (Fig. 5.19A). The 3D analysis displayed the localization within the complex. Interestingly, the first three putative phosphorylation motifs $S^{26}P$, $T^{31}P$ and $S^{41}P$ are part of a highly flexible stretch, which is not resolved by the crystal structure. The flexibility of this part results in potentially easier accessibility for the kinase. Notably, the orientation of the T75 region of ATG5 would sterically correspond with a role as docking site during a possible phosphorylation at ATG12 residues 1-52, whereas the orientation of the

other two motifs T65P and S111P seem rather unfavorable with respect to this hypothesis (Fig. 5.19B).

A

```
  1 MTDDKDVLRD VWFGRIPTCF TLYQDEITER EAEPYYLLLP RVSYLTLVTD 50
 51 KVKKHFQKVM RQEDISEIWF EYEGTPLKWH YPIGLLFDLL ASSSALPWNI 100
101 TVHFKSFPEK DLLHCPSKDA IEAHFMSCMK EADALKHKSQ VINEMQKKDH 150
151 KQLWMGLQND RFDQFWAINR KLMEYPAEEN GFRYIPFRIY QTTTERPFIQ 200
201 KLFRPVAADG QLHTLGDLLK EVCPSAIDPE DGEKKNQVMI HGIEPMLETP 250
251 LQWLSEHLSY PDNFLHISII PQPTD 275
```

```
  1 MAEEPQSVLQ LPTSIAAGGE GLTDVSPETT TPEPPSSAAV SPGTEEPAGD 50
 51 TKKKIDILLK AVGDTPIMKT KKWAVERTRT IQGLIDFIKK FLKLVASEQL 100
101 FIYVNQSFAP SPDQEVGTLY ECFGSDGKLV LHYCKSQAWG 140
```

<u>previously mutated residues</u>   residues of flexible loop ATG12 (1-52)
possible phosphorylation motives in ATG12
conjugation residues

B

Fig. 5.19: The sequence of ATG12 harbors five canonical p38 MAPK phosphorylation motifs. **(A)** Linear sequence of the human ATG5 (upper part) and ATG12 (lower part), which are covalently conjugated by K130 (ATG5) and G140 (ATG12). L90 and E73 of ATG5 are marked in red, whereas ATG5 T75 is depicted in green. Further interesting residues of ATG5 and ATG12 are highlighted in color or by underlining as shown in the legend. **(B)** 3D structure of the ATG12–5 conjugate (Protein Data Bank [PDB] ID: 4GDK), where ATG5 is shown in light orange, and ATG12 is displayed in light blue. L90, E73 and T75 of ATG5 are depicted in red and green, respectively. Additionally, ATG12 K53 is highlighted in black as the most N-terminal residue solved by structural analysis. The less exposed and backwards oriented possible p38-phosphorylation motifs S111(P) and T65(P) are marked in purple.

5.3.11 The ATG12–5 conjugate is phosphorylated by p38

To investigate whether ATG12 is indeed a target of p38-mediated phosphorylation, *in vitro* kinase assays with the respective recombinant proteins were prepared. Thereupon ATG5 WT, ATG5^{T75A} and ATG12–5 were either incubated with

the active p38 WT, the kinase-inactive p38 kinase mutant (KM) or the kinase buffer only. The detection of the phosphorylation was performed via a Western blot-antibody directed against phospho-threonine. Compared to the ATG5 WT and the T75A mutant sample, a clear phospho-specific signal at the molecular weight corresponding to ATG12–5 was identified for the ATG5–12 conjugate incubated with p38 WT (Fig. 5.20).
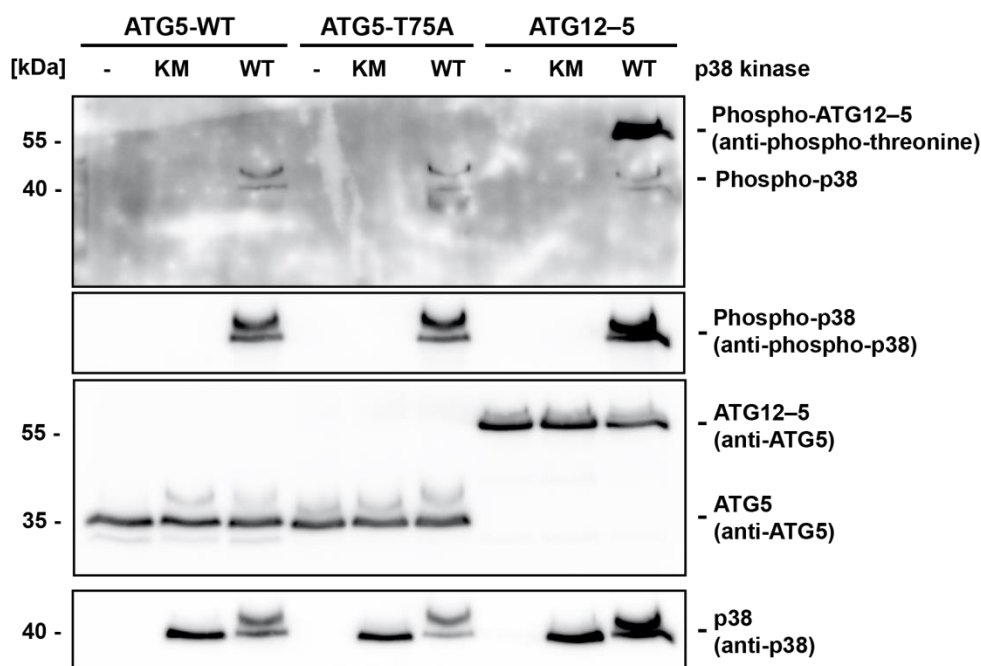
Fig. 5.20: ATG12–5 is phosphorylated by p38 *in vitro*. 1 µg substrate per *in vitro* kinase sample was incubated with kinase buffer only or with buffer supplemented with 200 ng of kinase. Either p38 WT or the kinase-deficient p38 KM mutant was used for the assay. The kinase buffer consisted of 250 µM ATP.

An additional *in vitro* kinase experiment was performed to restrict the possibilities of phosphorylated residues on ATG12. For this, ATG12–5 full length was compared to ATG12–5 truncated, where the flexible region (amino acids 1-52) of ATG12 was missing. It needs to be mentioned, that within this first stretch two SP and one TP motif were located (see Fig. 5.19). A complete loss of the phosphorylation signal would indicate that one or more residues of the flexible loop were targeted by p38.

For Western blot analysis the similar size of the ATG12–5 truncated and the p38 kinase turned out to be problematic. Since the T180/Y182-phosphorylated, active p38 WT kinase is recognized by the phospho-threonine specific antibody (Fig. 5.21), this

93

conceivably led to difficulties in the correct assignment of the bands of the kinase and substrate. To solve this problem, a phospho-threonine-proline motif antibody was used, which was supposed to be more specific for the phosphorylated substrate motif. Unfortunately, the WT kinase was also detected clearly by the new motif antibody (Fig. 5.21). Comparing the ATG12–5 full length and the truncated sample, in the height of approximately 40 kDa an additional third phosphorylation signal was detected for the shortened substrate sample. An overlap of this phosphorylation signal with the ATG12–5 truncated-band, gained by developing with the ATG5-specific antibody was indeed confirmed. Nevertheless, the same three-band-pattern was observed in this sample after incubation with the phospho-p38 and the p38 total antibody, thus a clear assignment of the band remains difficult (Fig. 5.21). From this experiment, a crude pre-determination of the phosphorylated residues in ATG12 was not possible.
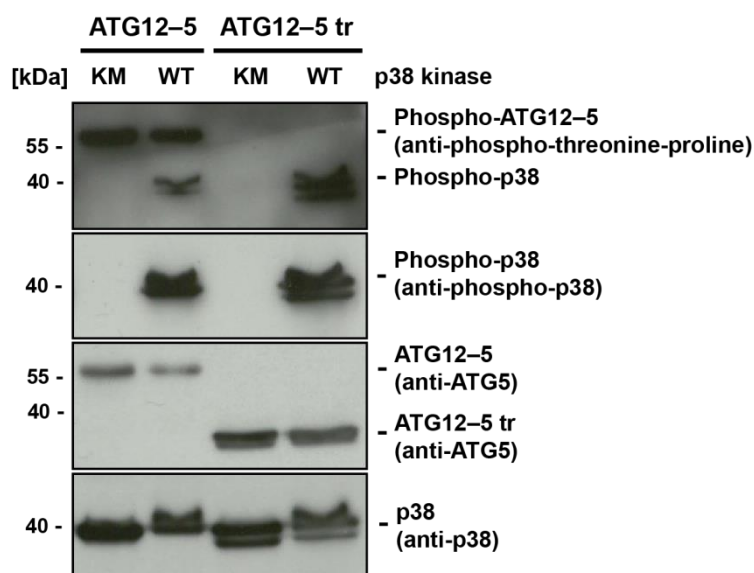
Fig. 5.21: The position of possible target residues for p38-mediated phosphorylation on ATG12 could not be pre-determined by an *in vitro* kinase-Western blot approach. ATG12–5 full length was tested in comparison to ATG12–5 truncated (tr), which lacks the amino acids 1-52. Per sample 1 µg substrate was incubated with either 200 ng of the p38 WT or the kinase-deficient p38 KM mutant. The kinase buffer consisted of 250 µM ATP.

Another difficulty shown by this experiment was the pre-phosphorylation of the ATG12–5 conjugate in the new protein batch, since a clear phosphorylation signal of the substrate was also detected after incubation with the mutant form of the kinase (Fig. 5.21). Likely, the phosphorylation resulted from the ATG12–5-synthesis in the insect-derived production cell line, as it was confirmed to be independent of any

treatment and successfully removed by treatment of the recombinant protein with Antarctic Phosphatase (Fig. 5.22A). In order to identify the phosphorylated residue(s) on ATG12, mass spectrometry analysis of a respective *in vitro* kinase sample was performed. For this, the recombinant ATG12–5 was firstly dephosphorylated to ensure that later detected phosphorylated amino acids only originate from p38-mediated phosphorylation (Fig. 5.22B). However, the activity of the phosphatase will be contra-productive during the following p38-mediated re-phosphorylation. Thus, in order to inactivate the zinc-dependent Antarctic Phosphatase, the zinc chelator TPEN was added before the kinase reaction was started. The different steps of this experimental setup were controlled by Western blotting (Fig. 5.22B).
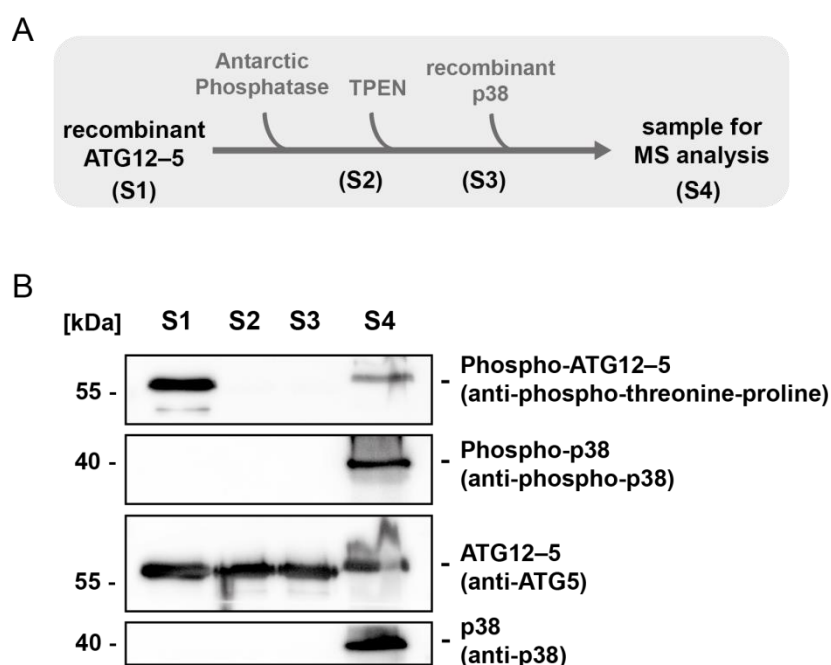
Fig. 5.22: The initially phosphorylated ATG12–5 conjugate was de-phosphorylated by Antarctic Phosphatase and thereafter used as a substrate for an *in vitro* kinase assay. (A) Procedure of Antarctic Phosphatase-mediated dephosphorylation and subsequent p38 MAPK-mediated re-phosphorylation of ATG12–5 in the presence of the zinc-chelator TPEN. **(B)** The batch sample for the mass spectrometry experiment consisted of 5 µg substrate, which was incubated with 25 units of the phosphatase for 30 min at RT. TPEN was added to a final concentration of 1 mM prior to the addition of 200 ng p38 WT kinase per µg of substrate. The kinase buffer consisted of 250 µM ATP. At each step 1 µg substrate was separated for Western blot analysis. To probe for phosphorylation of ATG12–5, the phospho-threonine-proline motif antibody was used.

Next to the analysis of the *in vitro* kinase sample (S4) by Western blot, a preliminary mass spectrometry experiment was performed with the residual part. Since the N-terminus of ATG12 was known to be highly flexible and well accessible,

the hypothesis was that one of the three canonical phospho-acceptor sites within this region is phosphorylated by p38. Thus, by use of the protease AspN, an ATG12-peptide from amino acid 24 to 49 was generated (compare Fig. 5.19) and analyzed via LC-MS/MS. Interestingly, the results suggested a p38-mediated phosphorylation of serine 36 or serine 37 instead of a classical serine-proline or threonine-proline motif.

5.4 p38-mediated regulation of autophagy during *S. aureus* infection

5.4.1 *S. aureus* induces autophagy during infection of fibroblasts

Many types of bacteria are known to induce an autophagic response in the infected cells. Originally, a specific form of autophagy named xenophagy is used by the infected cell to directly degrade the invading pathogen and thereby reduce the harm of the infection. Naturally, some bacteria evolved strategies to counteract this or even profit from the autophagic structures[281].

In this study, the influence of *S. aureus* infection on the autophagic machinery of murine embryonic fibroblast (MEF) cells was investigated. The workflow of a typical infection experiment is depicted in Figure 5.23A. Imaging of NIH/3T3 cells, which were stably transduced with GFP-LC3B, showed in the untreated condition only some GFP-positive dot-like structures, which represent autophagic vacuoles (autophagosomes) (Fig. 5.23B). The induction of autophagy via HBSS treatment resulted in an increased number of cytoplasmic dots. A strong influence on the GFP-LC3B appearance was detected after 3 h infection with the RFP-expressing *S. aureus* strain SH1000-RFP. Especially in the vicinity of the red, coccoid-shaped bacteria an accumulation of GFP-LC3B-positive structures was visible. Some of the bacteria were already completely surrounded by an LC3B-positive vacuole (autophagosome) (Fig. 5.23B). An enhanced number of autophagosomes alone is not sufficient to confirm a true induction of autophagic flux upon infection.
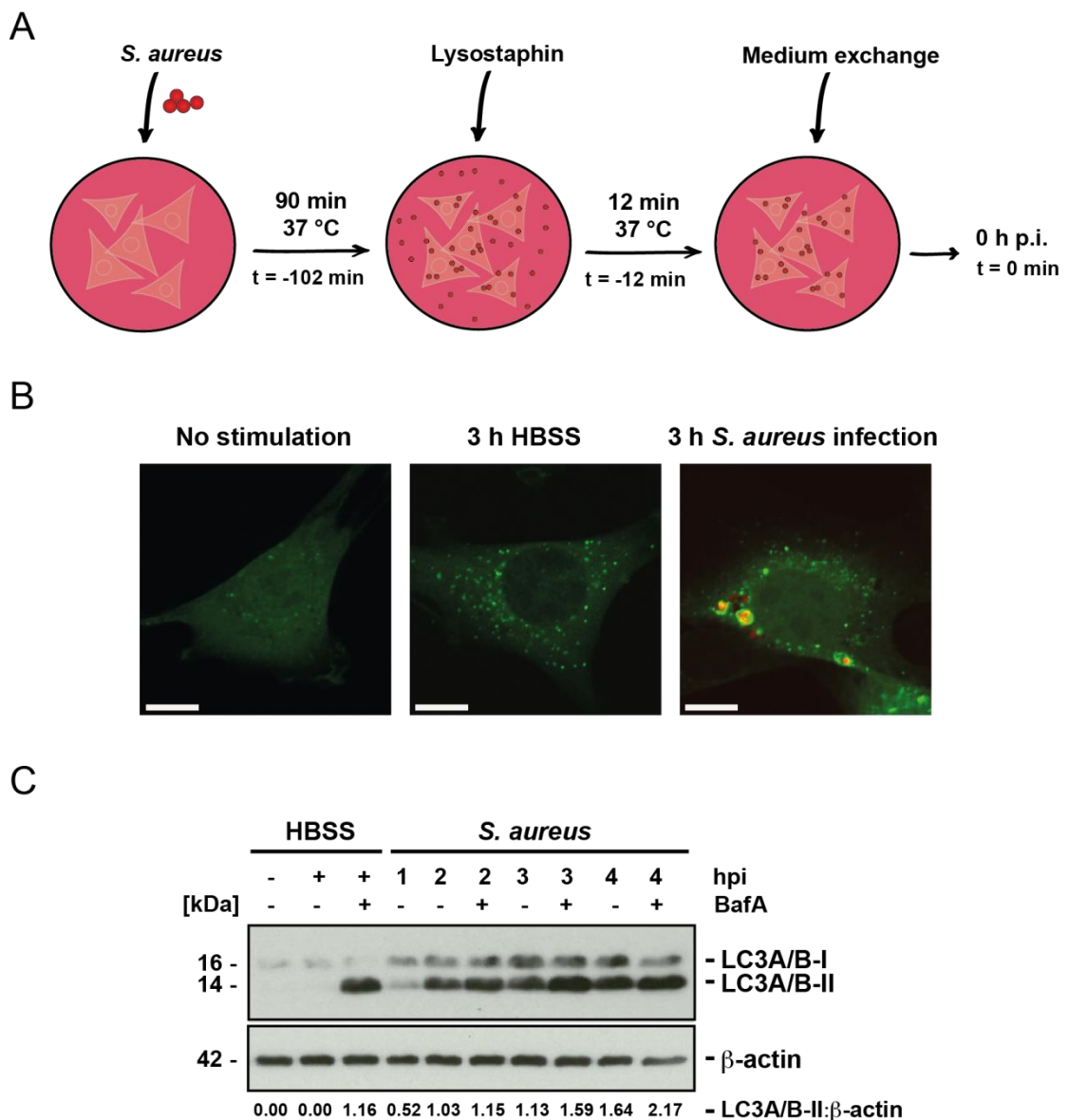
Fig. 5.23: *S. aureus* **infection in MEFs induced a strong induction of GFP-LC3B positive autophagic structures. (A)** Principle workflow of a typical infection experiment: *S. aureus* was added with a multiplicity of infection (MOI) of 8 on the seeded MEFs. After 90 min of incubation all non-invaded, extracellular bacteria were lysed via lysostaphin treatment (10 μg/mL). Exchange of the medium started the kinetic (t=0 min/0 hpi). **(B)** Comparison of the appearance of GFP-positive dots in NIH/3T3 cells stably expressing GFP-LC3B. The cells were either left unstimulated, starved (3 h HBSS) or infected with the RPF-expressing *S. aureus* strain SH1000-RFP. Scale bar: 10 μm. **(C)** *S. aureus* infection kinetic for Western blot analysis was performed in large T-immortalized MEF cells in the presence or absence of BafA (2 h, 100 nM). As reference samples, non-treated cells as well as HBSS treated cells ±BafA were included. Equal loading was ensured by probing the membrane with β-actin. Quantification of the bands was performed with ImageJ.

Thus, Western blot experiments were performed to monitor endogenous LC3 levels in the presence or absence of the lysosomal inhibitor BafA. During a kinetic approach, large T-immortalized WT MEF cells were infected with the *S. aureus* strain

SH1000 WT for different time periods. As reference samples, non-treated and starved (HBSS) MEFs in the presence or absence of BafA treatment were included. Comparing the signals of the lipidated, autophagy-active LC3A/B-II, a clear induction during the analyzed time course of *S. aureus* infection was detected. In terms of the calculated LC3A/B-II to loading ratios, the magnitude at 3 and 4 hours post infection (hpi) was even higher than the classical starvation-induced autophagic flux (HBSS together with BafA) (Fig. 5.23C).

Of note, LC3 is not only important during autophagy but also triggers another vesicle-based enclosure mechanism called LC3-associated phagocytosis (LAP)[299]. This pathway was shown to be independent of the preinitiation complex formation[300] and by definition only forms single-membrane structures. In order to define the mechanism of *S. aureus*-dependent LC3-II induction more closely, the membrane structure of the vesicles was investigated by a transmission electron microscopy experiment in cooperation with Prof. Dr. Manfred Rohde and his co-workers (Helmholtz-Centre for Infection Research, Braunschweig). Indeed, the autophagosomal character of the membranes that subsequently surround the bacteria-containing vacuoles displayed a double-layered structure (Fig. 5.24).
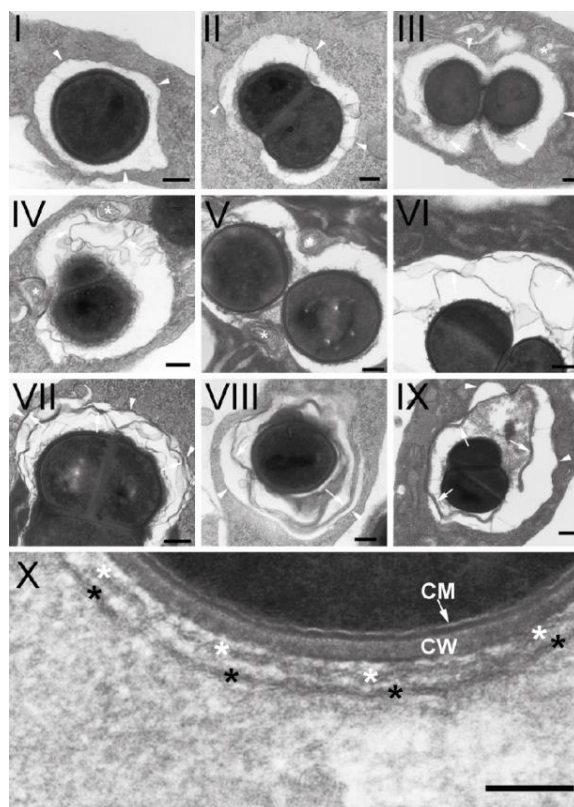
Fig. 5.24: *S. aureus* **is enclosed in double-membrane (autophagic) vesicles during infection in NIH/3T3 cells.** Transmission electron microscopy of *S. aureus*-infected NIH/3T3 cells. In the first images the bacteria-containing vacuoles were observed to fuse with multilamellar membranes **(III to V)**. The images **VI to VII** displayed autophagic structures, which started to form in the vicinity of the bacterial cell. The subsequent surrounding of the intracellular bacterium is shown in the images **VIII to IX**. In the final magnified image **X,** the double-membrane character of the host-derived structures nearby the bacterial cell wall is depicted. Asterisks show the multilamellar membranes in close proximity to bacterial-containing vacuoles, arrows indicate the host-derived membrane structures in the remaining images. CM: bacterial cytoplasmic membrane, CW: bacterial cell wall. Scale bar: 200 nm.

5.4.2 *S. aureus* induces selective autophagy in infected fibroblasts

The term autophagy has been subdivided in bulk and selective autophagy and the understanding and relevance of the latter greatly increased during recent years[301]. The targeted degradation of invasive pathogens, known as xenophagy, is mediated by receptors that connect the cargo to LC3-II and thereby to the forming autophagosome. Usually, the bacterium is associated with ubiquitin-tagged proteins, which in turn can be recognized by autophagic receptor proteins[302].

Consequently, immunofluorescence experiments were performed to address the question of whether *S. aureus* is associated with ubiquitinylated proteins in order to recruit the autophagic machinery. NIH/3T3 cells stably expressing GFP-LC3B were

infected with SH1000-RFP and were stained for ubiquitinylation via the FK2 antibody (Fig. 5.25A).
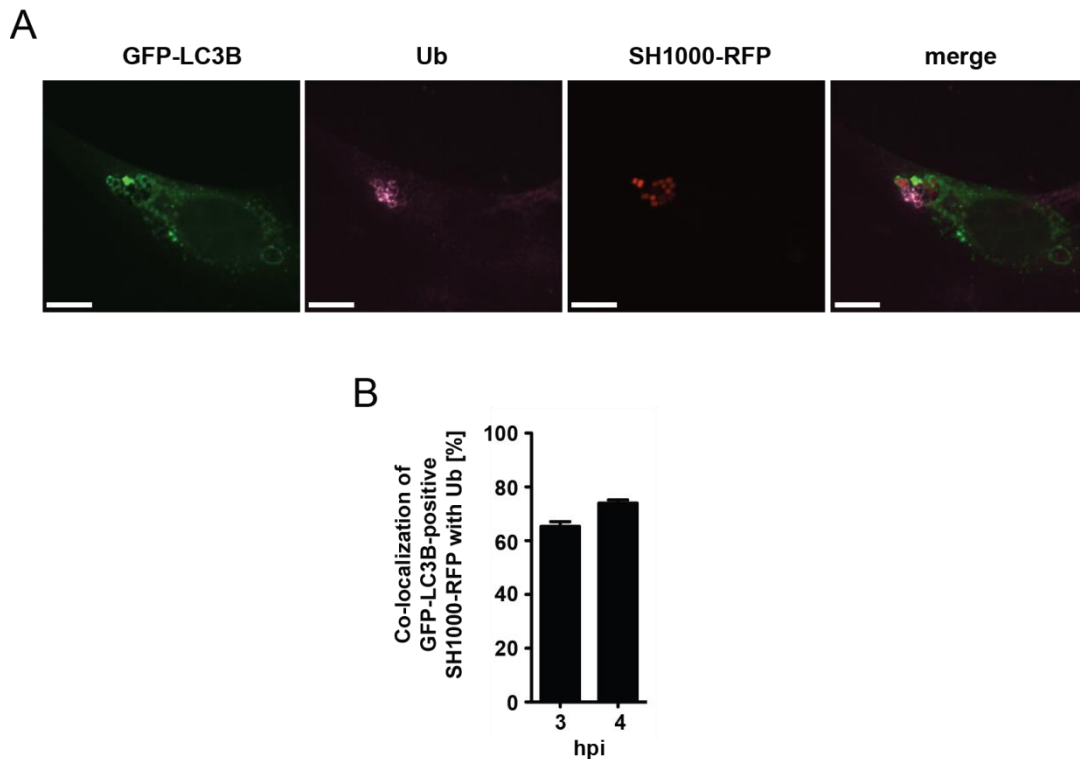
Fig. 5.25: Intracellular *S. aureus* is targeted by ubiquitin. (A) NIH/3T3 cells stably expressing GFP-LC3B were infected with the RPF-expressing *S. aureus* strain SH1000-RFP for the indicated time periods. Ubiquitinylated proteins were stained by the FK2 antibody and images were taken by confocal microscopy at a magnification of 60x. Scale bar: 10 μm. **(B)** Quantification of the experiment shown in (A), visualized is the percentage of GFP-LC3B-positive *S. aureus* that co-localized with ubiquitin-tagged proteins. 50 cells were analyzed per condition. Data is represented as the mean ±SEM of three independent experiments.

The representative image displays a clear accumulation of ubiquitin-positive proteins surrounding the bacteria. The ubiquitin signal was detected in close proximity to GFP-LC3-positive autophagic structures that were found to engulf most of the bacteria (Fig. 5.25A). During the analyzed time periods of 3 and 4 hpi, the percentage of GFP-LC3B-positive bacteria that were found to co-localize with ubiquitin reached approximately three fourth (Fig. 5.25B).

In terms of xenophagy, next to others, the proteins p62 and optineurin (OPTN) have previously been described as autophagic receptors[201,213,212]. Hence, the localization of p62 and OPTN was analyzed in infected cells by immunofluorescence experiments. When it came to p62, GFP-LC3B-expressing NIH/3T3 cells were infected

with SH1000-RFP prior to staining with an antibody against the autophagic receptor (Fig. 5.26).
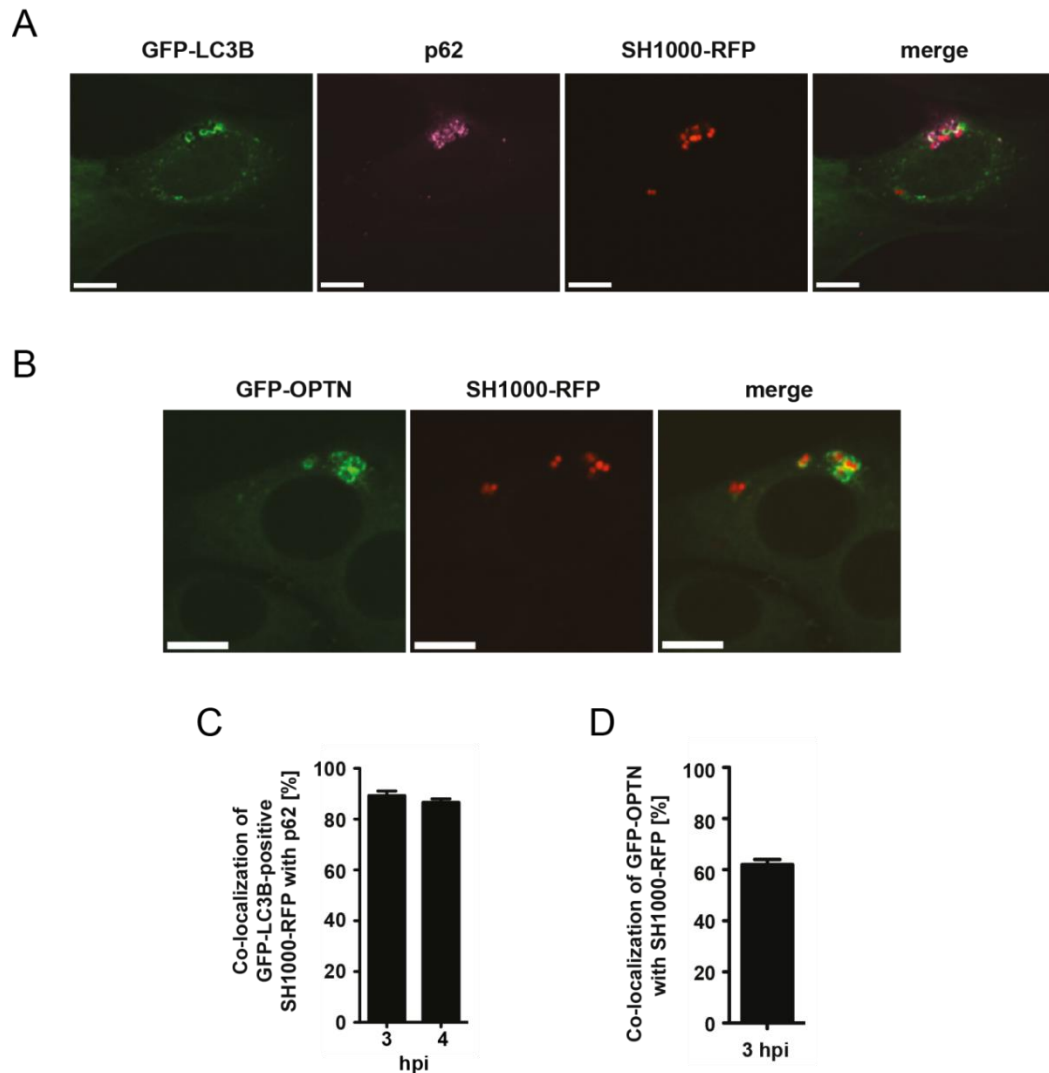
Fig. 5.26: Intracellular *S. aureus* co-localized with the autophagic receptors p62 and OPTN.
(A) NIH/3T3 cells stably expressing GFP-LC3B were infected with the RFP-expressing *S. aureus* strain SH1000-RFP for the indicated time periods. The autophagic receptor p62 was stained by a monoclonal antibody and images were taken by confocal microscopy. Scale bar: 10 μm. **(B)** NIH/3T3 WT cells were transfected with GFP-OPTN prior to infection with SH1000-RFP and analyzed at a confocal microscopy. Scale bar: 10 μm. **(C)** Quantification of the experiment shown in (A), visualized is the percentage of GFP-LC3B-positive *S. aureus* that co-localized with p62. 50 cells were analyzed per condition. Data is represented as mean ±SEM of three independent experiments. **(D)** Quantification of the experiment shown in (B), visualized is the percentage of intracellular *S. aureus* that is associated with GFP-OPTN obtained from 50 cells per condition. Data is represented as the mean ±SEM of two independent experiments.

The representative image demonstrates that p62 specifically accumulated nearby *S. aureus* and co-localized with the GFP-tagged autophagic structures (Fig. 5.26A). This was true for almost 90% of the GFP-LC3B-asscociated bacteria (Fig. 5.26C). The co-localization of OPTN with *S. aureus* during the infection of fibroblasts was investigated by transient transfection of NIH/3T3 WT cells with GFP-OPTN and subsequent infection with SH1000-RFP. At 3 hpi the majority of the invaded *S. aureus* co-localized with GFP-OPTN (Fig. 5.26B and D).

5.4.3   *S. aureus* is able to inhibit autophagic degradation

Previous studies revealed that some bacteria, e.g. *Salmonella enterica* serovar Typhimurium or Group A *Streptococcus* (GAS) are targeted by autophagy for degradation[193,204] However, these and other bacteria like *Listeria monocytogenes* and *Shigella flexneri* have also evolved multiple strategies to at least partially evade degradation[217,303–306]. To investigate the intracellular fate of *S. aureus* after being recognized by the autophagic machinery infected GFP-LC3B-expressing NIH/3T3 cells were stained with LysoTracker Deep Red. This reagent accumulates in acidic compartments, thus the more of *S. aureus* co-localizes with acidic compartments, the more likely the bacteria were truly degraded in the final step of autophagy. In the depicted image, no co-localization of SH1000-RFP and LysoTracker-positive acidic compartments was detected (Fig. 5.27A). Indeed only around 15%±7 of the GFP-LC3B-associated bacteria (Fig. 5.27B) and 24%±3 (3 hpi) and 27%±2 (4 hpi) of all intracellular *S. aureus* were found in or associated with an acidic compartment (Fig. 5.27C).
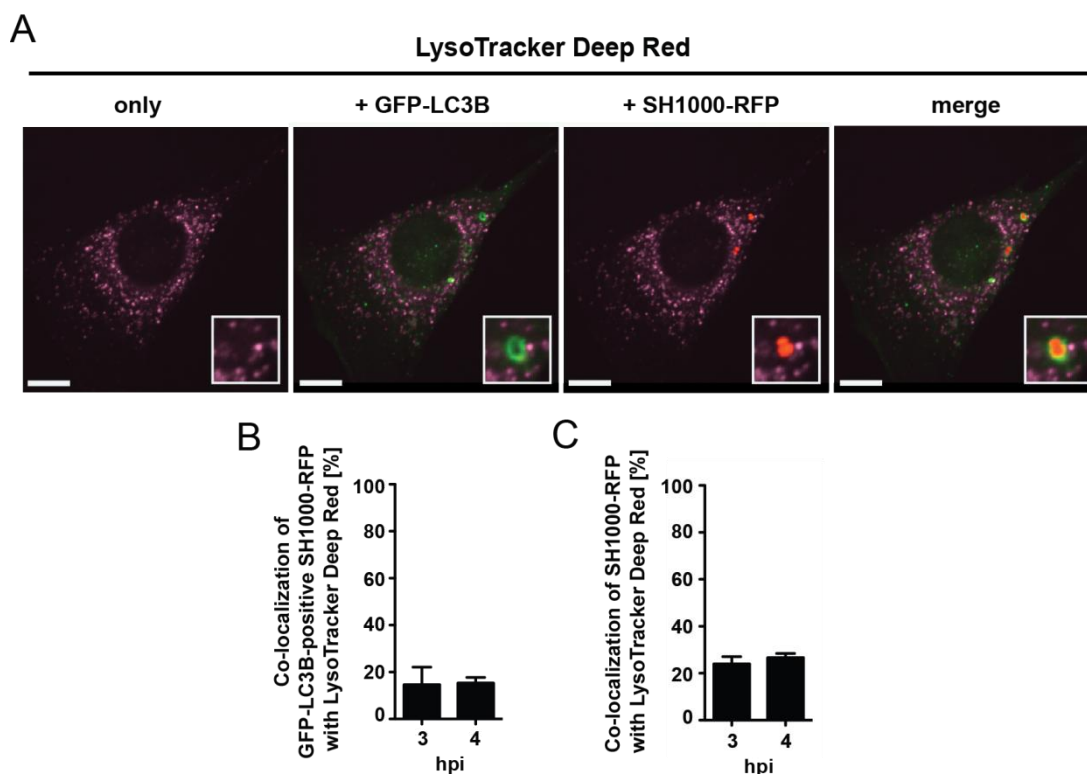
Fig. 5.27: Only a minor fraction of *S. aureus* co-localized with LysoTracker Deep Red-positive acidic compartments. (A) NIH/3T3 cells stably expressing GFP-LC3B were infected with the RPF-expressing *S. aureus* strain SH1000-RFP for the indicated time periods. Acidic compartments were stained by LysoTracker Deep Red prior to fixation and images were taken by confocal microscopy. Scale bar: 10 μm. **(B)** Quantification of the experiment shown in (A), visualized is the percentage of GFP-LC3B-positive *S. aureus* that co-localized with LysoTracker Deep Red in 50 cells per condition. Data is represented as the mean ±SEM of three independent experiments. **(C)** Quantification of the experiment shown in (A). The percentage of total *S. aureus* that co-localized with LysoTracker Deep Red is shown. 50 cells were analyzed per condition. Data is represented as the mean ±SEM of three independent experiments.

To further verify the assumption that the majority of *S. aureus* can escape from autophagosomes, e.g. by disturbing the autophagic flux, the level of the autophagic receptor p62 was monitored during an infection kinetic. Differences in the amount of p62 have been reported as an indicator for altered autophagic degradation[307]. Autophagy induction by HBSS treatment decreased the amount of p62, whereas the presence of the lysosomal inhibitor BafA restored the initial level. Upon *S. aureus* infection, the amount of the receptor was slightly reduced at 2 hpi, but restored again at 3 hpi and even enhanced at 4 hpi (Fig. 5.28). Thus, these results pointed to a *S. aureus*-mediated blockade of the autophagic flux as well.
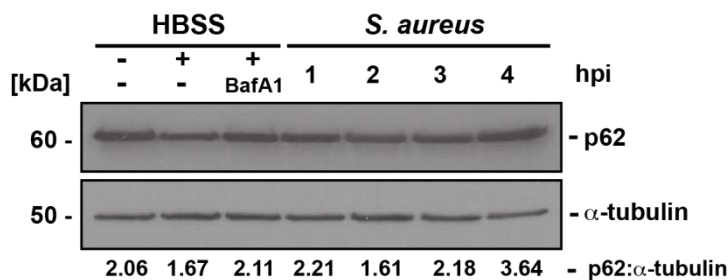
Fig. 5.28: *S. aureus* **infection resulted in an accumulation of p62, thus a reduced autophagic degradation of the protein.** NIH/3T3 WT cells were infected with the WT *S. aureus* strain SH1000 for the indicated time periods and the samples were prepared for Western blot analysis. As reference samples non-treated cells as well as HBSS treated cells in the absence or presence of BafA (100 nM) were included. Equal loading was verified by probing the membrane with α-tubulin. Quantification of the bands was performed with ImageJ.

5.4.4 The MAPK p38 is activated during *S. aureus* infection

Although many principles of bacterial evading strategies were studied so far, often the detailed mechanisms are still unknown. Most likely *S. aureus* inhibits or delays the fusion of autophagosomes with lysosomes, since it was shown to be engulfed by LC3B-positive vacuoles (see Fig. 5.23B, Fig. 5.25A, Fig. 5.26A and video in Neumann Y.; Bruns S.A. *et al.*[288]) but at the same time it was demonstrated to only ending-up to a minor extent in acidic compartments (Fig. 5.27). A previous study revealed that a comparable block of the autophagic flux is induced via specific activation and translocation of the MAP kinase p38[133]. Therefore the role of the p38 during *S. aureus* infection was analyzed next.

First, Western blot analysis with a SH1000 WT infection kinetic was performed and the membrane was probed with a phospho-p38 (p-p38)-specific antibody. MEFs infected with *S.* Typhimurium (*Sal.*) and HBSS-treated MEFs with or without addition of BafA were included as reference samples. Neither at 3 h post *S.* Typhimurium infection nor during 3 h starvation-induced autophagy, activation of p38 was detected. However, upon 2 h post *S. aureus* infection, phosphorylated p38 was identified, which accumulated after BafA treatment. The level of p38 activation increased in 3 hpi, again addition of BafA resulted in further enhancement of the phosphorylation signal. At 4 hpi the amount of activated p38 was the highest compared to the previous non-BafA samples, whereas treatment with the lysosomal inhibitor only led to a comparably reduced accumulation (Fig. 5.29A).
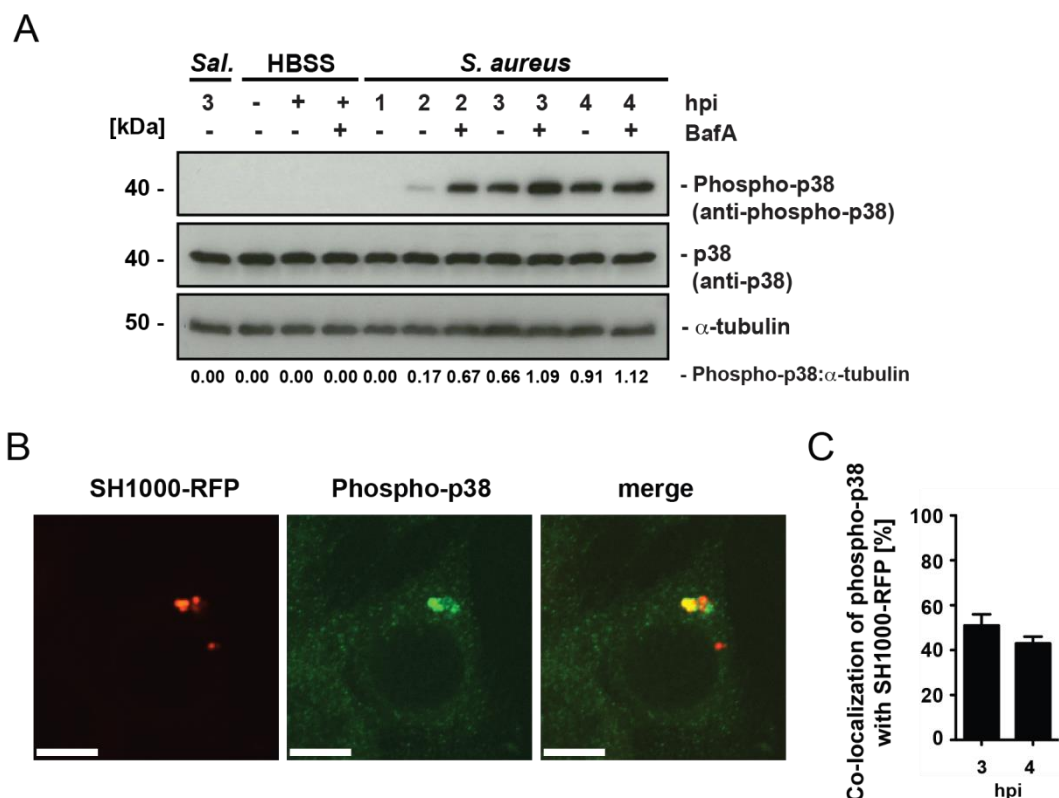
Fig. 5.29: *S. aureus* **infection induced phosphorylation and thereby activation of the MAPK p38 in its close vicinity. (A)** MEFs were infected with the WT *S. aureus* strain SH1000 for the indicated periods and prepared for Western blot analysis. Non-treated cells as well as 3 h-HBSS-treated cells in the presence or absence of BafA (100 nM) and *S.* Typhimurium (*Sal.*)-infected MEFs were included as reference samples. Equal loading was verified by probing the membrane with α-tubulin. Quantification of the signals was performed via ImageJ. **(B)** For the analysis via immunofluorescence, NIH/3T3 cells were infected with the RPF-expressing *S. aureus* strain SH1000-RFP for the indicated periods. After fixation, active p38 was stained by a phospho-p38-specific antibody and images were taken by confocal microscopy. Scale bar: 10 μm. **(C)** Quantification of the experiment shown in (B). The percentage of total intracellular *S. aureus* that co-localized with phospho-p38 is visualized for 50 cells per condition. Data is represented as the mean ±SEM of two independent experiments.

Next, the intracellular localization of the phosphorylated kinase was analyzed by immunofluorescence. After infection of NIH/3T3 WT cells with SH1000-RFP, the samples were prepared for staining with a phospho-p38-specific antibody. Clearly, phospho-p38 accumulated in the vicinity of the bacteria during infection. At 3 hpi the majority of *S. aureus* is associated with active p38, this percentage was slightly lower at 4 hpi (Fig. 5.29B and C).

Subsequently, further immunofluorescence experiments were performed to examine if phospho-p38 and autophagosomal structures co-localize. Indeed, the staining of activated p38 in NIH/3T3-GFP-LC3B cells infected with SH1000-RFP

revealed a high percentage of co-localization between phospho-p38-asscociated *S. aureus* and GFP-LC3B-tagged autophagic membrane structures (Fig. 5.30).
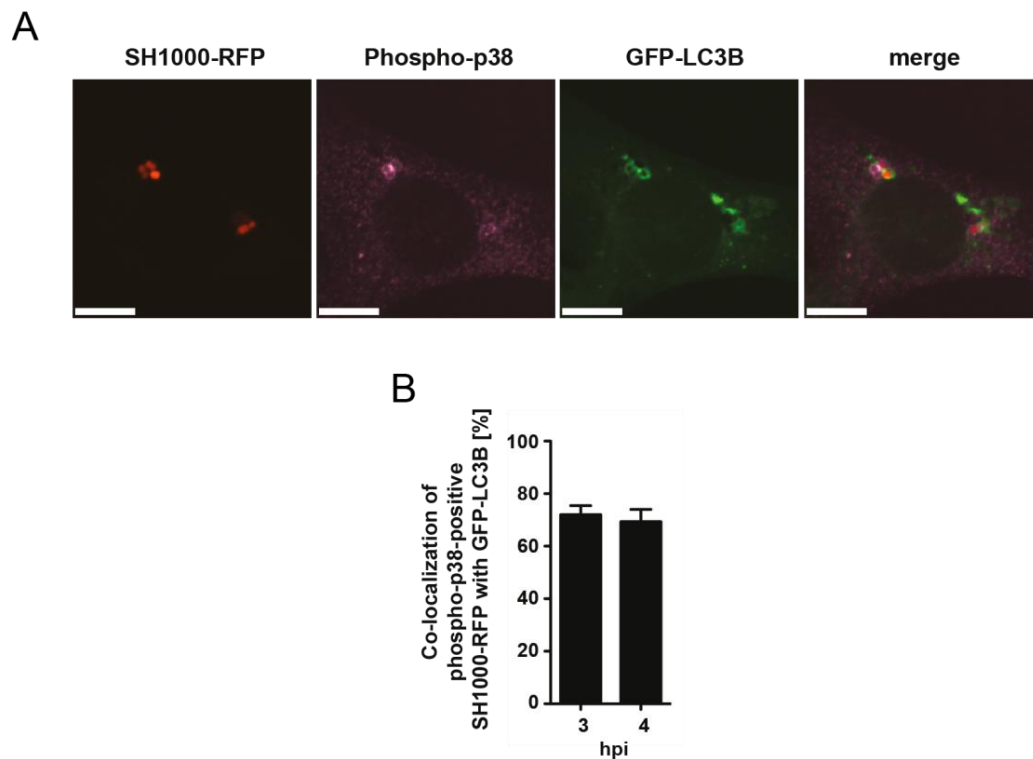
Fig. 5.30: Intracellular *S. aureus* was associated with phospho-p38 and simultaneously co-localized with GFP-LC3B-positive autophagic structures. (A) For immunofluorescence analysis NIH/3T3 cells stably expressing GFP-LC3B were infected with the RPF-expressing *S. aureus* strain SH1000-RFP for the indicated time periods. After fixation, active p38 was stained by a phospho-p38-specific antibody and images were taken by confocal microscopy at a magnification of 60x. Scale bar: 10 μm. **(B)** Quantification of the experiment shown in (A). Visualized is the percentage of phospho-p38-associated *S. aureus* that co-localized with GFP-LC3B. 50 cells were analyzed per condition. Data is represented as the mean ±SEM of three independent experiments.

Similar experiments were performed to investigate the localization of phospho-p38 relatively to ubiquitinylated proteins and to the autophagy receptor p62. In line with previous findings, phospho-p38-associated *S. aureus* co-localized with FK2-stained ubiquitin (Fig. 5.31A and C) and with p62 (Fig. 5.31B and D) at 3 and 4 hpi.
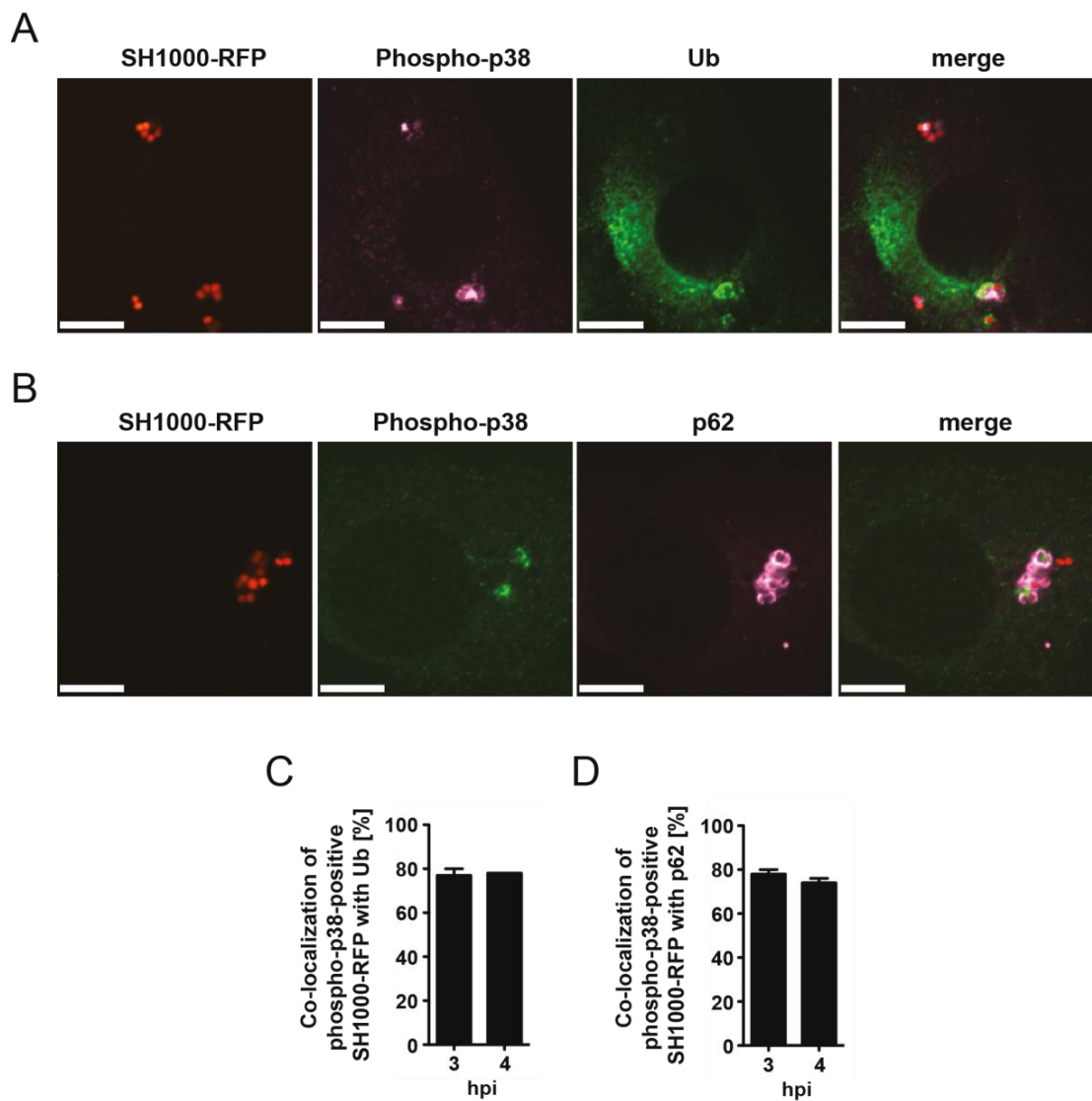
Fig. 5.31: Phospho-p38-positive *S. aureus* co-localized to ubiquitinylated proteins and to the autophagic receptor p62. For immunofluorescence analysis, NIH/3T3 cells stably expressing GFP-LC3B were infected with the RPF-expressing *S. aureus* strain SH1000-RFP for the indicated times. **(A)** After fixation, co-staining of active p38 and ubiquitin (FK2 antibody) was performed and images were taken by confocal microscopy at a magnification of 60x. Scale bar: 10 μm. **(B)** Upon fixation, co-staining of active p38 and p62 was performed, afterwards images were taken by confocal microscopy. Scale bar: 10 μm. **(C)** Quantification of the experiment shown in (A). The percentage of phospho-p38-associated *S. aureus* that co-localized with ubiquitin is shown for 50 cells per condition. Data is represented as the mean ±SEM of two independent experiments. **(D)** Quantification of the experiment shown in (B), visualized is the percentage of phospho-p38-associated *S. aureus* that co-localized with p62. 50 cells were analyzed for each condition. Data is represented as the mean ±SEM of two independent experiments.

5.4.5 p38 is an important mediator for the reduced autophagic degradation of *S. aureus*

One strategy to investigate the influence of phospho-p38 during infection is to analyze *S. aureus* infection in p38 KO MEFs. Therefore, p38 KO and WT cells were infected with SH1000-RFP and stained with CytoID, which is specific for autophagic vacuoles. Notably, the co-localization of *S. aureus* with CytoID-positive vacuoles was clearly enhanced in the p38 KO MEFs compared to their WT counterparts (Fig. 5.32).
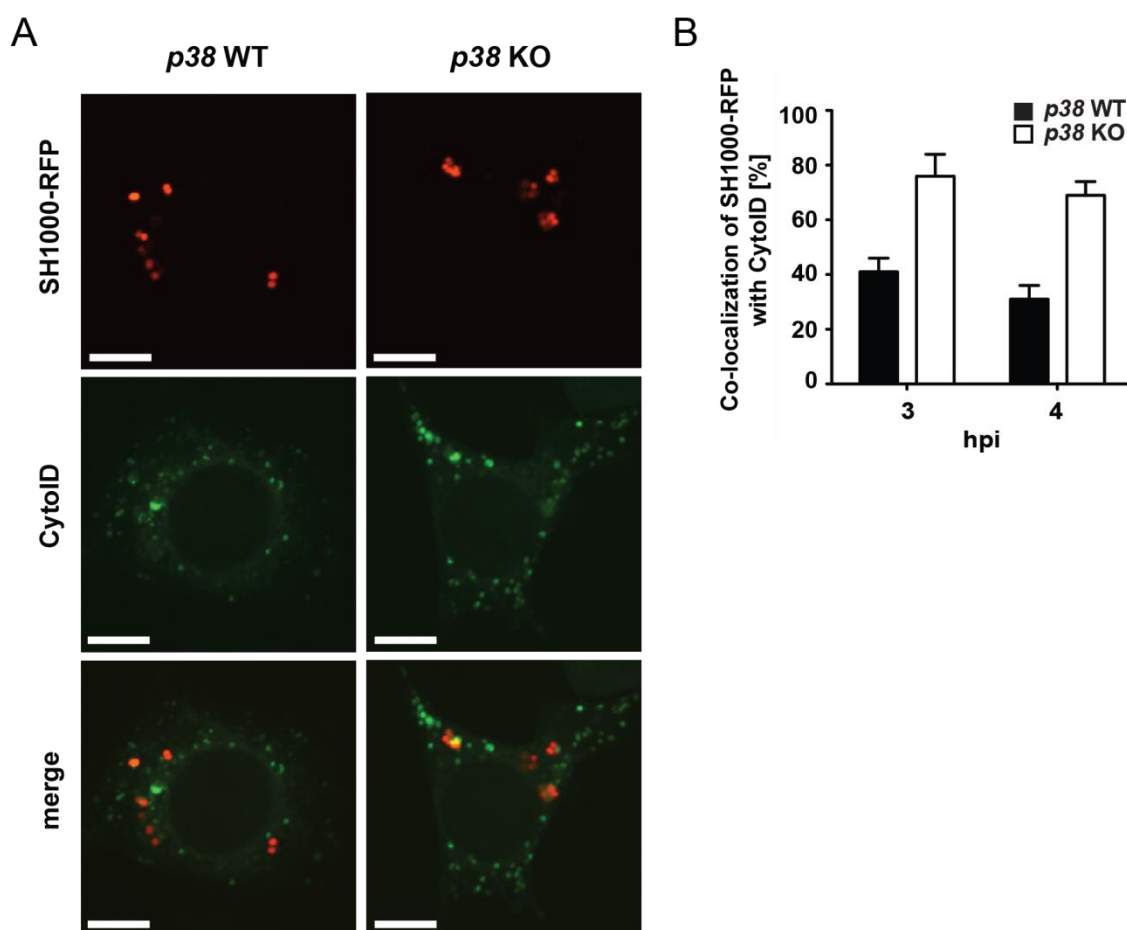
Fig. 5.32: Co-localization of *S. aureus* with CytoID-stained autophagic vacuoles was elevated in p38 KO cells. (A) For immunofluorescence analysis, p38 KO and WT MEFs were infected with the RPF-expressing *S. aureus* strain SH1000-RFP for 3 and 4 hours. Prior to the fixation, staining with CytoID (autophagic vacuoles) was performed. Images were taken by confocal microscopy. Scale bar: 10 μm. **(B)** Quantification of the experiment shown in (A), visualized is the percentage of total *S. aureus* that co-localized with autophagic vacuoles (CytoID) for 50 cells per condition. Data is represented as the mean ±SEM of two independent experiments.

5.4.6 Impact of p38 on the intracellular fate of *S. aureus* is not dependent on ATG5 T75

Since an association between p38 and ATG5, which negatively regulates the autophagic flux, was previously identified in non-infected MEFs, a possible role of this interaction during *S. aureus* infection was analyzed. ATG5 KO MEFs reconstituted either with ATG5 WT or ATG5^{T75A} were infected with SH1000-RFP and stained with LysoTracker Deep Red. From the similar levels of co-localization for *S. aureus* and acidic compartments in both cell lines it can be concluded that the mutation at T75 had only a marginal influence on the phospho-p38-mediated evading strategy of *S. aureus* (Fig. 5.33).
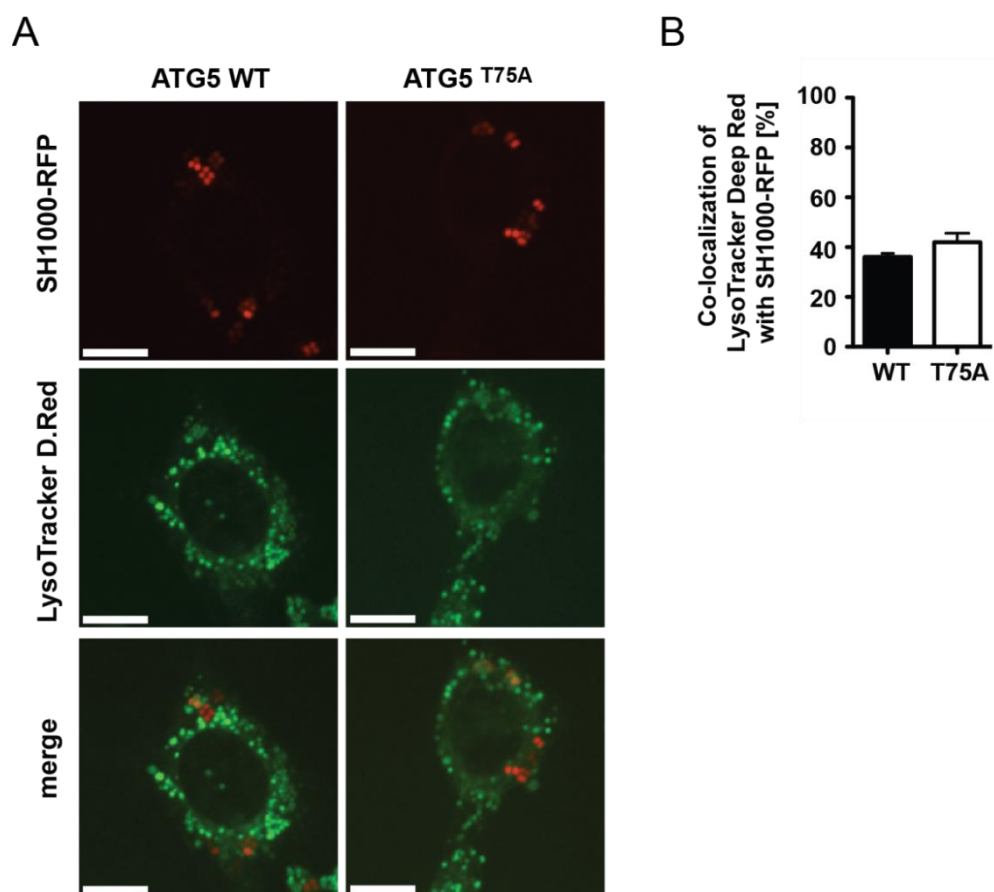
Fig. 5.33: Co-localization of *S. aureus* with LysoTracker Deep Red-stained acidic compartments is similar between ATG5 WT and ATG5^{T75A} MEFs. (A) ATG5 KO MEFs reconstituted with ATG5^{T75A}-c-myc or ATG5 WT-c-myc were infected with the RPF-expressing *S. aureus* strain SH1000-RFP for immunofluorescence analysis. At 4 hpi, prior to the fixation, staining with LysoTracker Deep Red (acidic compartments) was performed. Images were taken by confocal microscopy. Scale bar: 10 μm. **(B)** Quantification of the experiment shown in (A). The percentage of total *S. aureus* that co-localized with acidic compartments (LysoTracker Deep Red) is shown for 50 cells per condition. Data is represented as the mean ±SEM of four independent experiments.

5.5 Evaluation of a high-fat diet on Gadd45β KO compared to WT mice

During the past years of research, it has been demonstrated that autophagy is not only important for energy homeostasis by providing free amino acids, but is also crucial for maintaining lipid metabolism[308]. Interestingly, a number of studies were able to link dysfunctional autophagy, e.g. in adipose tissue[276], liver[256] or heart[309,310] to various metabolic disorders.

In order to further investigate the influence of autophagy specifically on obesity, an experimental setup for a high-fat diet feeding with two different mouse lines was established. The study was performed with Gadd45β KO x GFP-LC3 (KO) mice and GFP-LC3 (WT) mice. The role of Gadd45β as one initiator of the p38-dependent negative regulation during the autophagic flux has previously been shown[133]. The utilized WT and Gadd45β KO mice colonies were separated in control (ctrl)- and high-fat diet (hfd)-fed group with a starting number of six male and six female mice each. The diets were fed for 17 weeks and during this time the weight was monitored weekly. Additionally, blood plasma of the animals was analyzed with respect to typical metabolic parameters such as glucose and triglycerides after 8 to 10 weeks of feeding as well as at the end of the experiment. Due to difficulties in breeding the respective colonies, the feeding of the GFP-LC3 (WT) group started 16 weeks earlier than the Gadd45β KO x GFP-LC3 (Gadd45β KO) group.

5.5.1 Gadd45β KO females are more susceptible to high-fat diet-induced weight gain than WT females

In the WT mouse line, the high-fat diet group successively gained weight during the feeding, however the male animals (dark red) displayed a more strict, fast and stable weight increase than the females (light red). The female high-fat diet group showed a delayed diet-dependent weight increase, starting approximately after 7 weeks of feeding. Additionally, a high weight-fluctuation between individual female animals was noted. The corresponding control diet-fed mice of both sex (light and dark green) gained weight in an expectable way during the experiment (Fig. 5.34A).

In the group of the Gadd45β KO mice both, the control male and female mice showed a similar weight curve progression (light and dark green), which was comparable to the respective WT animals. The male high-fat diet animals (dark red) gained a lot of weight already during the first 3 weeks of feeding, whereas the females (salmon red) started to significantly gain weight after a feeding period of approximately 4 weeks. Surprisingly, the weight of the females hereafter increased strongly until in week 7 where it decreased compared to the previous week. Nevertheless, the further weight gain of the Gadd45β KO females was even more pronounced than the weight gain of the corresponding high-fat diet-fed males (Fig. 5.34B).
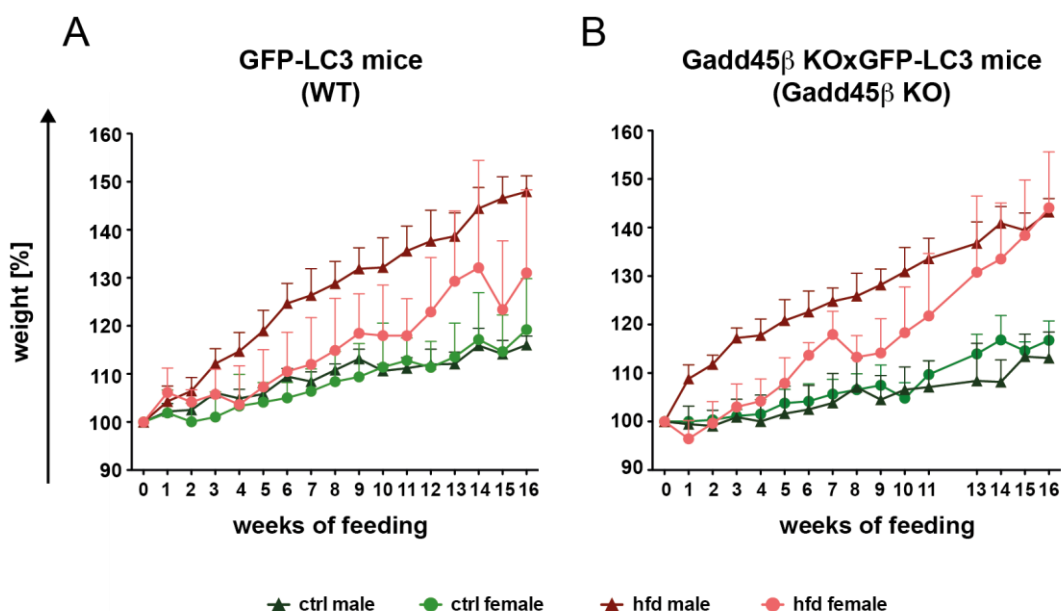
Fig. 5.34: High-fat diet feeding revealed an increased susceptibility of female Gadd45β KO mice in terms of weight gain compared to WT females. (A) Weight monitoring for GFP-LC3 (WT) mice during the high-fat diet experiment. The groups sizes were as follows: ctrl male: n=5; ctrl female n=6; hfd male: n=6; hfd female n=5. **(B)** Weight monitoring for Gadd45β KO x GFP-LC3 (Gadd45β KO) mice during the high-fat diet experiment. The number of mice monitored were as follows: ctrl male: n=3; ctrl female n=6; hfd male: n=4; hfd female n=5. Data is represented as the mean ±SD.

Overall, the WT and Gadd45β KO males had very similar weight curves and finished the feeding with a comparable weight gain according to the respective diet. The weight gain of the WT and Gadd45β KO females after feeding with the control diet was the same compared to their male counterparts. Importantly, whereas the WT females showed a medium weight gain upon high-fat diet, a much steeper weight

curve and a much higher final weight was observed for the Gadd45β KO females. They ended up with a weight gain similar to their male high-fat diet-fed counterparts, which suggests that Gadd45β KO females are much more susceptible to weight gain during a high-fat diet (Fig. 5.34).

5.5.2 High-fat diet-fed Gadd45β KO animals had a minor increase in glucose levels compared to WT mice

Next to weight monitoring, the concentration of glucose, triglycerides, HDL cholesterol and total cholesterol in the plasma of the animals were measured once after 8 to 10 weeks and a second time at the end of the feeding. In terms of glucose, neither after 8 weeks nor after 16 weeks of feeding, any alterations were noticed in the WT mice in response to the diets. In the Gadd45β KO animals, a slight increase in the glucose level was observed for both sexes at the end of the feeding (Fig. 5.35).
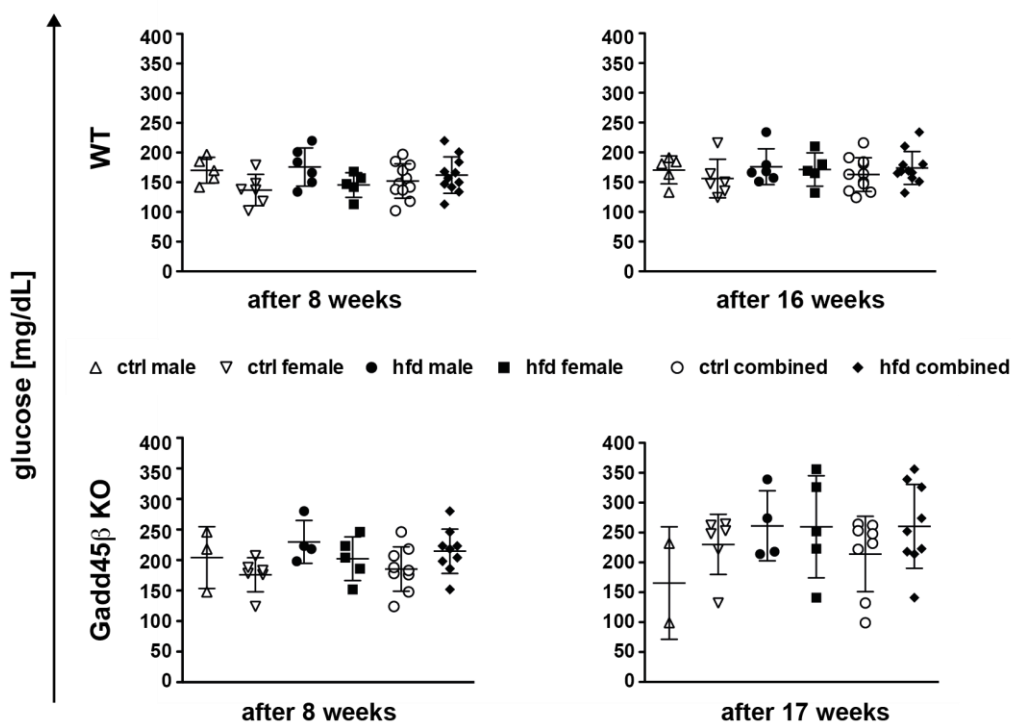
Fig. 5.35: Following high-fat diet feeding, Gadd45β KO animals displayed a slight increase in the glucose level in comparison to WT mice. The measurement was performed in plasma gained from heart perfusion (Gadd45β KO, 17 weeks) or retro-orbital (all others) blood draw. Glucose-specific test stripes and a Reflotron device were used. The group sizes for the WT mice were as follows: ctrl male: n=5; ctrl female n=6; hfd male: n=6; hfd female n=5. The Gadd45β KO mice consisted of the following subgroups: ctrl male: n=3 (17 weeks n=2); ctrl female n=6; hfd male: n=4; hfd female n=5. The combined groups included both sexes. Data is represented as the mean ±SD.

5.5.3 Triglyceride levels were higher in Gadd45β KO mice compared to WT mice following high-fat diet feeding

After 8 weeks of separate feeding no differences in the triglyceride concentration were observed in WT mice. However, after 16 weeks, the individual spreading in the two control groups increased slightly towards a lower triglyceride concentration. In terms of the Gadd45β KO animals, at week 8 both sexes of mice, which received the high-fat diet, showed a large individual distribution towards an increased triglyceride concentration, compared to the low triglyceride level of the control diet-fed mice (Fig. 5.36).
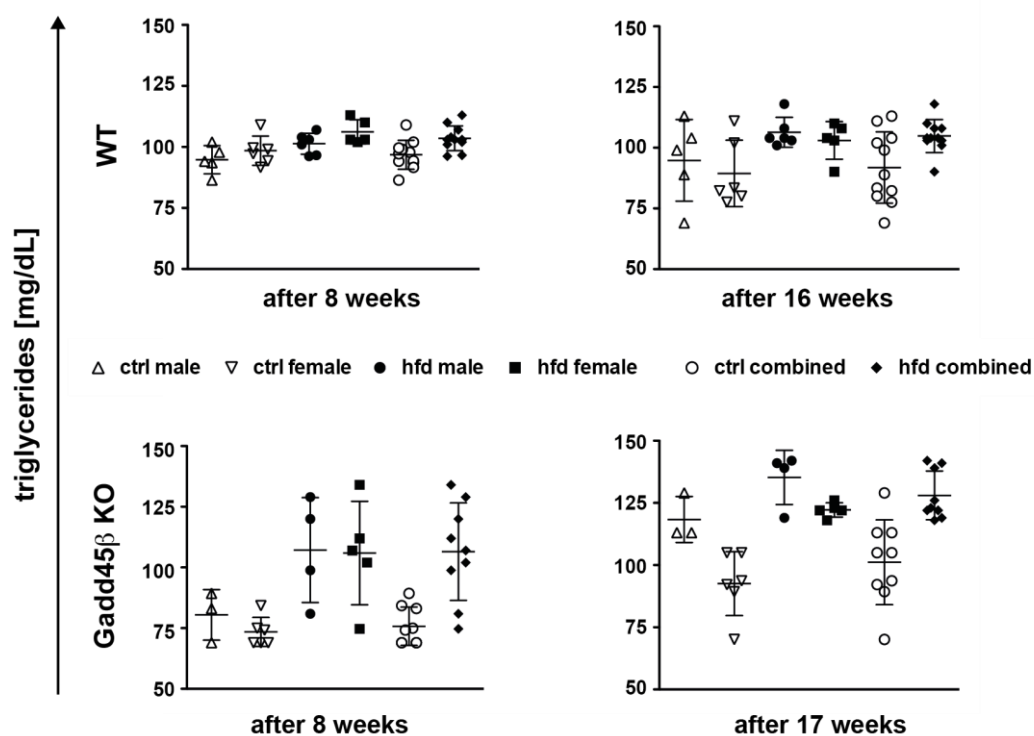
Fig. 5.36: Triglyceride concentration is increased in Gadd45β KO compared to WT mice following high-fat diet feeding. The measurement was performed in plasma collected from heart perfusion (Gadd45β KO, 17 weeks) or retro-orbital (all others) blood draw. For the analysis a Reflotron device together with triglyceride-specific test stripes was used. Due to apparatus restriction, levels below 70 mg/dL were noted as 69 mg/dL. For the analysis the WT mice group sizes were as follows: ctrl male: n=5; ctrl female n=6; hfd male: n=6; hfd female n=5. The Gadd45β KO mice subgroups were represented as follows: ctrl male: n=3; ctrl female n=6; hfd male: n=4; hfd female n=5. Next to the gender specific analysis also the combination of both genders is depicted. Data is represented as the mean ±SD.

The endpoint measurement revealed a rise in the triglyceride concentration in male control animals and a slight increase in the corresponding female group. All high-

fat diet-fed males showed high triglyceride concentrations, also the female mice ended up at high triglyceride levels (Fig. 5.36). Thus, the triglyceride levels were raised comparably more in high-fat diet-fed Gadd45β KO than WT mice.

5.5.4   Male Gadd45β KO and WT animals displayed higher HDL cholesterol concentrations during high-fat diet feeding

A further parameter analyzed was HDL cholesterol. Concerning the WT group, all control diet-fed mice displayed a similar low level throughout both measurements. In the high-fat diet group a gender difference was observed after 10 weeks of feeding (Fig. 5.37).
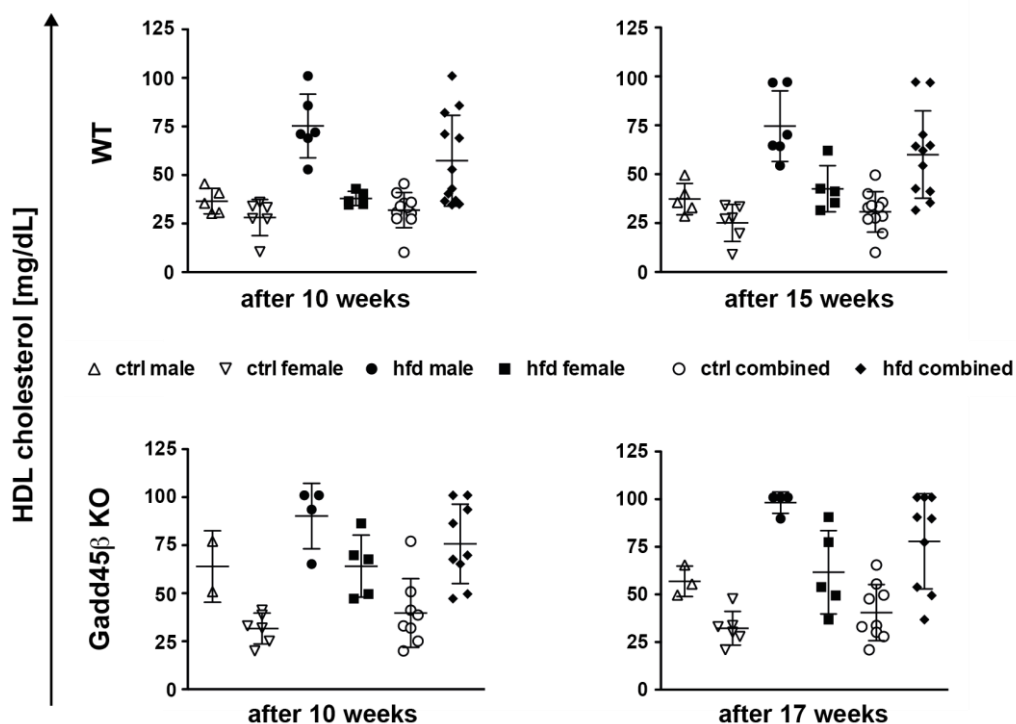
Fig. 5.37: High-fat diet feeding of Gadd45β KO and WT mice induced increased HDL cholesterol levels in both lines in particular for the male animals. The measurement was performed in plasma collected from heart perfusion (Gadd45β KO, 17 weeks) or retro-orbital (all others) blood draw. For the analysis a Reflotron device together with HDL cholesterol-specific test stripes was used. Due to apparatus restriction, levels above 100 mg/dL were noted as 101 mg/dL. The number of WT mice analyzed were as follows: ctrl male: n=5; ctrl female n=6; hfd male: n=6; hfd female n=5. The groups sizes for the Gadd45β KO mice were as follows: ctrl male: n=2 (17 weeks n=3); ctrl female n=6; hfd male: n=4; hfd female n=5. In addition to the gender-specific analysis, also the combination of both sexes was visualized. Data is represented as the mean ±SD.

For the male animals, higher HDL cholesterol concentrations were measured, which remained on a high level until the end of the experiment. The Gadd45β KO mice displayed a similar pattern in the high-fat diet group, already after 10 weeks the males showed more enhanced HDL cholesterol concentrations compared to the females, although the gender difference was smaller than in the WT animals (Fig. 5.37).

5.5.5 Male mice displayed increased total cholesterol levels upon high-fat diet feeding

Finally, the total cholesterol levels were monitored during the high-fat diet experiment. The bottom detection limit of the Reflotron device was problematic. Concentrations below 100 mg/dL were not measurable, which resulted especially for the control diet-fed animals in a manually fixed value of 99 mg/dL (Fig. 5.38).
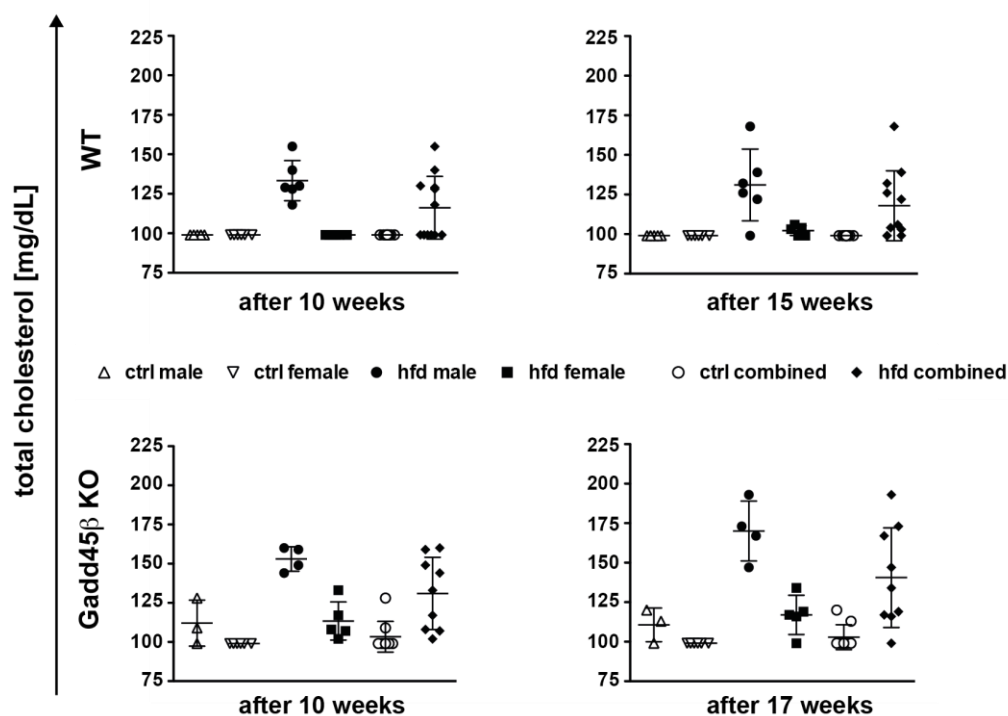
Fig. 5.38: High-fat diet feeding of Gadd45β KO and WT mice induced elevated total cholesterol levels in male animals of both lines. The measurement was performed in plasma collected from heart perfusion (Gadd45β KO, 17 weeks) or retro-orbital (all others) blood draw. Cholesterol-specific test stripes and a Reflotron device were used. Due to apparatus restriction, levels below 100 mg/dL were noted as 99 mg/dL. The number of mice analyzed for the WT genotype were as follows: ctrl male: n=5; ctrl female n=6; hfd male: n=6; hfd female n=5. The Gadd45β KO group was represented by the following mice numbers: ctrl male: n=3; ctrl female n=6; hfd male: n=4; hfd female n=5. The respective combined groups included both sexes. Data is represented as mean ±SD.

Still the data was useful, for example in the WT group a clearly measurable, increased cholesterol concentration was detected for the male animals receiving the high-fat diet. In the Gadd45β KO group, the males displayed higher total cholesterol levels compared to their female counterparts, in particular in the high-fat diet fed groups. However, in comparison to the WT females receiving the high-fat diet, the high-fat diet-fed Gadd45β KO female animals showed enhanced cholesterol levels (Fig. 5.38).

5.5.6 Lymphocyte populations were not altered by the high-fat diet

After the feeding was finished, the mice were sacrificed and a number of additional analyses were performed. In order to check for any immunological differences initiated by the different diets, peripheral lymph nodes (pLN) and the spleen (SP) were isolated from all mice and the cells were stained for lymphocyte populations followed by flow cytometric analysis. The separate feeding did not specifically alter the frequency of T cells (CD3$^+$), B cells (CD19$^+$), helper T cells (CD3$^+$CD4$^+$), cytotoxic T cells (CD3$^+$CD8$^+$) or regulatory T cells (CD3$^+$CD4$^+$CD25$^+$) in either mouse line (Fig. 5.39). The same was true for the CD62L/CD44-stained subsets (naïve cells, memory cells, activated cells) of the helper and the cytotoxic T cell compartment (data not shown). Of note, the frequency of regulatory T cells within the spleen of Gadd45β KO animals was clearly diminished compared to WT mice, but this was observed independent of the feeding and therefore, rather related to the genotype (Fig. 5.39).
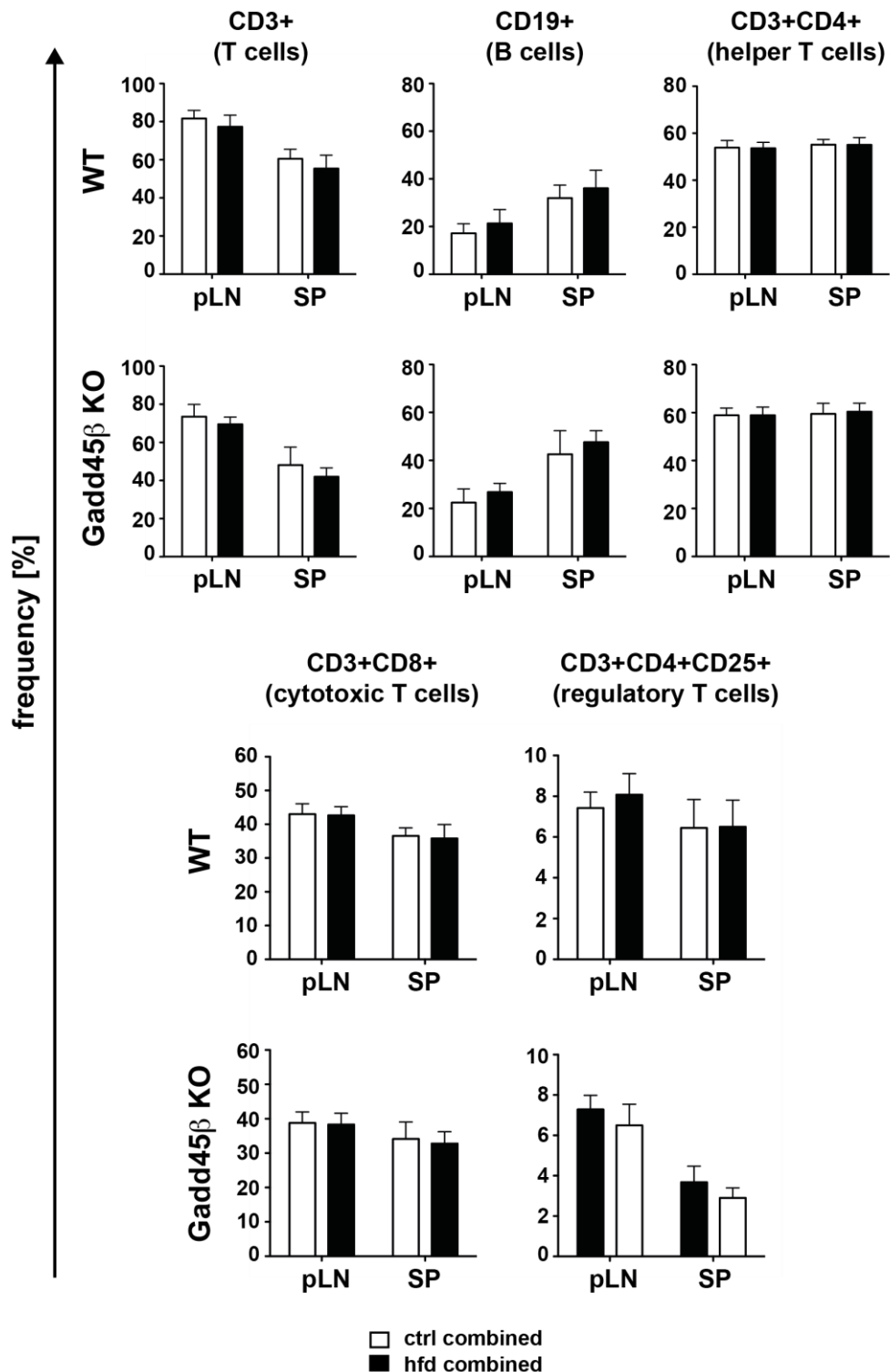
Fig. 5.39: High-fat diet feeding of Gadd45β KO and WT mice did not have an effect on the frequency of lymphocyte populations in peripheral lymph nodes (pLN) or the spleen (SP). Cells were isolated and stained with fluorochrome-conjugated antibodies against the characteristic cell surface markers. Subsequently, cells were analyzed by flow cytometry. Both sexes are combined in this graph. The group sizes for the WT mice were n=11 each for ctrl and hfd. The number of mice analyzed from the Gadd45β KO genotype were n=9 for ctrl and hfd. Data is represented as the mean ±SD.

5.5.7 Histological analysis revealed a fatty diet-induced pathology, especially in the liver of Gadd45β KO females compared to their WT counterparts

Different further tissues were isolated for histological analysis. The liver is the preferred organ to evaluate the influence of high-fat diet induced obesity, as this will result in a clearly detectable fatty liver phenotype[311]. Additionally, the scapular fat pad, which is located on the shoulder, was chosen for analysis. Since it is composed of two different types of adipose tissue; the brown adipose tissue (BAT) and the white adipose tissue (WAT), the influence of the diet with respect to a possible conversion of BAT into a WAT phenotype upon diet-induced obesity can be compared in this fat pad[276,312]. Finally, the gonadal fat pad in the abdominal cavity of the mice was isolated and analyzed, since this is one of the main depots of WAT, especially in male animals[312]. Subsequently, H&E staining of organ and adipose tissue sections were performed and evaluated blindly in cooperation with Dr. Marina Pils, Dr. Ulrike Heise and co-workers from the mousepathology platform (Helmholtz-Centre for Infection Research, Braunschweig). Total histological scores were determined by addition of single scores, which represent tissue-specific criteria, to assess the total pathology of the tissue.

5.5.7.1 The livers of males and Gadd45β KO females displayed a considerable pathology upon high-fat diet feeding

The resulting total histological scores for the livers of the male WT mice revealed a notably enhanced pathology upon the high-fat feeding, whereas the females had a low total score or no visible pathology after the high-fat diet. In fact their score pattern was similar to the control diet-fed group. Both male and female Gadd45β KO animals gained a minor total score during the control diet feeding, which was elevated in the high-fat group of both sexes (Fig. 5.40A). Thus, the liver of the female Gadd45β KO animals was clearly more affected by the fatty diet than their WT counterparts.

This effect is nicely visualized by an increased number of lipid droplets and related structural changes in the representative H&E image of the female Gadd45β KO liver (Fig. 5.40B, VIII). In line with the scores, both male high-fat diet-fed groups displayed a similar pathologic pattern (II and IV). In contrast, the high-fat diet-fed WT females did not show alterations in the tissue structure (VI).

118

LIVER

A

B
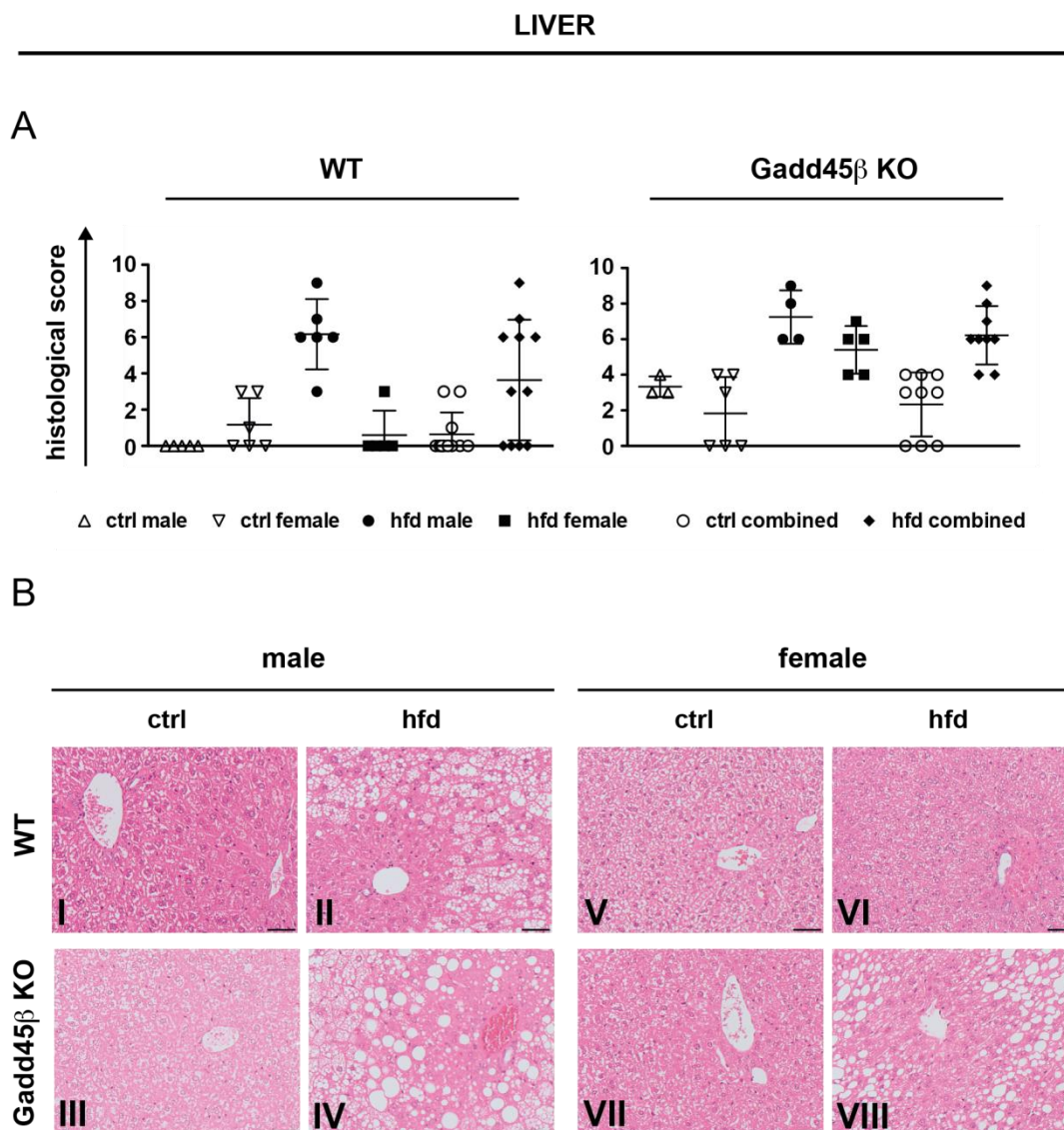
Fig. 5.40: High-fat diet feeding induced a considerable liver pathology in female Gadd45β KO mice but not in WT females. (A) The total histological score of each mouse was determined by addition of single scores. For liver tissue, the overall fatty change, the grade of inflammation and the area involved were evaluated. The number of mice analyzed for the WT genotype were as follows: ctrl male: n=5; ctrl female n=6; hfd male: n=6; hfd female n=5. The Gadd45β KO mice analyzed were grouped as follows: ctrl male: n=3; ctrl female n=6; hfd male: n=4; hfd female n=5. The combined groups included both genders. Data is represented as the mean ±SD. **(B)** Representative H&E images of liver sections. Images were taken at a magnification of 20x. Scale bar: 50 μm.

5.5.7.2   *The scapular fat pad in high-fat diet-fed Gadd45β KO females showed a low-grade pathology compared to no alterations in WT females*

With respect to the scapular fat pad, the WT female control diet group did not show a significant change in the histological score dependent on the diet, whereas the male animals had a pronounced pathology when fed with the fatty diet. In the

119

Gadd45β KO mice, the females showed minor pathologic alterations upon the high-fat diet. For the males, a moderate histological score was observed already when fed with the control diet. After the high-fat diet feeding, the score was further increased in these mice (Fig. 5.41A).
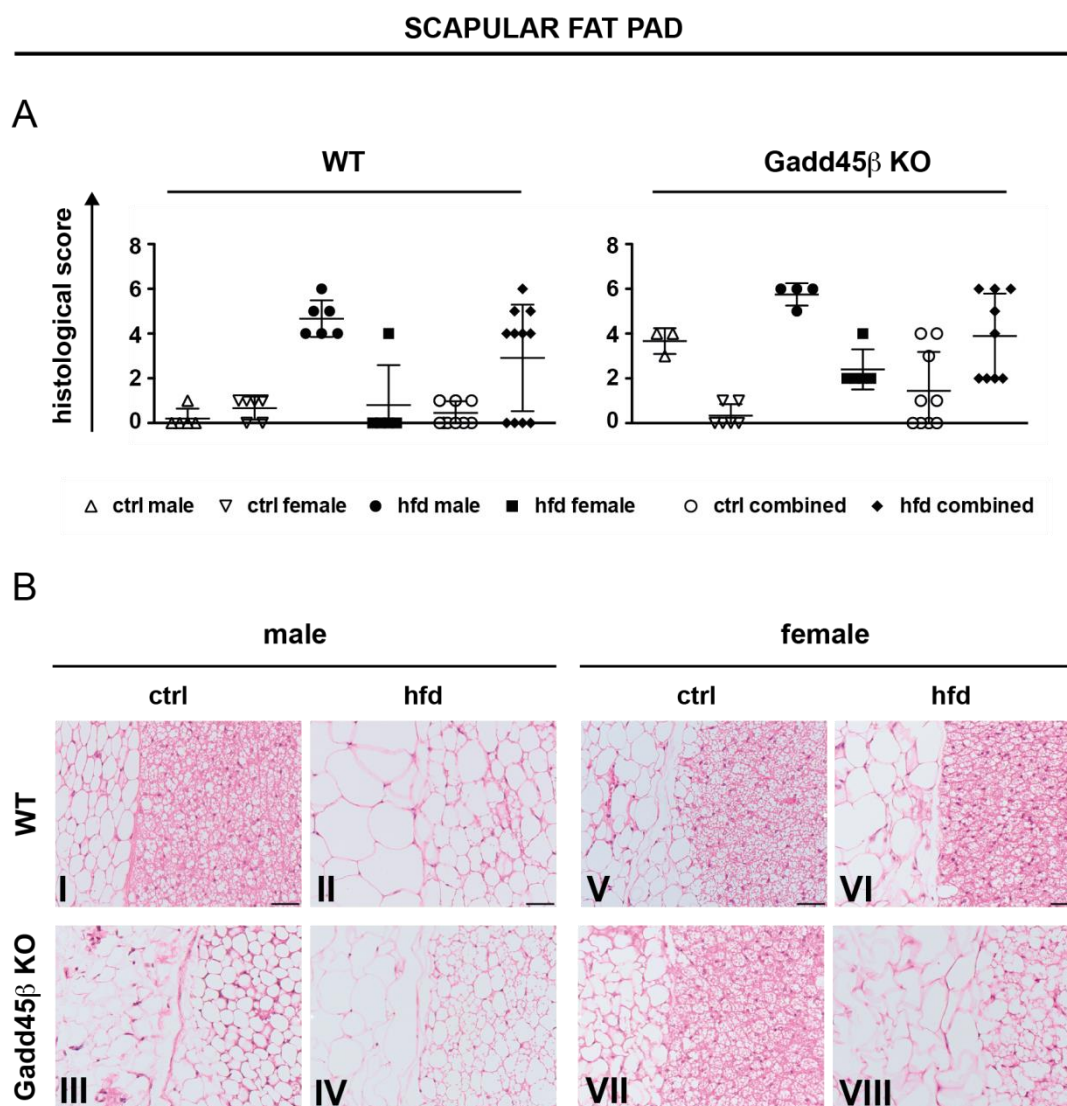
Fig. 5.41: Low-grade pathology in the scapular fat pad was induced by high-fat diet feeding in the female Gadd45β KO, but not in the WT animals. (A) The total histological score of each mouse was determined by addition of single scores. For scapular fat tissue, the sizes of the lipocytes and of the brown fat cells as well as the grade of inflammation were evaluated. The number of WT animals analyzed were as follows: ctrl male: n=5; ctrl female n=6; hfd male: n=6; hfd female n=5. The group sizes for the Gadd45β KO mice were as follows: ctrl male: n=3; ctrl female n=6; hfd male: n=4; hfd female n=5. For comparison also a combination of both sexes is depicted. Data is represented as the mean ±SD. **(B)** Representative H&E images of scapular fat pad sections. Images were taken at a magnification of 20x. Scale bar: 50 μm.

Thus, in line with the previous findings, the Gadd45β KO females receiving the high-fat diet displayed medium histological scores in scapular tissue compared to the unaffected WT females. These findings are visualized by the respective H&E images, where for the WT control diet-fed animals (Fig. 5.41B; I and V) the WAT is shown as big-sized, unilocular structures (left) and the clearly separated BAT is represented by a more dense, multilocular pattern (right). In the males the fatty diet resulted in an increased size of the WAT fat cells and the BAT changed its appearance towards the classical WAT phenotype (II). For the females only a minor increased in WAT adipose cells were detected upon the high-fat diet (VI). In the Gadd45β KO group, the high-fat diet-fed females displayed a significantly altered phenotype, comparable to the males (VIII and IV).

5.5.7.3 *The gonadal fat pad was more enlarged and showed a low-grade pathology in the high-fat diet-fed Gadd45β KO females in contrast to the WT animals*

The histological analysis of the gonadal fat pad revealed a low-grade histological score upon fatty diet in the WT male animals. All other mice display a healthy tissue structure (Fig. 5.42A). In the Gadd45β KO group, a low-grade score was observed for the control fed-mice, which increased slightly in the fatty diet-fed mice. This trend in the Gadd45β KO mice was independent of the sex (Fig. 5.42A). Before the gonadal fat pad was prepared for histological analysis, the weight of the tissue was determined. As expected from the weight curves, male animals from both lines had significantly more gonadal fat, when fed with high-fat diet. Nevertheless the Gadd45β KO male animals accumulated more fat during the control diet feeding compared to the WT counterparts. In the female groups the gonadal fat pads were smaller in the Gadd45β KO females after the control diet but almost as heavy as the pads of the corresponding males after the fatty diet. In contrast, the female WT animals displayed only a minor rise in the weight of the gonadal fat pad (Fig. 5.42B).

GONADAL FAT PAD
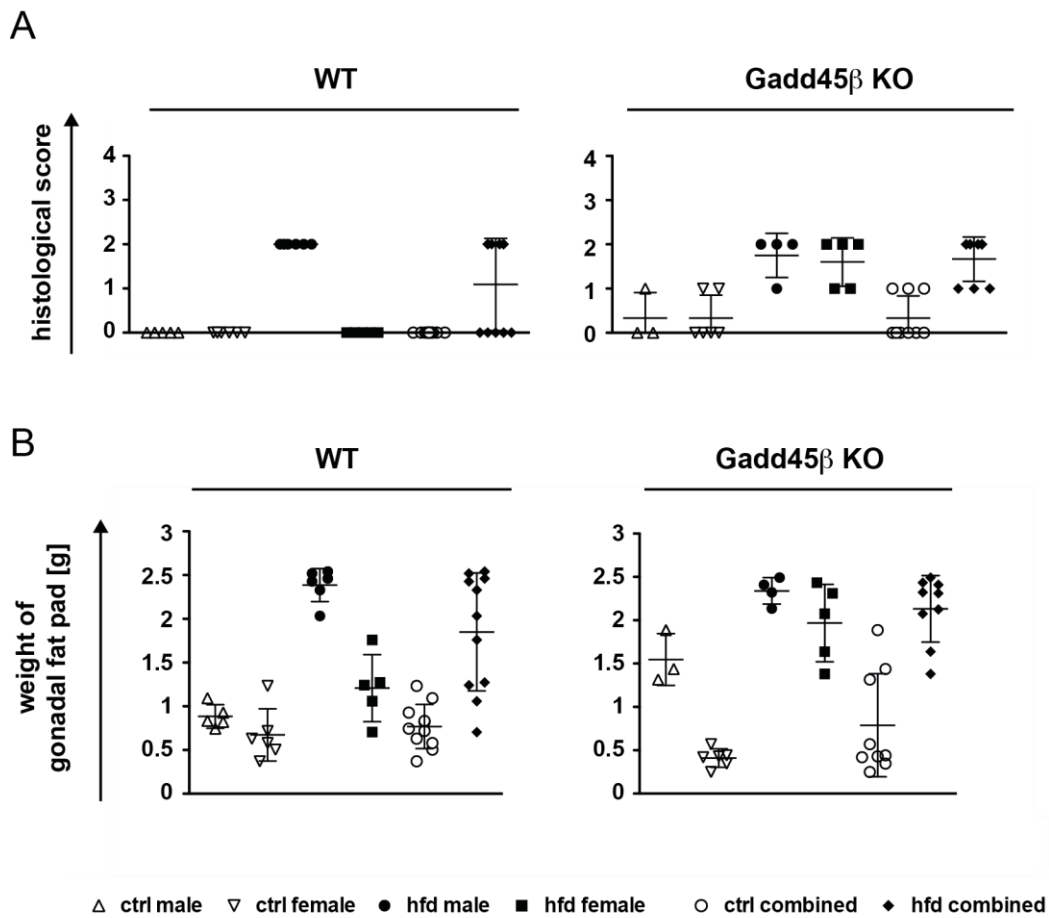
Fig. 5.42: High-fat diet feeding induced an increased size and low-grade pathology of the gonadal fat pad in female Gadd45β KO mice but not in WT females. (A) The total histological sore of each mouse was determined by addition of single scores. For gonadal fat tissue the size of the lipocytes and the grade of inflammation were evaluated. **(B)** Prior to the histological analysis, the weight of fat pads was determined. The number of mice analyzed for the WT genotype were as follows: ctrl male: n=5; ctrl female n=6; hfd male: n=6; hfd female n=5. The group sizes for the Gadd45β KO mice were as follows: ctrl male: n=3; ctrl female n=6; hfd male: n=4; hfd female n=5. The combined groups included both sexes. Data is represented as mean ±SD.

6 Discussion

6.1 Generation of ATG5 WT, ATG5^{T75A} and ATG5^{T75E} transgenic mice via recombinase-mediated cassette exchange

In a previous study, an inhibitory effect of the Gadd45β-p38-ATG5 signaling cascade on the autophagic flux was reported[133]. Since the activation of Gadd45β was mediated by LPS/TLR4 stimulation, the authors concluded that this pathway acts as a negative feedback mechanism, for instance to control autophagy levels after a strong immune-related induction. However, there may be additional, still unknown physiological roles of this signaling cascade. To identify the further functional relevance of the described p38-dependent regulation, a the generation of a transgenic mouse model was started, where the coding sequence of either ATG5 WT or the ATG5 mutants T75A (mimics inhibited regulation by p38) or T75E (mimics constitutive regulation by p38) was introduced in the ROSA26 locus under the control of the EF1α promoter. Unfortunately, the analysis of transgenic littermates revealed, that even though the sequence was successfully integrated (Fig. 5.6A), the mRNA expression in the analyzed spleen and liver tissue displayed a mosaic pattern (Fig. 5.6B). Some animals only show expression in one of the tissues, some animals do not show any transgene expression at all. The EF1α promoter is known to be ubiquitously and reliably expressed, i.e. in various mammalian cell types[313], in the spleen[314], the liver[315] and in hematopoietic cells[316]. In addition, the EF1α promoter activity within the ROSA26 locus was confirmed by a previous study[317]. Most likely, the EF1α-dependent mosaic expression identified during this thesis is due to a beforehand unknown epigenetic silencing mechanism of the promoter within this locus. Notably, experiments performed by our cooperation partners could reveal an efficient silencing of the Tet promoter in the ROSA26 locus. The observed spontaneous promoter methylation resulted in an expression pattern of the transgene, which is similar to the herein described findings for EF1α. Interestingly, this effect was preferably observed after the undirected differentiation of ES cells *in vitro* and after subcutaneous injection of the ES cells in recipient mice *in vivo* (Dr. Natascha Gödecke und Prof. Dr. Dagmar Wirth, Helmholtz-Centre for Infection Research - personal communication - manuscript in preparation).

6.2 Role of ATG5 during p38-mediated regulation of autophagic maturation

The p38-mediated inhibition of the autophagosome-lysosome fusion was demonstrated in a previous study, where an accumulation of autophagosomes was observed in ATG5[T75A]-reconstituted MEFs[133]. However, the molecular mechanism downstream of ATG5 that led to this morphological finding are still not determined.

Since the TECPR1 protein was identified to tether autophagosomes and lysosomes by interacting with the ATG12–5 conjugate[52,97], the hypothesis was that the phosphorylation by p38 induces a structural change, which may alter the interaction to TECPR1. The co-immunoprecipitation experiments performed during this thesis however, did not display a difference in the interaction of ATG5[T75A] or ATG5[T75E] cells to TECPR1 (see Fig. 5.7). Notably, these experiments were performed without any prior stimulation, thus under basal autophagy conditions. Hence, a pronounced induction of the autophagic flux by a stimulus like LPS may result in a reduced functional interaction of the mutants with TECPR1 that is hidden in the current setting. Nevertheless, it seems unlikely that an altered interaction to TECPR1 is the main mechanism responsible for the inhibited autophagosome-lysosome fusion. The interaction of the ATG5 mutants with ATG16L1, which was also addressed in these experiments, was comparable to the WT sample as well. This finding was expected, since an altered association of ATG12–5 with ATG16L1 would rather lead to an incomplete formation of autophagosomes instead of their accumulation[51,318,319].

So far, next to TECPR1 and ATG16L1, no other direct ATG5 interaction partner is known to play a role during autophagy maturation. With regard to the previously published p38-ATG5-dependent regulation[133], this would suggest the existence of a so far unknown binding partner that either itself promotes the fusion process or serves as an adapter for other maturation-mediators. One example of an identified direct regulator of maturation is the SNARE syntaxin17, which has been reported to be specifically recruited to completed autophagosomes, although the exact mechanism has not been elucidated yet[93,98]. For sure, the two transmembrane domains of syntaxin17 are essential and sufficient for the specific localization. Of note, their organization in a closely packed hairpin-like structure is quite unusual for SNAREs and depends on two intrinsic glycine-zipper motifs. Taken together, these structural

characteristics of syntaxin17 result in the cytosolic exposure of the C-terminus[93]. Next to the already exposed N-terminal region, this part is accessible for possible regulating interactions after recruitment. Furthermore, regulation of syntaxin17 and thereby the maturation step is mediated by the initial translocation of the SNARE protein from the cytosol to autophagosomes. Most probably, this depends on the interaction with an autophagsome-residing protein of unknown nature serving as a syntaxin17 receptor[93].

Contrary to syntaxin17, ATG14L as a regulatory Beclin1-interaction partner and part of the PtdIns3K complex is involved in the initiation stage of autophagy[39]. Moreover, ATG14L was also shown to orchestrate endocytic trafficking by interaction with the SNARE-associated protein Snapin[320]. Recently, ATG14L was reported to contribute to autophagososme-lysosome-fusion by forming specific homo-oligomers, which interact with syntaxin17, thereby stabilizing the association of this autophagosomal SNARE with its partner SNAP29[94]. Interestingly, cells reconstituted with ATG14L mutants lacking the ability to homo-oligomerize and consequently the syntaxin17 binding capacity, displayed the same phenotype of accumulated autophagosomes compared to ATG5^{T75A} cells[94]. This finding indicates that the role of ATG14L at mature autophagosomes is distinct from the function during autophagy initiation, which was not impaired. In a kinetic experiment it was shown that ATG14L dissociates from autophagic structures slightly later than ATG5 and ULK1[321]. However, the autophagosomal stage that corresponds to the dissociation of ATG5 appears to be unclear, since an early-on publication reported the dissociation of ATG5 right before or after the closure[57] and a more recent study showed the essential role for autophagosomally-associated ATG5 during the fusion step[97]. In the case of ATG14L, a small portion of the PtdIns3K complex or individual complex members may reside at the autophagosomal membrane during further steps, which would explain the presence of ATG14L at mature autophagosomes. Alternatively, a re-recruitment of ATG14L occurs[94], which would implicate a specific interaction partner mediating this translocation.

In addition to ATG14L, members of the homotypic fusion and protein sorting complex (HOPS) such as Vps33A and Vps16 were recently shown to interact with syntaxin17 in order to promote the maturation step[87]. Similar to syntaxin17, the recruitment of the HOPS proteins occurs at the stage of autophagosomes. However,

depletion of HOPS did not result in a reduced translocation of syntaxin17, thus this complex does not function as a recruiting receptor, but rather recognizes an accumulation of phospholipids in the presence of syntaxin17[87]. Another group of proteins that is also important during endocytic trafficking, and actually can be regulated by HOPS acting as guanosine exchange factor (GEF) or guanosine activating protein (GAP)[322] is the family of Rab proteins. Rab7, one particular member of these small guanosine triphosphate (GTP)-ases, is associated with the membrane of autophagosomes after starvation[84,85]. Interestingly, (over-)expression of a Rab7 GDP-mutant form or the usage of Rab7 RNA interference (RNAi) resulted in the accumulation of autophagosomes caused by an impaired fusion with lysosomes. Considering its role during endocytosis, it was therefore proposed that Rab7 is important for the recruitment and organization of various factors mediating trafficking of the autophagosome towards the lysosome[86] and the fusion of their membranes. Recently, a study in fat cells of Drosophila revealed the importance of the caffeine, calcium and zinc 1(Ccz1)-monensin sensitive protein 1(Mon1)-Rab7 module for autophagosome maturation, where the heterodimer Ccz1-Mon1 acts as GEF for Rab7. Most likely, the recruitment of Ccz1-Mon1 is mediated by the high abundance of PtdIns(3)P on the autophagosomal membrane, since the translocation was demonstrated to occur independently of HOPS or syntaxin17 in this study. In their proposed model, Ccz1-Mon1 first attracts Rab7, which in turn interacts with the HOPS complex, and afterwards initiates the downstream molecular steps, which are necessary for fusion[323].

6.3 Analysis of the ATG5-p38 interaction

In general, phosphorylation is the major posttranslational mechanism involved in autophagy regulation. A number of autophagy proteins harbor phospho-acceptor sites in order to fine-tune their activity. For instance, Beclin1 was identified as an Akt-phosphorylation target, resulting in the inhibition of autophagy and the Akt-dependent promotion of tumorigenesis[324]. A similar role was described for the epidermal growth factor receptor (EGFR)-mediated phosphorylation of Beclin1[325]. Most of the direct regulatory phosphorylation steps involving key autophagy proteins, are important during the initiation steps of autophagy. However, one study performed

126

in neurons demonstrated that the phosphorylation of LC3 by the protein kinase A (PKA) at serine 12 leads to reduced recruitment of LC3 to autophagosomes[326]. In addition, the previously discovered[133] and herein further described p38-mediated phosphorylation of the ATG12–5 complex is an additional example of a phospho-dependent regulation in the axis of the ubiquitin-like conjugation systems.

The interaction between the autophagy protein ATG5 and the stress MAPK p38 was identified within cells for the first time in this thesis (Fig. 5.8). Functionally, the binding enables p38-mediated phosphorylation and thereby marks a crucial step during the regulating signaling cascade that leads to inhibition of autophagosome-lysosome fusion. Specific interaction of a MAPK and its substrate is typically mediated by an interplay of the kinase docking groove with characteristic amino acid stretches on the surface of the substrate, named the docking site[159]. The central motif defining the region of interest in the ATG5 sequence was T[75]P, which was previously assumed to be the phospho-acceptor site[133]. However, a MS-based approach performed in the context of a cooperation did not confirm this model (Tab. 5.1), which pointed to a different role of threonine 75 in the p38-ATG5 interaction. Interestingly, in this thesis co-immunoprecipitation experiments with the mutants ATG5[T75A] and ATG5[T75E] that were previously shown to mimic the condition of a restrained p38-dependent regulation (T75A) or a permanent regulation (T75E)[133], displayed a reduced interaction with p38 for the T75A mutant compared to the ATG5 WT. Notably, these results demonstrated that the nature of the exchanged residues during mutagenesis experiments is crucial here, since the T75E mutant did not show a clear alteration in the interaction with p38. Of note, the structures of ATG5[T75A] and ATG5[T75E], which were generated and analyzed by a cooperation partner (Dr. Stefan Leupold and Dr. Andrea Scrima, Helmholtz-Centre for Infection Research, Braunschweig – data not shown) itself however only displayed very little variation in the 3D structure compared to the ATG5 WT. Nevertheless, T75 seems to be important for the proper interaction with the p38 kinase within the cellular environment.

Typical docking domains of p38 substrates are composed of basic stretches that are often led or followed by hydrophobic amino acids (Tab. 2.2). Hence, potential crucial motifs that correspond to this known linear pattern are located near the T75 (3D structure) and are exposed to the surface were identified (Fig. 5.9, Fig. 5.10 and

127

Fig. 5.13). These were mutated and their binding capacity to p38 was investigated. Choosing the kind of mutational amino acid-exchange is generally guided by two major conditions: the need to disturb the interaction with the partner protein clearly enough to detect a difference, but at the same time not to influence the structural integrity of the protein. Most likely, amino acid residues that are oriented towards the surface, which is essential for mediating docking interactions, are less involved in the central architecture of the protein at least if this is a monomer. Nevertheless, surface residues contribute to the solubility of the protein which can be impaired by mutational changes especially *in vitro* due to the lack of potentially stabilizing factors that are present within a cell. The interactions of the chosen mutants ATG5^{L90S} and ATG5^{L90Q} as well as ATG5$^{K78E/H80D}$ with the kinase were diminished in transfected HEK293T cells, whereas for example the mutations K51E/K53E and K58E/R61S did not result in an altered interaction (see Fig. 5.11 and Fig. 5.14). These data suggest a p38-docking region on ATG5, which most likely includes T75, K78, H80 and L90. Containing at least one lysine or one leucine, this site shows partial similarities to the classical sites described in other p38-substrates. Further structural analyses are needed to compare the binding mode of ATG5 to the well-studied model of MAPKAPK2, which revealed allosteric enhancement of the kinase activity by the docking interaction[147]. Additionally, the contribution of other residues to the docking should be elucidated in future experiments.

Functional consequences of the reduced interaction properties of the mutated forms ATG5^{T75A}, ATG^{L90S}, ATG5^{L90Q} and ATG5^{E73K} were investigated in retro-virally reconstituted ATG5 KO MEFs. Of note, the mutant ATG5$^{K78E/H80D}$ was not considered further, since the initially observed problems with a proper expression of the mutant (Fig. 5.10) were even more evident during the production of recombinant protein performed by a cooperation partner (Dr. Caroline Behrens – personal communication). After the induction of autophagy by starvation and the treatment with the inhibitor BafA, the readout was performed by Western blot (LC3A/B-II level) and FACS (mCitrine-hLC3B level) analyses of the reconstituted cell lines. Despite the reduced interaction patterns observed in the co-immunoprecipitation experiments (Fig. 5.12 and Fig. 5.14), significant alterations in the autophagic flux were not observed. However, the Western blot data displayed high variations in the measured LC3A/B-II level of the ATG5^{L90Q} and the ATG5^{E73K} MEFs under induced (HBSS vs. HBSS

together with BafA) and basal (DMEM vs. DMEM together with BafA) autophagy conditions (see Fig. 5.16). In some of the repetition experiments, a comparably increased LC3-II-accumulation was detected by the use of the inhibitor BafA, which would serve as an indicator for an increased, less regulated autophagic flux and correspond to the co-immunoprecipitation data[133,327]. Surprisingly, in the case of the T75A-mutant, the previously reported pronounced induction of autophagy during starvation[133] was not visible in the Western blot experiments with the new retro-virally reconstituted cell lines. Notably, the cell lines used in the cited study were generated by plasmid transfection and subsequent selection of transfected cells via treatment with geneticin (G418). Typically, stable transfection results in a comparably variable number of randomly integrated copies per cell, which largely influences the expression of the protein of interest. Retro-viral transduction is characterized by a more restricted number of integrations, since a single cell is only infected by one to a few viral particles. A general problem during reconstitution by both methods, transfection and transduction, is the fact, that the loci of integration are not pre-determined. Thus, the expression of the protein of interest may vary due to its genomic localization between different transductions as well as between different transfections. Overall, the results obtained in this thesis would favor a direct modification of the genomic ATG5 sequence in the future, for instance by advanced techniques like CRISPR-Cas9[328]. Thereby the expression of the protein of interest would be within its natural locus and under the control of the native promoter.

In the FACS analysis of the mCitrine-hLC3B expressing cell lines, no obvious differences between the reconstituted WT and the reconstituted mutant cells were observed in terms of the total LC3-level during basal or stimulation-induced autophagy (Fig. 5.18). Notably, compared to the non-reconstituted reference cells, the ATG5 WT reconstituted cells showed a clearly weaker response upon the HBSS and BafA treatment. The alterations observed in Western blot analysis between reference and reconstituted WT cells were even more pronounced using the total mCitrine-hLC3B-level as a read-out. In addition, however the cells were sorted for a preferably comparable initial mCitrine-hLC3B-expression pattern, differences between the cell lines remained (see Fig. 5.17A). In general after a transfection or transduction procedure, the LC3-I form was reported to be comparably abundant which may lead to a high background signal. A method that would allow to distinguish between LC3-I and

LC3-II in a FACS-based approach is the permeabilization of the cells with saponin prior to the analysis[329]. Via the resulting small pores in the membrane, the cytosolic LC3-I will be rinsed-out, whereas the LC3-II is "captured" in the perforated cells due to its integration in the autophagosomal membrane. The most elegant experiment would probably be a combination of the saponin treatment with an intracellular staining for the endogenous LC3 to circumvent transfection or transduction artefacts[329]. For now, the reduced interaction between p38 and the ATG5 mutants T75A, L90S and L90Q could not be pin-pointed to distinct functional alterations during classical induced autophagy. Perhaps, the specific stimulation of the Gadd45β-p38 pathway by the co-transfection of Gadd45β and MEKK4 or by LPS stimulation is needed to augment the effect. Furthermore, in future mutagenesis experiments the single mutations should be combined to obtain an almost completely lost interaction with p38.

Concerning the phosphorylation site that is targeted by p38, *in vitro* kinase assays were performed during this thesis including not only free ATG5 but also the functional ATG12–5 conjugate as a substrate. By the usage of phospho-threonine antibodies, the conjugate was demonstrated to be phosphorylated by p38 and not ATG5 alone (see Fig. 5.20). This finding was in line with the MS data, revealing that T75 is not the phosphorylation target of p38 and suggests a model, in which ATG5 serves as docking platform for p38, thereby facilitating the phosphorylation of the conjugated ATG12.

Since the sequence of ATG12 harbors five canonical MAPK-phosphorylation motifs (S/TP) (see Fig. 5.19), further experiments were performed to identify the phospho-acceptor site(s) for p38. A structurally outstanding attribute of ATG12 is the flexible N-terminal stretch (amino acids 1-52), which seems to be easily accessible and harbors three of the classical phosphorylation motifs. Hence, during a preliminary MS approach, a specific peptide including the amino acids 24 to 49 of ATG12 was analyzed after performing an *in vitro* kinase assay with ATG12–5 and p38. Surprisingly, the therein detected phosphorylation was located at serine 36 or 37, thus at a non-canonical motif. Notably, about 85% of the so far known p38α substrates are phosphorylated at S/TP motifs[136]. However, examples for substrates with a phosphorylated serine that is not followed by a proline are the cell cycle phosphatase Cdc25A (motif: S76S)[330], the downstream kinase Mnk2 (S74F)[331] as well as the transcription factor and cellular tumor antigen p53 (S15Q)[332]. One part of the MS

sample was analyzed by Western blot in parallel and displayed a signal after probing with an antibody generated against phospho-threonine-proline (Fig. 5.22), which also was reported to recognize phospho-serine-proline motifs. Thus, this antibody might exert cross-reactivities towards other phosphorylated amino acid motifs. Therefore, the preliminary results concerning the phospho-acceptor site need to be interpreted carefully and require further confirmation. Nevertheless, the rather unusual putative phospho-acceptor site in combination with a usage of the ATG12-conjugation partner ATG5 as docking adaptor seems to be a highly specific regulation mechanism. In future experiments the exact interaction mode between p38 and ATG12–5 needs to be elucidated.

6.4 p38-mediated regulation of autophagy during *S. aureus* infection

Xenophagy is one form of selective autophagy that specifically targets invading pathogens. Whereas some types of bacteria such as *S*. Typhimurium[193,213,215,333] have already been intensively studied in the context of autophagy, only a few studies dealing with the role of autophagy during *S. aureus* infection were published so far. Schnaith *et al.* reported increased proliferation of *S. aureus* within autophagosomal compartments of infected HeLa cells[283]. For this, *S. aureus* prevents the degradation of bacteria-containing autophagosomes most likely by inhibition of autophagosome-lysosome fusion. The authors suggest that a bacterial factor that depends on the virulence regulator system *agr* (accessory gene regulator) is able to control the autophagic response, since bacteria that lack *agr* were unable to initiate autophagy. As a result of the high replication in autophagosomes, Schnaith *et al.* observed that *S. aureus* evades from these vacuoles, which subsequently leads to host cell death. Taken together, this study demonstrated that the bacterium utilizes the autophagic defense mechanism of the host for its own benefit. To further elucidate the molecular mechanisms that are responsible for *S. aureus*-induced autophagy, Mestre *et al.* investigated the role of α-hemolysin (Hla), a pore-forming cytotoxin that is secreted under the control of the *agr* system during *S. aureus* infection[282]. Mestre and co-workers reported an induction of autophagy upon Hla-treatment of CHO cells, whereas infection with a *S. aureus* strain deficient for Hla did not lead to an autophagic

response. Additionally, secreted Hla inhibits the maturation of bacterial-containing autophagic vacuoles, thus, enables intracellular survival of *S. aureus*. In line with a previous report, where α-toxin was identified as a crucial factor for the phagosomal escape of internalized *S. aureus* in CFT-1 cells[334], Hla-proficient bacteria are more frequently found in the cytoplasm. However, similar to Schnaith and colleagues, Mestre *et al*. observed ongoing replication already within autophagosomes. Importantly, the Hla-induced autophagic response upon *S. aureus* infection relied on ATG5 and included LC3 recruitment but was independent of the canonical autophagy initiators Beclin1 and PtdIns3K[282].

In this thesis, the autophagic response upon *S. aureus* infection was investigated in fibroblast cells. Hence, the cells used were non-professional phagocytes, similar to the studies described above. Of particular interest was the further elucidation of the intracellular bacterial fate and the host factors involved. In line with previous reports[282,283], infected WT MEF cells displayed induced levels of LC3A/B-II, visible by Western blot. In addition, the increased formation of LC3-positive vacuoles that partly surround *S. aureus* were identified in immunofluorescence analysis of NIH/3T3 WT cells stably expressing GFP-LC3 (Fig. 5.23).

In the past years, a non-conventional formation of LC3-decorated vacuoles, which originally was discovered during TLR-signaling in macrophages[299], was investigated and named as LC3-associated phagocytosis (LAP). LAP requires some of the key autophagic players such as ATG5, ATG7, Rubicon and Beclin1, whereas others like ULK1 are dispensable[299,335]. Another difference to the canonical formation of autophagosomes is the architecture of the encapsulating membrane, since it is only single-layered during LAP. Internalized dead cells and microbes like *Saccharomyces cerevisiae* were shown to be targeted by LAP in order to promote their clearance[299,336]. However, for *L. monocytogenes* the association of the bacteria-containing vacuole with LC3 was shown to result in the formation of a replication niche, the spacious *Listeria*-containing phagosome (SLAP)[337]. This pathway is distinct from the recognition of *ActA*-deficient, cytosolic *L. monocytogenes*, which includes ubiquinylation, translocation of autophagy receptors like p62 and subsequent recruitment of the canonical autophagic machinery[218]. LAP and classical xenophagy can be distinguished by investigating the membrane structure of the bacteria-containing vacuole. The here

performed transmission electron microscopy analysis revealed a clear double-layered character of the *S. aureus*-engulfing structure in NIH/3T3 cells (see Fig. 5.24).

As mentioned above, selective autophagy of pathogens typically is initiated by the action of ubiquitinases. The ub-tagged cargo is recognized by autophagy receptors that additionally harbor a LC3-II binding domain, which facilitates the engulfment of the cargo in a forming autophagosome[77,204,211–213]. Hence, the involvement of these key proteins in xenophagy was analyzed by immunofluorescence and Western blot during infection with *S. aureus*. Indeed, next to GFP-LC3, the frequent co-localization of *S. aureus* with ubiquitin and the autophagy receptors p62 as well as optineurin was shown (see Fig. 5.25 and Fig. 5.26). The previous reports dealing with *S. aureus*-induced autophagy displayed the pathogen-mediated inhibition of autophagosomal maturation to prevent its own degradation[282,283]. In line with these results obtained in HeLa and CHO cells, also *S. aureus*-infected NIH/3T3 cells showed a disturbed autophagic flux represented by only a small portion of GFP-LC3-engulfed bacteria that co-localize with acidic compartments (see Fig. 5.27). This was further supported by the accumulation of p62 at the peak of infection (see Fig. 5.28), which results from an impaired autophagic degradation.

Different types of invading bacteria were reported to delay or inhibit autophagosome-lysosome fusion for their own survival such as *Coxiella brunetti*[338], *Brucella abortus*[339] and *Legionella pneumophila*[340]. *Coxiella brunetti*, e.g. utilizes the manipulated autophagosome directly as a replicative niche. The molecular mechanisms underlying this specific modulation of the autophagic flux are still largely unknown. Next to the interplay with autophagosomal maturation, also other regulatory strategies that circumvent the degradation or the targeting of bacteria by the autophagic machinery were identified. One example is the globally widespread, clinical-isolated clone M1T1 of Group A *Streptococcus* (GAS). In contrast to the serotype M6, this specific strain of GAS is not efficiently cleared by selective autophagy. Instead, it can evade into the cytoplasm, where high bacterial proliferation is favored. This finding was functionally connected to the expression of the bacterial cysteine protease SpeB, which degrades the autophagy receptors p62, NDP52 and NBR1[341]. Moreover, the well characterized autophagy target *S.* Typhimurium also has developed a mechanism to reduce the autophagic flux in order to promote bacterial

replication within in the host cell. Hence, the deubiquitinase SseL, which is activated by the virulence factor system *Salmonella* pathogenicity island-2 (SPI-2) encoded type III secretion systems (T3SS) (SPI2 T3SS), degrades host-derived ubiquitin-structures that associate with the SCV after the secretion of virulence factors. Thus, this mechanism counteracts the initial host-response upon *S.* Typhimurium infection by impairing the recruitment of autophagic receptors[342]. In addition, *L. pneumophila* was shown to interfere with the LC3-conjugation system by the Dot/Icm apparatus-dependent virulence effector RavZ. This cysteine protease cleaves autophagosomal LC3-II as well as LC3-II that undergoes recycling. Notably, the resulting cytosolic form of LC3 is unable to be re-conjugated, which results in an effective inhibitory mechanism[306].

Interestingly, in the case of *S. aureus* infection, specific activation and translocation of the host MAP kinase p38 was observed in infected NIH/3T3 cells (Fig. 5.29). Further immunofluorescence staining experiments revealed a high frequency of phospho-p38-associated *S. aureus* co-localizing with GFP-LC3, ubiquitin or p62 (Fig. 5.30 and Fig. 5.31). Strikingly, infection of p38-deficient cells with *S. aureus* resulted in a higher percentage of *S. aureus* that co-localized with autophagic vacuoles (Fig. 5.32). Thus, the recruitment and activation of p38 has a protective role for the targeted *S. aureus*. This host kinase inhibits the autophagic flux and prevents autophagic degradation of the bacteria by an unknown mechanism.

Activation of p38 during *S. aureus* infection was only rarely reported beforehand. Investigations towards the intracellular signaling in human macrophages during *S. aureus* infection by Miller and colleagues revealed an activation of p38 already 1 h post infection[343]. Moreover, p38 activity was shown to be important for the cellular response towards the pore-forming α-toxin of *S. aureus*. In contrast to the role during streptolysin secretion, phosphorylated p38 was shown to mediate the recovery of the host cell after α-toxin-dependent pore formation[344]. However, the specific translocation to autophagosomes associated with *S. aureus* reveals a new bacteria-determined and bacteria-beneficial role for this kinase.

p38-mediated inhibition of the autophagosome-lysosome fusion was already reported in the context of an interaction with the autophagy protein ATG5[133]. Hence, ATG5[T75A] mutant cells, which represent a reduced targeting of p38, were infected with

S. aureus. However, the mutation of T75 did not alter the intracellular co-localization of *S. aureus* with acidic compartments (Fig. 5.33). For sure, these findings implicate the need for further experiments, for instance to elucidate the molecular steps leading to the specific activation and translocation of p38. Additionally, the downstream mediators of the impaired autophagic flux during *S. aureus* infection are still unknown. Moreover, factors involved in the bacterial recognition and ubiquitinylation of *S. aureus* are still not identified.

6.5 Evaluation of a high-fat diet on Gadd45β KO compared to WT mice

Next to the investigation of genetic mouse models, high-fat diet feeding of mice is a well-established method to study metabolic disorders, such as obesity and associated diseases[345]. However, a high variation compared to other published data may arise during such experiments, for instance from different susceptibilities of the mouse strains used, the age of the mice, the duration of the feeding and the composition of the food. In particular, mice with C57BL/6J background were shown to appropriately model the associated metabolic changes and for this, are preferably used for diet-induced obesity experiments, whereas other mouse strains are rather diet-resistant[345,346]. Moreover, the feeding of a corresponding control diet instead of the usual chow diet is a critical factor to ensure a proper comparison with the reference group[347,348]. In the experiment performed in this thesis, the effects of diet-induced obesity in Gadd45β KO and WT mice were evaluated in males and females. Next to weight gain, also blood parameters like glucose, triglycerides, HDL cholesterol and total cholesterol were analyzed to measure the respective metabolic response. Resting blood glucose levels were previously shown to increase upon high-fat diet[345,349]. For the concentration of triglycerides a decrease or no change was reported in mice[350,351]. The levels of total cholesterol are described to be elevated[351] and in particular an increased HDL cholesterol concentration has been reported during high-fat conditions[352,353].

The diet-dependent weight gain observed in the WT animals was more pronounced in the male animals (see Fig. 5.34A), which corresponds to the literature,

since energy metabolism and fat distribution is known to be highly influenced by sex hormones[354–356]. Surprisingly, the Gadd45β KO females gained weight in the same range compared to their male counterparts (Fig. 5.34B), which was also represented by a comparably increased gonadal fat pad (Fig. 5.42). In line with increased weight gain, high-fat diet-fed female Gadd45β KO mice additionally displayed slightly higher resting glucose and HDL cholesterol levels (Fig. 5.35 and Fig. 5.37) in addition to elevated cholesterol levels (Fig. 5.38). Interestingly, the Gadd45β KO animals in total displayed moderately increased triglyceride concentrations in response to the high-fat diet compared to the respective WT mice (Fig. 5.36). Due to its role as a central metabolic organ, high-fat diet severely affects the liver, which was shown by the elevated histological scores in male high-fat animals. The observed frequent inclusion of large fat drops in the lobe of the liver resemble the morphological changes in a developing non-alcoholic fatty liver disease (NAFLD)[357]. In line with the other obtained data, the livers of high-fat diet-fed Gadd45β KO females displayed a comparable pathology to the males (Fig. 5.40). In all high-fat groups except the WT females, the beforehand clearly morphologically separated brown adipose tissue (BAT) progressively shifted towards a white adipose tissue (WAT) phenotype within the scapular fat pad. In general, the individual cell sizes were remarkably elevated in these high-fat diet groups (Fig. 5.41). As shown in a previous study, this change is associated with an increased amount of stored triglycerides and suggested to come along with an enhanced level of mitophagy in the BAT[358]. Overall, the histological results correspond well to the measured differences between the different groups in the evaluated metabolic parameters. Taken together, the herein observed higher susceptibility of Gadd45β KO mice, in particular the females, to a high-fat diet, suggests an at least partly gender-dependent regulatory link between Gadd45β expression and lipid metabolism.

Interestingly, a recent study demonstrated that the induction of Gadd45β during short-time fasting of mice regulates the uptake of fatty acids in hepatocytes[359]. In detail, Fuhrmeister and colleagues observed an accumulation of triglycerides in the livers of Gadd45β KO mice after over night fasting and subsequent re-feeding. Of note, no difference to the WT animals was observed in the serum of the fasted animals. Furthermore, they investigated the effect of a high-fat diet on male Gadd45β KO mice.

The constant high nutrient input led to increased insulin levels in the serum of the KO animals, which is tantamount with a pronounced insulin resistance. Notably, further investigation of the underlying molecular mechanism during Gadd45β-mediated metabolic regulation in hepatocytes did not reveal a connection to a Gadd45β-dependent altered autophagic flux in the liver. They identified the fatty acid binding protein 1 (FABP1) as an interaction partner of Gadd45β and moreover demonstrated that in Gadd45β-deficient hepatocytes FABP1 translocated from the cytoplasm towards the plasma membrane and microsomes. Strikingly, this redistribution of FABP1 was observed in genetically-induced obese and diabetic mouse models as well. Finally, the overexpression of Gadd45β resulted in a reduced frequency of activated long-chain fatty acids in hepatocytes and a normalized glucose homeostasis. Altogether, this report displayed an important regulatory role of Gadd45β in the liver, which probably protects the cells from an accumulation of long-chain fatty acids after a fasting-feeding period[359]. These conclusions are highly relevant to further confirm and clarify the herein described Gadd45β-dependent effects during high-fat diet feeding. Since Fuhrmeister and colleagues worked solely with male animals, the herein observed impact of the Gadd45β-deficiency specifically during high-fat diet induced obesity in females is an interesting addition to their findings.

In general, gender-depending differences may either account for altered expression levels of the protein of interest and/or encounter for a complex interplay with sex hormones. Indeed, a recent publication revealed significant differences in the Gadd45β mRNA expression levels measured in the brain of neonatal males and females. Until the juvenile period, Gadd45β mRNA levels were shown to be elevated in the amygdala of female animals. Interestingly, the observed effect was reversed by the injection of the steroid hormone derivate dihydrotestosterone[360]. However, this finding probably plays rather a role during the early-on development and is unlikely to interfere with the herein observed gender-specific effect of adult mice.

Next to the metabolic parameters also several lymphocyte populations of the spleen and the peripheral lymph nodes were analyzed after the high-fat diet feeding. In these analyses, a reduced number of regulatory T cells (T_{reg}) was found in the spleen of Gadd45β KO mice compared to WT mice. This result was independent of the feeding condition, thus rather accounts for a genetic and organ-specific effect due to

the deficiency of Gadd45β (Fig. 5.39). Notably, in previous studies Gadd45β was identified as target of the T_{reg}-specific transcription factor forkhead-box P3 (FoxP3)[361]. A further study described, that the methylation status of the T_{reg} cell-specific demethylated region (TSDR) within the FoxP3 locus is crucial for T_{reg} stability[362]. Hence, a functional link between the presence of Gadd45β as a known mediator of demethylation and the frequency of T_{regs} can be speculated. Nevertheless, this observation needs further clarification and confirmation. Immune cells from metabolic tissues, i.e. liver or adipose tissue, need to be analyzed in the future to investigate inflammatory responses during a high-fat diet feeding more in depth. Especially in adipose tissue, high-fat diet induced obesity is associated with a complex pro-inflammatory signaling that involves a close interplay between adipocytes, adipocyte-resting T cells (ART)[363–365] and specifically polarized adipose tissue macrophages (ATM)[366–368]. Interestingly, the initiation and progression of this signaling is not only driven by cytokine secretion via the innate immune system of adipocytes and ATM, but also depends on a MHC class II-dependent adaptive immune response that was exclusively observed in adipocytes upon obesity[369]. In the latter, subsequent re-modeling of the ART sub-types was shown to lead to a pro-inflammatory interaction with the adipocytes, which is followed by the recruitment of ATM.

In summary, the herein discussed data suggested an interesting and putatively gender-dependent role for Gadd45β during obesity. To confirm and enlarge these conclusions, further and more comprehensive investigation is needed in the future. Notably, this should include improvements in the experimental settings, for instance in terms of the number of animals and the starting time of the feeding for the groups.

6.6 Concluding remarks

Autophagy is well known for its protective role during several unfavorable conditions a eucaryotic cell needs to cope with. Degradation of own intracellular content enables nutrient and energy supply upon prolonged starvation and specific targeting of invading pathogens by the autophagic machinery contributes to the clearance of the pathogen. Thus, the molecular mechanisms, which are responsible for autophagy regulation, are of particular interest. The previously identified Gadd45β-

initiated signaling cascade resulted in an inhibited autophagosome-lysosome fusion, which was mediated by the interaction of the MAP kinase p38 and the autophagosomal ATG5 protein. This pathway was suggested to serve as a negative feedback loop, important to dampen the autophagic flux after a strong initiation, i.e. after stimulation with LPS. In order to use this knowledge to specifically modify autophagy or to derive similar mechanisms in other cellular contexts, a more detailed understanding of the interplay between the involved factors is needed. The biochemical investigations performed during this thesis confirmed the interaction between p38 and ATG5 and identified residues that are important for the proper docking of the kinase. Hence, these amino acids represent potential target amino acids for a directed modulation of the autophagic regulation at the level of the p38-ATG5 interaction. Thereby a manipulation of the upstream cascade members that fulfill multiple other autophagy-independent functions is avoided. Interestingly, the results of *in vitro* kinase experiments followed by Western blot and mass spectrometry analysis performed to identify the phosphorylation target of p38, pointed to the autophagy protein ATG12, which is covalently attached to ATG5. In the by now proposed model, ATG5 acts as docking and pre-orientation platform for the p38-mediated phosphorylation of ATG12. This would represent a highly specific regulatory step, in particular because it is restricted to the function of ATG5 during autophagy. However, additional experiments are needed to further underline this hypothesis and to verify its relevance in cellular environment.

Infection with *S. aureus*, especially the methicillin-resistant *S. aureus* (MRSA), is an emerging danger for skin-wounded patients in hospitals. Restriction of *S. aureus*-associated pathology especially depends on the molecular mechanisms, which allow intracellular survival and persistence of the bacteria within a host (skin) cell. In this thesis, infection of fibroblast cells with *S. aureus* was demonstrated to induce selective autophagy in order to clear the bacteria by lysosomal degradation. However, despite the efficient recognition and subsequent engulfment of *S. aureus* within an autophagosome, only a minor fraction of the bacteria was shown to end up in acidic degradative compartments. Importantly, the underlying *S. aureus*-dependent impairment of autophagosome-lysosome fusion was demonstrated to be mediated by the specific activation and recruitment of the MAP kinase p38 to the autophagosomes. Altogether, the results provided by this thesis reveale a so far unknown evading

strategy of *S. aureus* from autophagic degradation, which involves the manipulation of a host kinase. These findings now represent a starting point for subsequent experiments to elucidate the upstream molecular steps responsible for the phosphorylation of p38 and to identify the downstream factors, which perform the block in the autophagic flux. Hence, the gained knowledge leads to a more detailed understanding of *S. aureus*-dependent modulations within an infected cell and possibly will demonstrate new strategies to counteract the resulting bacterial benefits in the future.

Obesity is one major factor that contributes to the development of type 2 diabetes and other metabolic diseases. In these days a growing part of the human population, especially in industrialized countries, is affected by the results of an unbalanced, rather fat-rich nutrition. This development, also with respect to the impact on the health systems, leads to an increasing interest in the understanding of the underlying regulatory mechanisms. The relevance of autophagy during obesity was shown for instance in the context of insulin-resistance and the accumulation of white adipose tissue (WAT). To further understand the complex interplay between these two metabolic pathways, the effect of a constant nutrient overload on adipose and liver tissue of mice with an altered autophagic regulation is investigated during this thesis. Interestingly, the lack of Gadd45β led to an increased susceptibility of female mice to high-fat diet-induced obesity in terms of weight gain, metabolic blood plasma parameters and tissue pathology. Since Gadd45β, next to its recently shown role in autophagy regulation, induces multiple other signaling pathways, further studies are needed to elucidate the molecular steps and the cellular function behind the observed findings. Nevertheless, these initial data for sure underline the importance of a gender-dependent contemplation in metabolism experiments.

7 ABBREVIATIONS

In addition to the following abbreviations, the known abbreviations for the SI units and the one- and three-letter-code for amino acids were used in this thesis.

AA	amino acid
Ab	antibody
AMBRA1	activating molecule in Beclin1-regulated autophagy 1
AMP/ATP	adenosine monophosphate/adenosine triphosphate
AMPK	adenosine monophosphate-activated protein kinase
ATG	autophagy-related
BafA	bafilomycin A1
BAT	brown adipose tissue
BCA	bicinchoninic acid
Bcl-2	B cell lymphoma-2
bp	base pair
BSA	bovine serum albumin
CD	cluster of differentiation
cDNA	complementary DNA
CDS	coding sequence
CHO cells	chinese hamster ovary cells
ctrl	control
DC	dendritic cells
dH_2O	deionized, filtered water
dL	deciliter
DMEM	Dulbecco's modified eagle's medium
DNA	deoxyribonucleic acid
dNTP	desoxyribonucleosid triphosphate
E. coli	*Escherichia coli*
EF1α	human elongation factor 1α
EMCV	encephalomyocarditis virus
ER	endoplasmic reticulum
ERK	extracellular signal-regulated kinase
e.v.	empty vector
FCS	fetal calf serum
Fig.	Figure
FIP200	focal adhesion kinase (FAK) family kinase-interacting protein of 200 kDa
Gadd45	growth arrest and DNA damage-induced 45
GAS	Group A *Streptococcus*
gDNA	genomic DNA

GFP	green fluorescent protein
gMFI	geometric mean fluorescence intensity
H&E	hematoxylin and eosin
hATG5	human ATG5
hfd	high-fat diet
hLC3B	human LC3, isoform B
HBSS	Hank's balanced salt solution
HDL	high density lipoprotein
HEK293T cells	human embryonic kidney 293T cells
hpi	hours post infection
IF	immunofluorescence
Ig	immunoglobulin
IL	interleukin
IP	immunoprecipitation
IRES	internal ribosomal entry site
JNK	c-jun N-terminal kinase
kb	kilo bases
kDa	kilodalton
KM	kinase-inactive mutant (of p38)
KO	knock out
LAP	LC3-associated phagocytosis
LC	liquid chromatography
LC3	microtubule-associated protein 1 light chain 3
LC3A/B	LC3, isoform A and B
LIR	LC3 interaction region
L. monocytogenes	*Listeria monocytogenes*
LPS	lipopolysaccharide
MAP kinase	mitogen-activated protein kinase
mCitrine	modified Citrine
MEF cells	murine embryonic fibroblast cells
MHC	major histocompatibility complex
min	minutes
MOI	multiplicity of infection
mRNA	messenger RNA
MS	mass spectrometry
mTORC1	mammalian target of rapamycin complex 1
NBR1	neighbor of BRCA1 gene 1
NDP52 (CALCOCCO2)	nuclear dot protein 52 kDa (calcium binding and coiled coil domain 2)
NF-κB	nuclear factor κB
n.t.	not transfected
OD_{600}	optical density at 600 nm
OPTN	optineurin

PCR	polymerase chain reaction
PE	phosphatidylethanolamine
PFA	paraformaledyde
pLN	peripheral lymph nodes
RFP	red fluorescent protein
RMCE	recombinase-mediated cassette exchange
RNA	ribonucleic acid
RNAi	RNA interference
ROS	reactive oxygen species
rpm	rounds per minute
RT	room temperature
RT PCR	reverse transcriptase PCR
S. aureus	*Staphylococcus aureus*
SD	standard deviation
SDS-PAGE	SDS-polyacrylamide gel electrophoresis
SEM	standard error of the mean
SNARE	soluble (*N*-ethylmaleimide-sensitive factor) attachment protein receptor
S. Typhimurium	*Salmonella enterica* serovar Typhimurium
Tab.	Table
TCR	T cell receptor
TGF	transforming growth factor
TNF	tumor necrosis factor
TNF-R	tumor necrosis factor receptor
TPEN	N,N,N',N'-tetrakis(2-pyridylmethyl)ethane-1,2-diamine
TRAF	TNF receptor-associated factor
UBA	ubiquitin-associated
ULK	UNC-5 like autophagy activating kinase
UV	ultra-violet
UVRAG	UV radiation resistance-associated gene
WAT	white adipose tissue
WT	wild type

8 Literature

1. Yang, Z. & Klionsky, D. J. Mammalian autophagy: Core molecular machinery and signaling regulation. *Curr. Opin. Cell Biol.* **22,** 124–131 (2010).

2. Feng, Y., He, D., Yao, Z. & Klionsky, D. J. The machinery of macroautophagy. *Cell Res.* **24,** 24–41 (2014).

3. Mizushima, N. & Klionsky, D. J. Protein turnover via autophagy: implications for metabolism. *Annu. Rev. Nutr.* **27,** 19–40 (2007).

4. Deretic, V. & Levine, B. Autophagy, immunity, and microbial adaptations. *Cell Host Microbe* **5,** 527–49 (2009).

5. de Reuck, A. V. S. & Cameron, M. P. Conference - Ciba Foundation Symposium on Lysosomes, London, J.A. Chruchill Ltd. in (1963).

6. De Duve, C., Pressman, B. C., Gianetto, R., Wattiaux, R. & Appelmans, R. Tissue Fractionation Studies 6. Intracellular distribution patterns of enzymes in rat-liver tissue. *Biochem J* **60,** 604–617 (1955).

7. Novikoff, A. B., Beaufey, H. & De Duve, C. Electron microscopy of lysosome-rich fractions from rat liver. *J. Biophys. Biochem. Cytol.* **2,** 179–184 (1956).

8. Ashford, T. P. & Porter, K. R. Cytoplasmic components in hepatic cell lysosomes. *J. Cell Biol.* **12,** 198–202 (1962).

9. Novikoff, A. B. & Essner, E. Cytolysomes and mitochondrial degeneration. *J. Cell Biol.* **15,** 140–146 (1962).

10. Deter, R. L. & de Duve, C. Influence of glucagon, an inducer of cellular autophagy, on some physical properties of rat liver lysosomes. *J. Cell Biol.* **33,** 437–449 (1967).

11. Deter, R. L., Baudhuin, P. & de Duve, C. Participation of lysosomes in cellular autophagy induced in rat liver by glucagon. *J. Cell Biol.* **35,** C11–C16 (1967).

12. Tsukada, M. & Ohsumi, Y. Isolation and characterization of autophagy-defective mutants of *Saccharomyces cerevisiae*. *FEBS Lett.* **333,** 169–74 (1993).

13. Thumm, M. *et al.* Isolation of autophagocytosis mutants of *Saccharomyces cerevisiae*. *FEBS Lett.* **349,** 275–80 (1994).

14. Matsuura, A., Tsukada, M., Wada, Y. & Ohsumi, Y. Apg1p, a novel protein kinase required for the autophagic process in *Saccharomyces cerevisiae*. *Gene* **192,** 245–250 (1997).

15. Straub, M., Bredschneider, M. & Thumm, M. AUT3, a serine/threonine kinase gene, is essential for autophagocytosis in *Saccharomyces cerevisiae*. *J. Bacteriol.* **179,** 3875–3883 (1997).

16. Kametaka, S., Matsuura, A., Wada, Y. & Ohsumi, Y. Structural and functional analyses of APG5 a gene involved in autophagy in yeast. *Gene* **178,** 139–143 (1996).

17. Funakoshi, T., Matsuura, A., Noda, T. & Ohsumi, Y. Analyses of APG13 gene involved in autophagy in yeast, *Saccharomyces cerevisiae*. *Gene* **192,** 207–213 (1997).

18. Mizushima, N. *et al.* A protein conjugation system essential for autophagy. *Nature* **395,** 395–8 (1998).

19. Mizushima, N., Sugita, H., Yoshimori, T. & Ohsumi, Y. A new protein conjugation system in human. The counterpart of the yeast Apg12p conjugation system essential for autophagy. *J. Biol. Chem.* **273,** 33889–33892 (1998).

20. Wesselborg, S. & Stork, B. Autophagy signal transduction by ATG proteins: from hierarchies to networks. *Cell. Mol. Life Sci.* (2015). doi:10.1007/s00018-015-2034-8

21. Kunz, J. B., Schwarz, H. & Mayer, A. Determination of four sequential stages during microautophagy *in vitro*. *J. Biol. Chem.* **279,** 9987–9996 (2004).

22. Li, W., Li, J. & Bao, J. Microautophagy: lesser-known self-eating. *Cell. Mol. Life Sci.* **69,** 1125–36 (2012).

23. Kiššova, I. *et al.* Selective and non-selective autophagic degradation of mitochondria in yeast. *Autophagy* **3,** 329–336 (2007).

24. Bellu, A. R. *et al.* Glucose-induced and nitrogen-starvation-induced peroxisome degradation are distinct processes in *Hansenula polymorpha* that involve both common and unique genes. *FEMS Yeast Res.* **1,** 23–31 (2001).

25. Dice, J. F. Peptide sequences that target cytosolic proteins for lysosomal proteolysis. *Trends Biochem. Sci.* **15,** 305–9 (1990).

26. Chiang, H. L., Terlecky, S. R., Plant, C. P. & Dice, J. F. A role for a 70-kilodalton heat shock protein in lysosomal degradation of intracellular proteins. *Science* **246,** 382–5 (1989).

27. Cuervo, A. M. & Dice, J. F. A receptor for the selective uptake and degradation of proteins by lysosomes. *Science* **273,** 501–3 (1996).

28. Cuervo, A. M., Knecht, E., Terlecky, S. R. & Dice, J. F. Activation of a selective pathway of lysosomal proteolysis in rat liver by prolonged starvation. *Am. J. Physiol. - Cell Physiol.* **269,** C1200–C1208 (1995).

29. Kiffin, R., Christian, C., Knecht, E. & Cuervo, A. M. Activation of chaperone-mediated autophagy during oxidative stress. *Mol. Biol. Cell* **15,** 4829–4840 (2004).

30. Sancak, Y. *et al.* Ragulator-Rag complex targets mTORC1 to the lysosomal surface and is necessary for its activation by amino acids. *Cell* **141,** 290–303 (2010).

31. Kim, D.-H. *et al.* mTOR interacts with raptor to form a nutrient-sensitive complex that signals to the cell growth machinery. *Cell* **110,** 163–75 (2002).

32. Sancak, Y. *et al.* PRAS40 is an insulin-regulated inhibitor of the mTORC1 protein kinase. *Mol. Cell* **25,** 903–15 (2007).

33. Jung, C. H. *et al.* ULK-Atg13-FIP200 complexes mediate mTOR signaling to the autophagy machinery. *Mol. Biol. Cell* **20,** 1992–2003 (2009).

34. Ganley, I. G. *et al.* ULK1·ATG13·FIP200 complex mediates mTOR signaling and is essential for autophagy. *J. Biol. Chem.* **284,** 12297–12305 (2009).

35. Hosokawa, N. *et al.* Nutrient-dependent mTORC1 Association with the ULK1-Atg13-FIP200 Complex Required for Autophagy. *Mol. Biol. Cell* **20,** 1981–1991 (2009).

36. Russell, R. C. *et al.* ULK1 induces autophagy by phosphorylating Beclin-1 and activating VPS34 lipid kinase. *Nat. Cell Biol.* **15,** 741–50 (2013).

37. Egan, D. F. *et al.* Small molecule inhibition of the autophagy kinase ULK1 and identification of ULK1 substrates. *Mol. Cell* **59,** 285–297 (2015).

38. Liang, C. *et al.* Autophagic and tumour suppressor activity of a novel Beclin1-binding protein UVRAG. *Nat. Cell Biol.* **8,** 688–698 (2006).

39. Zhong, Y. *et al.* Distinct regulation of autophagic activity by Atg14L and Rubicon associated with Beclin 1-phosphatidylinositol-3-kinase complex. *Nat. Cell Biol.* **11,** 468–76 (2009).

40. Itakura, E., Kishi, C., Inoue, K. & Mizushima, N. Beclin 1 forms two distinct phosphatidylinositol 3-kinase complexes with mammalian Atg14 and UVRAG. *Mol. Biol. Cell* **19,** 5360–72 (2008).

41. Axe, E. L. *et al.* Autophagosome formation from membrane compartments enriched in phosphatidylinositol 3-phosphate and dynamically connected to the endoplasmic reticulum. *J. Cell Biol.* **182,** 685–701 (2008).

42. Lamb, C. A., Yoshimori, T. & Tooze, S. A. The autophagosome: origins unknown, biogenesis complex. *Nat. Rev. Mol. Cell Biol.* **14,** 759–74 (2013).

43. Xie, Y. *et al.* Posttranslational modification of autophagy-related proteins in macroautophagy. *Autophagy* **11,** 28–45 (2015).

44. Hayashi-Nishino, M. *et al.* A subdomain of the endoplasmic reticulum forms a cradle for autophagosome formation. *Nat. Cell Biol.* **11,** 1433–1437 (2009).

45. Ylä-Anttila, P., Vihinen, H., Jokitalo, E. & Eskelinen, E. L. 3D tomography reveals connections between the phagophore and endoplasmic reticulum. *Autophagy* **5,** 1180–1185 (2009).

46. Hailey, D. W. *et al.* Mitochondria supply membranes for autophagosome biogenesis during starvation. *Cell* **141,** 656–67 (2010).

47. Young, A. R. J. *et al.* Starvation and ULK1-dependent cycling of mammalian Atg9 between the TGN and endosomes. *J. Cell Sci.* **119,** 3888–900 (2006).

48. Ravikumar, B., Moreau, K., Jahreiss, L., Puri, C. & Rubinsztein, D. C. Plasma membrane contributes to the formation of pre-autophagosomal structures. *Nat. Cell Biol.* **12,** 747–757 (2010).

49. Longatti, A. & Tooze, S. A. Recycling endosomes contribute to autophagosome formation. *Autophagy* **8,** 1682–3 (2012).

50. Itakura, E. & Mizushima, N. Characterization of autophagosome formation site by a hierarchical analysis of mammalian Atg proteins. *Autophagy* **6,** 764–76 (2010).

51. Mizushima, N. *et al.* Mouse Apg16L, a novel WD-repeat protein, targets to the autophagic isolation membrane with the Apg12-Apg5 conjugate. *J. Cell Sci.* **116,** 1679–1688 (2003).

52. Kim, J. H. *et al.* Insights into autophagosome maturation revealed by the structures of ATG5 with its interacting partners. *Autophagy* **11,** 75–87 (2015).

53. Gammoh, N., Florey, O., Overholtzer, M. & Jiang, X. Interaction between FIP200 and ATG16L1 distinguishes ULK1 complex-dependent and -independent autophagy. *Nat. Struct. Mol. Biol.* **20,** 144–9 (2013).

54. Nishimura, T. *et al.* FIP200 regulates targeting of Atg16L1 to the isolation membrane. *EMBO Rep.* **14,** 284–91 (2013).

55. Dooley, H. C. *et al.* WIPI2 links LC3 conjugation with PI3P, autophagosome formation, and pathogen clearance by recruiting Atg12-5-16L1. *Mol. Cell* **55,** 238–252 (2014).

56. Suzuki, K. *et al.* The pre-autophagosomal structure organized by concerted functions of APG genes is essential for autophagosome formation. *EMBO J.* **20,** 5971–81 (2001).

57. Mizushima, N. *et al.* Dissection of autophagosome formation using Apg5-deficient mouse embryonic stem cells. *J. Cell Biol.* **152,** 657–667 (2001).

58. Tanida, I., Ueno, T. & Kominami, E. Human light chain 3/MAP1LC3B is cleaved at its carboxyl-terminal Met121 to expose Gly120 for lipidation and targeting to autophagosomal membranes. *J. Biol. Chem.* **279,** 47704–47710 (2004).

59. Kabeya, Y. *et al.* LC3, a mammalian homologue of yeast Apg8p, is localized in autophagosome membranes after processing. *EMBO J.* **19,** 5720–5728 (2000).

60. Sou, Y. -s., Tanida, I., Komatsu, M., Ueno, T. & Kominami, E. Phosphatidylserine in addition to phosphatidylethanolamine is an *in vitro* target of the mammalian Atg8 modifiers, LC3, GABARAP, and GATE-16. *J. Biol. Chem.* **281,** 3017–3024 (2006).

61. Otomo, C., Metlagel, Z., Takaesu, G. & Otomo, T. Structure of the human ATG12~ATG5 conjugate required for LC3 lipidation in autophagy. *Nat Struct Mol Biol* **20,** 59–66 (2013).

62. Sakoh-Nakatogawa, M. *et al.* Atg12–Atg5 conjugate enhances E2 activity of Atg3 by rearranging its catalytic site. *Nat. Struct. Mol. Biol.* **20,** 433–439 (2013).

63. Weidberg, H. *et al.* Supplement - LC3 and GATE-16/GABARAP subfamilies are both essential yet act differently in autophagosome biogenesis. *EMBO J.* **29,** 1792–802 (2010).

64. Weidberg, H. *et al.* LC3 and GATE-16 N termini mediate membrane fusion processes required for autophagosome biogenesis. *Dev. Cell* **20,** 444–54 (2011).

65. Fujita, N. *et al.* An Atg4B mutant hampers the lipidation of LC3 paralogues and causes defects in autophagosome closure. *Mol. Biol. Cell* **19,** 4651–4659 (2008).

66. Sou, Y. -s. *et al.* The Atg8 conjugation system is indispensable for proper development of autophagic isolation membranes in mice. *Mol. Biol. Cell* **19,** 4762–4775 (2008).

67. Mizushima, N. Methods for monitoring autophagy. *Int. J. Biochem. Cell Biol.* **36,** 2491–502 (2004).

68. Mizushima, N. in *Methods in Enzymology* **452,** 13–23 (Elsevier Inc., 2009).

69. Green, D. R. & Levine, B. To be or not to be? How selective autophagy and cell death govern cell fate. *Cell* **157,** 65–75 (2014).

70. He, H. *et al.* Post-translational modifications of three members of the human MAP1LC3 family and detection of a novel type of modification for MAP1LC3B. *J. Biol. Chem.* **278,** 29278–29287 (2003).

71. Sagiv, Y., Legesse-Miller, A., Porat, A. & Elazar, Z. GATE-16, a membrane transport modulator, interacts with NSF and the Golgi v-SNARE GOS-28. *EMBO J.* **19,** 1494–504 (2000).

72. Kittler, J. T. *et al.* The subcellular distribution of GABARAP and its ability to interact with NSF suggest a role for this protein in the intracellular transport of GABAA receptors. *Mol. Cell. Neurosci.* **18,** 13–25 (2001).

73. Xin, Y. *et al.* Cloning, expression patterns, and chromosome localization of three human and two mouse homologues of GABAA receptor-associated protein. *Genomics* **74,** 408–413 (2001).

74. Kabeya, Y. *et al.* LC3, GABARAP and GATE16 localize to autophagosomal membrane depending on form-II formation. *J. Cell Sci.* **117,** 2805–12 (2004).

75. Weidberg, H. *et al.* LC3 and GATE-16/GABARAP subfamilies are both essential yet act differently in autophagosome biogenesis. *EMBO J.* **29,** 1792–1802 (2010).

76. Pankiv, S. *et al.* p62/SQSTM1 binds directly to Atg8/LC3 to facilitate degradation of ubiquitinated protein aggregates by autophagy. *J. Biol. Chem.* **282,** 24131–45 (2007).

77. von Muhlinen, N. *et al.* LC3C, bound selectively by a noncanonical LIR motif in NDP52, is required for antibacterial autophagy. *Mol. Cell* **48,** 329–42 (2012).

78. Kimura, S., Noda, T. & Yoshimori, T. Dissection of the autophagosome maturation process by a novel reporter protein, tandem fluorescent-tagged LC3. *Autophagy* **3,** 452–460 (2007).

79. Kirisako, T. *et al.* The reversible modification regulates the membrane-binding state of Apg8/Aut7 essential for autophagy and the cytoplasm to vacuole targeting pathway. *J. Cell Biol.* **151,** 263–76 (2000).

80. Berg, T. O., Fengsrud, M., Stromhaug, P. E., Berg, T. & Seglen, P. O. Isolation and characterization of rat liver amphisomes: evidence for fusion of autophagosomes with both early and late endosomes. *J. Biol. Chem.* **273,** 21883–21892 (1998).

81. Tooze, J. *et al.* In exocrine pancreas, the basolateral endocytic pathway converges with the autophagic pathway immediately after the early endosome. *J. Cell Biol.* **111,** 329–45 (1990).

82. Chua, C. E. L., Gan, B. Q. & Tang, B. L. Involvement of members of the Rab family and related small GTPases in autophagosome formation and maturation. *Cell. Mol. Life Sci.* **68,** 3349–58 (2011).

83. Ao, X., Zou, L. & Wu, Y. Regulation of autophagy by the Rab GTPase network. *Cell Death Differ.* **21,** 348–58 (2014).

84. Gutierrez, M. G., Munafó, D. B., Berón, W. & Colombo, M. I. Rab7 is required for the normal progression of the autophagic pathway in mammalian cells. *J. Cell Sci.* **117,** 2687–97 (2004).

85. Jäger, S. *et al.* Role for Rab7 in maturation of late autophagic vacuoles. *J. Cell Sci.* **117,** 4837–48 (2004).

86. Pankiv, S. *et al.* FYCO1 is a Rab7 effector that binds to LC3 and PI3P to mediate microtubule plus end–directed vesicle transport. *J. Cell Biol.* **188,** 253–269 (2010).

87. Jiang, P. *et al.* The HOPS complex mediates autophagosome-lysosome fusion through interaction with syntaxin 17. *Mol. Biol. Cell* **25,** 1327–1337 (2014).

88. Zucchi, P. C. & Zick, M. Membrane fusion catalyzed by a Rab, SNAREs, and SNARE chaperones is accompanied by enhanced permeability to small molecules and by lysis. *Mol. Biol. Cell* **22,** 4635–4646 (2011).

89. Jahn, R. & Scheller, R. H. SNAREs — engines for membrane fusion. *Nat. Rev. Mol. Cell Biol.* **7,** 631–643 (2006).

90. Moreau, K., Ravikumar, B., Renna, M., Puri, C. & Rubinsztein, D. C. Autophagosome precursor maturation requires homotypic fusion. *Cell* **146,** 303–17 (2011).

91. Fader, C. M., Sánchez, D. G., Mestre, M. B. & Colombo, M. I. TI-VAMP/VAMP7 and VAMP3/cellubrevin: two v-SNARE proteins involved in specific steps of the autophagy/multivesicular body pathways. *Biochim. Biophys. Acta - Mol. Cell Res.* **1793,** 1901–1916 (2009).

92. Furuta, N., Fujita, N., Noda, T., Yoshimori, T. & Amano, A. Combinational soluble N-ethylmaleimide-sensitive factor attachment protein receptor proteins VAMP8 and Vti1b mediate fusion of antimicrobial and canonical autophagosomes with lysosomes. *Mol. Biol. Cell* **21,** 1001–10 (2010).

93. Itakura, E., Kishi-Itakura, C. & Mizushima, N. The hairpin-type tail-anchored SNARE syntaxin 17 targets to autophagosomes for fusion with endosomes/lysosomes. *Cell* **151,** 1256–1269 (2012).

94. Diao, J. *et al.* ATG14 promotes membrane tethering and fusion of autophagosomes to endolysosomes. *Nature* **520,** 563–6 (2015).

95. Behrends, C., Sowa, M. E., Gygi, S. P. & Harper, J. W. Network organization of the human autophagy system. *Nature* **466,** 68–76 (2010).

96. Ogawa, M. *et al.* A Tecpr1-dependent selective autophagy pathway targets bacterial pathogens. *Cell Host Microbe* **9,** 376–389 (2011).

97. Chen, D. *et al.* A mammalian autophagosome maturation mechanism mediated by TECPR1 and the Atg12-Atg5 conjugate. *Mol. Cell* **45,** 629–641 (2012).

98. Itakura, E. & Mizushima, N. Syntaxin 17 - The autophagosomal SNARE. *Autophagy* **9,** 1–3 (2013).

99. Dunn, W. A. Studies on the mechanisms of autophagy: maturation of the autophagic vacuole. *J. Cell Biol.* **110,** 1935–45 (1990).

100. Lawrence, B. P. & Brown, W. J. Autophagic vacuoles rapidly fuse with pre-existing lysosomes in cultured hepatocytes. *J. Cell Sci.* **102,** 515–526 (1992).

101. Zhou, J. *et al.* Activation of lysosomal function in the course of autophagy via mTORC1 suppression and autophagosome-lysosome fusion. *Cell Res.* **23,** 508–23 (2013).

102. Eskelinen, E.-L. & Saftig, P. Autophagy: A lysosomal degradation pathway with a central role in health and disease. *Biochim. Biophys. Acta - Mol. Cell Res.* **1793,** 664–673 (2009).

103. Zakeri, Z., Bursch, W., Tenniswood, M. & Lockshin, R. A. Cell death: programmed, apoptosis, necrosis, or other? *Cell Death Differ.* **2,** 87–96 (1995).

104. McEwan, D. G. & Dikic, I. The Three Musketeers of Autophagy: phosphorylation, ubiquitylation and acetylation. *Trends Cell Biol.* **21,** 195–201 (2011).

105. Inoki, K., Li, Y., Zhu, T., Wu, J. & Guan, K.-L. TSC2 is phosphorylated and inhibited by Akt and suppresses mTOR signalling. *Nat. Cell Biol.* **4,** 648–657 (2002).

106. Inoki, K. *et al.* TSC2 integrates Wnt and energy signals via a coordinated phosphorylation by AMPK and GSK3 to regulate cell growth. *Cell* **126,** 955–68 (2006).

107. Bach, M., Larance, M., James, D. E. & Ramm, G. The serine/threonine kinase ULK1 is a target of multiple phosphorylation events. *Biochem. J.* **440,** 283–91 (2011).

108. Mack, H. I. D., Zheng, B., Asara, J. M. & Thomas, S. M. AMPK-dependent phosphorylation of ULK1 regulates ATG9 localization. *Autophagy* **8,** 1197–214 (2012).

109. Löffler, A. S. *et al.* Ulk1-mediated phosphorylation of AMPK constitutes a negative regulatory feedback loop. *Autophagy* **7,** 696–706 (2011).

110. Jung, C. H., Seo, M., Otto, N. M. & Kim, D.-H. ULK1 inhibits the kinase activity of mTORC1 and cell proliferation. *Autophagy* **7,** 1212–21 (2011).

111. Nazio, F. *et al.* mTOR inhibits autophagy by controlling ULK1 ubiquitylation, self-association and function through AMBRA1 and TRAF6. *Nat. Cell Biol.* **15,** 406–416 (2013).

112. Di Bartolomeo, S. *et al.* The dynamic interaction of AMBRA1 with the dynein motor complex regulates mammalian autophagy. *J. Cell Biol.* **191,** 155–68 (2010).

113. Ma, L. *et al.* Phosphorylation and functional inactivation of TSC2 by Erk implications for tuberous sclerosis and cancer pathogenesis. *Cell* **121,** 179–93 (2005).

114. Wang, J. *et al.* A Non-canonical MEK/ERK Signaling Pathway Regulates Autophagy via Regulating Beclin 1. *J. Biol. Chem.* **284,** 21412–21424 (2009).

115. Corcelle, E. *et al.* Control of the autophagy maturation step by the MAPK ERK and p38: Lessons from environmental carcinogens. *Autophagy* **3,** 57–59 (2007).

116. Pattingre, S. *et al.* Role of JNK1-dependent Bcl-2 phosphorylation in ceramide-induced macroautophagy. *J. Biol. Chem.* **284,** 2719–2728 (2009).

117. Wei, Y., Pattingre, S., Sinha, S., Bassik, M. & Levine, B. JNK1-mediated phosphorylation of Bcl-2 regulates starvation-induced autophagy. *Mol. Cell* **30,** 678–88 (2008).

118. Pattingre, S. *et al.* Bcl-2 antiapoptotic proteins inhibit Beclin 1-dependent autophagy. *Cell* **122,** 927–39 (2005).

119. Han, J., Lee, J.-D., Bibbs, L. & Ulevitch, R. J. A MAP kinase targeted by endotoxin and hyperosmolarity in mammalian cells. *Science (80-.).* **265,** 808–811 (1994).

120. Lee, J. C. *et al.* A protein kinase involved in the regulation of inflammatory cytokine biosynthesis. *Nature* **372,** 739–46 (1994).

121. Rousseau, S., Houle, F., Landry, J. & Huot, J. p38 MAP kinase activation by vascular endothelial growth factor mediates actin reorganization and cell migration in human endothelial cells. *Oncogene* **15,** 2169–77 (1997).

122. Rouse, J. *et al.* A novel kinase cascade triggered by stress and heat shock that stimulates MAPKAP kinase-2 and phosphorylation of the small heat shock proteins. *Cell* **78,** 1027–37 (1994).

123. Freshney, N. W. *et al.* Interleukin-1 activates a novel protein kinase cascade that results in the phosphorylation of Hsp27. *Cell* **78,** 1039–49 (1994).

124. Faust, D. *et al.* Differential p38-dependent signalling in response to cellular stress and mitogenic stimulation in fibroblasts. *Cell Commun. Signal.* **10,** 6 (2012).

125. Han, J., Lee, J. D., Tobias, P. S. & Ulevitch, R. J. Endotoxin induces rapid protein tyrosine phosphorylation in 70Z/3 cells expressing CD14. *J. Biol. Chem.* **268,** 25009–14 (1993).

126. Jiang, Y. *et al.* Characterization of the structure and function of a new mitogen-activated protein kinase (p38beta). *J. Biol. Chem.* **271,** 17920–17926 (1996).

127. Li, Z., Jiang, Y., Ulevitch, R. J. & Han, J. The primary structure of p38gamma: a new member of p38 group of MAP kinases. *Biochem. Biophys. Res. Commun.* **228,** 334–340 (1996).

128. Lechner, C., Zahalka, M. A., Giot, J. F., Møller, N. P. & Ullrich, A. ERK6, a mitogen-activated protein kinase involved in C2C12 myoblast differentiation. *Proc. Natl. Acad. Sci. U. S. A.* **93,** 4355–9 (1996).

129. Mertens, S., Craxton, M. & Goedert, M. SAP kinase-3, a new member of the family of mammalian stress-activated protein kinases. *FEBS Lett.* **383,** 273–276 (1996).

130. Wang, X. S. *et al.* Molecular cloning and characterization of a novel p38 mitogen-activated protein kinase. *J. Biol. Chem.* **272,** 23668–74 (1997).

131. Jiang, Y. *et al.* Characterization of the structure and function of the fourth member of p38 group mitogen-activated protein kinases, p38delta. *J. Biol. Chem.* **272,** 30122–30128 (1997).

132. Cuenda, A. & Rousseau, S. p38 MAP-Kinases pathway regulation, function and role in human diseases. *Biochim. Biophys. Acta - Mol. Cell Res.* **1773,** 1358–1375 (2007).

133. Keil, E. *et al.* Phosphorylation of Atg5 by the Gadd45β-MEKK4-p38 pathway inhibits autophagy. *Cell Death Differ.* **20,** 321–32 (2013).

134. Livingstone, C., Patel, G. & Jones, N. ATF-2 contains a phosphorylation-dependent transcriptional activation domain. *EMBO J.* **14,** 1785–97 (1995).

135. Ben-Levy, R., Hooper, S., Wilson, R., Paterson, H. F. & Marshall, C. J. Nuclear export of the stress-activated protein kinase p38 mediated by its substrate MAPKAP kinase-2. *Curr. Biol.* **8,** 1049–1057 (1998).

136. Trempolec, N., Dave-Coll, N. & Nebreda, A. R. SnapShot: p38 MAPK substrates. *Cell* **152,** 924–924.e1 (2013).

137. Häussinger, D. *et al.* Involvement of p38 MAPK in the regulation of proteolysis by liver cell hydration. *Gastroenterology* **116,** 921–935 (1999).

138. vom Dahl, S. *et al.* Cell hydration controls autophagosome formation in rat liver in a microtubule-dependent way downstream from p38 MAPK activation. *Biochem. J.* **354,** 31–6 (2001).

139. Desideri, E. *et al.* MAPK14 / p38 α -dependent modulation of glucose metabolism affects ROS levels and autophagy during starvation. *Autophagy* **10,** 1–14 (2014).

140. Hubbard, V. M. *et al.* Macroautophagy regulates energy metabolism during effector T cell activation. *J. Immunol.* **185,** 7349–7357 (2010).

141. Henson, S. M. *et al.* p38 signaling inhibits mTORC1-independent autophagy in senescent human CD8+ T cells. *J. Clin. Invest.* **124,** 4004–4016 (2014).

142. Webber, J. L. & Tooze, S. a. Coordinated regulation of autophagy by p38alpha MAPK through mAtg9 and p38IP. *EMBO J.* **29,** 27–40 (2010).

143. Enslen, H., Brancho, D. M. & Davis, R. J. Molecular determinants that mediate selective activation of p38 MAP kinase isoforms. *EMBO J.* **19,** 1301–11 (2000).

144. Han, J. *et al.* Characterization of the structure and function of a novel MAP kinase kinase (MKK6). *J. Biol. Chem.* **271,** 2886–2891 (1996).

145. Dérijard, B. *et al.* Independent human MAP-kinase signal transduction pathways defined by MEK and MKK isoforms. *Science* **267,** 682–5 (1995).

146. Jiang, Y. *et al.* Structure-function studies of p38 mitogen-activated protein kinase. Loop 12 influences substrate specificity and autophosphorylation, but not upstream kinase selection. *J. Biol. Chem.* **272,** 11096–102 (1997).

147. Tokunaga, Y., Takeuchi, K., Takahashi, H. & Shimada, I. Allosteric enhancement of MAP kinase p38α's activity and substrate selectivity by docking interactions. *Nat. Struct. Mol. Biol.* **21,** 704–711 (2014).

148. Wilson, K. P. *et al.* Crystal structure of p38 mitogen-activated protein kinase. *J. Biol. Chem.* **271,** 27696–27700 (1996).

149. Dai, T. *et al.* Stress-activated protein kinases bind directly to the delta domain of c-Jun in resting cells: implications for repression of c-Jun function. *Oncogene* **10,** 849–55 (1995).

150. Barsyte-Lovejoy, D., Galanis, A. & Sharrocks, A. D. Specificity determinants in MAPK signaling to transcription factors. *J. Biol. Chem.* **277,** 9896–9903 (2002).

151. Yang, S. H., Yates, P. R., Whitmarsh, A. J., Davis, R. J. & Sharrocks, A. D. The Elk-1 ETS-domain transcription factor contains a mitogen-activated protein kinase targeting motif. *Mol. Cell. Biol.* **18,** 710–20 (1998).

152. Yang, S., Galanis, A. & Sharrocks, A. D. Targeting of p38 mitogen-activated protein kinases to MEF2 transcription factors. **19,** 4028–4038 (1999).

153. Yang, S. H., Whitmarsh, A. J., Davis, R. J. & Sharrocks, A. D. Differential targeting of MAP kinases to the ETS-domain transcription factor Elk-1. *EMBO J.* **17,** 1740–9 (1998).

154. Tanoue, T., Maeda, R., Adachi, M. & Nishida, E. Identification of a docking groove on ERK and p38 MAP kinases that regulates the specificity of docking interactions. *EMBO J.* **20,** 466–79 (2001).

155. Tanoue, T., Adachi, M., Moriguchi, T. & Nishida, E. A conserved docking motif in MAP kinases common to substrates , activators and regulators. *Nat. Cell Biol.* **2,** 110–116 (2000).

156. Chang, C. I., Xu, B. E., Akella, R., Cobb, M. H. & Goldsmith, E. J. Crystal structures of MAP kinase p38 complexed to the docking sites on its nuclear substrate MEF2A and activator MKK3b. *Mol. Cell* **9,** 1241–1249 (2002).

157. ter Haar, E., Prabhakar, P., Prabakhar, P., Liu, X. & Lepre, C. Crystal structure of the p38 alpha-MAPKAP kinase 2 heterodimer. *J. Biol. Chem.* **282,** 9733–9 (2007).

158. Zhang, Y.-Y. *et al.* A distinct interaction mode revealed by the crystal structure of the kinase p38α with the MAPK binding domain of the phosphatase MKP5. *Sci. Signal.* **4,** ra88 (2011).

159. Sharrocks, A. D., Yang, S. & Galanis, A. Docking domains and substrate- specificity determination for MAP kinases. *Trends Biochem. Sci.* **25,** 448–453 (2000).

160. Galanis, A., Yang, S.-H. & Sharrocks, A. D. Selective targeting of MAPKs to the ETS domain transcription factor SAP-1. *J. Biol. Chem.* **276,** 965–973 (2001).

161. McCoy, C. E., Campbell, D. G., Deak, M., Bloomberg, G. B. & Arthur, J. S. C. MSK1 activity is controlled by multiple phosphorylation sites. *Biochem. J.* **387,** 507–17 (2005).

162. White, A., Pargellis, C. A., Studts, J. M., Werneburg, B. G. & Farmer, B. T. Molecular basis of MAPK-activated protein kinase 2:p38 assembly. *Proc. Natl. Acad. Sci. U. S. A.* **104,** 6353–8 (2007).

163. Tomas-Zuber, M., Mary, J.-L., Lamour, F., Bur, D. & Lesslauer, W. C-terminal elements control location, activation threshold, and p38 docking of ribosomal S6 kinase B (RSKB). *J. Biol. Chem.* **276,** 5892–5899 (2001).

164. Jacobs, D., Glossip, D., Xing, H., Muslin, A. J. & Kornfeld, K. Multiple docking sites on substrate proteins form a modular system that mediates recognition by ERK MAP kinase. *Genes Dev.* **13,** 163–75 (1999).

165. Fantz, D. A., Jacobs, D., Glossip, D. & Kornfeld, K. Docking sites on substrate proteins direct extracellular signal-regulated kinase to phosphorylate specific residues. *J. Biol. Chem.* **276,** 27256–27265 (2001).

166. Fornace, A. J., Alamo, I. & Hollander, M. C. DNA damage-inducible transcripts in mammalian cells. *Proc. Natl. Acad. Sci. U. S. A.* **85,** 8800–4 (1988).

167. Fornace, A. J. *et al.* Mammalian genes coordinately regulated by growth arrest signals and DNA-damaging agents. *Mol. Cell. Biol.* **9,** 4196–203 (1989).

168. Abdollahi, A., Lord, K. A., Hoffman-Liebermann, B. & Liebermann, D. A. Sequence and expression of a cDNA encoding MyD118: a novel myeloid differentiation primary response gene induced by multiple cytokines. *Oncogene* **6,** 165–7 (1991).

169. Zhang, W. *et al.* CR6: A third member in the MyD118 and Gadd45 gene family which functions in negative growth control. *Oncogene* **18,** 4899–907 (1999).

170. Zhan, Q. *et al.* The gadd and MyD genes define a novel set of mammalian genes encoding acidic proteins that synergistically suppress cell growth. *Mol. Cell. Biol.* **14,** 2361–71 (1994).

171. Salvador, J. M., Brown-Clay, J. D. & Fornace, A. J. Gadd45 in stress signaling, cell cycle control, and apoptosis. *Adv. Exp. Med. Biol.* **793,** 1–19 (2013).

172. Selvakumaran, M. *et al.* The novel primary response gene MyD118 and the proto-oncogenes myb, myc, and bcl-2 modulate transforming growth factor beta 1-induced apoptosis of myeloid leukemia cells. *Mol. Cell. Biol.* **14,** 2352–60 (1994).

173. Yoo, J. *et al.* Transforming growth factor-beta-induced apoptosis is mediated by Smad-dependent expression of GADD45b through p38 activation. *J. Biol. Chem.* **278,** 43001–7 (2003).

174. De Smaele, E. *et al.* Induction of Gadd45beta by NF-kappaB downregulates pro-apoptotic JNK signalling. *Nature* **414,** 308–13 (2001).

175. Takekawa, M. *et al.* Smad-dependent GADD45beta expression mediates delayed activation of p38 MAP kinase by TGF-beta. *EMBO J.* **21,** 6473–82 (2002).

176. Vairapandi, M., Balliet, A. G., Fornace, A. J., Hoffman, B. & Liebermann, D. A. The differentiation primary response gene MyD118, related to GADD45, encodes for a nuclear protein which interacts with PCNA and p21WAF1/CIP1. *Oncogene* **12,** 2579–94 (1996).

177. Vairapandi, M., Balliet, A. G., Hoffman, B. & Liebermann, D. A. GADD45b and GADD45g are cdc2/cyclinB1 kinase inhibitors with a role in S and G2/M cell cycle checkpoints induced by genotoxic stress. *J. Cell. Physiol.* **192,** 327–38 (2002).

178. Takekawa, M. & Saito, H. A family of stress-inducible GADD45-like proteins mediate activation of the stress-responsive MTK1/MEKK4 MAPKKK. *Cell* **95,** 521–30 (1998).

179. Mita, H., Tsutsui, J., Takekawa, M., Witten, E. A. & Saito, H. Regulation of MTK1/MEKK4 kinase activity by its N-terminal autoinhibitory domain and GADD45 binding. *Mol. Cell. Biol.* **22,** 4544–55 (2002).

180. Miyake, Z., Takekawa, M., Ge, Q. & Saito, H. Activation of MTK1/MEKK4 by GADD45 through induced N-C dissociation and dimerization-mediated trans autophosphorylation of the MTK1 kinase domain. *Mol. Cell. Biol.* **27,** 2765–76 (2007).

181. Takekawa, M. *et al.* Conserved docking site is essential for activation of mammalian MAP kinase kinases by specific MAP kinase kinase kinases. *Mol. Cell* **18,** 295–306 (2005).

182. Ju, S. *et al.* Gadd45b and Gadd45g are important for anti-tumor immune responses. *Eur. J. Immunol.* **39,** 3010–8 (2009).

183. Chi, H., Lu, B., Takekawa, M., Davis, R. J. & Flavell, R. A. GADD45beta/GADD45gamma and MEKK4 comprise a genetic pathway mediating STAT4-independent IFNgamma production in T cells. *EMBO J.* **23,** 1576–86 (2004).

184. Papa, S. *et al.* Gadd45 beta mediates the NF-kappa B suppression of JNK signalling by targeting MKK7/JNKK2. *Nat. Cell Biol.* **6,** 146–53 (2004).

185. Cho, H. J. *et al.* Gadd45b mediates Fas-induced apoptosis by enhancing the interaction between p38 and retinoblastoma tumor suppressor. *J. Biol. Chem.* **285,** 25500–5 (2010).

186. Yamamoto, Y., Moore, R., Flavell, R. A., Lu, B. & Negishi, M. Nuclear receptor CAR represses TNFalpha-induced cell death by interacting with the anti-apoptotic GADD45B. *PLoS One* **5,** e10121 (2010).

187. Larsen, C. M. *et al.* Growth arrest- and DNA-damage-inducible 45beta gene inhibits c-Jun N-terminal kinase and extracellular signal-regulated kinase and decreases IL-1beta-induced apoptosis in insulin-producing INS-1E cells. *Diabetologia* **49,** 980–9 (2006).

188. Ijiri, K. *et al.* A novel role for GADD45beta as a mediator of MMP-13 gene expression during chondrocyte terminal differentiation. *J. Biol. Chem.* **280,** 38544–55 (2005).

189. Ma, D. K. *et al.* Neuronal activity-induced Gadd45b promotes epigenetic DNA demethylation and adult neurogenesis. *Science* **323,** 1074–7 (2009).

190. Kundu, M. *et al.* Ulk1 plays a critical role in the autophagic clearance of mitochondria and ribosomes during reticulocyte maturation. *Blood* **112,** 1493–502 (2008).

191. Iwata, J. *et al.* Excess peroxisomes are degraded by autophagic machinery in mammals. *J. Biol. Chem.* **281,** 4035–41 (2006).

192. Øverbye, A., Fengsrud, M. & Seglen, P. O. Proteomic analysis of membrane-associated proteins from rat liver autophagosomes. *Autophagy* **3,** 300–22

193. Birmingham, C. L., Smith, A. C., Bakowski, M. A., Yoshimori, T. & Brumell, J. H. Autophagy controls *Salmonella* infection in response to damage to the *Salmonella*-containing vacuole. *J. Biol. Chem.* **281,** 11374–83 (2006).

194. Ichimura, Y. *et al.* Structural basis for sorting mechanism of p62 in selective autophagy. *J. Biol. Chem.* **283,** 22847–22857 (2008).

195. Noda, N. N. *et al.* Structural basis of target recognition by Atg8/LC3 during selective autophagy. *Genes to Cells* **13,** 1211–1218 (2008).

196. Kirkin, V. *et al.* A role for NBR1 in autophagosomal degradation of ubiquitinated substrates. *Mol. Cell* **33,** 505–16 (2009).

197. Geisler, S. *et al.* PINK1/Parkin-mediated mitophagy is dependent on VDAC1 and p62/SQSTM1. *Nat. Cell Biol.* **12,** 119–31 (2010).

198. Bjørkøy, G. *et al.* p62/SQSTM1 forms protein aggregates degraded by autophagy and has a protective effect on huntingtin-induced cell death. *J. Cell Biol.* **171,** 603–14 (2005).

199. Komatsu, M. *et al.* Homeostatic levels of p62 control cytoplasmic inclusion body formation in autophagy-deficient mice. *Cell* **131,** 1149–63 (2007).

200. Kim, P. K., Hailey, D. W., Mullen, R. T. & Lippincott-Schwartz, J. Ubiquitin signals autophagic degradation of cytosolic proteins and peroxisomes. *Proc. Natl. Acad. Sci. U. S. A.* **105,** 20567–74 (2008).

201. Zheng, Y. T. *et al.* The adaptor protein p62/SQSTM1 targets invading bacteria to the autophagy pathway. *J. Immunol.* **183,** 5909–5916 (2009).

202. Tyedmers, J., Mogk, A. & Bukau, B. Cellular strategies for controlling protein aggregation. *Nat. Rev. Mol. Cell Biol.* **11,** 777–88 (2010).

203. Boyle, K. B. & Randow, F. The role of 'eat-me' signals and autophagy cargo receptors in innate immunity. *Curr. Opin. Microbiol.* **16,** 339–348 (2013).

204. Nakagawa, I. *et al.* Autophagy defends cells against invading Group A *Streptococcus*. *Science (80-.).* **306,** 1037–1040 (2004).

205. Steele-Mortimer, O., Méresse, S., Gorvel, J. P., Toh, B. H. & Finlay, B. B. Biogenesis of *Salmonella typhimurium* containing vacuoles in epithelial cells involves interactions with the early endocytic pathway. *Cell. Microbiol.* **1,** 33–49 (1999).

206. Garcia-del Portillo, F., Stein, M. A. & Finlay, B. B. Release of lipopolysaccharide from intracellular compartments containing *Salmonella typhimurium* to vesicles of the host epithelial cell. *Infect. Immun.* **65,** 24–34 (1997).

207. Bowe, F. *et al.* At least four percent of the *Salmonella typhimurium* genome is required for fatal infection of mice. *Infect. Immun.* **66,** 3372–7 (1998).

208. Brumell, J. H., Rosenberger, C. M., Gotto, G. T., Marcus, S. L. & Finlay, B. B. SifA permits survival and replication of *Salmonella typhimurium* in murine macrophages. *Cell. Microbiol.* **3,** 75–84 (2001).

209. Hensel, M. *et al.* Simultaneous identification of bacterial virulence genes by negative selection. *Science* **269,** 400–3 (1995).

210. Deiwick, J. *et al.* The translocated *Salmonella* effector proteins SseF and SseG interact and are required to establish an intracellular replication niche. *Infect. Immun.* **74,** 6965–6972 (2006).

211. Perrin, A. J., Jiang, X., Birmingham, C. L., So, N. S. Y. & Brumell, J. H. Recognition of bacteria in the cytosol of mammalian cells by the ubiquitin system. *Curr. Biol.* **14,** 806–11 (2004).

212. Thurston, T. L. M., Ryzhakov, G., Bloor, S., von Muhlinen, N. & Randow, F. The TBK1 adaptor and autophagy receptor NDP52 restricts the proliferation of ubiquitin-coated bacteria. *Nat. Immunol.* **10,** 1215–21 (2009).

213. Wild, P. *et al.* Phosphorylation of the autophagy receptor optineurin restricts *Salmonella* Growth. *Science (80-.).* **333,** 228–233 (2011).

214. Thurston, T. L. M., Wandel, M. P., von Muhlinen, N., Foeglein, A. & Randow, F. Galectin 8 targets damaged vesicles for autophagy to defend cells against bacterial invasion. *Nature* **482,** 414–8 (2012).

215. Fiskin, E., Bionda, T., Dikic, I. & Behrends, C. Global analysis of host and bacterial ubiquitinome in response to *Salmonella* Typhimurium infection. *Mol. Cell* **62,** 1–15 (2016).

216. Kreibich, S. *et al.* Autophagy proteins promote repair of endosomal membranes damaged by the *Salmonella* type three secretion system 1. *Cell Host Microbe* **18,** 527–37 (2015).

217. Ogawa, M. *et al.* Escape of intracellular *Shigella* from autophagy. *Science (80-.).* **307,** 727–731 (2005).

218. Yoshikawa, Y. *et al. Listeria monocytogenes* ActA-mediated escape from autophagic recognition. *Nat. Cell Biol.* **11,** 1233–1240 (2009).

219. LaRock, D. L., Chaudhary, A. & Miller, S. I. *Salmonellae* interactions with host processes. *Nat. Rev. Microbiol.* **13,** 191–205 (2015).

220. Ogston, A. Micrococcus poisoning. *J. Anat. Physiol.* **17,** 24–58 (1882).

221. Koch, R. *Untersuchung über die Aetiologie der Wundinfektionskrankheiten*. (Vogel, 1878).

222. Packalen, T. & Bergqvist, S. *Staphylococci* in throat and nose and antistaphylolysin titre. *Acta Med. Scand.* **127,** 291–312 (1947).

223. Williams, R. E. O. Skin and nose carriage of bacteriophage types of *Staph. aureus. J. Pathol. Bacteriol.* **58,** 259–268 (1946).

224. Gould, J. C. & McKillop, E. J. The carriage of *Staphylococcus pyogenes var. aureus* in the human nose. *J. Hyg. (Lond).* **52,** 304–10 (1954).

225. Devenish, E. A. & Miles, A. A. Control of *Staphylococcus aureus* in an operating-theatre. *Lancet* **233,** 1088–1094 (1939).

226. Williams, R. E. *et al.* Nasal *staphylococci* and sepsis in hospital patients. *Br. Med. J.* **2,** 658–62 (1959).

227. McCaig, L., McDonald, L., Mandal, S. & Jernigan, D. *Staphylococcus aureus* –associated skin and soft tissue infections in ambulatory care. *Emerg. Infect. Dis.* **12,** 1715–1723 (2006).

228. Jevons, M. P. 'Celbenin' - resistant *Staphylococci. Br. Med. J.* **1,** 124 (1961).

229. Bacon, A. E., Jorgensen, K. A., Wilson, K. H. & Kauffman, C. A. Emergence of nosocomial Methicillin-resistant *Staphylococcus aureus* and therapy of colonized personnel during a hospital-wide outbreak. *Infect. Control* **8,** 145–150 (1987).

230. Moran, G. J. *et al.* Methicillin-Resistant *S. aureus* Infections among Patients in the Emergency Department. *N. Engl. J. Med.* **355,** 666–674 (2006).

231. Daum, R. S. Skin and soft-tissue infections caused by Methicillin-resistant Staphylococcus aureus. *N. Engl. J. Med.* **357,** 380–390 (2007).

232. David, M. Z. & Daum, R. S. Community-associated methicillin-resistant *Staphylococcus aureus*: epidemiology and clinical consequences of an emerging epidemic. *Clin. Microbiol. Rev.* **23,** 616–87 (2010).

233. Mölne, L., Verdrengh, M. & Tarkowski, A. Role of neutrophil leukocytes in cutaneous infection caused by *Staphylococcus aureus. Infect. Immun.* **68,** 6162–7 (2000).

234. Morath, S., Stadelmaier, A., Geyer, A., Schmidt, R. R. & Hartung, T. Synthetic lipoteichoic acid from *Staphylococcus aureus* is a potent stimulus of cytokine release. *J. Exp. Med.* **195,** 1635–40 (2002).

235. Takeuchi, O., Hoshino, K. & Akira, S. Cutting edge: TLR2-deficient and MyD88-deficient mice are highly susceptible to *Staphylococcus aureus* infection. *J. Immunol.* **165,** 5392–6 (2000).

236. Olaru, F. & Jensen, L. E. *Staphylococcus aureus* stimulates neutrophil targeting chemokine expression in keratinocytes through an autocrine IL-1alpha signaling loop. *J. Invest. Dermatol.* **130,** 1866–76 (2010).

237. Miller, L. S. *et al.* MyD88 mediates neutrophil recruitment initiated by IL-1R but not TLR2 activation in immunity against *Staphylococcus aureus. Immunity* **24,** 79–91 (2006).

238. von Bernuth, H. *et al.* Pyogenic bacterial infections in humans with MyD88 deficiency. *Science* **321,** 691–6 (2008).

239. Picard, C. *et al.* Pyogenic bacterial infections in humans with IRAK-4 deficiency. *Science* **299,** 2076–9 (2003).

240. Cho, J. S. *et al.* IL-17 is essential for host defense and is efficacious as an immunotherapy against cutaneous *Staphyloccocus aureus* infection in mice. *J. Clin. Invest.* **120,** 1762–1773 (2010).

241. Ma, C. S. *et al.* Deficiency of Th17 cells in hyper IgE syndrome due to mutations in STAT3. *J. Exp. Med.* **205,** 1551–7 (2008).

242. Renner, E. D. *et al.* Novel signal transducer and activator of transcription 3 (STAT3) mutations, reduced T(H)17 cell numbers, and variably defective STAT3 phosphorylation in hyper-IgE syndrome. *J. Allergy Clin. Immunol.* **122,** 181–7 (2008).

243. Gresham, H. D. *et al.* Survival of *Staphylococcus aureus* inside neutrophils contributes to infection. *J. Immunol.* **164,** 3713–22 (2000).

244. Voyich, J. M. *et al.* Insights into mechanisms used by *Staphylococcus aureus* to avoid destruction by human neutrophils. *J. Immunol.* **175,** 3907–3919 (2005).

245. Kubica, M. *et al.* A potential new pathway for *Staphylococcus aureus* dissemination: the silent survival of *S. aureus* phagocytosed by human monocyte-derived macrophages. *PLoS One* **3,** e1409 (2008).

246. Peschel, A. *et al. Staphylococcus aureus* resistance to human defensins and evasion of neutrophil killing via the novel virulence factor MprF is based on modification of membrane lipids with l-lysine. *J. Exp. Med.* **193,** 1067–76 (2001).

247. Collins, L. V. *et al. Staphylococcus aureus* strains lacking D-alanine modifications of teichoic acids are highly susceptible to human neutrophil killing and are virulence attenuated in mice. *J. Infect. Dis.* **186,** 214–9 (2002).

248. Schreiner, J. *et al.* Staphylococcus aureus phenol-soluble modulin peptides modulate dendritic cell functions and increase *in vitro* priming of regulatory T cells. *J. Immunol.* **190,** 3417–26 (2013).

249. Peschel, A. *et al.* Inactivation of the dlt operon in *Staphylococcus aureus* confers sensitivity to defensins, protegrins, and other antimicrobial peptides. *J. Biol. Chem.* **274,** 8405–10 (1999).

250. Jin, T. *et al. Staphylococcus aureus* resists human defensins by production of staphylokinase, a novel bacterial evasion mechanism. *J. Immunol.* **172,** 1169–76 (2004).

251. Shompole, S. *et al.* Biphasic intracellular expression of *Staphylococcus aureus* virulence factors and evidence for Agr-mediated diffusion sensing. *Mol. Microbiol.* **49,** 919–27 (2003).

252. Giese, B. *et al.* Expression of δ-toxin by *Staphylococcus aureus* mediates escape from phago-endosomes of human epithelial and endothelial cells in the presence of β-toxin. *Cell. Microbiol.* **13,** 316–29 (2011).

253. Grosz, M. *et al.* Cytoplasmic replication of *Staphylococcus aureus* upon phagosomal escape triggered by phenol-soluble modulin-alpha. *Cell. Microbiol.* **16,** 451–465 (2014).

254. Surewaard, B. G. J. *et al. Staphylococcal* alpha-phenol soluble modulins contribute to neutrophil lysis after phagocytosis. *Cell. Microbiol.* **15,** 1427–37 (2013).

255. O'Keeffe, K. M. *et al.* Manipulation of autophagy in phagocytes facilitates *Staphylococcus aureus* bloodstream infection. *Infect. Immun.* **83,** 3445–3457 (2015).

256. Singh, R. *et al.* Autophagy regulates lipid metabolism. *Nature* **458,** 1131–5 (2009).

257. Kohout, M., Kohoutova, B. & Heimberg, M. The regulation of hepatic triglyceride metabolism by free fatty acids. *J. Biol. Chem.* **246,** 5067–74 (1971).

258. Kuerschner, L., Moessinger, C. & Thiele, C. Imaging of lipid biosynthesis: how a neutral lipid enters lipid droplets. *Traffic* **9,** 338–52 (2008).

259. Sinha, R. A. *et al.* Thyroid hormone regulation of hepatic lipid and carbohydrate metabolism. *Trends Endocrinol. Metab.* **25,** 538–545 (2014).

260. Souza, S. C. *et al.* Modulation of hormone-sensitive lipase and protein kinase A-mediated lipolysis by perilipin A in an adenoviral reconstituted system. *J. Biol. Chem.* **277,** 8267–72 (2002).

261. Vaughan, M., Berger, J. E. & Steinberg, D. Hormone-sensitive lipase and monoglyceride lipase activities in adipose tissue. *J. Biol. Chem.* **239,** 401–9 (1964).

262. Dupont, N. *et al.* Neutral lipid stores and lipase PNPLA5 contribute to autophagosome biogenesis. *Curr. Biol.* **24,** 609–620 (2014).

263. Kaushik, S. & Cuervo, A. M. Degradation of lipid droplet-associated proteins by chaperone-mediated autophagy facilitates lipolysis. *Nat. Cell Biol.* **17,** 759–70 (2015).

264. Kaushik, S. & Cuervo, A. M. AMPK-dependent phosphorylation of lipid droplet protein PLIN2 triggers its degradation by CMA. *Autophagy* **12,** 432–8 (2016).

265. Rambold, A. S., Cohen, S. & Lippincott-Schwartz, J. Fatty acid trafficking in starved cells: Regulation by lipid droplet lipolysis, autophagy, and mitochondrial fusion dynamics. *Dev. Cell* **32,** 678–692 (2015).

266. Settembre, C. *et al.* TFEB controls cellular lipid metabolism through a starvation-induced autoregulatory loop. *Nat. Cell Biol.* **15,** 647–58 (2013).

267. O'Rourke, E. J. & Ruvkun, G. MXL-3 and HLH-30 transcriptionally link lipolysis and autophagy to nutrient availability. *Nat. Cell Biol.* **15,** 668–76 (2013).

268. Kassi, E. *et al.* Metabolic syndrome: definitions and controversies. *BMC Med.* **9,** 48 (2011).

269. Ezaki, J. *et al.* Liver autophagy contributes to the maintenance of blood glucose and amino acid levels. *Autophagy* **7,** 727–736 (2011).

270. Kuma, A. *et al.* The role of autophagy during the early neonatal starvation period. *Nature* **432,** 1032–1036 (2004).

271. Yang, L. *et al.* Defective hepatic autophagy in obesity promotes ER stress and causes insulin resistance. *Cell Metab.* **11,** 467–478 (2010).

272. Liebich, H. G. *Funktionelle Histologie der Haussäugetiere und Vögel.* (2010).

273. Vernon, R. G. & Clegg, R. A. in *New perspectives in adipose tissue: structure, Function and Development* (eds. Cryer, A. & Van, R. L. R.) 65–86 (1985).

274. Slavin, B. G. in *New perspectives in adipose tissue: Structure, Function and Development* (eds. Cryer, A. & Van, R. L. .) 23–43 (1985).

275. Himms-Hagen, J. in *New perspectives in adipose tissue: Structure, Function and Development* (eds. Cryer, A. & Van, R. L. R.) 199–222 (1985).

276. Zhang, Y. *et al.* Adipose-specific deletion of autophagy-related gene 7 (atg7) in mice reveals a role in adipogenesis. *Proc. Natl. Acad. Sci.* **106,** 19860–19865 (2009).

277. Baerga, R., Zhang, Y., Chen, P.-H., Goldman, S. & Jin, S. Targeted deletion of autophagy-related 5 (atg5) impairs adipogenesis in a cellular model and in mice. *Autophagy* **5,** 1118–30 (2009).

278. Singh, R. *et al.* Autophagy regulates adipose mass and differentiation in mice. *J. Clin. Invest.* **119,** 3329–3339 (2009).

279. Goldman, S. J., Zhang, Y. & Jin, S. Autophagic degradation of mitochondria in white adipose tissue differentiation. *Antioxid. Redox Signal.* **14,** 1971–8 (2011).

280. Kovsan, J. *et al.* Altered autophagy in human adipose tissues in obesity. *J. Clin. Endocrinol. Metab.* **96,** E268-77 (2011).

281. Gomes, L. C. & Dikic, I. Autophagy in antimicrobial immunity. *Mol. Cell* **54,** 224–233 (2014).

282. Mestre, M. B., Fader, C. M., Sola, C. & Colombo, M. I. Alpha-hemolysin is required for the activation of the autophagic pathway in *Staphylococcus aureus*-infected cells. *Autophagy* **6,** 110–125 (2010).

283. Schnaith, A. *et al. Staphylococcus aureus* subvert autophagy for induction of caspase-independent host cell death. *J. Biol. Chem.* **282,** 2695–706 (2007).

284. Yang, L., Li, P., Fu, S., Calay, E. S. & Hotamisligil, G. S. Defective hepatic autophagy in obesity promotes ER stress and causes insulin resistance. *Cell Metab.* **11,** 467–478 (2010).

285. Bruns, S. Untersuchungen zu einer potentiellen p38 MAPK *docking domain* im Autophagie-Protein ATG5 - Masterarbeit. (2012).

286. Adams, R. H. *et al.* Essential role of p38alpha MAP kinase in placental but not embryonic cardiovascular development. *Mol Cell* **6,** 109–116 (2000).

287. Sibbald, M. J. J. B. *et al.* Partially overlapping substrate specificities of *staphylococcal* Group A sortases. *Proteomics* **12,** 3049–3062 (2012).

288. Neumann, Y. *et al. Staphylococcus aureus* eludes selective autophagy by activating a host cell kinase. *Autophagy* (2016). doi:10.1080/15548627.2016.1226732

289. Mizushima, N., Yamamoto, A., Matsui, M., Yoshimori, T. & Ohsumi, Y. In Vivo Analysis of Autophagy in Response to Nutrient Starvation Using Transgenic Mice Expressing a Fluorescent Autophagosome Marker. *Mol. Biol. Cell* **15,** 1101–1111 (2004).

290. Gupta, M. *et al.* Hematopoietic cells from Gadd45alpha- and Gadd45beta-deficient mice are sensitized to genotoxic-stress-induced apoptosis. *Oncogene* **24,** 7170–9 (2005).

291. Haenebalcke, L. *et al.* Efficient ROSA26-based conditional and/or inducible transgenesis using RMCE-compatible F1 hybrid mouse embryonic stem cells. *Stem Cell Rev.* **9,** 774–85 (2013).

292. Seligman, A. M., Wasserkrug, H. L. & Hanker, J. S. A new staining method (OTO) for enhancing contrast of lipid--containing membranes and droplets in osmium tetroxide--fixed tissue with osmiophilic thiocarbohydrazide(TCH). *J. Cell Biol.* **30,** 424–432 (1966).

293. Sandhu, U. *et al.* Strict control of transgene expression in a mouse model for sensitive biological applications based on RMCE compatible ES cells. *Nucleic Acids Res.* **39,** e1 (2011).

294. Kearse, M. *et al.* Geneious Basic: an integrated and extendable desktop software platform for the organization and analysis of sequence data. *Bioinformatics* **28,** 1647–9 (2012).

295. Abràmoff, M. D., Magalhães, P. J. & Ram, S. J. Image processing with imageJ. *Biophotonics Int.* **11,** 36–41 (2004).

296. Bardwell, A. J., Frankson, E. & Bardwell, L. Selectivity of docking sites in MAPK kinases. *J. Biol. Chem.* **284,** 13165–13173 (2009).

297. Mauvezin, C., Nagy, P., Juhász, G. & Neufeld, T. P. Autophagosome-lysosome fusion is independent of V-ATPase-mediated acidification. *Nat. Commun.* **6,** 7007 (2015).

298. Shvets, E. & Elazar, Z. Flow cytometric analysis of autophagy in living mammalian cells. *Methods Enzymol.* **452,** 131–41 (2009).

299. Sanjuan, M. A. *et al.* Toll-like receptor signalling in macrophages links the autophagy pathway to phagocytosis. *Nature* **450,** 1253–1257 (2007).

300. Henault, J. *et al.* Noncanonical autophagy is required for type I interferon secretion in response to DNA-immune complexes. *Immunity* **37,** 986–997 (2013).

301. Stolz, A., Ernst, A. & Dikic, I. Cargo recognition and trafficking in selective autophagy. *Nat. Cell Biol.* **16,** 495–501 (2014).

302. Rogov, V., Dötsch, V., Johansen, T. & Kirkin, V. Interactions between autophagy receptors and ubiquitin-like proteins form the molecular basis for selective autophagy. *Mol. Cell* **53,** 167–78 (2014).

303. Baxt, L. A., Garza-Mayers, A. C. & Goldberg, M. B. Bacterial subversion of host innate immune pathways. *Science (80-.).* **340,** 697–701 (2013).

304. Lam, G. Y., Czuczman, M. A., Higgins, D. E. & Brumell, J. H. *Interactions of* Listeria monocytogenes *with the autophagy system of host cells - Chapter 2*. *Advances in Immunology* **113,** (Elsevier Inc., 2012).

305. Dong, N. *et al.* Structurally distinct bacterial TBC-like GAPs link Arf GTPase to Rab1 inactivation to counteract host defenses. *Cell* **150,** 1029–1041 (2012).

306. Choy, A. *et al.* The *Legionella* effector RavZ inhibits host autophagy through irreversible Atg8 deconjugation. *Science* **338,** 1072–6 (2012).

307. Mizushima, N. & Yoshimori, T. How to interpret LC3 immunoblotting. *Autophagy* **3,** 4–7 (2007).

308. Singh, R. & Cuervo, A. M. Lipophagy: connecting autophagy and lipid metabolism. *Int. J. Cell Biol.* **2012,** 282041 (2012).

309. Ren, S. Y. & Xu, X. Role of autophagy in metabolic syndrome-associated heart disease. *Biochim. Biophys. Acta* **1852,** 225–31 (2015).

310. Zhang, Y., Xu, X. & Ren, J. MTOR overactivation and interrupted autophagy flux in obese hearts. *Autophagy* **9,** 1–3 (2013).

311. Czaja, M. J. *et al.* Functions of autophagy in normal and diseased liver. *Autophagy* **9,** 1131–1158 (2013).

312. Casteilla, L., Pénicaud, L., Cousin, B. & Calise, D. in *Methods in Molecular bBology Adipose Tissue Protocols* (ed. Yang, K.) **456,** 23–38 (2008).

313. Qin, J. Y. *et al.* Systematic comparison of constitutive promoters and the doxycycline-inducible promoter. *PLoS One* **5,** e10611 (2010).

314. Wang, N., Rajasekaran, N., Hou, T. & Mellins, E. D. Transgene expression in various organs post BM-HSC transplantation. *Stem Cell Res.* **12,** 209–21 (2014).

315. Nguyen, A. T., Dow, A. C., Kupiec-Weglinski, J., Busuttil, R. W. & Lipshutz, G. S. Evaluation of gene promoters for liver expression by hydrodynamic gene transfer. *J. Surg. Res.* **148,** 60–6 (2008).

316. Ramezani, A., Hawley, T. S. & Hawley, R. G. Lentiviral vectors for enhanced gene expression in human hematopoietic cells. *Mol. Ther.* **2,** 458–69 (2000).

317. Chen, C., Krohn, J., Bhattacharya, S. & Davies, B. A Comparison of Exogenous Promoter Activity at the ROSA26 Locus Using a PhiC31 Integrase Mediated Cassette Exchange Approach in Mouse ES Cells. *PLoS One* **6,** e23376 (2011).

318. Fujita, N. *et al.* The Atg16L complex specifies the site of LC3 lipidation for membrane biogenesis in autophagy. *Mol. Biol. Cell* **19,** 2092–100 (2008).

319. Saitoh, T. *et al.* Loss of the autophagy protein Atg16L1 enhances endotoxin-induced IL-1 beta production. *Nature* **456,** 264-U68 (2008).

320. Kim, H. J. *et al.* Beclin-1-interacting autophagy protein Atg14L targets the SNARE-associated protein Snapin to coordinate endocytic trafficking. *J. Cell Sci.* **125,** 4740–50 (2012).

321. Koyama-Honda, I., Itakura, E., Fujiwara, T. K. & Mizushima, N. Temporal analysis of recruitment of mammalian ATG proteins to the autophagosome formation site. *Autophagy* **9,** 1491–1499 (2013).

322. Zhang, X.-M., Walsh, B., Mitchell, C. A. & Rowe, T. TBC domain family, member 15 is a novel mammalian Rab GTPase-activating protein with substrate preference for Rab7. *Biochem. Biophys. Res. Commun.* **335,** 154–61 (2005).

323. Hegedus, K. *et al.* The Ccz1-Mon1-Rab7 module and Rab5 control distrinct steps of autophagy. *Mol. Biol. Cell* (2016).

324. Wang, R. C. *et al.* Akt-mediated regulation of autophagy and tumorigenesis through Beclin 1 phosphorylation. *Science* **338,** 956–9 (2012).

325. Wei, Y. *et al.* EGFR-mediated beclin 1 phosphorylation in autophagy suppression, tumor progression, and tumor chemoresistance. *Cell* **154,** 1269–1284 (2013).

326. Cherra, S. J. *et al.* Regulation of the autophagy protein LC3 by phosphorylation. *J. Cell Biol.* **190,** 533–539 (2010).

327. Klionsky DJ, Abdelmohsen K, Abe A, Abedin MJ, Abeliovich H, Acevedo Arozena A, Adachi H, Adams CM, Adams PD, Adeli K, Adhihetty PJ, Adler SG, Agam G, Agarwal R, Aghi MK, Agnello M, Agostinis P, Aguilar PV, Aguirre-Ghiso J, Airoldi EM, Ait-Si-Ali S, Akemat, Z. Guidelines for use and interpretation of assays for monitoring autophagy (3rd edition). *Autophagy* **12,** 1–222 (2016).

328. Inui, M. *et al.* Rapid generation of mouse models with defined point mutations by the CRISPR/Cas9 system. *Sci. Rep.* **4,** 5396 (2014).

329. Eng, K. E., Panas, M. D., Karlsson Hedestam, G. B. & McInerney, G. M. A novel quantitative flow cytometry-based assay for autophagy. *Autophagy* **6,** 634–641 (2010).

330. Goloudina, A. *et al.* Regulation of human Cdc25A stability by Serine 75 phosphorylation is not sufficient to activate a S phase checkpoint. *Cell Cycle* **2,** 473–8

331. Waskiewicz, A. J., Flynn, A., Proud, C. G. & Cooper, J. A. Mitogen-activated protein kinases activate the serine/threonine kinases Mnk1 and Mnk2. *EMBO J.* **16,** 1909–20 (1997).

332. She, Q. B., Chen, N. & Dong, Z. ERKs and p38 kinase phosphorylate p53 protein at serine 15 in response to UV radiation. *J. Biol. Chem.* **275,** 20444–9 (2000).

333. Kageyama, S. *et al.* The LC3 recruitment mechanism is separate from Atg9L1-dependent membrane formation in the autophagic response against Salmonella. *Mol. Biol. Cell* **22,** 2290–2300 (2011).

334. Jarry, T. M., Memmi, G. & Cheung, A. L. The expression of alpha-haemolysin is required for Staphylococcus aureus phagosomal escape after internalization in CFT-1 cells. *Cell. Microbiol.* **10,** 1801–14 (2008).

335. Martinez, J. *et al.* Molecular characterization of LC3-associated phagocytosis reveals distinct roles for Rubicon, NOX2 and autophagy proteins. *Nat. Cell Biol.* **17,** 893–906 (2015).

336. Martinez, J. *et al.* Microtubule-associated protein 1 light chain 3 alpha (LC3)-associated phagocytosis is required for the efficient clearance of dead cells. *Proc. Natl. Acad. Sci. U. S. A.* **108,** 17396–401 (2011).

337. Lam, G. Y., Cemma, M., Muise, A. M., Higgins, D. E. & Brumell, J. H. Host and bacterial factors that regulate LC3 recruitment to *Listeria monocytogenes* during the early stages of macrophage infection. *Autophagy* **9,** 985–995 (2013).

338. Gutierrez, M. G. *et al.* Autophagy induction favours the generation and maturation of the *Coxiella*-replicative vacuoles. *Cell. Microbiol.* **7,** 981–93 (2005).

339. Pizarro-Cerdá, J. *et al. Brucella abortus* transits through the autophagic pathway and replicates in the endoplasmic reticulum of nonprofessional phagocytes. *Infect. Immun.* **66,** 5711–24 (1998).

340. Amer, A. O. & Swanson, M. S. Autophagy is an immediate macrophage response to *Legionella pneumophila*. *Cell. Microbiol.* **7,** 765–78 (2005).

341. Barnett, T. C. *et al.* The globally disseminated M1T1 clone of Group A *Streptococcus* evades autophagy for intracellular replication. *Cell Host Microbe* **14,** 675–682 (2013).

342. Mesquita, F. S. *et al.* The *Salmonella* deubiquitinase Ssel inhibits selective autophagy of cytosolic aggregates. *PLoS Pathog.* **8,** (2012).

343. Miller, M. *et al.* Mapping of interactions between human macrophages and *Staphylococcus aureus* reveals an involvement of MAP kinase. *J. Proteome Res.* **10,** 4018–32 (2011).

344. Husmann, M. *et al.* Differential role of p38 mitogen activated protein kinase for cellular recovery from attack by pore-forming *S. aureus* α-toxin or streptolysin O. *Biochem. Biophys. Res. Commun.* **344,** 1128–1134 (2006).

345. Surwit, R. S., Kuhn, C. M., Cochrane, C., McCubbin, J. A. & Feinglos, M. N. Diet-induced type II diabetes in C57BL/6J mice. *Diabetes* **37,** 1163–7 (1988).

346. Rossmeisl, M., Rim, J. S., Koza, R. A. & Kozak, L. P. Variation in type 2 diabetes--related traits in mouse strains susceptible to diet-induced obesity. *Diabetes* **52,** 1958–66 (2003).

347. Warden, C. H. & Fisler, J. S. Comparisons of diets used in animal models of high-fat feeding. *Cell Metab.* **7,** 277 (2008).

348. Benoit, B. *et al.* High-fat diet action on adiposity, inflammation, and insulin sensitivity depends on the control low-fat diet. *Nutr. Res.* **33,** 952–60 (2013).

349. Winzell, M. S. & Ahre, B. The high-fat diet-fed mouse: a model for studying mechanisms and treatment of impaired glucose tolerance and type 2 diabetes. *Diabetes* **53,** S215-219 (2004).

350. Gao, S., He, L., Ding, Y. & Liu, G. Mechanisms underlying different responses of plasma triglyceride to high-fat diets in hamsters and mice: Roles of hepatic MTP and triglyceride secretion. *Biochem. Biophys. Res. Commun.* **398,** 619–626 (2010).

351. Eisinger, K. *et al.* Lipidomic analysis of serum from high fat diet induced obese mice. *Int. J. Mol. Sci.* **15,** 2991–3002 (2014).

352. Hayek, T. *et al.* Dietary fat increases high density lipoprotein (HDL) levels both by increasing the transport rates and decreasing the fractional catabolic rates of HDL cholesterol ester and apolipoprotein (apo) A-I. Presentation of a new animal model and mechanistic stud. *J. Clin. Invest.* **91,** 1665–1671 (1993).

353. Brinton, E. A., Eisenberg, S. & Breslow, J. L. A low-fat diet decreases high density lipoprotein (HDL) cholesterol levels by decreasing HDL apolipoprotein transport rates. *J. Clin. Invest.* **85,** 144–51 (1990).

354. Bégin-Heick, N. Of mice and women: the beta 3-adrenergic receptor leptin and obesity. *Biochem. Cell Biol.* **74,** 615–22 (1996).

355. Shi, H., Seeley, R. J. & Legg, D. E. J. C. Sexual differences in the control of energy homeostasis. *Frintiers Neuroendocrinol.* **30,** 396–404 (2009).

356. Yang, Y., Smith Jr., D. L., Keating, K. D., Allison, D. B. & Nagy, T. R. Variations in body weight, food intake and body composition after long-term high fat diet feeding in C57BL/6J mice. *Obes. (Silver Spring)* **22,** 2147–2155 (2014).

357. Clapper, J. R. *et al.* Diet-induced mouse model of fatty liver disease and nonalcoholic steatohepatitis reflecting clinical disease progression and methods of assessment. *Am. J. Physiol. Gastrointest. Liver Physiol.* **305,** G483-95 (2013).

358. Cummins, T. D. *et al.* Metabolic remodeling of white adipose tissue in obesity. *Am. J. Physiol. Endocrinol. Metab.* **307,** E262-77 (2014).

359. Fuhrmeister, J. *et al.* Fasting-induced liver GADD45β restrains hepatic fatty acid uptake and improves metabolic health. *EMBO Mol. Med.* 1–16 (2016). doi:10.15252/emmm.201505801

360. Kigar, S. L., Chang, L., Hayne, M. R., Karls, N. T. & Auger, A. P. Sex differences in Gadd45b expression and methylation in the developing rodent amygdala. *Brain Res.* **1642,** 461–466 (2016).

361. Marson, A. *et al.* Foxp3 occupancy and regulation of key target genes during T-cell stimulation. *Nature* **445,** 931–5 (2007).

362. Floess, S. *et al.* Epigenetic control of the foxp3 locus in regulatory T cells. *PLoS Biol.* **5,** e38 (2007).

363. Nishimura, S. *et al.* CD8+ effector T cells contribute to macrophage recruitment and adipose tissue inflammation in obesity. *Nat. Med.* **15,** 914–20 (2009).

364. Duffaut, C. *et al.* Interplay between human adipocytes and T lymphocytes in obesity: CCL20 as an adipochemokine and T lymphocytes as lipogenic modulators. *Arterioscler. Thromb. Vasc. Biol.* **29,** 1608–14 (2009).

365. Kintscher, U. *et al.* T-lymphocyte infiltration in visceral adipose tissue: a primary event in adipose tissue inflammation and the development of obesity-mediated insulin resistance. *Arterioscler. Thromb. Vasc. Biol.* **28,** 1304–10 (2008).

366. Lumeng, C. N. *et al.* Obesity induces a phenotypic switch in adipose tissue macrophage polarization. *J. Clin. Invest.* **117,** 175–184 (2007).

367. Fischer-Posovszky, P., Wang, Q. A., Asterholm, I. W., Rutkowski, J. M. & Scherer, P. E. Targeted deletion of adipocytes by apoptosis leads to adipose tissue recruitment of alternatively activated M2 macrophages. *Endocrinology* **152,** 3074–81 (2011).

368. Weisberg, S. P. *et al.* Obesity is associated with macrophage accumulation in adipose tissue. *J. Clin. Invest.* **112,** 1796–808 (2003).

369. Deng, T. *et al.* Class II major histocompatibility complex plays an essential role in obesity-induced adipose inflammation. *Cell Metab.* **17,** 411–422 (2013).

9 ACKNOWLEDGEMENTS

The first person I want to thank is my supervisor Prof Dr. Ingo Schmitz, who gave me the possibility to do my PhD thesis in his working group. He offered me an interesting and challenging project that combined different facets and enabled me to gain a deep scientific knowledge about the complex interrelations in biological signaling. Furthermore, the diversity of methods I was able to learn and to apply in his lab greatly sharpened my scientific profile. During my PhD thesis, I appreciated very much the supportive and helpful discussions with Prof. Dr. Ingo Schmitz, whose door was open at any time.

Special thanks goes to my colleagues Anne-Marie, Carlos, Christian, Claudia, Daniela, Konstantinos, Leon, Lisa, Neda, Sabrina, Tobi, Yan Yan and the former group members Alisha, Frida, Marc, Michaela, Ralf, Tanja and Yvonne. You created a really nice and joyful working atmosphere characterized by mutual motivation and support. Thus, you all contributed largely to the success of this thesis. Konstantinos and Frida, thank you very much for correcting my thesis and for giving a lot of helpful input during writing.

I want to thank the members of my thesis committee Prof. Dr. Dagmar Wirth and PD. Dr. Björn Stork for their support during the development of this thesis. Additionally, I want to thank Dr. Andrea Scrima and his co-workers for the close cooperation and Andrea especially for the help with PyMOL. In addition, I want to acknowledge Prof. Dr. Manfred Rohde and co-workers for the transmission electron microscopy analysis, Dr. Lothar Gröbe for his help with sorting, Dr. Marina Pils and Dr. Ulrike Heise and co-workers for the histological work as well as Dr. Josef Wissing and co-workers for the mass spectrometry analysis.

I am deeply grateful to my friends and my family, especially to my parents and my sister Neele, for all the great support and interest in my work.

Finally, I want to thank André for his understanding and willingness to manage this intense time despite our distance-relationship. Thank you for all the things next to work and science, for your incessantly encouragement and your love.

10 DECLARATION OF ORIGINALITY

Svenja Anne Bruns
Am Bruchtor 2a
38100 Braunschweig

Hiermit erkläre ich, dass ich die von mir eingereichte Dissertation mit dem Thema

Autophagy regulation by the p38 MAP kinase

selbständig verfasst, nicht schon als Dissertation verwendet habe und die benutzten Hilfsmittel und Quellen vollständig angegeben wurden.

Weiterhin erkläre ich, dass ich weder diese, noch eine andere Arbeit zur Erlangung des akademischen Grades doctor rerum naturalium (Dr. rer. nat.) an anderen Einrichtungen eingereicht habe.

Magdeburg, 27. September 2016

Svenja Bruns

11 CURRICULUM VITAE

Persönliche Details
Name	Svenja Anne Bruns
Geburtsdatum:	24. Oktober 1987 in Oldenburg
Nationalität:	Deutsch
Adresse:	Am Bruchtor 2a
	38100 Braunschweig

Schulausbildung
1994-1998	Grundschule Großenkneten
1998-2000	Graf-von-Zeppelin-Schule Ahlhorn (Orientierungsstufe)
2000-2004	Dietrich-Bonhoeffer-Gymnasium Ahlhorn
2004-2007	Gymnasium Graf-Anton-Günther-Schule Oldenburg (Abitur)

Studium
10/2007–08/2010	Biochemie Studium an der Universtät Bielefeld (B.Sc. Biochemie)
10/2010–12/2012	Biochemie Studium im Masterspezialisierungsprofil „Zelluläre Biochemie" an der Universität Bielefeld (M.Sc. Biochemie)
seit 02/2013	Promotionsstudium in der Arbeitsgruppe „Systemorientierte Immunologie und Entzündungsforschung" von Prof. Dr. Ingo Schmitz am Helmholtz-Zentrum für Infektionsforschung Braunschweig und der Otto-von-Guericke-Universität Magdeburg

Berufserfahrung
07/2007 - 08/2007	8-wöchiges Praktikum im Bereich Veterinärdiagnostik Lebensmittel- und Futtermittelsicherheit; AniCon Labor GmbH, Höltinghausen
08/2008 - 09/2008	4-wöchiges Praktikum im Bereich Veterinärdiagnostik, Lebensmittel- und Futtermittelsicherheit; Labor der Tierärztliche Gemeinschaftspraxis Wilms-Schulze Kump, Ellert, Klosterhalfen (WEK), Visbek
seit 02/2013	Wissenschaftliche Mitarbeiterin in der Arbeitsgruppe von Prof. Dr. Ingo Schmitz

Besondere Kenntnisse und Fähigkeiten
11/2013	FELASA B Kurs (tierexperimentelles Arbeiten)
02/2016	2-tägiger Kurs „Project Management for Young Scientists"
04/2016	3-tägiger Kurs „Career and Leadership Development"

Publikation
"Intracellular *Staphylococcus aureus* eludes selective autophagy by activating a host cell kinase." Neumann Y., Bruns SA., Rohde M., Prajsnar TK., Foster SJ und Schmitz I. *Autophagy* 2016 - im Druck (DOI: 10.1080/15548627.2016.1226732).

Magdeburg, 27. September 2016

Svenja Bruns